Control of Manipulators on Moving Platforms Under Disturbance

by

Jon Woolfrey

A thesis submitted in partial fulfilment of the
requirements for the degree of Doctor of Philosophy

at the
Centre for Autonomous Systems
Faculty of Engineering and Information Technology
University of Technology Sydney

February 2020

Certificate of Original Authorship

I, Jonathan Woolfrey, declare that this thesis is submitted in fulfilment of the requirements for the award of Doctor of Philosophy in the Faculty of Engineering and Information Technology at the University of Technology Sydney.

This thesis is wholly my own work unless otherwise reference or acknowledged. In addition, I certify that all information sources and literature used are indicated in the thesis.

This document has not been submitted for qualifications at any other academic institution.

This research is supported by the Australian Government Research Training Program.

Signed: Production Note: Signature removed prior to publication.

Date: 21st February 2020

Control of Manipulators on Moving Platforms Under Disturbance

by

Jon Woolfrey

A thesis submitted in partial fulfilment of the requirements for the degree of Doctor of Philosophy

Abstract

Mobile robots, such as underwater vehicles, drones, and rovers, are now being combined with manipulators to perform a variety of work in the field. But current state of the art in control assumes that disturbances from the environment are minimal. However, the effects of wind, waves, and rough terrain may make it difficult for the vehicle to maintain a steady base for the manipulator. Or, in some cases, the vehicle may lack the control authority to negate disturbances in all directions. In this thesis, predictions of the base motion are used to formulate control strategies that enable a manipulator to proactively counter, and even make use of, these disturbances.

Time series and Fourier series are commonly applied to many predictive control methods in literature. However, there are contradictory results in performance for different applications. To clarify these discrepancies, an objective comparison in prediction performance is made between time series, Fourier series, and Gaussian Process Regression (GPR) using motion data from underwater robots in waves. Analysis of the forecast errors and uncertainties show that GPR can produce better short-term. Furthermore, time series was found to be overconfident in the prediction, whereas Fourier series had the largest uncertainty.

A predictive control method is then presented that enables a manipulator on a free-moving platform to maintain a steady end-effector pose. By using forecasts of the base motion,

the manipulator can anticipate and negate this disturbance. Simulations and experiments are conducted, and it is shown that the proposed predictive control can reduce tracking error by 60% compared to a PID feedback controller. Moreover, kinematic constraints can be satisfied whilst simultaneously minimizing task error.

A control strategy is also developed that allows a redundant manipulator to use the inertial forces produced by base disturbance to reduce joint torque. Further improvements are made by predicting changes in gravitational acceleration with respect to the manipulator. It is shown that joint torques can be reduced by 25% compared to a local minimization of the weighted torque norm.

Lastly, a torque minimization method is presented for redundant manipulators handling large external forces. Most literature only addresses the internal dynamics. This thesis presents a method to minimize torque from both an external loading and the internal dynamics. This method can be applied to manipulators on moving platforms, and further enhanced by incorporating the base motion predictions.

Acknowledgements

Dr. Andrew To	For his generous help with data collection and conducting experiments for my research.
Clyde Webster	For his assistance with my research experiments.
Prof. Dikai Liu	For offering me the opportunity to complete my PhD, and unwavering support.
Dr. Gavin Paul	For giving me the opportunity to teach and share my knowledge.
Dr. Khoa Le	For his generosity in helping me with experiments.
Dr. Marc Carmichael	For the years of discussions, advice, and teaching opportunities.
Sheila Sutjipto	For her endless patience helping me with experiments and listening to me prattle on about my research.
Dr. Stephen Woodcock	For his guidance with time series prediction.
Dr. Teresa Vidal-Calleja	For her help with implenting Gaussian Process Regression.
Dr. Wenjie Lu	For all the knowledge, help, guidance, and support. I would not have made it this far otherwise.
My cat Kismet	For her emotional support, and constant reminders not to take life too seriously.
My parents	Christoper & Brigitte Woolfrey, for their endless years of care and support, without whom this would not have been possible.

Contents

List of Figures

List of Tables

Acronyms & Abbreviations

2D	2-Dimensional
ACFR	Australian Center for Field Robotics
ADCP	Acoustic Doppler Current Profiler
AGV	Autonomous Ground Vehicle
AIC	Akaike Information Criterion
AR	Autoregression
ARMA	Autoregression Moving-Average
AUV	Autonomous Underwater Vehicle
BIC	Bayes Information Criterion
CAS	Centre for Autonomous Systems
DOF	Degree(s)-of-Freedom
EJTM	External Joint Torque Minimization
EKF	Extended Kalman Filter
DLS	Damped Least Squares
GP	Gaussian Process
GPR	Gaussian Process Regression
IMU	Inertial Measurement Unit

KF	Kalman Filter
MA	Moving-Average
MKE	Minimum Kinetic Energy
MPC	Model Predictive Control
P	Proportional
PD	Proportional-Derivative
PEEC	Predictive End-Effector Control
PID	Proportional-Integral-Derivative
PJTM	Predictive Joint Torque Minimization
QP	Quadratic Programming
RMSE	Root Mean Squared Error
ROS	Robot Operating System
ROV	Remote Operated Vehicle
SAUVIM	Semi-Autonomous Underwater Vehicle for Intervention Missions
SPIR	Submerged Pile Inspection Robot
UAV	Unmanned Aerial Vehicle
UAVMS	Unmanned Aerial Vehicle-Manipulator System
UTS	University of Technology Sydney
UVMS	Underwater Vehicle-Manipulator System
WLN	Weighted Least Norm

Nomenclature

	General Formatting Style
$\mathrm{x} \in \mathbb{R}$	A scalar
$\mathbf{x} \in \mathbb{R}^{\mathrm{m}}$	A vector
$\hat{\mathbf{x}} \in \mathbb{R}^{\mathrm{m}}$	A unit vector
$\mathbf{X} \in \mathbb{R}^{\mathrm{m}\times\mathrm{n}}$	A matrix
	Operators
$\|\cdot\|$	Euclidean norm
$*$	Quaternion multiplication
$\mathrm{f}(\cdot) \in \mathbb{R}$	A scalar function
$\mathbf{f}(\cdot) \in \mathbb{R}^{\mathrm{m}}$	A vector function
$\mathbf{F}(\cdot) \in \mathbb{R}^{\mathrm{m}\times\mathrm{n}}$	A matrix function
$S(\cdot) \in \mathbb{R}^{\mathrm{m}\times\mathrm{m}}$	Skew-symmetric matrix operator
	Accents
$\dot{\mathrm{x}}$	First time-derivative dx/dt
$\ddot{\mathrm{x}}$	Second time-derivative $\mathrm{d}^2\mathrm{x}/\mathrm{dt}^2$
$\hat{\mathrm{x}}$	State estimate of x
	Specific Symbols
$\{\mathrm{F}\}$	A frame of reference in Cartesian space
$\mathbf{J}^{\dagger} \in \mathbb{R}^{\mathrm{n}\times\mathrm{m}}$	Pseudoinverse of a non-square matrix $\mathbf{J} \in \mathbb{R}^{\mathrm{m}\times\mathrm{n}}$, where $\mathrm{m} \neq \mathrm{n}$
$\mathbf{J}^{\dagger}_{\mathrm{W}} \in \mathbb{R}^{\mathrm{n}\times\mathrm{m}}$	Weighted pseudoinverse of a non-square matrix $\mathbf{J} \in \mathbb{R}^{\mathrm{m}\times\mathrm{n}}$

$\mathbf{N}_{\mathrm{W}} \in \mathbb{R}^{\mathrm{n}\times\mathrm{n}}$	Weighted null space projection matrix for a redundant manipulator.
$\mathbf{p} \in \mathbb{R}^3$	A position or translation vector in Cartesian space
${}^{\mathrm{A}}\mathbf{p} \in \mathbb{R}^3$	A position or translation vector specified in frame {A}
$\mathbf{p}_{\mathrm{A}}^{\mathrm{B}} \in \mathbb{R}^3$	A translation vector from frame {A} to frame {B}, w.r.t. {A}
$\mathbf{q} \in \mathbb{R}^{\mathrm{n}}$	Joint position vector for a manipulator
$\mathcal{Q} \in \mathbb{H}$	A quaternion
$\mathbf{R}_{\mathrm{A}}^{\mathrm{B}} \in \mathbb{SO}(3)$	A rotation matrix from frame {A} to frame {B}
$\sigma_{\mathrm{x}}^2 \in \mathbb{R}$	Variance of a single random variable x.
$\mathbf{\Sigma}_{\mathrm{x}} \in \mathbb{R}^{\mathrm{n}\times\mathrm{n}}$	Variance-covariance matrix of a set of random variables $\mathbf{x} \in \mathbb{R}^{\mathrm{n}}$
$\mathbf{T}_{\mathrm{A}}^{\mathrm{B}} \in \mathbb{SE}(3)$	A homogeneous transformation matrix from frame {A} to frame {B}
$\mathbf{w} \in \mathbb{R}^{\mathrm{m}}$	A wrench of forces and torques.
$\hat{\mathrm{y}}(\mathrm{t}+\mathrm{i}\vert\mathrm{t}+\mathrm{j})$	A state estimate of y at time $\mathrm{t}+\mathrm{i}$ from time $\mathrm{t}+\mathrm{j}$.

Glossary of Terms

Autonomous	Without human intervention.
Bathymetry	The measurement of depth of water in oceans, seas, or lakes.
End-effector	The extremity of a robot arm designed for interacting with the external environment.
Heave	Vertical motion (z-direction).
Manipulator	A robotic arm design to handle physical objects.
Pitch	Rotation about the y-axis.
Roll	Rotation about the x-axis .
Surge	Forward motion (x-direction).
Sway	Sideways motion (y-direction).
Yaw	Rotation about the z-axis .

Chapter 1

Introduction

Robotics have revolutionized manufacturing, increasing productivity due to their efficacy in performing repetitive tasks with speed and accuracy. Furthermore, they prevent the need for humans to labour in hazardous environments or handle unsafe materials. This makes autonomous machines ideal candidates to operate in extreme environments, such as underwater, in space, or on alien planets. A pertinent example of this is NASAs Mars Rover Curiosity, which had recently been decommissioned in February 2019 due to loss of communications after a recent dust storm, Fig. 1.1a (NASA, 2019). The deep sea also presents another frontier for exploration and research that precludes direct human intervention due to the water pressure, darkness, and lack of air. The GIRONA 500 AUV, for example, is a popular platform for oceanography and research, Fig. 1.1b (Girona Underwater Vision & Robotics, 2019). The Australian Centre for Field Robotics (ACFR) at the University of Sydney has also pioneered research in marine environments with underwater surveys conducted for oceanography, archaeology, and marine biology (University of Sydney, 2019).

However, these examples are predominantly concerned with observation tasks. As technology advances, robots operating in the field will extend beyond survey missions (such as collecting visual and other sensory information) to performing physical work. In the past, this has primarily revolved around human operators controlling a Remote Operated Vehicle (ROV), and mostly for underwater intervention tasks. On one hand, this circumvents the need for numerous challenges required for autonomy, such as vision processing, path planning, dynamic modelling, and control. On the other, bandwidth is a limiting factor in aquatic communication which has prompted semi-autonomy for underwater intervention. Full autonomy, however, can not only liberate human labour, but circumvent

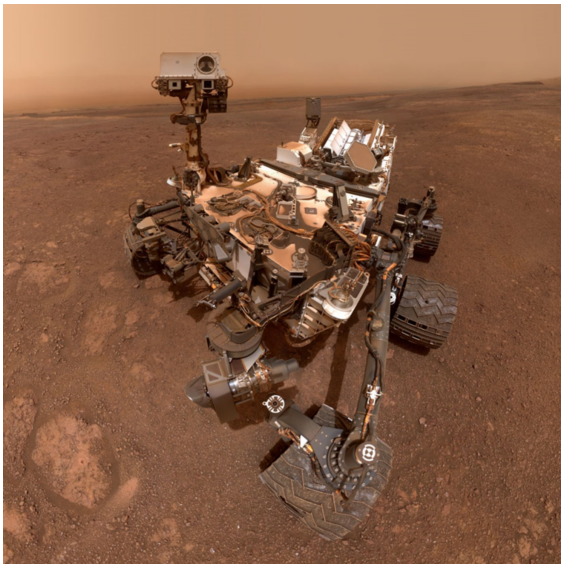

(A) The Mars Rovers Curiosity (NASA, 2019).

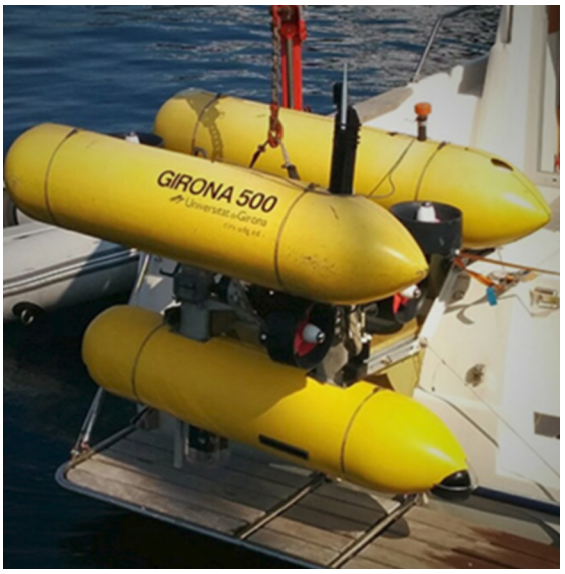

(B) The GIRONA 500 AUV (Girona Underwater Robotics & Vision, 2019).

FIGURE 1.1: Two examples of field robots designed for observation tasks in harsh environments.

finite attention spans and leverage the speed and precision of robotic systems. To that end, autonomous mobile manipulation is proliferating from the marine environment to space and interplanetary missions, agriculture, and even construction. In response to the bandwidth constraints concerning ROVs, the Semi-Autonomous Underwater Vehicle for Intervention Missions (SAUVIM) project was initiated to enable retrieval of objects from the ocean floor with minimal human oversight (Fig. 1.2a) (Yuh et al., 1998; Marani et al., 2009; Marani & Yuh, 2014), . This Underwater Vehicle-Manipulator System (UVMS) circumvented said communications problems by having autonomous controls systems execute tasks given high-level objectives issues by human operators. Furthermore, it precluded the need for any divers to enter the water meaning retrieval missions could be conducted for a longer time and at greater depths.

Similarly, the TRIDENT project features the GIRONA 500 AUV retrofitted with a manipulator enabling it to grasp objects on the ocean floor (Fig. 1.2b)(Sanz et al., 2010; Simetti et al., 2014). Several other projects have also explored underwater manipulation with the GIRONA 500 AUV, such as Maurelli et al. (2016) and the PANDORA project by Cieslak et al. (2015). Both examined how to perform underwater valve-turning operations.

Many of these AUVs and UVMS operate in conditions where water currents are steady and irrotational. Furthermore, the impact of waves and sea swell diminish with increasing depth from the surface of the water (Dean & Dalrymple, 1991). Platforms such as the

(A) The SAUVIM UVMS (Autonomous Underwater Vehicle Applications Centre, 2020)

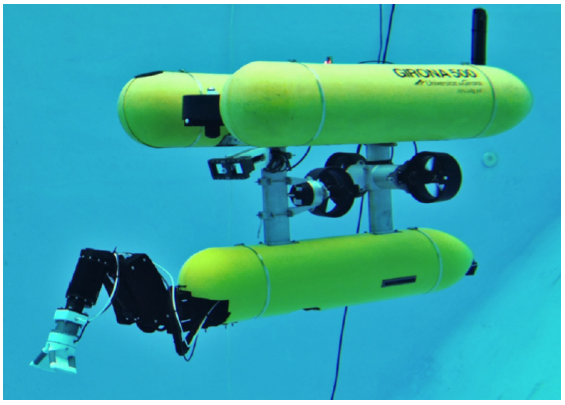

(B) The GIRONA 500 equipped with a manipulator (Girona Underwater Robotics & Vision, 2019)

(C) An example of an Unmanned Aerial Vehicle-Manipulator System (UAVMS) (Lunni et al., 2017)

(D) An UAVMS for infrastructure inspection (Jiminez-Cano et al., 2015)

FIGURE 1.2: Examples of non-inertial mobile-manipulator systems.

SAUVIM and GIRONA 500 can operate up to 500m underwater, and thus have little concern for these types of disturbances.

Contrarily, the Submerged Pile Inspection Robot SPIR being developed at the University of Technology Sydney (UTS) does not have this luxury (Fig. 1.3). This system is designed to perform high-pressure water cleaning of underwater infrastructure. The aquatic environment causes accelerated deterioration to said structures, and regular inspections are required by human divers to ensure the structural integrity. Marine growth in brackish and saline water can cover the surface of these structures, and hence must first be removed before inspections can be conducted. This can either be done through hand-scraping (a laborious task in itself), or high-pressure water blasting. Not only is the underwater environment difficult for humans to work in due to the cold and turbidity but working with high-pressure fluids can have fatal consequences if adequate safety precautions are not fulfilled (Industrial Relations Commission NSW, 2011). Furthermore, there is the threat

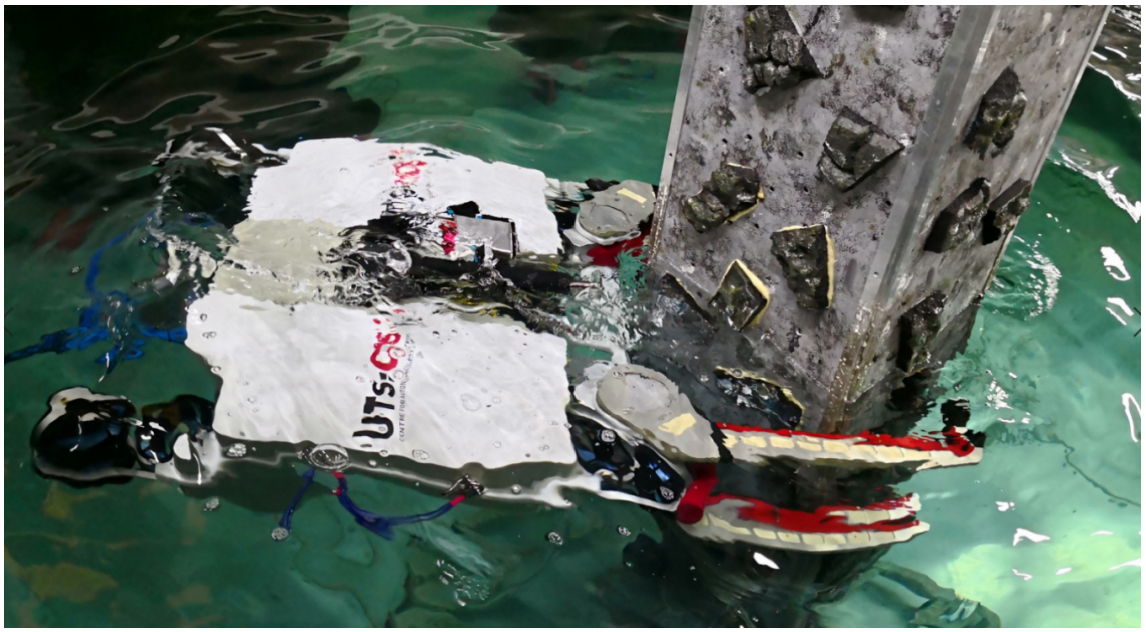

FIGURE 1.3: The SPIR is designed to operate in shallow bathymetry to clean infrastructure.

of predatory animals such as bull sharks in the vicinity (Heupel & Simpfendorfer, 2008). This makes automation an ideal solution.

The rivers and estuaries that the SPIR must work in can feature current flows up to 3 m/s, and turbulence and vortices manifest around bridge support structures (Keshavarzi et al., 2014). The effects of waves in the open sea are also strongest at the surface of the water, precisely where the marine growth is at its most dense (Southgate & Myers, 1985; Kerckhof et al., 2010). High-pressure blasting requires deft control to ensure removal of marine growth without damaging the underlying infrastructure. The hydrodynamic disturbances in these environments could make it difficult for the robot to remain steady.

There is also the case of manipulators attached to Unmanned Aerial Vehicle (UAV). Much of the research and control for UAVMS also operate under the assumption of minimal disturbance. These are becoming increasingly popular for performing object retrieval (Jones 2017; Garimella & Kobilarov, 2016; Lunni et al., 2017). Many of these demonstrations are confined to indoor environments, sheltered from the effects of wind. However, there is increasing need for UAVMS to perform intervention tasks in outdoor environments, such as civil infrastructure inspection with active contact forces (Jiminez-Cano et al., 2015). These small, light-weight vehicles are prone to the effects of wind which could impede their ability to perform accurately if the local weather is not permitting.

Mobile manipulators equipped to Autonomous Ground Vehicle (AGV)s are also becoming more common. Planetary rovers equipped with manipulators may be working on the surface of Mars in the near future, in place of the Curiosity rover (Bussman et al., 2018). Even here on Earth, mobile manipulation is being explored as an avenue for agricultural tasks (Lehnert et al., 2016). Generally, the vehicle serves as a platform to transport the manipulator between locals and remains as a sturdy base when not in use. It is conceivable these vehicle-manipulator systems may be required to perform whilst driving on rough terrain, as is being explored by some researchers (Nguyen & Dancowicz, 2015; Sandy et al., 2017).

In the examples presented thus far, the manipulator has always been accompanied by a vehicle, which can be used to provide support for the manipulator whilst it conducts work. But reliance on the vehicle alone to compensate for disturbances may not be pragmatic nor feasible for several reasons:

- The vehicle may be underactuated, and thus may not have the control authority to negate disturbances in all degrees of freedom:
- The popular quadcopter morphology for UAVs cannot control position independent of orientation.
- A vehicle driving on ground will move with the surface of the terrain, which the manipulator must accept.
- Manipulators on ship platforms in sea swell are subject to large inertial forces which can impede performance (Love et al., 2004; From et al., 2009; From et al., 2011). Unlike their AUV counterparts, the ship cannot be controlled to assist the manipulator. The arm itself must contend with this undesirable motion.
- The control frequency of the vehicle is often much lower than that of the manipulator. This makes it difficult to synchronize the vehicle and manipulator control under a unified framework. It is also not uncommon to have decoupled control in which a manipulator will act on the observed motion of the vehicle platform (Simetti et al., 2014, Yuh et al., 2001; Antonelli et al., 2009).
- The vehicle may simply be unable to overcome the disturbances entirely.

As such, a steady base for a mobile manipulator cannot always be guaranteed. There are two immediate consequences to any form of base motion. Kinematically, the end-effector

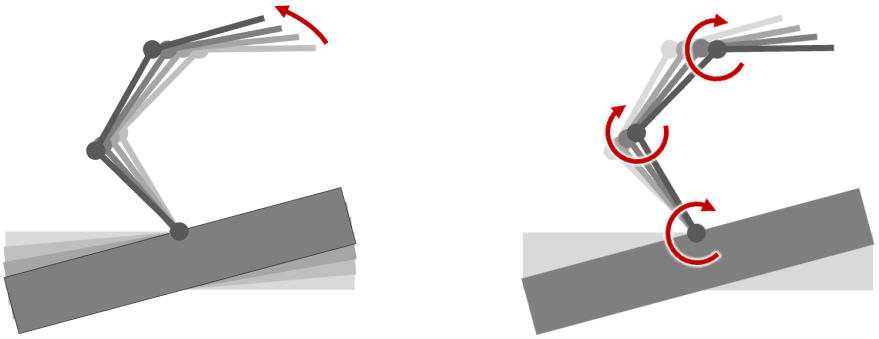

(A) Motion of the manipulator base causes motion of the end-effector.

(B) The manipulator joints must be controlled to counter base motion.

FIGURE 1.4: Kinematic effects of base motion must be accounted for through the joint control.

velocities of the vehicle-manipulator system are given by:

$$\begin{bmatrix} \mathbf{v} \\ \boldsymbol{\omega} \end{bmatrix} = \begin{bmatrix} \mathbf{J}_{\mathrm{v}}\dot{\mathbf{q}} + \mathbf{v}_{\mathrm{b}} + \boldsymbol{\omega}_{\mathrm{b}} \times \mathbf{r} \\ \mathbf{J}_{\omega}\dot{\mathbf{q}} + \boldsymbol{\omega}_{\mathrm{b}} \end{bmatrix}, \tag{1.1}$$

where:

- $\mathbf{v}, \boldsymbol{\omega} \in \mathbb{R}^3$ are the linear and angular velocities of the end-effector respectively,
- $\mathbf{J}_{\mathrm{v}}, \mathbf{J}_{\omega} \in \mathbb{R}^{3\times \mathrm{n}}$ are the linear and angular components of the manipulator Jacobian respectively,
- $\dot{\mathbf{q}} \in \mathbb{R}^{\mathrm{n}}$ are the manipulator joint velocities,
- $\mathbf{v}_{\mathrm{b}}, \boldsymbol{\omega}_{\mathrm{b}} \in \mathbb{R}^3$ are the linear and angular velocities of the base respectively, and
- $\mathbf{r} \in \mathbb{R}^3$ is the translation vector from the base to the end-effector.

Movement of the vehicle or base of the manipulator results in motion of the end-effector, which will interfere with the end-effector control (Fig. 1.4a). Disturbances from the angular motion of the base are also amplified at the end-effector through the cross-product of $\boldsymbol{\omega}_{\mathrm{b}} \times \mathbf{r}$.

Certainly, conventional methods such as feedback control could be applied to correct for any errors in the desired joint state or end-effector pose. But, by definition, feedback control will necessarily lag the effects caused by disturbances. They could also be sufficiently large that feedback control alone is inadequate without some sort of feedforward cancellation (Love et al., 2004). Moreover, by the time the manipulator has moved, the

base may also have moved. The system may therefore be continually trying to pursue a desired target state.

Suppose also the future pose of the base could be predicted for a given number of time steps. With this information, the manipulator could manoeuvre itself to counter disturbances in advance, thereby negating any potential error. Furthermore, a sequence of future poses (or velocities, accelerations) could be used to formulate a strategy that encompasses the effects of all disturbances across some finite horizon.

Contribution #1: *Based on this notion, this thesis presents a Predictive End-Effector Control (PEEC) method for a manipulator subject to undesired base motion. The proposed method uses predictions of the base motion to formulate an optimal control strategy to track a desired end-effector trajectory for a finite prediction-control horizon. This also encompasses kinematic constraints on the joint position and velocity to ensure feasible control whilst reducing task error from disturbances. Under the specific test conditions in both simulation and experiment presented in this thesis, the proposed method was found to reduce tracking error by over 60% compared to a PID feedback controller. This PEEC method is presented in Chapter 4.*

Consider also the dynamics of a vehicle-manipulator system:

$$\begin{bmatrix} \boldsymbol{\tau} \\ \mathbf{f}_\mathrm{b} \end{bmatrix} = \begin{bmatrix} \mathbf{M}_\mathrm{qq} & \mathbf{M}_\mathrm{qb} \\ \mathbf{M}_\mathrm{qb}^\mathrm{T} & \mathbf{M}_\mathrm{bb} \end{bmatrix} \begin{bmatrix} \ddot{\mathbf{q}} \\ \ddot{\mathbf{b}} \end{bmatrix} + \begin{bmatrix} \mathbf{C}_\mathrm{qq} & \mathbf{C}_\mathrm{qb} \\ \mathbf{C}_\mathrm{bq} & \mathbf{C}_\mathrm{bb} \end{bmatrix} \begin{bmatrix} \dot{\mathbf{q}} \\ \dot{\mathbf{b}} \end{bmatrix}, \tag{1.2}$$

- $\boldsymbol{\tau} \in \mathbb{R}^\mathrm{n}$ is the manipulator joint torques,
- $\mathbf{f}_\mathrm{b} \in \mathbb{R}^6$ is a wrench of forces and moments on the vehicle,
- $\dot{\mathbf{q}}, \ddot{\mathbf{q}} \in \mathbb{R}^\mathrm{n}$ are the joint velocities and accelerations respectively,
- $\dot{\mathbf{b}}, \ddot{\mathbf{b}} \in \mathbb{R}^6$ is the velocity and acceleration of the vehicle,
- $\mathbf{M}_\mathrm{i,j}$ for $\mathrm{i,j} \in \{\mathrm{q}, \mathrm{b}\}$ is an inertia matrix, and
- $\mathbf{C}_\mathrm{i,j}$ for $\mathrm{i,j} \in \{\mathrm{q}, \mathrm{b}\}$ is a Coriolis matrix.

Due to their inertial coupling, any motion of the base will induce forces and torques in the manipulator structure. These must be accounted for in the manipulator control, else the ability for the manipulator to control its end-effector might be impeded. The dynamic and kinematic coupling between the vehicle and manipulator need not be entirely problematic, though. The joint torques for the manipulator can be isolated from Eqn. (1.2) like so:

$$\boldsymbol{\tau} = \mathbf{M}_\mathrm{qq}\ddot{\mathbf{q}} + \mathbf{M}_\mathrm{qb}\ddot{\mathbf{b}} + \mathbf{C}_\mathrm{qq}\dot{\mathbf{q}} + \mathbf{C}_\mathrm{qb}\dot{\mathbf{b}}, \tag{1.3}$$

which reveals that the joint torques are independent of the base inertia $\mathbf{M}_{\mathrm{bb}}$. This feature was also noted by From et al (2009). Dynamic properties of the base are not required to control the manipulator. Only knowledge of the base motion, $\dot{\mathbf{b}}, \ddot{\mathbf{b}}$, is necessary.

The forward kinematics of the manipulator in isolation of a vehicle or base can be expressed as:

$$\mathbf{x} = \mathbf{f}(\mathbf{q}), \tag{1.4}$$

where $\mathbf{f}(\mathbf{q}) : \mathbb{R}^{\mathrm{n}} \mapsto \mathbb{R}^6$ gives the end-effector pose as a function of the joint positions. Taking the time-derivative leads to:

$$\frac{\mathrm{d}\mathbf{x}}{\mathrm{dt}} = \frac{\partial \mathbf{f}}{\partial \mathbf{q}} \frac{\mathrm{d}\mathbf{q}}{\mathrm{dt}} \tag{1.5}$$

$$\dot{\mathbf{x}} = \mathbf{J}(\mathbf{q})\dot{\mathbf{q}} \tag{1.6}$$

in which $\mathbf{J} = \begin{bmatrix} \mathbf{J}_{\mathrm{v}}^{\mathrm{T}} & \mathbf{J}_{\omega}^{\mathrm{T}} \end{bmatrix}^{\mathrm{T}} \in \mathbb{R}^{6\times \mathrm{n}}$ is the manipulator Jacobian. If this matrix has more columns than rows, i.e., $\mathrm{n} > 6$, and has full rank then the manipulator is considered redundant. There are infinite joint motions $\dot{\mathbf{q}}$ that can satisfy a required end-effector motion $\dot{\mathbf{x}}$. This redundancy could be used to leverage the base motion to assist the manipulator, rather than attempt to oppose it.

Angeles (2002) makes the analogy that a manipulator subject to gravitational acceleration is equivalent to a manipulator on a platform accelerating upward (Fig. 1.5). The manipulator must apply forces equal and opposite to those produced by gravity in order to maintain its composure. And, by extension, this same principle applies to all linear and angular acceleration of the base, as well as centripetal forces.

Standard dynamic modelling and control methods are sufficient to negate these effects. However, a redundant system would be able to simultaneously track an end-effector trajectory whilst using the base motion to supplement its own control. In addition to the forces induced by the base motion, the change in base orientation also results in a change of the gravity vector with respect to the manipulator (Fig. 1.6).

Given forecasts of the future base orientation, the change in gravity could be anticipated. These predictions could then be used by the manipulator to assist self-motion. In doing so, the manipulator would expend less energy by taking advantage of disturbances rather than working against them. This idea has already been explored to some degree by From et al (2011) for manipulators operating on ship platforms. However, they did not consider the use of redundancy for multiple task execution.

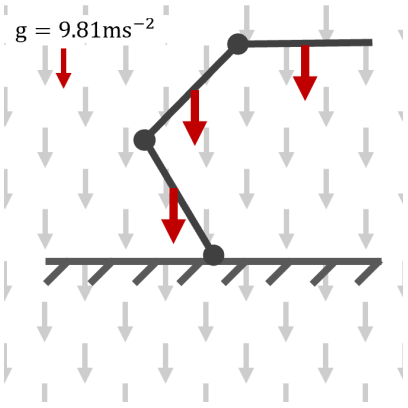

(A) A manipulator in a gravitational field.

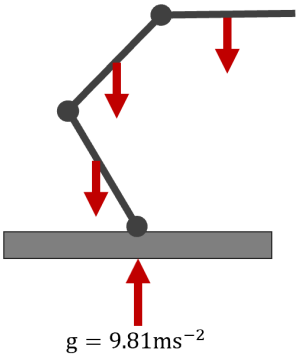

(B) A manipulator accelerating upward.

FIGURE 1.5: A manipulator in a gravity field is equivalent to a manipulator accelerating upward.

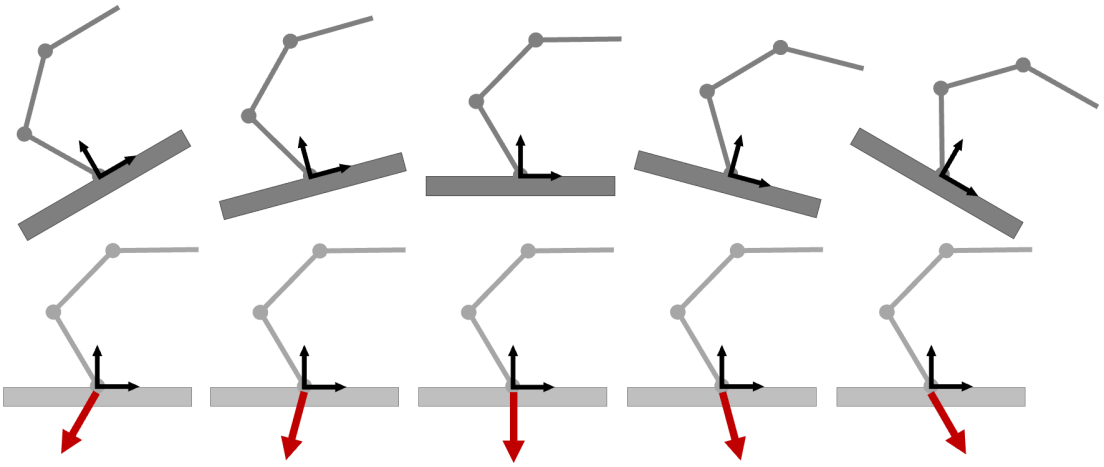

FIGURE 1.6: The gravity vector with respect to a mobile manipulator.

Contribution #2: *A Predictive Joint Torque Minimization (PJTM) method is presented which allows a redundant manipulator to use forces from base motion disturbance to reduce joint torque and track an end-effector trajectory simultaneously. Furthermore, by incorporating predictions for the change in gravity with respect to the manipulator, the joint torque can be further reduced. The proposed method is compared to a local minimization in the weighted least norm WLN of joint torques, and shown to reduce the total torque by 25%. The PJTM method is presented in Chapter 5.*

The effectiveness of these proposed control methods is dependent on how accurately the base motion can be predicted. Accurate forecasts of the base motion disturbance are critical to the effectiveness of the proposed control methods. A common forecasting method is time series, which uses past state observations to make predictions about the future (Box

et al., 2016). Fourier series, which models periodicity with a superposition of sinusoids, is a popular method for marine applications (From et al., 2011; Kormushev & Caldwell, 2013) or even heart motion (Yuen et al., 2008; Bowthorpe & Tavakoli, 2016). These prediction methods have been successfully applied to their respective predictive control strategies. But as will be seen in Chapter 2, there is little consistency in the application and performance results across the literature. Moreover, the advent of machine learning techniques provides potential new forecasting methods (Williams & Rasmussen, 2016; Roberts et al 2013).

Contribution #3: *Three different prediction methods were applied to inertial measurement unit IMU data of two different AUVs under wave excitation. The analysis of the results showed that Gaussian Process Regression (GPR) has better short-term prediction accuracy than time series or Fourier series. Furthermore, the vehicle morphology can fundamentally change the statistical properties of the motion data, even with similar external conditions. This affected both the prediction accuracy and uncertainty. This analysis is presented in Chapter 3.*

One of the tacit ideas behind adding a manipulator to a mobile robot is to perform intervention tasks. Any interaction performed by the manipulator necessarily requires that it generates joint torques to negotiate with the forces at the end-effector. Redundancy in a vehicle-manipulator system can be exploited to support the task being executed. Some examples include minimizing drag to an AUV (Marani & Yuh, 2014), avoiding joint limits (Cieslak et al., 2015), or wheel alignment for an AGV (Bussmann et al., 2018). But, as was previously noted, support from the vehicle cannot always be guaranteed. A redundant manipulator could instead configure itself to minimize joint torque required for the task.

Indeed, torque minimization methods of redundant manipulators with fixed bases have been explored (Hollerbach & Suh, 1988; Nedungadi & Kazerouinian, 1989; Kang & Freeman, 1992; Zhang et al., 2013). However, all these examples are concerned with the effects of internal dynamic torque. Torque minimization methods dealing with the external forces has not yet been addressed. Figure 1.7 demonstrates how the configuration of a redundant manipulator can affect its ability to support heavy objects.

Joint torque minimization has several implications for mobile manipulators, beyond satisfying motor limits. For one, the amount of energy required to perform a given task can be reduced. This can help increase the longevity with which they can operate in the field without the need for recharging. Furthermore, it is possible for a small manipulator to handle large or uncertain forces. This can decrease the size, weight, and cost in the

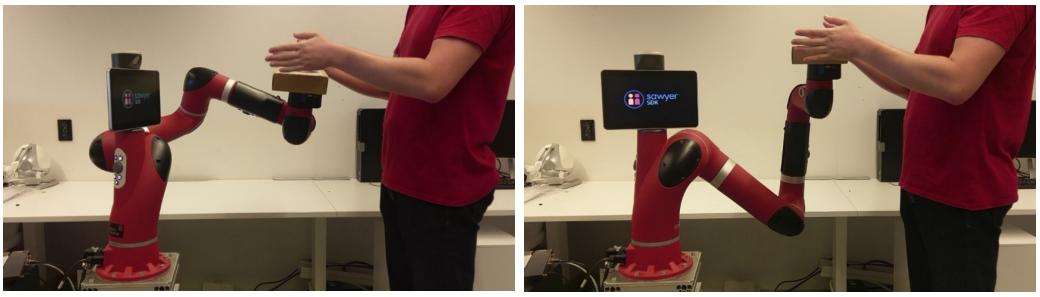

(A) A compliant posture. (B) A stiff posture.

FIGURE 1.7: The configuration of the robot arm affects its ability to withstand large external forces.

system design. A lighter manipulator also requires less effort to move, thereby reinforcing the energy saving benefits previously mentioned.

Previous related work in autonomous, high-pressure blasting presented many issues with the manipulator control due to the high forces involved (Liu et al., 2008; Paul et al., 2010; Manamperi et al., 2011). One advantage this research had was that the static environment permitted offline planning. Bussmann et al. (2018) proposed to use wheel alignment of a planetary rover to support a manipulator with force control. The aforementioned SPIR also has two grabbing arms to secure itself to bridge columns, but it cannot configure itself in a manner that aids high-pressure blasting. Furthermore, the hydrodynamic disturbances may perturb the vehicle. The manipulator must then negate disruptive base motion and manage the blasting forces simultaneously.

Contribution #4: *An External Joint Torque Minimization (EJTM) method is presented for joint torque reduction of redundant manipulators with large external forces. It is shown that this method can reduce the total torque compared to a conventional WLN method for tasks like weightlifting and high-pressure blasting. Furthermore, the proposed method can satisfy joint limit constraints whilst reducing the total joint torque. The method is validated both on fixed platforms and moving platforms under disturbance. And, by incorporating the PJTM method, further reductions in joint torque can be achieved. This is presented in Chapter 6.*

In Scope: In this thesis, the fundamental question to be addressed is: *How can a manipulator be controlled when operating from an unstable, moving platform?* The scope of concepts concerning this thesis are illustrated in Fig. 1.8. For this body of work, the manipulator base is assumed to uncontrolled and free moving. The base is considered as a single, rigid body. As such, the state propagation of the base in discrete time can be

modelled as:

$$\mathbf{b}_{k+1} = \mathbf{A}\mathbf{b}_k + \mathbf{C}\mathbf{d}_k, \tag{1.7}$$

- $\mathbf{b} \in \mathbb{R}^m$ is the base state,
- $\mathbf{A} \in \mathbb{R}^{m \times m}$ is the state propagation matrix,
- $\mathbf{d} \in \mathbb{R}^n$ is a disturbance to the base, and
- $\mathbf{C} \in \mathbb{R}^{m \times n}$ is the disturbance input matrix.

Due to the inertia, for sufficiently small time intervals the state at the next step will not deviate far from the current state: $\mathbf{b}_{k+1} \approx \mathbf{b}_k$. Then, for the k^{th} step from some initial condition:

$$\mathbf{b}_k = \mathbf{A}^k\mathbf{b}_0 + \sum_{i=1}^{k-1} \mathbf{A}^i\mathbf{C}\mathbf{d}_{i-1}, \tag{1.8}$$

where it becomes evident that any shocks or impulses to the system through $\mathbf{d}$ are diffused over time through the state propagation matrix. Due to these properties it is assumed that the base motion will exhibit some continuity over time, making it amenable to prediction. In general, no assumptions are made about how or why the base may move. That said, some of the specific case studies refer to scenarios of floating mobile manipulation, such as the SPIR. It has been noted that the vehicle body of an UVMS or UAVMS can indeed be used to support or assist the control of the manipulator. But, as aforementioned, this cannot always be guaranteed. Furthermore, it is not feasible that a non-inertial platform remains steady, particularly in the presence of strong external forces such as waves or wind. The manipulator must still adopt real-time control to compensate for this issue. To further this point, the use of decoupled control between vehicle and manipulator is common in practice. In these situations, the manipulator is acting as though it were free-floating. As such, the control methods in this thesis are agnostic. It could be applied to an UVMS, UAVMS, an AGV, or even on a ship platform.

Kinematic feasibility is also a minor concern addressed within this thesis. Manipulators on fixed bases in static environments have the advantage of pre-planned joint motion that can guarantee satisfying kinematic constraints with offline planning. Conversely, real-time control of manipulators must adopt clever control strategies to adhere to position and speed limits. This problem is exacerbated by the base disturbances where fast, unguided motion of the manipulator may be required to compensate. Two different methods in this thesis are considered to address this problem. The first is to adopt the WLN method for joint control using a redundant manipulator as proposed by Chan & Dubey (1995). The

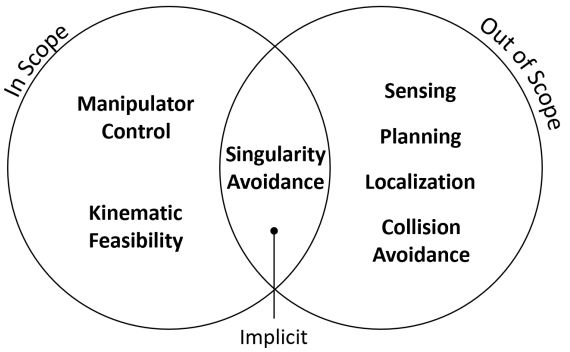

FIGURE 1.8: The scope of topic areas in this thesis.

predictive control method in Chapter 4 is also shown to account for joint constraints under disturbance, and does not require redundancy.

Out of Scope: Another concern with real-time control in manipulation is the issue of kinematic singularities. There are many well-known methods that are assumed knowledge in this thesis (Wampler, 1896; Chiaverini, 1991). It is also possible to utilize redundancy in the system to optimize manipulability and avoid singularities (Marani & Yuh, 2014). All these methods are readily integrated into the research presented in this thesis. Both self-collision and with nearby obstacles may also be of concern with manipulation in unstructured environments. These dangers are only further exacerbated by indiscriminate motion of the manipulator base. It is assumed for this thesis that the environment in which the manipulator operates is obstacle free. That said, there are several effective methods in literature that could be applied. Khatib (1986) proposed a framework for obstacle avoidance for manipulators or mobile robots using artificial potential fields. Chen et al. (2015) used a WLN method for moving obstacles, though this may only be suitable with highly redundant mechanisms. And Dariush et al. (2010) adapted the WLN method for joint limit avoidance developed by Chan & Dubey (1995) to include self-collision avoidance. Accurate manipulation tasks require accurate knowledge of the base pose with respect to the world frame. Much of the research with AUVs is devoted to the problem of underwater perception. This is due to the low bandwidth of underwater communication, poor vision, and noisy data from technology like sonar and Acoustic Doppler Current Profiler (ADCP)s. For this thesis, the current base pose is assumed to be known, from which predictions are made. Issues of localization and uncertainty may be a point of future research. Although, recent research that combines vision and an IMU (Sandy et al., 2017) can provide accurate pose estimation at 1000Hz. Similarly, the challenges of perception and planning, particularly under conditions of disturbance and uncertainty, are out of scope for this thesis. It

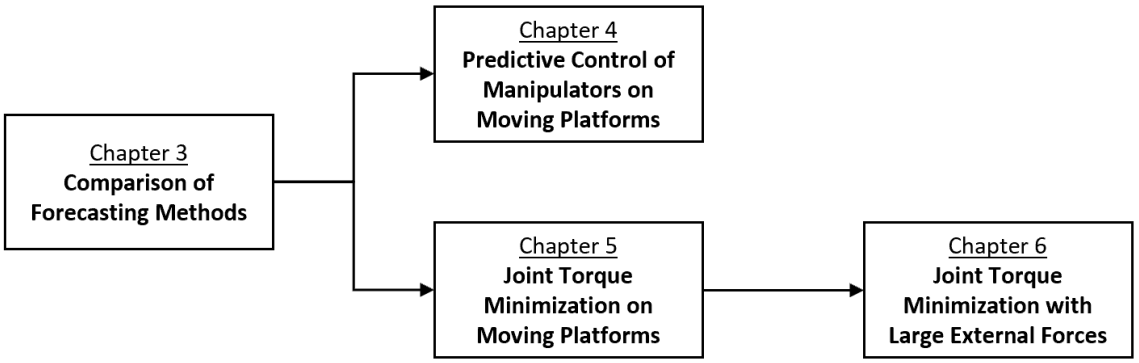

FIGURE 1.9: The flow of ideas in this thesis.

is assumed that task requirements for the manipulator are already planned. The primary concern is how to automate the manipulator once this information is given.

1.1 Thesis Outline

This thesis is divided in to 5 main chapters, starting with a review of related work in Chapter 2. The relationship between proceeding Chapters 3 to 6 it is shown in Fig. 1.9.

Chapter 2: This covers a review of related work in the current literature:

- It is shown that the literature regarding accurate intervention tasks for mobile manipulators under disturbance in scant. Moreover, much of the literature on predictive control for AUVs, and even some UAVMS are concerned with motion planning and energy minimization, rather than accurate task performance.
- On that note, the majority of literature for torque minimization of manipulators only considers the internal dynamic torque, emphasising the reduction in kinetic energy minimization. None thus far have addressed how to configure the manipulator to reduce torques imposed by large external forces. As previously mentioned, this could be an important issue for intervention and force control in the field, particularly when acting under uncertainty.
- There also does not appear to be much consistency in the application and results of different forecasting methods across the various predictive control literature. It is not clear as to whether these differing results are a consequence of the type of data being used, the model parameters chosen, or even the process by which they were arrived at.

Chapter 3: An objective comparison is made between time series, Fourier series, and GPR to clarify the discrepancies in model performance found in the literature. As a case study, these three methods are used to forecast IMU data for 2 different AUVs subject to wave disturbances in shallow water. In addition, forecast uncertainty is considered as an important metric for evaluation that has been previously lacking in much of the related literature.

Chapter 4: A novel predictive control method is presented. Using forecasts of the base motion, a predictive control strategy is developed that allows the manipulator to counter the base motion to maintain a steady end-effector pose or perform accurate trajectory tracking. Both simulation and experimental results on a real robot show that this method can reduce tracking error by 60% compared to a Proportional-Integral-Derivative (PID) feedback controller, under the given test conditions.

Chapter 5: A novel method for joint torque minimization of redundant manipulators under base disturbance is developed. By forecasting the change in base orientation, redundancy in the manipulator is used to take advantage of the relative change in gravitational forces with respect to the manipulator. By applying well-known null space control methods, the manipulator can simultaneously perform tasks with its end-effector whilst using the base motion to reduce torque.

Chapter 6: In the final chapter, the problem of torque minimization with large payload forces is addressed. Current state of the art methods only considers the internal dynamic torque. This chapter develops an alternative method that reduces both the joint torques from external loading and the internal dynamic torque. The method is first shown to work on manipulators with fixed bases, using two case studies: heavy-lifting, and high-pressure blasting. Then, the method is shown to work under base motion. By combining this with the gravitational predictions of Chapter 5, further reductions in joint torque can be made.

1.2 Publications

- Woolfrey, J., Liu, D. and Carmichael, M., 2016, May. *Kinematic control of an autonomous underwater vehicle-manipulator system (auvms) using autoregressive prediction of vehicle motion and model predictive control.* In 2016 IEEE International Conference on Robotics and Automation (ICRA) (pp. 4591-4596). IEEE.

- Woolfrey, J., Lu, W. and Liu, D., 2019. *A Control Method for Joint Torque Minimization of Redundant Manipulators Handling Large External Forces.* Journal of Intelligent & Robotic Systems, pp.1-14.
- Woolfrey, J., Lu, W., Vidal-Calleja, T. and Liu, D., 2019. *Clarifying clairvoyance: Analysis of forecasting models for near-sinusoidal periodic motion as applied to AUVs in shallow bathymetry.* Ocean Engineering, 190, p.106385.
- Woolfrey, J., Lu, W., Liu, D.K., 2019, *Predictive Control of Manipulators Operating on Moving Platforms Under Disturbance*, submitted to IEEE Transactions on Robotics (TRO) [Under Review].

Chapter 2

Review of Related Work

2.1 Intervention Tasks in Field Robotics

Despite the current state of technology, fully autonomous mobile manipulation has only been advanced within the past 10 years. Prior, intervention tasks (primarily underwater) were conducted by human operators through a ROV. As Yuh et al. (1998) note, deep-sea intervention via a human operator becomes difficult with the low bandwidth afforded by wireless underwater communications. This prompted the development of the SAUVIM project. Being semi-autonomous, only high-level commands needed to be issued to the system, which then enabled it to further execute its own low-level control. The SAUVIM was designed with the intent for hooking cables to objects on the sea floor for recovery missions. Results of early field trials in both a pool and harbour were presented by Marani et al. (2009). The authors claimed this to be some of the first of its kind.

With a 3.5m long frame, oil-filled manipulator, and 8 thrusters weighing 23kg each (Yuh et al., 1998), the SAUVIM's design intent was to operate in deep-sea locations where disturbances are minimal. The effects of wave decrease with the increasing distance from the surface of a body of water (Dean & Dalrymple, 1991), and hence sea swell is of little concern to the accuracy of the intervention tasks.

There has been a proliferation of research and literature around UVMS for intervention tasks in the following years since the SAUVIM. The TRIDENT project was declared not long after, also for the purpose of object retrieval (Sanz et al., 2010). This system featured the Girona 500 AUV which has 6-Degree(s)-of-Freedom (DOF), coupled with a 7DOF manipulator. The Girona 500 is smaller and lighter than the SAUVIM, and

hence more susceptible to disturbances. This may be a potential issue for task accuracy. Experiments with the TRIDENT were presented by Simetti et al., (2014) showing its capability to grasp objects with a robotic hand from the bottom of a pool. Once more, the environment poses little problem in the way disturbance (aside from fluid drag).

The same GIRONA 500 vehicle was also combined with a 4-DOF manipulator in other underwater manipulation tasks. The PANDORA project, for instance (Maurelli et al., 2016) sought to achieve autonomous mobile manipulation through learning by demonstration from human operators. Similar research by Cieslak et al. (2015) also featured the same hardware for valve-turning operations, once more with trials conducted in a pool. Their work highlighted the ability to use redundancy in the system (6-DOF base + 4-DOF arm = 10-DOF robot) for achieving multiple tasks of ordered priority.

Other work in underwater valve turning was presented by Jin et al. (2017). The novel feature to this research was an AUV with 2 arms; one to be used for valve turning, and the other for gripping infrastructure to provide support during the task against external forces. The same group of researchers also presented a 4-bar mechanism for scraping starfish off shellfish farms (Jin et al., 2016). Their opening paragraph notes the need for autonomous systems to supplant humans in these hazardous environments.

AUV technology has also been employed for biological surveying and population control of the Crown of Thorns Starfish (COTS) in the Great Barrier Reef, Australia (Clement et al., 2005; Dayoub et al., 2015). Both the census data and culling of this invasive species is conducted by human divers, which is both prone to error, and the limits to human endurance and manpower. The long-term goal is the development of an autonomous UVMS to replace humans with this type of work, but the research thus far has predominantly focused on the issues of underwater perception and object classification. Other related research has focused on the delivery method for acetic acid injection (Takemura et al., 2015). The shallow bathymetry of the coral reefs may pose a problem to the accurate control required for executing these injections into the starfish.

The recent popularity with drone technology has also compelled researchers to explore mobile manipulation with a UAV. An interesting piece of research by Jiminiez-Cano et al. (2015) featured a quadcopter with a manipulator mounted on the top of the vehicle (Fig. 1.2d). This configuration makes the system inherently unstable, and disturbances to the base could make precise intervention tasks more difficult. This system was designed for infrastructure inspection, which necessitates that a sensor be in contact with the inspection

surface at all times. Their real-world results highlighted that physical contact with an external surface helped stabilize the system, however.

Mobile manipulators are also making their way into agriculture. Lehnert et al. (2016), for example, demonstrated a 6-DOF manipulator picking sweet peppers. Although, their work focused mainly on the perception and planning side for how to best grasp produce. When operating from a fixed base, the manipulator control is trivial compared to moving platforms (i.e., underwater and aerial vehicles). However, it is conceivable that such a system could operate from the back of a mobile robot. Terrain out in the field is not guaranteed to be smooth, and the manipulator will require more sophisticated control methods to account for this fact.

Outer space and inter-planetary manipulation tasks are also becoming more common. Some recent work by the German Aerospace Center (Deutsches Zentrum f́ur Luft und Raumfahrt) showcases problems and solutions to complex mobile manipulation tasks. Giordano et al. (2018), for instance, showed how manipulators can be used to conduct work in space. However, the common effects of wind, waves, and turbulence that make terrestrial and marine intervention tasks difficult are absent in this scenario. Bussmann et al. (2018) features force control for mobile manipulators on planetary rovers. Of course, the advantage here is that the solid ground helps provide support to the manipulator itself.

2.2 Control of Manipulators Mounted on Mobile Platforms

Control strategies for mobile manipulation become more complex when stability of the base cannot be guaranteed. Early work on floating mobile manipulation (Kosuge et al., 1991) was presented even before that of the aforementioned SAUVIM project. The authors considered a scenario in which a manipulator was mounted atop a vessel floating on the water's surface. Both the manipulator dynamics and buoyant forces of the water affected the pose of this platform. Their simulations showed that accurate trajectory tracking of the manipulator could not be achieved without accounting for the disturbances affecting the base. Later, Kajita & Kosuge (1997) showed how buoyant and restoring forces of a floating vessel could be used to assist a mobile manipulator when applying forces via the end-effector. In doing so, the number of actuators in the manipulator could be reduced, instead relying on the passive dynamics of the base for assistance.

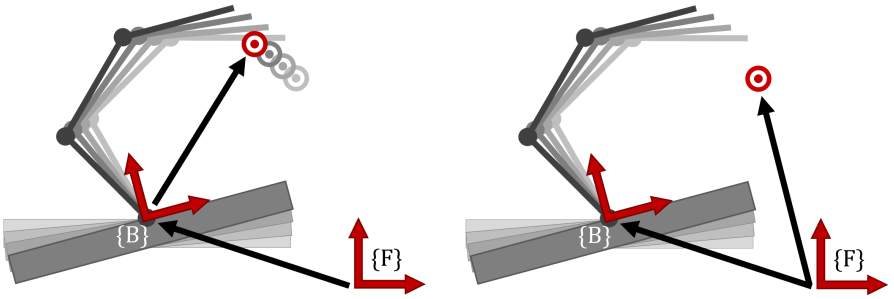

(A) A task specified relative to the manipulator.

(B) A task specified relative to the world frame.

FIGURE 2.1: Relative motion between the world frame and manipulator results in task error.

Other scenarios with control of manipulators on moving bases were considered by Nguyen & Dancowicz (2015). In their research, the dynamics of the system was assumed to be unknown. As such, the controller for the system had to learn and adapt to the changing dynamic effects as the manipulator base moved relative to the inertial frame. They considered two case scenarios: one of a manipulator operating on a ship platform in sea swell, and another on a terrestrial vehicle on rough terrain. One limitation of this work was that the manipulators were underactuated, and hence cannot achieve full position and orientation control at the end-effector without assistance from an actuated base. Moreover, the task for the manipulator was considered relative to the base or platform, not an external fixed frame. Ergo, the relative motion between the manipulator and target due to the base motion was present (Fig. 2.1). This is not the case for the scenario being considered in this thesis.

Ishitsuka et al. (2004) studied acceleration-level control for a 2-DOF manipulator mounted on an AUV. An interesting insight from their research showed how the configuration of the arm affected its ability to recover from disturbances from base displacement. More specifically, the end-effector compensated fastest in directions with greatest manipulability. This could lead to potential research for choosing arm postures that afford better performance and disturbance recovery when performing intervention tasks.

In the aforementioned valve-turning tasks (Cieslak et al., 2015; Maurelli et al., 2016) the Girona 500 AUV with a 4-DOF arm provided a 10-DOF, redundant system. Redundancy such as this could be used to achieve additional tasks whilst the end-effector of the manipulator conducts work. Once such example, as presented by Antonelli (2014) showed

simulations of a redundant UVMS performing trajectory tracking of the end-effector whilst the vehicle realigned itself to reduce fluid drag from water currents.

The low frequency and bandwidth of underwater sensing technology can also pose problems for the subsequent control of the manipulator. Antonelli et al. (2000) showed that it is better use statistical estimations of the vehicle velocity for the manipulator control rather than the low-frequency, low-resolution measurements provided by on-board sensors. In doing so, this helped to improve task performance of the manipulator. Additionally, noise and chattering were filtered out which helped to reduce oscillations and energy consumption from the proceeding manipulator control.

Vision information and IMU data were combined by Sandy et al. (2017) to provide accurate pose estimation for the end-effector of a mobile manipulator at a rate of 1000 Hz. They then used PID control to keep the end-effector stationary whilst the base was moved in a 2-Dimensional (2D) plane. No knowledge of the base motion was assumed, and yet the manipulator was able to maintain accuracy under 5mm. If the base motion was known (as proposed in Chapter 1), this could greatly improve accuracy of the end-effector control.

2.3 Forecasting Methods for Predictive Control

2.3.1 Analysis of Motion Data

As a case study, motion data in this thesis is modelled off of two AUVs designed for shallow water intervention tasks. As noted in Chapter 1, the effects of wave forces are strongest near the surface of the water (Dean & Dalrymple, 1991). The first AUV is the aforementioned SPIR (Fig. 2.2a). The second is a prototype known as the Antarctic AUV, also being developed at UTS (Fig. 2.2b). Due to the sinusoidal nature of wave motion, the subsequent motion data recorded from these vessels exhibits periodicity. This creates autocorrelation over time, making the data easier to forecast. This may not always be the case in other situations, i.e. with UAVs or even AGVs. As noted in Chapter 1, though, the dynamics of a rigid body should be continuous and thus predictable to some degree. The following predictive control methods presented in Chapter 4 and Chapter 5 do not rely on periodicity in the motion data.

Each of the vehicles was placed in a test tank at different times and subjected to manually generated wave disturbances. IMU data were recorded for the analysis. A sample of the heave acceleration for the SPIR can be seen in Fig. 2.3. Although the test tank is not

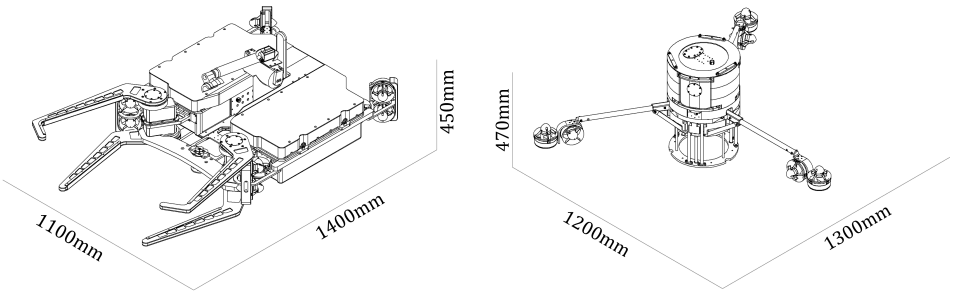

(A) An illustration of the SPIR. (B) An illustration of the Antarctic AUV.

FIGURE 2.2: Two different AUVs were used to test motion data.

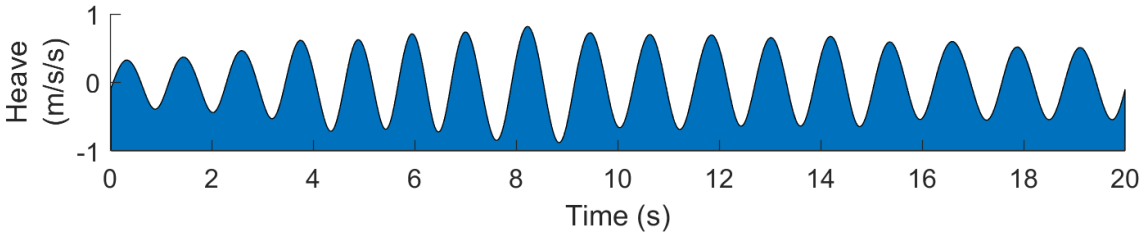

FIGURE 2.3: A sample of the IMU data collected from the SPIR.

indicative of the types of wave motion that might be experienced in the open sea, it does provide some unique advantages:

1. The harmonics of the tank produces similar waveforms for both AUVs. This removes any effects in the subsequent data that may be unique to a geographic location under different weather conditions. This in turn accentuates the differences in motion that are distinctive to the vehicle's shape and mass.
2. The walls of the tank will rebound waves, producing interference patterns and more complex waveforms. These effects can be used to test the robustness of the different prediction models to different patterns and changes over time.

Immediately, the data in Fig. 2.3 exhibits a sinusoidal waveform. Indeed, wave theory asserts that undulations in a body of water can be modelled by a superposition of sinusoids (Dean & Dalrymple, 1991). Using this method, the data in Fig 2.3 were decomposed in to four discrete sinusoids as shown in Fig 2.4.

This model was used by Fernandez & Hollinger (2016) to simulate an AUV operating in the open sea. Likewise, Kormushev & Caldwell (2013) chose this model to estimate hydrodynamic disturbances to an AUV. Both the frequency and amplitude of these disturbances may change over time, with location, or with the local weather. Ergo, an adequate prediction model must be able to adapt its parameters to best reflect the local conditions. From

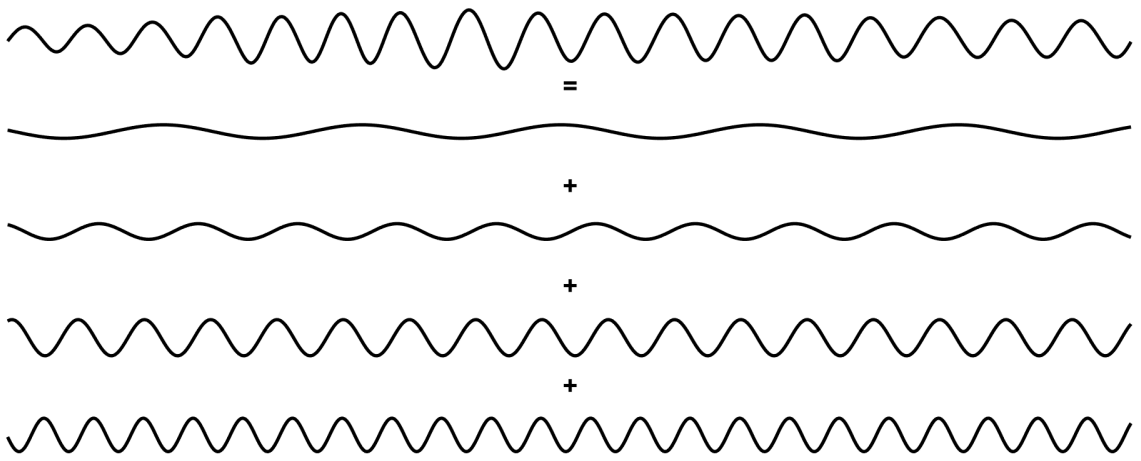

FIGURE 2.4: The SPIR motion data decomposed in to a sum of 4 sinusoids.

et al. (2011) achieved this by optimising a sinusoidal model with each control loop. The drawback to their method was that only the amplitudes were adjusted. The fundamental frequency remained unchanged, which is not guaranteed in reality.

Kormushev & Caldwell (2013) were able to optimise both amplitude and frequency by using machine learning. Parker & Anderson (1990) proposed to use an Extended Kalman Filter (EKF) to track hidden frequencies in near-sinusoidal data. Yuen et al. (2008) took this idea and extended it to forecast motion prediction for beating-heart surgery. This prediction method was then successfully applied to the predictive control scheme by Bowthorpe & Tavakoli (2016).

Another approach to analysing the motion data is to see how it relates to itself over time. This is pertinent to data where deterministic models cannot be used to explain the data generation process. Observations at a given time, y(t), were plotted against lagged observations for the previous two time steps $y(t - \Delta t)$, $y(t - 2\Delta t)$ (Fig. 2.5). There is a strong correlation in the data across time. This relationship leads to two potential methods for prediction.

The first of these is that linear regression can be performed across time, i.e., autoregression Autoregression (AR) (Fig. 2.6a). A thorough reference on this prediction method, known as time series, can be found in Box et al. (2016). Time series was also used for predicting ship motion by From et al. (2011) for control of manipulators operating on ship platforms, and Woolfrey et al. (2016) in predictive control for a manipulator operating on an AUV in shallow bathymetry. From et al. (2011) compared this method to a superposition of sinusoids, concluding that that former had better prediction performance than the latter.

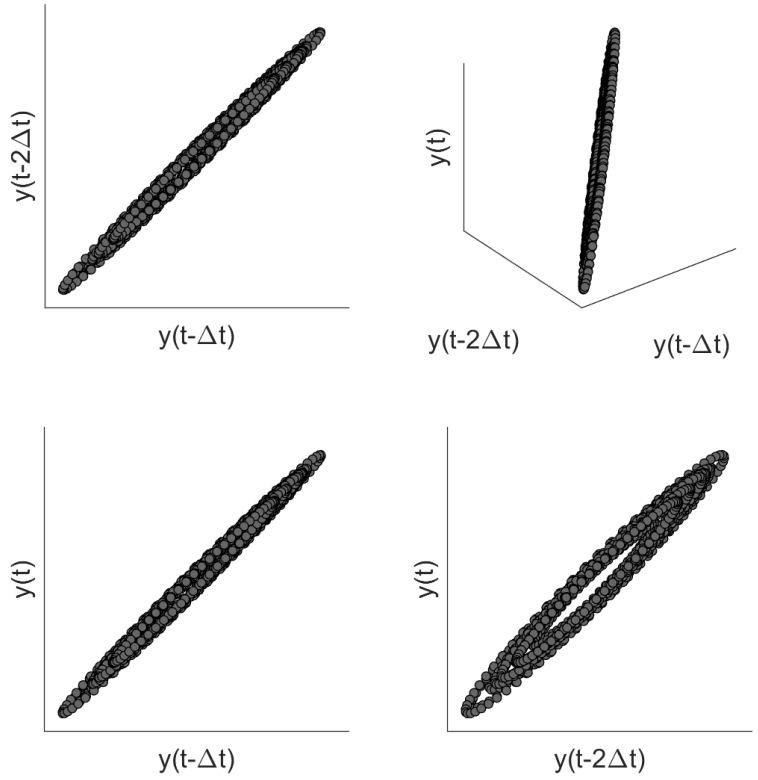

FIGURE 2.5: The motion data exhibits strong correlation across time.

Both From et al. (2011) and Woolfrey et al. (2016) used a simple AR model. However, Becker et al. (2008) applied mixed forms of Autoregression Moving-Average (ARMA) for predicting hand tremor during micro-surgery. By appending Moving-Average (MA) terms, forecasts are adjusted based on previous prediction errors. The conclusion of this research was that an ARMA model was more accurate than a pure AR model. Furthermore, Yuen et al. (2008) compared an AR time series model to a discrete Fourier series (a superposition of sinusoids) with the EKF. Their conclusion was that the EKF outperformed time series for predicting heart motion.

In studying ship motion prediction, Yang et al. (2008) criticised AR stating that it had poor long-term performance. Instead, they developed a time series model that used previous state observations and system inputs (their definition of an input is unclear). For one, this assumes system inputs are known, which is often not the case in time series applications. Secondly, the ARMA model may end up performing a similar function.

Another insight from the motion data is that it forms a joint probability across time (Fig 2.6b). Thus, a conditional distribution can be evaluated to predict future states given historical data. This idea leads naturally to the application of GPR. This method

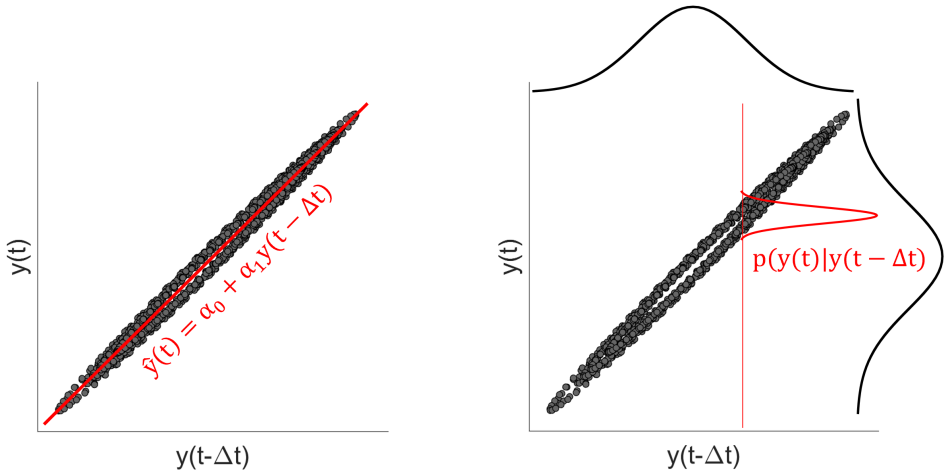

(A) Regression across time. (B) Condtional distribution.

FIGURE 2.6: Both linear regression and conditional probability can be used to predict the data.

has been applied successfully to time series forecasting of a variety of other phenomena. But, to this author's knowledge, has not yet been applied to the specific application of predictive control. Roberts et al. (2013) give a thorough reference on the theory and application of GPR. They also provide many examples of time series modelling for natural phenomena with periodicity, such as tide heights and stellar light curves. Other examples can be found in the modelling of physiology (Dürichen et al., 2015), and respiratory data (Brahim-Belhouari & Bermak, 2004). Detailed literature on GPR can be found in Williams & Rasmussen (2006).

2.4 Forecast Accuracy

It is self-evident that accurate forecasts are crucial for disturbance rejection in predictive control. Metrics for forecast accuracy are useful not only in comparing the performance between different models, but also determining the parameters within a given model. As was previously mentioned, there was little agreement amongst literature as to whether AR, ARMA, or Fourier series was the superior prediction method. Likewise, there is little consistency in the choice of metrics for model selection and evaluation (although this may explain the contradictions in results).

2.4.1 Root Mean Squared Error (RMSE)

A rational approach to evaluate prediction accuracy is to measure the Root Mean Squared Error (RMSE) between the predicted state and the realized state observation for i steps ahead:

$$\mathrm{RMSE} = \sqrt{\mathrm{n}^{-1} \sum_{\mathrm{i}=1}^{\mathrm{n}} \big(\hat{\mathrm{y}}(\mathrm{t}+\mathrm{i}|\mathrm{t}+\mathrm{i}) - \hat{\mathrm{y}}(\mathrm{t}+\mathrm{i}|\mathrm{t})\big)^2}, \tag{2.1}$$

where $\hat{\mathrm{y}}(\mathrm{t}+\mathrm{i}|\mathrm{t})$ is the prediction for the state outcome at time $\mathrm{t}+\mathrm{i}$ made from time origin t, and $\hat{\mathrm{y}}(\mathrm{t}+\mathrm{i}|\mathrm{t}+\mathrm{i})$ is the state estimate at time $\mathrm{t}+\mathrm{i}$. A smaller RMSE implies a more accurate prediction model. This metric was used by Becker et al. (2008), From et al. (2011), and Woolfrey et al. (2016) for determining the type of times series model and the number of parameters. However, there are two disadvantages with RMSE:

1. It does not give a measure of prediction performance against the minimum standard of a last-value predictor. Indeed, it is possible to perform worse than this.
2. It does not allow for comparison of a model across different dimensions.

This second point is of particular importance. RMSE is adequate for one-dimensional systems, as might be applied by Becker et al. (2008), or Bowthorpe & Tavakoli (2016). However, non-inertial platforms exhibit 6-DOF and thus it becomes difficult to objectively compare a single model's ability to predict both position (in meters) and orientation (in radians).

2.4.2 Akaike Information Criterion (AIC)

It is well known that high estimation accuracy can be achieved by overfitting a model with more parameters then necessary (although, for real time control computational cost can place hard limits on this factor). Akaike (1974) proposed the popular Akaike Information Criterion (AIC) which gives a sum between estimation accuracy and parsimony of the model:

$$\mathrm{AIC} = -2\ln(\mathcal{L}) + 2\mathrm{k}, \tag{2.2}$$

where $\mathcal{L}(\theta, \mathrm{y})$ is the maximum log-likelihood of the parameters θ given observation y, and k is the number of model parameters. Here, the limit of $-2\ln(\mathcal{L})$ as $\mathcal{L} \to 1$ is 0. A smaller metric indicates a better model. This method was employed by Yuen et al. (2008) for heart motion prediction to determine the number of AR terms for time series, and the number of sinusoids for the Fourier series.

2.4.3 Bayes Information Criterion (BIC):

This metric, proposed by Schwarz (1978), extends the AIC by adding a non-linear penalty term for the number of model parameters and the number of observations:

$$\mathrm{BIC} = -2\ln(\mathcal{L}) + 2\ln(\mathrm{n})\mathrm{k}, \tag{2.3}$$

where n is the number of data points or observations. Yang et al. (2008) opted for the Bayes Information Criterion (BIC) over the AIC in predicting ship motion, stating that the results of AIC are unreliable (Kashyap, 1980). Note also that neither BIC or AIC give an indication of model performance versus a last-value predictor.

2.4.4 Theil's Inequality Coefficient

Evidently, there is not much consistency in the use of different forecast metrics in predictive control literature, and each has its own limitations. In this thesis, Theil's Inequality Coefficient (Theil, 1966) is employed as a metric for mean prediction accuracy. This gives the ratio of the predicted changes versus the actual changes of the data:

$$\mathrm{U}^2 = \frac{\sum_{\mathrm{i}=1}^{\mathrm{n}} \Big(\hat{\mathrm{y}}(\mathrm{t}+\mathrm{i}|\mathrm{t}+\mathrm{i}) - \hat{\mathrm{y}}(\mathrm{t}+\mathrm{i}|\mathrm{t})\Big)^2}{\sum_{\mathrm{i}=1}^{\mathrm{n}} \Big(\hat{\mathrm{y}}(\mathrm{t}+\mathrm{i}|\mathrm{t}+\mathrm{i}) - \hat{\mathrm{y}}(\mathrm{t}|\mathrm{t})\Big)^2}. \tag{2.4}$$

Unlike RMSE, this metric is dimensionless and thus it is possible to objectively compare a model's ability to predict the linear motion of a vehicle against angular motion. From this equation, $\mathrm{U}^2 = 0$ for a perfect prediction, whereas $\mathrm{U}^2 > 1$ means the model performs worse than a naïve last-value predictor. Theil (1966) also provides statistical decompositions to identify the sources of prediction error. Obviously, this metric does not evaluate parsimony as does the AIC or BIC. However, this can be manually evaluated in the model selection process.

2.4.5 Standard Error of Predictions for Assessing Forecast Uncertainty

Forecast uncertainty can provide useful information in motion planning and control. From et al. (2011) factored in forecast uncertainty in the motion planning for manipulators operating on ships. And both Hyunh et al. (2015) and Jones & Hollinger (2017) incorporated

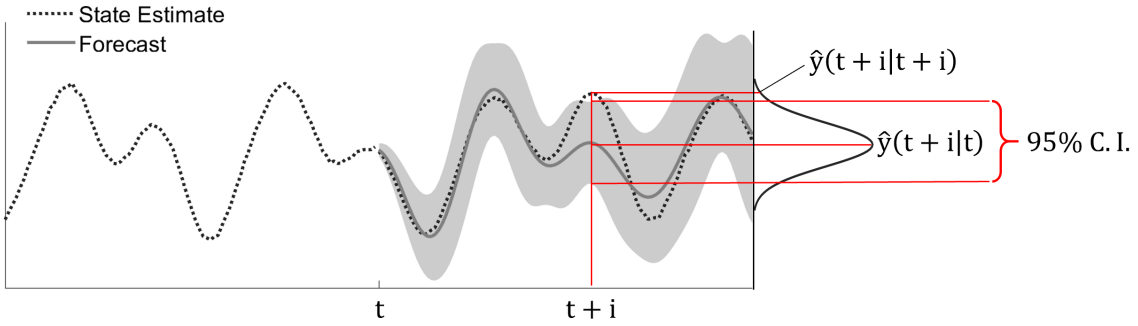

FIGURE 2.7: An example of a predicted observation falling outside the 95% confidence interval of the forecast.

uncertainty in the motion planning of AUV. Fang & Williams (2014) also challenged assumptions about different probability distributions and how they bound trajectories in robotic systems. Evidently, sound information about forecast uncertainty can provide a better basis for planning and control. For instance, if the forecast uncertainty underestimates the prediction error, this could lead to a false sense of security in applications that require collision avoidance. Conversely, an overly conservative estimate may hinder planning, exploration and control.

A useful metric for incorporating forecast uncertainty into the prediction assessment is to take the normalized prediction error, referred to as the Normalized Estimation Error Squared (NEES) (Li et al., 2001):

$$\sigma^2{}_{\mathrm{SE}}(\mathrm{i}) = \mathrm{n}^{-1} \sum_{\mathrm{i}=1}^{\mathrm{n}} \frac{\left(\hat{\mathrm{y}}(\mathrm{t}+\mathrm{i}|\mathrm{t}+\mathrm{i}) - \hat{\mathrm{y}}(\mathrm{t}+\mathrm{i}|\mathrm{t})\right)^2}{\sigma^2(\mathrm{t}+\mathrm{i}|\mathrm{t})}, \tag{2.5}$$

where $\sigma^2(\mathrm{t}+\mathrm{i}|\mathrm{t})$ is the forecast uncertainty for the i^{th} step ahead forecast. The square root of Eqn. (2.5) will give the average number of standard deviations that the state $\hat{\mathrm{y}}(\mathrm{t}+\mathrm{i}|\mathrm{t}+\mathrm{i})$ is from the forecast mean $\hat{\mathrm{y}}(\mathrm{t}+\mathrm{i}|\mathrm{t})$. Thus when $\sigma_{\mathrm{SE}} > 1.96$, the state observation exceeds the 95% confidence interval of the forecast. This means the prediction model is unable to sufficiently encompass the prediction errors. This concept is visualised in Fig 2.7.

2.5 Predictive Control

Very little exists in the way of predictive control for manipulators on moving platforms. Moreover, much of the predictive control literature pertains to minimum-energy motion planning, rather than control strategies that neutralize disturbances. Some work was done

by From et al. (2009) in which they studied the dynamics of a manipulator operating on ship platforms in high seas. Their research noted that, due to the large inertia of the system, shifting gravitational forces and those imposed by the ship motion hindered task performance if not adequately accounted for. Different methods for predicting the ship motion were studied in continuing research (From et al., 2011). By using forecasts of this motion, optimal planning for the manipulator was devised to reduce joint torque in the manipulator. This enabled it to use the forces to initiate self-motion, rather than fight against it. As with Nguyen & Dancowicz (2015), however, the manipulator task was specified relative to the base or ship platform. Hence, task error was only a consequence of the system dynamics, and not the kinematic effects of the base motion affecting the end-effector motion (Fig. 2.1).

In previous work (Woolfrey et al., 2016), it was shown that by predicting base motion, a mobile manipulator could act to counter these disturbances and maintain a steady end-effector pose. Both From et al. (2011) and Woolfrey et al. (2016) solved the predictive control in the joint space of the manipulator. In the research presented by From et al. (2011), the joint configuration was only constrained at the beginning and end of the planned task to achieve a desired end-effector pose. The joint state was free to move in between with the base motion, implying the end-effector remained uncontrolled. Conversely, the method proposed by Woolfrey et al. (2016) required satisfying nonlinear constraints for the entire control horizon in order to maintain the required end-effector pose. Although feasible, this approach increases in complexity with both the increase of forecast horizon and degrees of freedom in the system. This problem is revisited in Chapter 4, in which an efficient Quadratic Programming (QP) solution is proposed with linear constraints to satisfy the kinematic restrictions.

Strategies for predictive control methods subject to disturbances prove to be more fruitful when reviewing AUV, sans manipulator.

Some of the earliest literature on control of an AUV under wave disturbances was proposed by Riedel et al. (2000). On-board sensors were used to estimate the external sea state. From this, a statistical method known as AR was used to predict disturbances to the vehicle. Details on how this was implemented are lacking. However, these predictions were coupled with a Sliding Mode Control (SMC) scheme and shown to reduce position error of the AUV in the presence of disturbances.

A similar problem was addressed by Medagoda & Williams (2014) for an AUV descending through a water column with strong lateral currents. An ADCP was used to sense

the direction and magnitude of these currents in advance. Then, Model Predictive Control (MPC) was used to proactively control the AUV and reduce the effects of hydrodynamic disturbances on the position tracking. A counterpoint to this method is that Riedel (2000) argued against the use of external sensing. Rather, on-board sensing and statistical estimation techniques could instead be used to reduce monetary and weight costs of the AUV design. This philosophy necessitates some form of disturbance prediction.

Fernández & Hollinger (2016) also applied MPC to perform station-keeping of an AUV in shallow bathymetry. Simulations of a 2-DOF AUV under wave disturbances showed that this predictive strategy reduced position error over a PID feedback controller. However, no forecasting method was presented per se, as the simulation data was given directly to the predictive controller. In practice, this type of foresight is not possible, and some method of prediction must be used in its stead.

Predictive control appears to be a popular method for long-term motion planning of AUV in the open ocean. For instance, Hyunh et al. (2015) showed that ocean currents can change in magnitude and direction over several hours (a short time period for long-distance travel of marine vessels). By using predictions of the ocean currents, they developed an A*-based path planning algorithm. This was able to produce energy-efficient trajectories by factoring in the direction, magnitude and uncertainty of the hydrodynamic disturbances. Similar research was also presented by Jones & Hollinger (2017) that also found energy-efficient trajectories under strong current disturbances. They noted that factoring in uncertainty added robustness, and that their proposed method was more efficient than A*.

Real-time control of a system subject to local disturbances is a different problem to long-term planning for open ocean AUVs, however. More relevant work by Kormushev & Caldwell (2013) studied energy minimization for real time control of AUVs. Using machine learning, they were able to estimate local, sinusoidal disturbances, learn to ignore certain effects and buffer against others. This was integrated into a PID controller, although they claimed it could be extended to any control method.

UAVs equipped with manipulators also present analogous problems, though the fluid effects of air are (in most cases) negligible compared to that of water. Garimella & Kobilarov (2015) applied MPC for a quadcopter with a 2-DOF manipulator for optimal motion planning. Their results showed that the system could retrieve objects faster than that of a PID controller. Lunni et al. (2017) also applied MPC to a UAVMS, where the end-effector was constrained to follow a given trajectory. By using redundancy in the system, they were

able to reduce joint torques by realigning the centre of gravity of the system and increase the manipulability of the arm. Neither of these methods, however, factor in external disturbances. Research that is perhaps closer to the disturbance compensation problem is presented by Pflimlin et al. (2004). Adaptive control was used to stabilize a UAV (sans manipulator) with wind forces acting on the system.

In terms of manipulators operating in space, Giordano et al. (2018) addressed the problem of how to control a mobile manipulator after impact disturbances injected momentum into the system. The control method they developed managed to negate drift and maintain an effective workspace for the given task by controlling the centre of mass of the system. In doing so, this minimized the use of base actuators, thereby reducing energy consumption and conserving fuel.

Of the literature presented thus far, few aside from Woolfrey et al. (2016) have considered the effects that relative base motion has on task performance for a mobile manipulator. Study of predictive control in other applications yields the potential of such strategies. For instance, Bowthorpe & Tavakoli (2016) investigated the problem of tracking the surface of a heart via tele-operated devices for beating heart surgery. Their results showed that combining heart motion predictions with predictive control could successfully reduce error between a semi-autonomous surgical device and the surface of a heart. In doing so, a human surgeon was relieved of the burden of performing the real-time compensation.

2.6 Other Control Methods for Disturbance Compensation

The undesired base motion of a mobile manipulator could also be conceptualised as a disturbance to some nominal model. Disturbance observation methods are popular for underwater manipulation due to the difficulty of modelling hydrodynamic forces. Yuh et al. (2001) developed an adaptive disturbance observer to address this problem. This enabled a feedforward term to be included into the control loop to counteract disturbances directly. Adaptive control gains were also introduced to account for model uncertainty and changes in external conditions. One drawback to this method is that the disturbance estimated were smoothed with a lowpass filter, thereby introducing lag in the signal. Furthermore, their research could not guarantee asymptotic tracking of a desired trajectory. Santhakumar (2013) introduced a nonlinear disturbance observer with adaptive controller for a simulated underwater manipulator, and Venkatesan et al. (2014) used a disturbance observer coupled with sliding mode control. Sensing the velocity of an underwater vehicle

can also be difficult due to the limitations of underwater technology. To this end, Antonelli et al. (2000) developed an observer to estimate the vehicle velocity. However, the drawback to this method is that is requires a dynamic model, which could be difficult to model. Furthermore, from Eqn. (2.7), it was noted that the kinematic and dynamic disturbances introduced into the manipulator are independent of the base/vehicle dynamics hence knowledge of these properties adds little value in the way of controlling the manipulator itself. Furthermore, if disturbances were estimated at the dynamic level, then they must be forecast and propagated through the system model, Eqn. (1.7). Not only does this increase the computational cost, but this also compounds model uncertainty with the forecast uncertainty. This can be foregone by sensing and predicting from the base motion directly.

Output regulation theory is also another control method that deals with external disturbance rejection to a system. The literature predominantly addresses linear systems, though some research has been applied to nonlinear systems (Isidori & Byrnes, 2000, Chen & Huang, 2015). Often, it is assumed that the external disturbances are generated from an autonomous, linear system:

$$\dot{\mathbf{d}} = \mathbf{C}\mathbf{d}, \tag{2.6}$$

which implies either:

- The eigenvalues of $\mathbf{C}$ have positive, real components in which case the system cannot be controlled,
- The eigenvalues of $\mathbf{C}$ have negative, real components in which case the disturbances will decay over time, or
- The eigenvalues of $\mathbf{C}$ have purely complex components, resulting in a smooth, sinusoidal disturbance.

Often, the disturbances are sinusoidal (Huang & Chen, 2004, Pavlov et al., 2007). Wu & Chuang (2003) applied output regulation theory to the control of a 2-link, planar manipulator. The first link of the manipulator moved at a constant angular velocity, viewed as a disturbance to the system. The second link had to move the end-effector at a constant angular velocity relative to the base or fixed frame. Output regulation theory was applied to reject this disturbance. However, given the complete kinematic model is known, the end-effector could be controlled sufficiently with a closed-form solution. Moreover, in many of these situations the external disturbances are of a constant velocity. This is

not guaranteed for a system in the open environment. In fact, Love et al. (2004) noted that disturbance modelling methods can fail if they do not account for shifts in frequency. Chen & Huang (2015) provide some theory for how this could be addressed.

Another impediment is that output regulation theory incorporates an internal model of the disturbance, even for nonlinear systems (Isidori & Byrnes, 2000; Byrnes & Isidori, 2003; Chen & Huang 2004). Disturbances generated to an AGV, UAV, or AUV or often stochastic, and hence an adequate model would be difficult to incorporate into this control method. Although wave theory models undulations of fluids with sinusoids, often the stochastic nature for a large body of water is represented via a probability distribution (Dean & Dalrymple, 1991). This makes disturbance estimation methods and stochastic forecasting techniques more desirable for the problem presented in this thesis.

2.7 Torque Minimization of Redundant Manipulators on Fixed Bases

It has been noted in some of the previous literature that redundancy can be employed to execute other tasks in addition to the end-effector control (Antonelli, 2000; Cieslak et al., 2015, Lunni et al., 2017). It is worth mentioning that From et al. (2011) did achieve torque minimization of a manipulator on a moving platform. However, since the manipulator itself was not redundant, it is not possible to execute both a task with the end-effector and reconfigure the joints to reduce joint torque at the same time. That said, much research has been done on the topic of dynamic torque minimization for redundant manipulators with fixed bases. Based on this premise, the potential exists that a redundant, mobile manipulator could utilize base disturbances to reduce joint torque and execute a task in a given fixed frame simultaneously.

Taking the time-derivative of Eqn. () gives the acceleration-level relationship between the end-effector and joints:

$$\ddot{\mathbf{x}} = \mathbf{J}(\mathbf{q})\ddot{\mathbf{q}} + \dot{\mathbf{J}}(\mathbf{q}, \dot{\mathbf{q}})\dot{\mathbf{q}}, . \tag{2.7}$$

Additionally, joint torques for a manipulator on a fixed base can be expressed as:

$$\boldsymbol{\tau} = \mathbf{M}(\mathbf{q})\ddot{\mathbf{q}} + \boldsymbol{\tau}_{\mathrm{c}}(\mathbf{q}, \dot{\mathbf{q}}) + \boldsymbol{\tau}_{\mathrm{g}}(\mathbf{q}), \tag{2.8}$$

in which:

- $\mathbf{M}(\mathbf{q}) \equiv \mathbf{M}_{\mathrm{qq}} \in \mathbb{R}^{\mathrm{n}\times\mathrm{n}}$ from Eqn. (),
- $\boldsymbol{\tau}_{\mathrm{c}}(\mathbf{q}, \dot{\mathbf{q}}) \equiv \mathbf{C}_{\mathrm{qq}}\dot{\mathbf{q}} \in \mathbb{R}^{\mathrm{n}}$ is joint torque component from Coriolis and centripetal forces from Eqn. (1.3), and
- $\boldsymbol{\tau}_{\mathrm{g}}(\mathbf{q}) \in \mathbb{R}^{\mathrm{n}}$ are joint torques due to gravitational forces.

Given a desired end-effector acceleration $\ddot{\mathbf{x}}$, a subsequent joint acceleration $\ddot{\mathbf{q}}$ can be solved via Eqn. (2.7) (see Appendix C). This can then be substituted into Eqn. (2.8) to obtain the necessary joint torques to move the manipulator.

As noted in Chapter 1, if the manipulator is redundant then there are theoretically infinite joint accelerations $\ddot{\mathbf{q}}$ that can achieve a desired end-effector acceleration $\ddot{\mathbf{x}}$. This property has been exploited by several researchers to minimize joint torque, albeit with respect to the internal dynamics of the system. A WLN solution to satisfy a given end-effector motion using Eqn. (2.7) is:

$$\ddot{\mathbf{q}} = \mathbf{J}_{\mathrm{W}}^{\dagger}\big(\ddot{\mathbf{x}} - \dot{\mathbf{J}}\dot{\mathbf{q}}\big) + \mathbf{N}_{\mathrm{W}}\ddot{\mathbf{q}}_{\mathrm{r}} \tag{2.9}$$

The derivation of this equation is shown in Appendix C. The various elements in Eqn. (2.9) are:

- $\mathbf{J}_{\mathrm{W}}^{\dagger} \in \mathbb{R}^{\mathrm{n}\times\mathrm{m}}$ is the weighted, pseudoinverse Jacobian that converts end-effector motion back to the joint space,
- $\mathbf{N}_{\mathrm{W}} \in \mathbb{R}^{\mathrm{n}\times\mathrm{n}}$ is the weighted null space projection matrix, and
- $\ddot{\mathbf{q}}_{\mathrm{r}} \in \mathbb{R}^{\mathrm{n}}$ defines redundant joint motions projected on to the null space.

Multiplying Eqn. (2.9) by the Jacobian $\mathbf{J}$ leads back to Eqn. (2.7) and hence $\ddot{\mathbf{q}}_{\mathrm{r}}$ has no influence on the end-effector motion $\ddot{\mathbf{x}}$.

Torque Minimization in the Null Space: Hollerbach & Suh (1988) proposed to minimize joint torque through two means. The first was to weight the joint equation by the inertia matrix, which gives local kinetic energy minimization. In addition, they defined the redundant task to keep the joint torques at the midpoint of their performance range:

$$\ddot{\mathbf{q}}_{\mathrm{r}} = \big(\mathbf{W}^{\frac{1}{2}}\mathbf{M}\mathbf{N}\big)^{\dagger}\Big(\mathbf{W}^{\frac{1}{2}}\frac{\boldsymbol{\tau}_{\max} + \boldsymbol{\tau}_{\min}}{2}\Big), \tag{2.10}$$

in which $\boldsymbol{\tau}_{\max} \in \mathbb{R}^{\mathrm{n}}$ is the maximum joint torque of the joints, and $\boldsymbol{\tau}_{\min} \in \mathbb{R}^{\mathrm{n}}$ is the minimum joint torque. The diagonal elements of $\mathbf{W} \in \mathbb{R}^{\mathrm{n}\times\mathrm{n}}$ were assigned based on torque limits for each joint.

Minimum Kinetic Energy Method: Nedungadi & Kazerouinian (1989) showed that a local optimization in the joint acceleration can lead to global minimization in kinetic energy. The optimal joint acceleration for this problem was given as:

$$\ddot{\mathbf{q}} = \mathbf{J}_{\mathrm{M}}^{\dagger}(\ddot{\mathbf{x}} - \dot{\mathbf{J}}\dot{\mathbf{q}}) - \mathbf{N}_{\mathrm{M}}\mathbf{M}^{-1}\boldsymbol{\tau}_{\mathrm{c}} \tag{2.11}$$

This is equivalent to Eqn. (2.9), where the general weighting matrix $\mathbf{W}$ is replaced with the manipulator inertia matrix $\mathbf{M}$, and the redundant task is $\ddot{\mathbf{q}}_{\mathrm{r}} \equiv -\mathbf{M}^{-1}\boldsymbol{\tau}_{\mathrm{c}}$.

Null Space Damping Method: Notice that the redundant task has not been defined at the velocity, $\dot{\mathbf{q}}_{\mathrm{r}}$, when using Eqn. (2.9). As a result, the null space velocities are uncontrolled. Both Hollerbach & Suh (1988) and Nedungadi & Kazerouinian (1989) noted that their control equations can lead to long-term instability in the manipulator because of this. Kang & Freeman (1992) added fictitious damping to the null space accelerations like so:

$$\ddot{\mathbf{q}}_{\mathrm{r}} = -\mathbf{M}^{-1}\boldsymbol{\tau}_{\mathrm{c}} - \gamma\dot{\mathbf{q}}, \tag{2.12}$$

where $\gamma = (0, 1)$ is a damping term. The authors claimed that not only did this guarantee stability of the null space, but it improved the torque minimization compared to Eqn. (2.11). This WLN method with null space damping will be used as a baseline performance measure for the torque minimization methods proposed in Chapter 5 and 6.

Simultaneous Velocity & Torque Minimization: To overcome the instability of the kinetic energy minimizing control, Zhang et al. (2013) proposed a dual optimisation of the form:

$$\min \tfrac{1}{2}\big(\mathrm{a}\dot{\mathbf{q}}^{\mathrm{T}}\dot{\mathbf{q}} + \mathrm{b}\boldsymbol{\tau}^{\mathrm{T}}\boldsymbol{\tau}\big), \tag{2.13}$$

where a and b are weighting coefficients on the velocities and torques respectively. This was solved via QP, which allowed for constraints on the joint position, velocity, and torque. The results of their research showed that it was possible to reduce torque whilst preventing any dramatic increase in the joint velocities.

Other Relevant Literature: One issue with the proposed control methods is that the Jacobian $\mathbf{J}$ can become ill-conditioned. Then, attempting to solve Eqn. (2.9) can lead to high joint accelerations and thus high joint torques. Chung et al. (2000) proposed a torque minimization with singularity robustness. First, fictitious damping was added to the null space, as per Kang & Freeman (1992). Then, a damped pseudoinverse Jacobian

was also applied. Although this idea is not new (Wampler, 1986), the damping coefficient for this latter case was attenuated by the dynamic manipulability of the system.

Computing the equations for dynamic control of a manipulator is considerably more difficult than at the velocity-level control. However, Flacco & De Luca (2015) developed a systematic method to convert acceleration level control schemes to the velocity level, whilst preserving torque optimization properties.

The literature presented on torque minimization, bar From et al. (2011), are concerned with manipulators on fixed bases. Furthermore, they only consider the internal dynamic torque. This leaves two unresolved problems:

1. As mentioned in Chapter 1, the dynamic coupling between the base and manipulator introduces additional joint torque into the dynamic model. Using a brute-force method, this can be negated. But utilizing these forces through a redundant manipulator has not yet been considered. This is a topic for consideration in Chapter 5.
2. The intent of mobile manipulation is in performing work (Marani et al., 2009; Simetti et al., 2014; Jin et al., 2017; Lehnert et al., 2016; Kajita & Kosuge, 1997). Applying or negating forces acting on the manipulator requires additional joint torque to that of Eqn. (2.8). How this might affect the torque minimization strategies remains unanswered.

Equation (2.8) can be extended to include external forces acting on the manipulator:

$$\boldsymbol{\tau} = \mathbf{M}\ddot{\mathbf{q}} + \boldsymbol{\tau}_{\mathrm{c}} + \boldsymbol{\tau}_{\mathrm{g}} + \mathbf{J}^{\mathrm{T}}\mathbf{R}\mathbf{w}, \tag{2.14}$$

where $\mathbf{R} \in \mathbb{SO}(\mathrm{m})$ is a rotation matrix from some arbitrary frame $\{\mathrm{i}\}$ on the manipulator to the origin frame $\{0\}$, and $\mathbf{w} \in \mathbb{R}^{\mathrm{m}}$ is a wrench of forces and torques expressed in frame $\{\mathrm{i}\}$. The previous methods of torque minimization presented (Eqns. (2.10 - 2.13) attempted to minimize Eqn. (2.8). However, with the addition of the term $\mathbf{J}^{\mathrm{T}}\mathbf{R}\mathbf{w}$, the properties of global kinetic energy minimization as proposed by Nedungadi & Kazerouinian (1989) and Kang & Freeman (1992) may not be guaranteed. In previous work, Woolfrey et al. (2019) showed that the addition of external forces can inadvertently increase the joint torque over the long term using these methods.

In Chapter 6, the torque minimization as proposed by Woolfrey et al. (2019) is re-visited. Some revisions are made with respect to the control equations which ensures stability.

Then the method is shown to be applicable even with a moving base under frequent, near-sinusoidal motion. Further reductions in joint torque can be made by using the predictive torque minimization method in Chapter 5.

2.8 Conclusions

It can be seen from the literature review that research exists in many of the related areas to the problem scenario presented in Chapter 1. Despite this, there are still clear problems which any combination thereof has not yet addressed:

1. Limited research has been conducted in to end-effector control of manipulators where the base motion cannot be adequately controlled. Furthermore, most literature on predictive control for autonomous mobile vehicles are concerned with optimal motion planning and energy reduction. Research on modelling and anticipating base disturbances, coupled with control strategies for end-effector control is still immature by contrast.

2. There is no consistency in the literature to indicate which prediction method is suitable, or how it ought to be evaluated. This is a critical starting point that should be addressed before control can even begin. To reiterate, From et al. (2011) state that AR is better than Fourier series for ship motion prediction, but Yang et al. (2008) claims that AR is poor at long-term forecast for such applications. Then Yuen et al. (2008) assert that Fourier series with an EKF is better than AR for predicting heart motion. And Becker et al. (2008) declared ARMA to be better than AR for predicting hand tremor. For evaluating the various methods, From et al. (2011) and Becker et al. (2008) used RMSE, Yuen et al. (2008) used AIC, Kashyap (1980) states that AIC is unreliable compared to BIC. All these applications exhibited periodicity in the data, too, and yet still no consensus exists.

   Also, this still does not account for forecast uncertainty. It has been shown that this can improve robustness of predictive control methods (From et al., 2011; Hyunh et al., 2015; Jones & Hollinger, 2017). From et al. (2011) were partial to AR because it had lower prediction error variance than Fourier series. But it is not evident this is desirable per se. Fang & Williams (2014) showed that even assumptions about the form of the uncertainty distribution can be inadequate for bounding trajectories.

3. Mobile manipulators on moving platforms (non-inertial platforms in particular) are subjected to forces from two main sources. The first being dynamic effects from inertial coupling with the base. The second being external forces, assuming they are employed to perform some form of work. From et al. (2011) had considered the dynamic effects of base motion for torque minimization of mobile manipulators, albeit without redundancy. If redundancy were available, it would be possible to simultaneously perform intervention tasks and minimize torque. The question then becomes how can these base disturbances be best employed to assist the manipulator? And can both the dynamic and external forces be accounted for simultaneously?

The various inconsistencies between forecasting methods are addressed in Chapter 3. Then, from this analysis, a predictive control strategy for the end-effector of a mobile manipulator is considered in Chapter 4. Finally, the torque minimization issue is divided in to two parts. Chapter 5 solves the problem of dynamic torque minimization by using base motion predictions. Then, in Chapter 6, torque minimization from external forces is studied. It is shown that this can be integrated with the dynamic torque minimization from base disturbances.

Chapter 3

Comparison of Forecasting Methods

3.1 Problem Formulation

It was posited that knowledge of the base motion for a mobile manipulator could be used to formulate a subsequent control strategy. This involved two potential avenues:

1. Proactively manoeuvring the manipulator to negate the base motion, thereby improving accuracy of the end-effector for intervention tasks, and
2. Utilizing the change in gravitational forces with respect to the manipulator to assist self-motion.

Suppose predictions of the base position $\hat{\mathrm{x}}(\mathrm{t}+\mathrm{i}),\ \hat{\mathrm{y}}(\mathrm{t}+\mathrm{i}),\ \hat{\mathrm{z}}(\mathrm{t}+\mathrm{i})$ and orientation in Euler angles $\hat{\phi}(\mathrm{t}+\mathrm{i}),\ \hat{\theta}(\mathrm{t}+\mathrm{i}),\ \hat{\psi}(\mathrm{t}+\mathrm{i})$ for $\mathrm{i} \in \{1, ..., \mathrm{L}\}$ steps ahead were given. Then the homogeneous transform of the base with respect to the fixed or inertial frame could be constructed:

$$\hat{\mathbf{T}}_{\mathrm{I}}^{\mathrm{B}}(\mathrm{t}+\mathrm{i}) = \begin{bmatrix} \hat{\mathbf{R}}_{\mathrm{I}}^{\mathrm{B}}(\mathrm{t}+\mathrm{i}) & \hat{\mathbf{p}}_{\mathrm{I}}^{\mathrm{B}}(\mathrm{t}+\mathrm{i}) \\ \mathbf{0}_{1\times 3} & 1 \end{bmatrix} \in \mathbb{SE}(3), \tag{3.1}$$

where:

- $\hat{\mathbf{R}}_{\mathrm{I}}^{\mathrm{B}}(\mathrm{t}+\mathrm{i}) \in \mathbb{SO}(3)$ is the predicted rotation matrix from the inertial frame {I} to the base frame {B}, constructed from the Euler angles, and
- $\hat{\mathbf{p}}_{\mathrm{I}}^{\mathrm{B}}(\mathrm{t}+\mathrm{i}) \in \mathbb{R}^3$ is the predicted position vector of the base {B} with respect to {I}.

By knowing the future base position (or even velocity, acceleration), it would be possible to move the manipulator to proactively counter this unwanted displacement. Furthermore, the gravity vector with respect to the manipulator, $\mathbf{g}_{\mathrm{B}} \in \mathbb{R}^3$ could be anticipated:

$$\hat{\mathbf{g}}_{\mathrm{B}}(\mathrm{t}+\mathrm{i}) = \hat{\mathbf{R}}_{\mathrm{B}}^{\mathrm{I}}(\mathrm{t}+\mathrm{i})\mathbf{g} \tag{3.2}$$

$$= \left(\hat{\mathbf{R}}_{\mathrm{I}}^{\mathrm{B}}(\mathrm{t}+\mathrm{i})\right)^{\mathrm{T}}\mathbf{g}, \tag{3.3}$$

where $\mathbf{g}$ is the gravity vector in the inertial frame. Alternatively, the gravity vector could be forecast directly from the base frame {B} with data from an IMU, for example. From et al. (2009) and From et al. (2011) had shown that by predicting the inertial forces, a manipulator on a ship could use these to minimize torque. This could be extended to minimize the torque of a redundant manipulator whilst performing intervention tasks under disturbance.

Before this can be achieved, the motion of the manipulator base must first be predicted. In Chapter 2, three different forecasting methods were introduced:

- Time series,
- Fourier series, and
- GPR.

The first two methods were applied to several different predictive control methods. However, it was noted there was no clear indication as to which prediction model is most suitable based on the literature. As such, the purpose of this chapter is to provide a clear and consistent comparison of these three methods.

3.1.1 Case Study using AUV Motion Disturbance

There are many conceivable scenarios in which the base motion of a mobile manipulator may disturb its kinematic and dynamic control. In order to keep the scope of this problem manageable, this chapter is restricted to studying AUV motion in shallow bathymetry. For one, there are numerous applications for UVMS as noted in Chapter 2. Furthermore, this type of periodic motion prediction problem is also applicable to surgical robotics (Yuen et al., 2008; Becker et al., 2008; Bowthorpe & Tavakoli, 2016). The results of this chapter will also provide a foundation for which to expand into other fields such as terrestrial vehicles and UAVs.

The review of related work in Chapter 2 also raises several questions about predicting marine vessel motion:

1. Did the AR model for ship motion prediction used by From et al. (2011) perform better than a superposition of sinusoids because it is better suited to the type of data? Or was it because it lacked an EKF that was applied by Yuen et al. (2008)?
2. Would using an ARMA time series model improve prediction accuracy versus the simpler AR model applied by From et al. (2011) and Woolfrey et al. (2016)?
3. How well to each of the prediction methods capture uncertainty about the future state?

It was also mentioned in Chapter 2 that evaluation of forecast uncertainty for predictive control literature is lacking. As Silver (2012) writes:

> The words predict and forecast are largely used interchangeably today, but in Shakespeares time, they meant different things ... Making a forecast typically implied planning under conditions of uncertainty. It suggested having prudence, wisdom, and industriousness, more like the way we now use the word foresight.

Knowledge of forecast uncertainty can improve the robustness of predictive motion planning and control (From et al., 2011; Huynh et al., 2015; Jones & Hollinger, 2017). Therefore, this chapter also examines how well the forecast uncertainty of the three aforementioned models bound the motion predictions. The results of these analyses could then translate to other predictive control problems for mobile manipulation.

Data Collection Process: The same motion data for the SPIR and Antarctic AUV introduced in Chapter 2 is studied here. To re-iterate, each of these AUVs was placed in a test tank at separate time. They were left to float freely on the surface of the water whilst a large object was used to displace water and generate waves. The IMU data was recorded at 50 Hz. The linear motion data is presented in m/s/s, and the angular motion data in rad/s.

3.2 Time Series

3.2.1 Structure of a Time Series Model

In time series modelling, the expected value of a state observation, $\hat{y}(t)$ is expressed as a weighted sum of previous state observations and prediction errors:

$$\hat{y}(t) = \sum_{i=1}^{p} \alpha_i y(t-i) - \sum_{j=1}^{q} \beta_j \varepsilon(t-j), \tag{3.4}$$

where:

- p is the number of AR terms,
- q is the number of MA terms, and
- $\varepsilon(t-j) = \hat{y}(t-j) - y(t-j) \sim \mathcal{N}\left(0, \sigma_\varepsilon^2\right)$ is the prediction error.

Equation (3.4) represents a stationary model, that is the data exhibit a long-term equilibrium. Models for nonstationary data can be found in Box et al. (2016). Although, it is worth noting that Eqn. (3.4) is robust and can be applied to non-stationary data for short-term forecasts. The coefficients $\alpha_i,\ i \in \{1, ..., p\}$ and $\beta_j,\ j \in \{1, ..., q\}$ can be optimised via linear least squares given a moving window of l historical state observations.

3.2.2 Determination of Model Parameters

Many different methods have been proposed for deciding the number of model parameters, p and q. This makes an objective evaluation across literature difficult:

- Yuen et al. (2008) used AIC to arrive at an AR(30) model,
- Conversely, Kashyap (1980) asserts AIC is unreliable,
- Becker et al. (2008) used RMSE and decided upon an ARMA model, and
- From et al. (2011) and Woolfrey et al. (2016) use RMSE for AR.

But, established methods of time series analysis (Box et al., 2016) states that the values for p and q are dictated by the number of statistically significant autocorrelation and partial-autocorrelation values in the data.

To determine the number of parameters, first the autocovariance γ_{i} must be calculated for a sample of data against the i^{th} lagged observation:

$$\gamma_{\mathrm{i}} = (\mathrm{n}-1)^{-1} \sum \big(\hat{\mathrm{y}}(\mathrm{t}|\mathrm{t}) - \bar{\mathrm{y}}\big)\big(\hat{\mathrm{y}}(\mathrm{t}-\mathrm{i}|\mathrm{t}-\mathrm{i}) - \bar{\mathrm{y}}\big). \tag{3.5}$$

Then, the autocovariance matrix can be constructed for $\mathrm{i} \in \{1, ...l\}$ lagged observations:

$$\boldsymbol{\Sigma}_\gamma = \begin{bmatrix} \gamma_0 & & & \\ \gamma_1 & \gamma_0 & & \\ \vdots & \vdots & \ddots & \\ \gamma_l & \gamma_{l-1} & \cdots & \gamma_0 \end{bmatrix} \tag{3.6}$$

Next, the autocorrelation matrix is calculated by dividing Eqn. (3.6) by the variance σ_γ^2 of the sample data:

$$\mathbf{P} = \sigma_{\mathrm{y}}^{-2}\boldsymbol{\Sigma}_\gamma = \begin{bmatrix} 1 & & & \\ \rho_1 & 1 & & \\ \vdots & \vdots & \ddots & \\ \rho_l & \rho_{l-1} & \cdots & 1 \end{bmatrix}. \tag{3.7}$$

If both $\boldsymbol{\Sigma}_\gamma$ and $\mathbf{P}$ are positive-definite, the data is considered stationary and hence Eqn. (3.4) is sufficient to model the data. The autocorrelation vector is readily extracted from Eqn. (3.7):

$$\boldsymbol{\rho} = \begin{bmatrix} \rho_1 & \rho_2 & \cdots & \rho_l \end{bmatrix}^{\mathrm{T}}. \tag{3.8}$$

Finally, partial-autocorrelation vector is found through:

$$\boldsymbol{\tau} = \mathbf{P}^{-1}\boldsymbol{\rho}. \tag{3.9}$$

Analysis of the autocorrelation values, $\boldsymbol{\rho}$ and the partial-autocorrelation values, $\boldsymbol{\tau}$ provide insight in to both the time series model, but also modelling for GPR.

3.2.3 Analysis of a Sample of AUV Motion Data

IMU data from the Antarctic AUV can be seen in Fig. 3.1, with the corresponding auto-correlation values and partial-autocorrelation values for up to $l = 50$ lagged observations. It was found that both the autocovariance matrix, $\mathbf{\Sigma}_\gamma$, and autocorrelation matrix $\mathbf{P}$ were positive-definite for this data set. The autocorrelation values show a slow, exponential decay which is indicative of an AR process (Box et al., 2016). The are also numerous significant values for the partial-autocorrelations, suggestive of a high-order AR model. An ARMA(40,0) model is applied in this chapter as a balance between sufficient prediction accuracy versus parsimony in the number of parameters. And, although the data do not indicate it, an ARMA(40,1) model is also evaluated in that correcting based on previous forecast errors may improve future results.

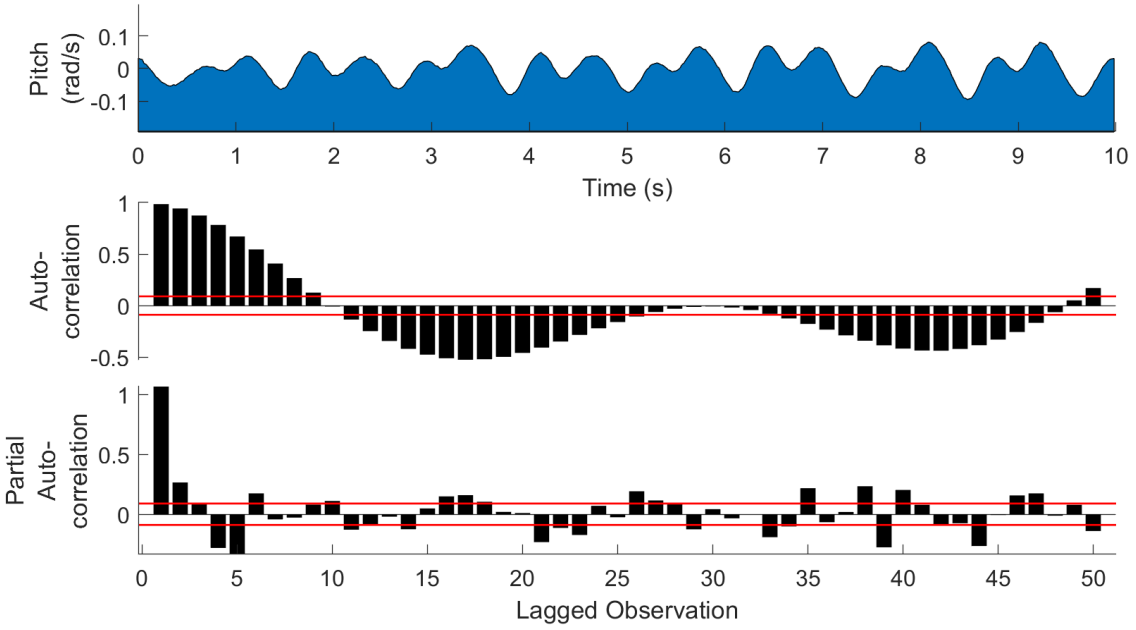

FIGURE 3.1: Correlograms for a sample of pitch motion (rad/s) shows statistically significant partial-autocorrelation values for up to 50 lagged observations.

3.2.4 Producing Forecasts with Time Series

Notice that, in Eqn. (3.4), the lagged observation of the state variable $\mathrm{y(t-i)}$ can itself be substituted with the same ARMA model ad-infinitum. This process leads to expressing the state propagation as a weighted sum of the state history and forecast error (Box et al., 2016). Equation (3.4) can then be written in an equivalent state space form:

$$\hat{\mathbf{y}}(\mathrm{t+1|t}) = \boldsymbol{\phi}(\mathrm{t})\hat{\mathbf{y}}(\mathrm{t|t}) + \boldsymbol{\psi}(\mathrm{t})\varepsilon(\mathrm{t}), \tag{3.10}$$

where:

- $\hat{\mathbf{y}}(\mathrm{t}|\mathrm{t}) = \begin{bmatrix} \hat{\mathrm{y}}(\mathrm{t}|\mathrm{t}) \\ \hat{\mathrm{y}}(\mathrm{t}+1|\mathrm{t}) \\ \vdots \\ \hat{\mathrm{y}}(\mathrm{t}+\mathrm{L}-1|\mathrm{t}) \\ \hat{\mathrm{y}}(\mathrm{t}+\mathrm{L}|\mathrm{t}) \end{bmatrix} \in \mathbb{R}^{\mathrm{L}+1}$,
- $\boldsymbol{\phi}(\mathrm{t}) = \begin{bmatrix} \mathbf{0}_{\mathrm{L}\times 1} & & \mathbf{I} & & \\ 0 & \alpha_{\mathrm{L}-2} & \cdots & \alpha_2 & \alpha_1 \end{bmatrix} \mathbb{R}^{(\mathrm{L}+1)\times(\mathrm{L}+1)}$,
- $\boldsymbol{\psi}(\mathrm{t}) = \begin{bmatrix} \psi_0 & \psi_1 & \cdots & \psi_{\mathrm{L}-1} & \psi_{\mathrm{L}} \end{bmatrix}^{\mathrm{T}}$,
- $\psi(\alpha, \beta)$ is a function of the coefficients (Eqn. (3.4)),
- L is the number of forecast lead terms, and
- $\varepsilon(\mathrm{t})$ is the 1-step-ahead prediction error, (Eqn. (3.4)).

The uncertainty propagation of this model is then calculated using:

$$\boldsymbol{\Sigma}_{\mathrm{y}}(\mathrm{t}+1|\mathrm{t}) = \boldsymbol{\phi}(\mathrm{t})\boldsymbol{\Sigma}_{\mathrm{y}}(\mathrm{t}|\mathrm{t})\boldsymbol{\phi}^{\mathrm{T}} + \sigma_{\varepsilon}^{2}\boldsymbol{\psi}(\mathrm{t})\boldsymbol{\psi}(\mathrm{t})^{\mathrm{T}}. \tag{3.11}$$

Equation (3.11) gives both the current state uncertainty and the prediction uncertainty. Furthermore, the state space form allows for the application of a Kalman Filter (KF). This will correct both the current state estimate *and* the forecasts when new sensor data is acquired. Details of the KF can be found in Appendix A. The observation matrix for Eqn. (3.10) is given by:

$$\mathbf{C} = \begin{bmatrix} 1 & \mathbf{0}_{1\times \mathrm{L}} \end{bmatrix}, \tag{3.12}$$

noting that only the current state $\hat{\mathrm{y}}(\mathrm{t}|\mathrm{t})$ is observable.

3.3 Fourier Series

3.3.1 Superposition of Sinusoids

According to wave theory (Dean & Dalrymple, 1991), the undulation of a body of water across a single dimension can be expressed as a discrete sum of m sinusoids:

$$\hat{\mathrm{y}}(\mathrm{t}) = \mathrm{c}_0(\mathrm{t}) + \sum_{\mathrm{i}=1}^{\mathrm{m}} \mathrm{r}_\mathrm{i}(\mathrm{t}) \sin(\theta_\mathrm{i}(\mathrm{t})) \tag{3.13}$$

$$= \mathrm{c}_0(\mathrm{t}) + \sum_{\mathrm{i}=1}^{\mathrm{m}} \mathrm{a}_\mathrm{i}\sin(\mathrm{i}\omega\mathrm{t}) + \mathrm{b}_\mathrm{i}\cos(\mathrm{i}\omega\mathrm{t}), \tag{3.14}$$

$$\theta_\mathrm{i}(\mathrm{t}) = \mathrm{i}\int_0^{\mathrm{t}} \omega(\tau)\mathrm{d}\tau + \phi_\mathrm{i}(\mathrm{t}), \quad \mathrm{i} \in \{1, ..., \mathrm{m}\}, \tag{3.15}$$

in which:

- c is a mean or constant,
- $\mathrm{r}_\mathrm{i} = \left(\mathrm{a}_\mathrm{i}^2 + \mathrm{b}_\mathrm{i}^2\right)^{1/2}$ is the amplitude of the i^{th} wave, and
- ω is the fundamental frequency.

Equation (3.13) is the polar form for this model, from which the rectangular form Eqn. (3.14) is derived through trigonometric identities. Given a sample of historical data, the coefficients in Eqn. (3.14) can be optimized using a Best Linear Unbiased (BLU) estimate:

$$\hat{\boldsymbol{\beta}} = \left(\mathbf{A}^\mathrm{T}\boldsymbol{\Sigma}_\mathrm{z}^{-1}\mathbf{A}\right)^{-1}\mathbf{A}^\mathrm{T}\boldsymbol{\Sigma}_\mathrm{z}^{-1}\mathbf{z} \tag{3.16}$$

$$\boldsymbol{\Sigma}_\beta = \left(\mathbf{A}^\mathrm{T}\boldsymbol{\Sigma}_\mathrm{z}^{-1}\mathbf{A}\right)^{-1}, \tag{3.17}$$

where:

- $\hat{\boldsymbol{\beta}} = \begin{bmatrix}\hat{\mathrm{c}}_0 & \hat{\mathrm{a}}_1 & \cdots & \hat{\mathrm{a}}_\mathrm{m} & \hat{\mathrm{b}}_1 & \cdots & \hat{\mathrm{b}}_\mathrm{m}\end{bmatrix}^\mathrm{T}$ is the estimate of the coefficients,
- $\mathbf{z} = \begin{bmatrix}\mathrm{z}(\mathrm{t}) & \cdots & \mathrm{z}(\mathrm{t}-l)\end{bmatrix}^\mathrm{T}$ are prior sensor or state observations,
- $\boldsymbol{\Sigma}_\mathrm{z} \in \mathbb{R}^{l\times l}$ is the uncertainty of said observations, and
- $\mathbf{A} = \begin{bmatrix} 1 & \sin(0) & \cdots & \sin(0) & \cos(0) & \cdots & \cos(0) \\ \vdots & \vdots & \vdots & \vdots & \vdots & \vdots & \vdots \\ 1 & \sin(\omega l\Delta\mathrm{t}) & \cdots & \sin(\mathrm{m}\omega l\Delta\mathrm{t}) & \cos(\omega l\Delta\mathrm{t}) & \cdots & \cos(\mathrm{m}\omega l\Delta\mathrm{t}) \end{bmatrix} \in \mathbb{R}^{l\times(2\mathrm{m}+1)}$

From et al. (2011) applied this least-squares optimisation to motion prediction of a ship in waves. However, this model only optimises the amplitudes for a given number of sinusoids. The fundamental frequency, ω remains constant. In actuality, this may change over time. Parker & Anderson (1990) applied an EKF to track hidden frequencies in noisy data. This was the method adopted by Yuen et al. (2008) and Bowthorpe & Tavakoli (2016) for use in predictive control for beating-heart surgery.

To apply the EKF method to the Fourier series, the state vector is denoted as:

$$\mathbf{x} = \begin{bmatrix} \mathrm{c}_0 & \mathrm{r}_1 & \cdots & \mathrm{r}_\mathrm{m} & \omega & \theta_1 & \cdots & \theta_\mathrm{m} \end{bmatrix}^\mathrm{T}, \tag{3.18}$$

in which $\theta_\mathrm{i} = \mathrm{atan2}(\mathrm{b_i}, \mathrm{a_i})$. An initial estimate for the state $\hat{\mathbf{x}}(0)$ can be found from Eqn. (3.17). The initial uncertainty is then computed via:

$$\boldsymbol{\Sigma}_\mathrm{x}(0) = \big(\partial\hat{\mathbf{x}}/\partial\hat{\boldsymbol{\beta}}\big)\boldsymbol{\Sigma}_\beta\big(\partial\hat{\mathbf{x}}/\partial\hat{\boldsymbol{\beta}}\big)^\mathrm{T} + \boldsymbol{\Sigma}_\mathrm{w}, \tag{3.19}$$

where $\boldsymbol{\Sigma}_\mathrm{w}$ is additional uncertainty to account for loss of information through linearization.

3.3.2 Extended Kalman Filter (EKF)

Equation (3.13) serves as the observation model for the state vector Eqn. (3.18). Since this is nonlinear, it requires an EKF to update the state vector when new information is acquired. The propagation for the state estimate $\hat{\mathbf{x}}$, and observation equation z are respectively:

$$\hat{\mathbf{x}}(\mathrm{t}+1|\mathrm{t}) = \mathbf{B}\hat{\mathbf{x}}(\mathrm{t}|\mathrm{t}) + \mathbf{s} \tag{3.20}$$

$$\mathrm{z}(\mathrm{t}+1) = \mathrm{y}\big(\hat{\mathbf{x}}(\mathrm{t}+1|\mathrm{t})\big) + \nu \tag{3.21}$$

where:

- $\mathrm{y}\big(\hat{\mathbf{x}}(\mathrm{t}|\mathrm{t}-1)\big)$ is the observation equation, equivalent to Eqn. (3.13),
- $\mathbf{s} \sim \mathcal{N}(\mathbf{0}, \boldsymbol{\Sigma}_\mathrm{s})$, and
- $\nu \sim \mathcal{N}(0, \sigma_\nu^2)$ is the sensor noise.

The state propagation matrix in Eqn. (3.20) is defined as:

$$\mathbf{B} \triangleq \begin{bmatrix} \mathbf{I}_{m+2} & & \mathbf{0} & & & \\ & \Delta t & 1 & 0 & \cdots & 0 \\ \mathbf{0} & 2\Delta t & 0 & 1 & \cdots & 0 \\ & \vdots & \vdots & \vdots & \ddots & \vdots \\ & m\Delta t & 0 & 0 & \cdots & 1 \end{bmatrix}. \tag{3.22}$$

Then the propagation of uncertainty about $\hat{\mathbf{x}}$ is given by:

$$\mathbf{\Sigma}_x(t+1|t) = \mathbf{B}\mathbf{\Sigma}_x(t|t)\mathbf{B}^T + \mathbf{\Sigma}_s, \tag{3.23}$$

with uncertainty $\mathbf{\Sigma}_s$ manually adjusted to produce sound results in the EKF. Calculating the Kalman Gain $\mathbf{K}$ is the same as in Appendix A. However, the observation matrix for the EKF is:

$$\mathbf{C}(t+1) \triangleq \frac{\partial y(\hat{\mathbf{x}}(t+1|t))}{\partial \hat{\mathbf{x}}(t+1|t)} \tag{3.24}$$

$$= \begin{bmatrix} 1 & \sin(\hat{\theta}_1) & \cdots & \sin(\hat{\theta}_m) & 0 & \hat{r}_1\cos(\hat{\theta}_1) & \cdots & \hat{r}_m\cos(\hat{\theta}_m) \end{bmatrix}, \tag{3.25}$$

The innovation for the state update is then computed as:

$$\epsilon(t+1) = z(t+1) - y(\hat{\mathbf{x}}(t+1|t)). \tag{3.26}$$

3.3.3 Forecasts from the Fourier Series with EKF

To produce forecasts at L time-steps ahead using the Fourier series, first the intrinsic state parameters and uncertainty must be propagated:

$$\hat{\mathbf{x}}(t+L|t) = \mathbf{B}^L\hat{\mathbf{x}}(t|t) \tag{3.27}$$

$$\mathbf{\Sigma}_x(t+L|t) = \mathbf{B}^L\mathbf{\Sigma}_x(t|t)(\mathbf{B}^L)^T + \sum_{i=0}^{L-1}\mathbf{B}^i\mathbf{\Sigma}_q(\mathbf{B}^i)^T. \tag{3.28}$$

The forecast of the state estimate $\hat{y}$ must be calculated from Eqn. (3.13), and its uncertainty using the linearized observation matrix $\mathbf{C}$ from Eqn. (3.25):

$$\hat{y}(t+L|t) = f(\hat{\mathbf{x}}(t+L|t)) \tag{3.29}$$

$$\sigma_y^2(t+L|t) = \mathbf{C}(t+L)\mathbf{\Sigma}_x(t+L|t)\mathbf{C}(t+L)^T. \tag{3.30}$$

3.4 Gaussian Process Regression

Both the time series and Fourier series apply a deterministic equation to model the covariance between data sets. These models assume that state observations are generated according to said equations. Any prediction errors are thus regarded as corruptions from noise (assuming the model is adequate to begin with). Conversely, a Gaussian Process (GP) models a distribution over functions. Inferences about an expected observation are produced from the covariance with nearby observations. As can be seen from the time series analysis (Fig. 3.1), the motion data of an AUV under wave excitation exhibits many statistically significant autocorrelation values over time. As was noted in Chapter 2, this temporal property has been utilized in applying GPR to wide variety of naturally occurring phenomena.

The set of current state estimates $\hat{\mathrm{y}}(\mathrm{t}|\mathrm{t})$ and future (predicted) values $\hat{\mathrm{y}}(\mathrm{t}+1|\mathrm{t})$ can be modelled via a joint Gaussian distribution:

$$\begin{bmatrix} \hat{\mathrm{y}}(\mathrm{t}|\mathrm{t}) \\ \hat{\mathrm{y}}(\mathrm{t}+1|\mathrm{t}) \end{bmatrix} \sim \mathcal{N}\left(\begin{bmatrix} \mu(\mathrm{t}) \\ \mu(\mathrm{t}+1) \end{bmatrix}, \begin{bmatrix} \boldsymbol{\Sigma}_{\mathrm{aa}} & \boldsymbol{\Sigma}_{\mathrm{ab}} \\ \boldsymbol{\Sigma}_{\mathrm{ab}}^{\mathrm{T}} & \boldsymbol{\Sigma}_{\mathrm{bb}} \end{bmatrix} \right), \tag{3.31}$$

where $\mu(\cdot)$ is a mean function and the covariance matrices between state observations are:

- $\boldsymbol{\Sigma}_{\mathrm{aa}} = cov(\mathbf{a}, \mathbf{a})$,
- $\boldsymbol{\Sigma}_{\mathrm{ab}} = cov(\mathbf{a}, \mathbf{b})$,
- $\boldsymbol{\Sigma}_{\mathrm{bb}} = cov(\mathbf{b}, \mathbf{b})$,

and input spaces to the time-series GP are:

- $\mathbf{a} = \begin{bmatrix} \hat{\mathrm{y}}(\mathrm{t}-1|\mathrm{t}-1) & \cdots & \hat{\mathrm{y}}(\mathrm{t}-l|\mathrm{t}-l) \end{bmatrix}^{\mathrm{T}}$
- $\mathbf{b} = \begin{bmatrix} \hat{\mathrm{y}}(\mathrm{t}|\mathrm{t}) & \cdots & \hat{\mathrm{y}}(\mathrm{t}-l+1|\mathrm{t}-l+1) \end{bmatrix}^{\mathrm{T}}$

for given inputs $\mathbf{a}, \mathbf{b}$. A prediction about future expected states given a window of historical state observations can then be made using:

$$\hat{\mathrm{y}}(\mathrm{t}+1|\mathrm{t}) = \mu(\mathrm{t}+1) + \boldsymbol{\Sigma}_{\mathrm{ab}}^{\mathrm{T}} \boldsymbol{\Sigma}_{\mathrm{aa}}^{-1} \big(\hat{\mathrm{y}}(\mathrm{t}|\mathrm{t}) - \mu(\mathrm{t}) \big) \tag{3.32}$$

$$\sigma_{\mathrm{y}}^2(\mathrm{t}+1|\mathrm{t}) = \boldsymbol{\Sigma}_{\mathrm{bb}} - \boldsymbol{\Sigma}_{\mathrm{ab}}^{\mathrm{T}} \boldsymbol{\Sigma}_{\mathrm{aa}}^{-1} \boldsymbol{\Sigma}_{\mathrm{ab}}. \tag{3.33}$$

A KF can readily be applied to the state estimates from Eqn. (3.32) and Eqn. (3.33).

3.4.1 Kernel Functions

The crux of GPR is in the kernel functions of the covariance matrix, a variety of which can be found in Rasmussen & Williams (2004), and Roberts et al. (2013). One useful property of kernel functions is that additions and products can be constructed to model complex data.

Matérn: The Matérn function equates to a continuous-time AR process (Rasmussen & Williams, 2006; Roberts, 2013) and hence is of particular interest here. As can be seen from the correlograms in Fig. 3.1, AUV motion under wave excitation has many statistically significant partial-autocorrelation values. The Matérn kernel function is:

$$cov_{\mathrm{M}}(\mathrm{a},\mathrm{b}) = \mathrm{h}^2 \frac{1}{\Gamma(\nu)2^{\nu-1}} \big(2\sqrt{\nu}\cdot\delta\big)\mathbb{B}_{\nu}\big(2\sqrt{\nu}\cdot\delta\big), \tag{3.34}$$

where $\delta = \lambda^{-1}|\mathrm{a}-\mathrm{b}|$, $\Gamma(\cdot)$ is the Gamma function, and $\mathbb{B}$ is the 2nd-order, modified Bessel function.

Rational Quadratic: This kernel function was combined with a periodic kernel by Roberts et al. (2013) to model changes in periodicity over time for stellar light curves. A similar formulation is thus employed in this chapter. The kernel function is given as:

$$cov_{\mathrm{RQ}}(\mathrm{a},\mathrm{b}) = \mathrm{h}^2 \left(1 + \frac{(\mathrm{a}-\mathrm{b})^2}{\alpha\lambda^2}\right)^{-\alpha}, \tag{3.35}$$

where h accounts for amplitude, λ is a length or time scale, and α is known as the index parameter.

Periodic Rational Quadratic: Periodicity can be introduced in to certain kernel functions by replacing $(\mathrm{a}-\mathrm{b})^2$ with $\sin^2\big(\pi(\mathrm{a}-\mathrm{b})/\mathrm{T}\big)$ with periodic parameter T. Substituting this in to the Rational Quadratic kernel Eqn. (3.35) becomes:

$$cov_{\mathrm{PRQ}}(\mathrm{a},\mathrm{b}) = \mathrm{h}^2 \left(1 + \frac{1}{\alpha\lambda^2}\sin^2\left(\pi\left|\frac{\mathrm{a}-\mathrm{b}}{\mathrm{T}}\right|\right)\right)^{-\alpha} \tag{3.36}$$

3.4.2 Mean Functions

Mean functions influence the behaviour of the expected output in a GP model. The mean function may be useful in accounting for steady disturbances in addition to the periodicity. The zero-mean, or even a constant mean function is the simplest:

$$\mu(\mathrm{t}) = \mathrm{c}, \quad \forall \mathrm{t}. \tag{3.37}$$

Assuming zero mean or constant is reasonable for local predictions as the kernel functions can account for complex behaviour. However, distance predictions are dominated by the mean. It was found that other mean functions, such as linear, did not improve forecasts of the GP and often optimization of the hyperparameters did not converge. As such, no further considerations are made.

3.5 Comparison of Forecast Models

3.5.1 Model Parameters

Time Series: Model parameters for the ARMA(p,q) format was chosen based on the time series analysis for small samples of data (Fig. 3.1). It was found that using $\mathrm{p} < 30$ lead to capricious forecasts when coupled with a KF. An ARMA(40,0) had stable forecasts up to 5 seconds ahead. An ARMA(50,0) is also feasible, but the latter was forgone in favour of model parsimony. To optimise the model parameters (Eqn. (3.4)), a lag length of $l = 250$ or 5 seconds worth of data was used. These were then used to formulate the state space model in Eqn. (3.10). Various combinations of ARMA(40,q) were also tested, though the prediction results did not improve (this is to be expected from the time series analysis). An ARMA(40,1) model is featured in this chapter to compare to the ARMA(40,0), as the former can correct forecasts based on the last prediction error.

Fourier Series: The Fourier series is presented here with $\mathrm{m} = 5$ and $\mathrm{m} = 10$ harmonics. In general, a higher number of harmonics leads to the Fourier series overfitting the data to noise. Note that Yuen et al. (2008) used $\mathrm{m} = 8$ for heart-motion prediction, so this appears to be a reasonable range for periodic motion data. The parameters in Eqn. (3.14) were optimised with $l = 400$ data points, or 8 seconds.

Gaussian Process Regression: The hyperparameters for the covariance functions Eqn. (3.34) and Eqn. (3.36) can be fitted via gradient descent optimization for the log-likelihood function (Rasmussen & Williams, 2006; Roberts et al., 2013). These were optimized on 600 samples within the data collected. Initial parameter values were randomized and several attempts at optimization were conducted to ensure convergence in the result. A moving window of $l = 100$ or 2 seconds of previous observations was used for the input space $\mathbf{a}, \mathbf{b}$ in Eqn. (3.32) of the GP. This was found to produce more accurate predictions than shorter windows.

3.5.2 Antarctic AUV

The Antarctic AUV prototype weighs approximately 17kg (Fig. 2.2b). The three prediction models were tested against the IMU data for 60 seconds worth of data. A sample is shown in Fig. 3.2.

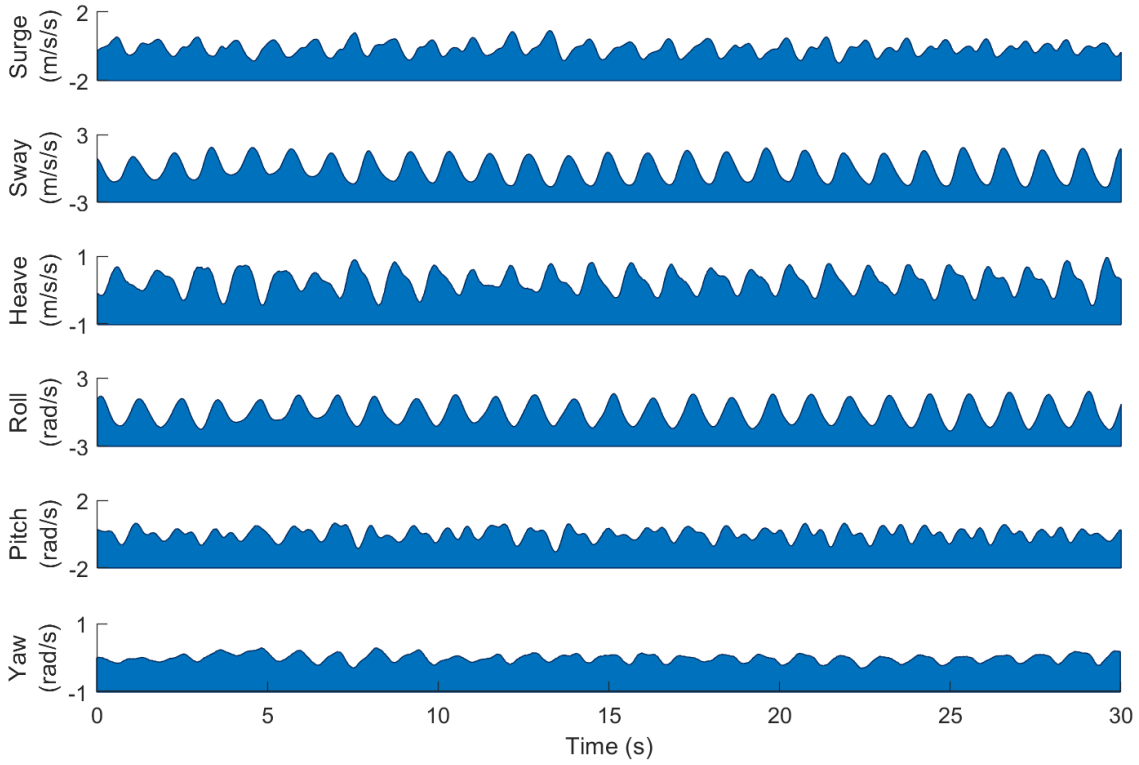

FIGURE 3.2: A 30s sample of IMU data recorded for the Antarctic AUV under wave excitation.

Mean Forecast Accuracy: Results for Theil's Coefficient for different forecasting methods can be seen in Table 3.1 for a prediction horizon of up to 5 seconds. A time series model with ARMA(40,0) produces forecasts that are more accurate than a last-value predictor for up to 5 seconds ahead. Becker et al. (2008) found that a mixed ARMA model produced better results for predicting hand tremor over AR. Earlier in this chapter, the question was posed as to whether using an ARMA model instead of AR might improve forecasts for marine vessels. The results here show that ARMA(40,1) over-corrects on the 1-step-ahead forecast (0.02 seconds), but mildly improves long term results. This is to be expected from the time series analysis (Fig. 3.1), which suggested an ARMA(p,0) process.

The Fourier series with m = 10 harmonics produces slightly better 1-step-ahead forecasts than the time-series, as was also noted by From et al. (2011). However, the long-term forecasts are not as accurate and do not adequately capture the periodicity (approximately 1.2 seconds). The GP model with the Periodic and Rational Quadratic covariance function has the best short-term forecasts and has comparable long-term results to the ARMA(40,0) model.

Forecast Uncertainty: Previous research by From et al. (2011) showed that time series had lower variance of prediction errors compared to Fourier series for ship motion prediction. The results in Table 3.2 show that the standard error of the time series model $\sigma_{\mathrm{SE}} > 3$, meaning the method exceeds the 99% confidence interval and is thus overconfident with its predictions. Conversely, the Fourier series with m = 10 harmonics is better at bounding the prediction errors for the 5 second forecast horizon. The GP methods underestimate prediction uncertainty for short forecasts horizons but provides a better confidence interval for the long term over the Fourier series.

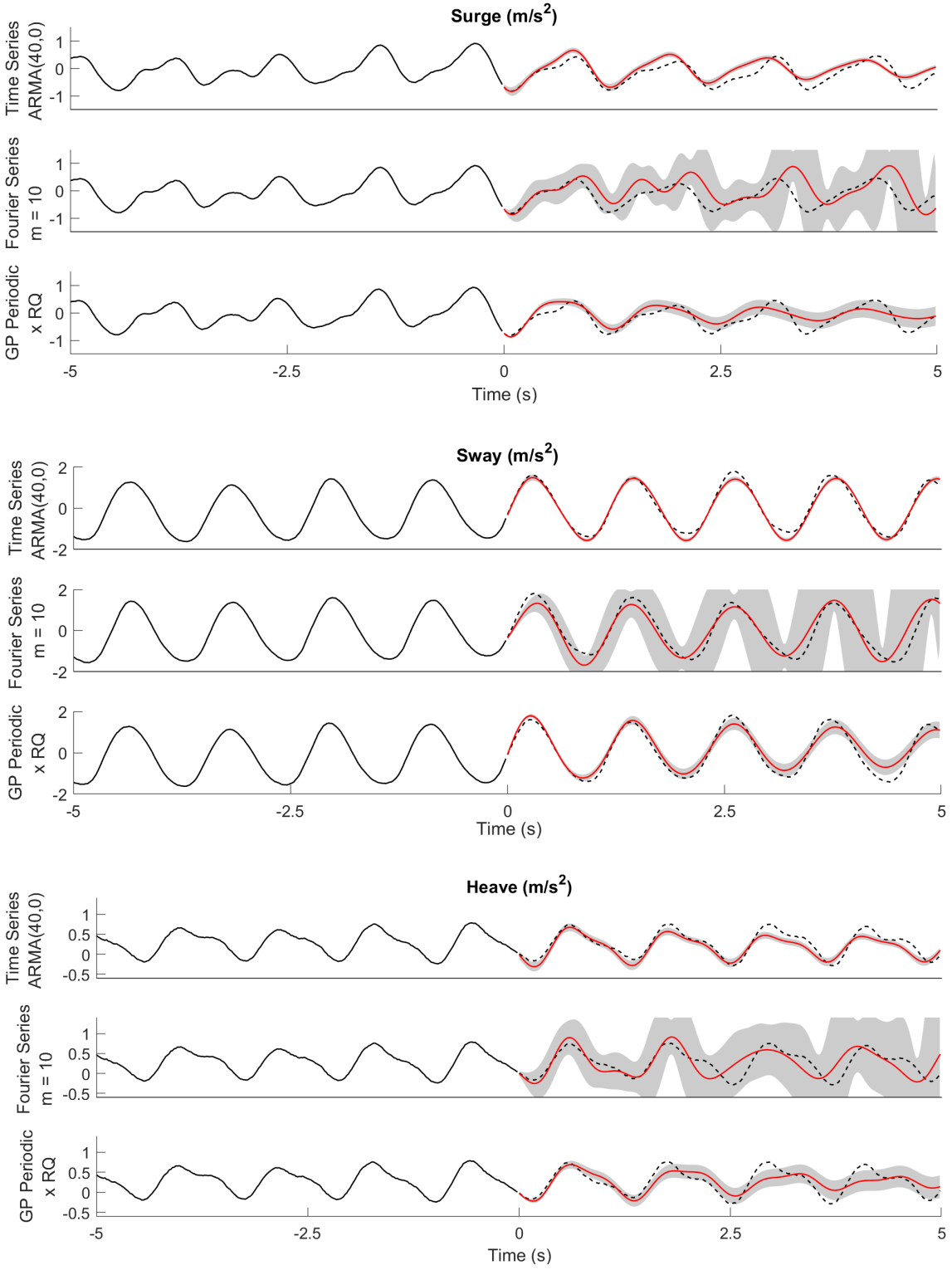

FIGURE 3.3: Forecasts of linear motion (red) for the Antarctic AUV prototype, with 95% confidence interval (grey)

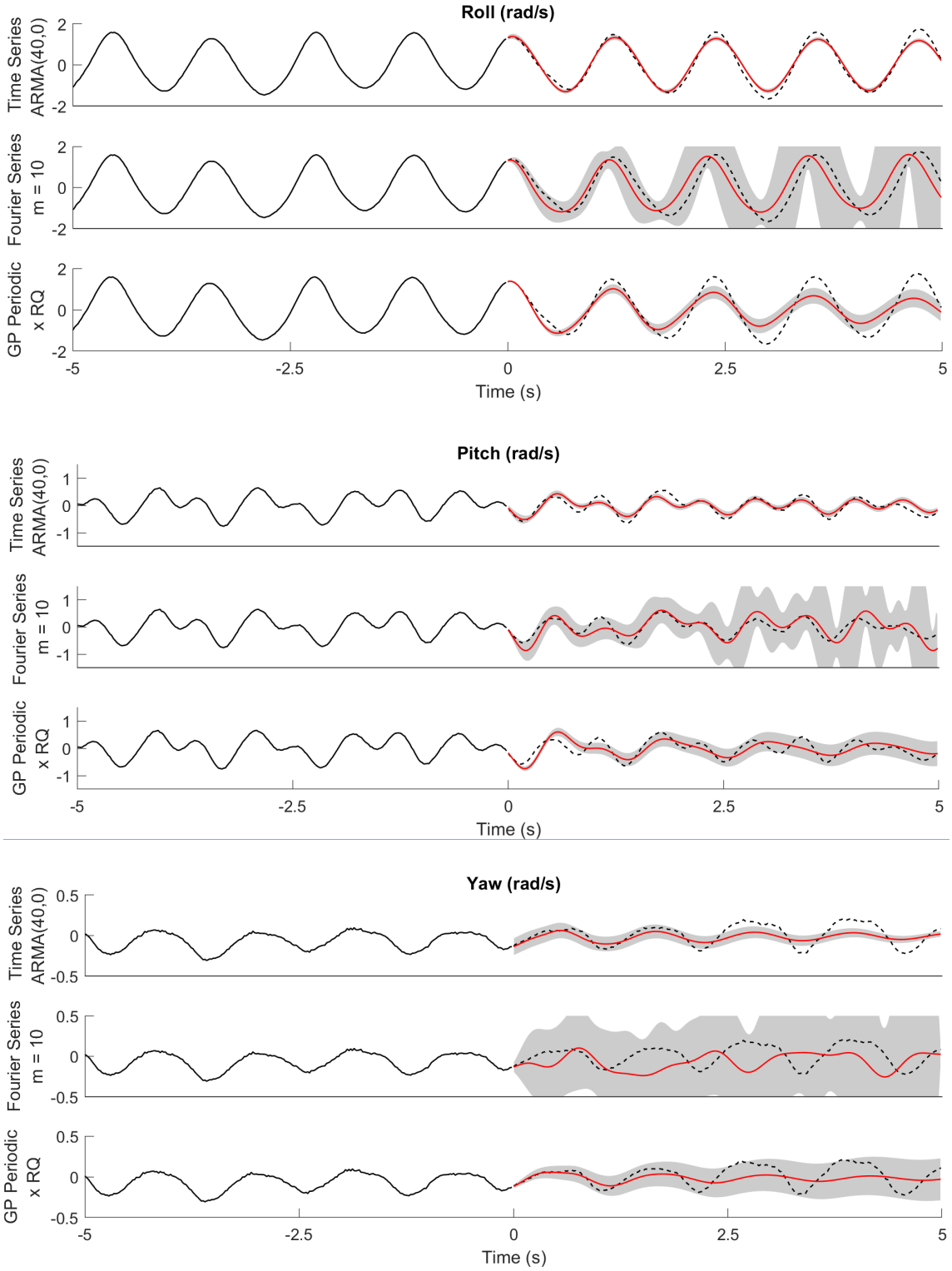

FIGURE 3.4: Forecasts of angular motion (red) for the Antarctic AUV prototype, with 95% confidence interval (grey).

TABLE 3.1: Theil's Coefficient for the forecasts of the Antarctic AUV data.

		Forecast Lead (s)																								
		0.02	*0.2*	*0.6*	*0.8*	*1.0*	*1.2*	*1.4*	*1.6*	*1.8*	*2.0*	*2.2*	*2.4*	*2.6*	*2.8*	*3.0*	*3.2*	*3.4*	*3.6*	*3.8*	*4.0*	*4.2*	*4.4*	*4.6*	*4.8*	*5.0*
ARMA(40,0)	Surge	0.49	0.41	0.40	0.42	0.59	0.89	0.54	0.46	0.46	0.48	0.76	0.91	0.58	0.52	0.51	0.56	0.90	0.79	0.56	0.54	0.54	0.64	1.08	0.75	0.58
	Sway	0.23	0.17	0.14	0.15	0.28	0.77	0.26	0.19	0.17	0.20	0.44	0.61	0.26	0.20	0.19	0.26	0.65	0.52	0.26	0.21	0.21	0.31	0.92	0.45	0.26
	Heave	0.47	0.29	0.28	0.30	0.46	0.99	0.50	0.44	0.44	0.49	0.77	0.96	0.59	0.52	0.53	0.62	1.01	0.93	0.62	0.56	0.56	0.68	1.10	0.88	0.64
	Roll	0.23	0.17	0.15	0.18	0.33	0.78	0.26	0.17	0.17	0.22	0.46	0.62	0.26	0.19	0.20	0.28	0.69	0.53	0.26	0.20	0.21	0.33	0.94	0.47	0.27
	Pitch	0.45	0.45	0.49	0.50	0.64	0.87	0.53	0.49	0.51	0.51	0.75	0.87	0.58	0.57	0.57	0.58	0.90	0.78	0.57	0.58	0.56	0.63	1.07	0.73	0.60
	Yaw	0.96	0.47	0.42	0.46	0.73	1.01	0.66	0.52	0.50	0.58	0.92	0.97	0.66	0.53	0.53	0.67	1.07	0.88	0.62	0.54	0.60	0.84	1.19	0.81	0.61
ARMA(40,1)	Surge	1.11	0.44	0.41	0.42	0.60	0.93	0.57	0.48	0.48	0.51	0.80	0.98	0.61	0.54	0.54	0.58	0.94	0.84	0.59	0.57	0.56	0.67	1.15	0.79	0.60
	Sway	0.40	0.16	0.13	0.15	0.25	0.71	0.24	0.17	0.15	0.18	0.38	0.54	0.23	0.17	0.17	0.22	0.56	0.45	0.23	0.17	0.18	0.26	0.78	0.39	0.22
	Heave	0.61	0.28	0.27	0.28	0.44	0.93	0.48	0.42	0.41	0.46	0.72	0.90	0.56	0.50	0.50	0.58	0.95	0.88	0.59	0.53	0.54	0.64	1.04	0.83	0.61
	Roll	0.46	0.17	0.15	0.18	0.33	0.74	0.24	0.16	0.15	0.20	0.42	0.57	0.24	0.18	0.18	0.25	0.63	0.48	0.23	0.18	0.19	0.29	0.83	0.41	0.24
	Pitch	0.81	0.44	0.49	0.50	0.65	0.87	0.54	0.49	0.52	0.52	0.76	0.88	0.58	0.57	0.57	0.58	0.90	0.79	0.57	0.59	0.57	0.64	1.08	0.74	0.60
	Yaw	1.41	0.46	0.40	0.43	0.69	0.97	0.63	0.49	0.46	0.54	0.86	0.90	0.61	0.49	0.49	0.62	0.99	0.81	0.56	0.49	0.54	0.77	1.08	0.73	0.55
Fourier Series (m = 5)	Surge	0.55	0.89	0.94	0.91	1.19	1.61	1.04	0.94	0.94	0.89	1.30	1.61	1.10	1.01	0.94	0.89	1.49	1.34	0.94	0.91	0.84	0.96	1.44	1.08	0.86
	Sway	0.25	0.33	0.30	0.40	0.78	1.94	0.69	0.49	0.48	0.65	1.36	1.82	0.77	0.55	0.57	0.83	1.95	1.51	0.78	0.58	0.64	0.94	2.50	1.39	0.81
	Heave	0.62	0.93	0.87	0.87	1.14	2.13	1.32	1.07	0.94	0.89	1.14	1.46	1.10	0.97	0.93	0.95	1.29	1.40	1.02	0.96	0.88	0.95	1.35	1.30	1.02
	Roll	0.31	0.43	0.39	0.48	0.89	1.93	0.74	0.50	0.48	0.61	1.19	1.68	0.73	0.51	0.52	0.73	1.67	1.48	0.76	0.57	0.61	0.88	2.20	1.33	0.78
	Pitch	0.49	0.80	0.86	0.86	1.08	1.38	0.88	0.79	0.80	0.79	1.08	1.25	0.92	0.90	0.89	0.83	1.24	1.11	0.88	0.85	0.82	0.95	1.51	1.05	0.89
	Yaw	0.56	0.66	0.60	0.72	1.15	1.44	0.81	0.62	0.59	0.71	1.07	1.07	0.71	0.58	0.59	0.75	1.17	1.04	0.83	0.72	0.83	1.12	1.45	1.03	0.80
Fourier Series (m = 10)	Surge	0.34	0.57	0.58	0.59	0.82	1.13	0.71	0.60	0.59	0.62	0.95	1.16	0.76	0.69	0.65	0.66	1.01	1.00	0.69	0.68	0.67	0.76	1.18	1.03	0.84
	Sway	0.22	0.36	0.32	0.44	0.83	2.13	0.69	0.46	0.45	0.64	1.31	1.89	0.82	0.60	0.63	0.89	2.29	1.86	0.87	0.71	0.76	1.09	3.09	1.60	0.86
	Heave	0.37	0.61	0.59	0.59	0.78	1.52	0.94	0.77	0.69	0.66	0.86	1.08	0.82	0.76	0.73	0.79	1.12	1.10	0.83	0.75	0.72	0.81	1.18	1.09	0.89
	Roll	0.20	0.32	0.28	0.36	0.66	1.36	0.51	0.35	0.35	0.47	0.93	1.33	0.59	0.41	0.43	0.59	1.34	1.21	0.59	0.46	0.51	0.71	1.82	1.08	0.58
	Pitch	0.38	0.67	0.71	0.71	0.96	1.22	0.78	0.73	0.73	0.73	1.04	1.20	0.85	0.81	0.76	0.79	1.21	1.12	0.86	0.79	0.80	0.92	1.51	1.09	0.85
	Yaw	0.54	0.77	0.72	0.88	1.36	1.71	1.00	0.77	0.77	0.89	1.29	1.29	0.86	0.72	0.74	0.93	1.43	1.19	0.82	0.74	0.81	1.10	1.41	1.00	0.76
GP (Matern)	Surge	0.26	0.47	0.48	0.50	0.69	0.90	0.55	0.51	0.53	0.57	0.83	0.93	0.63	0.58	0.58	0.62	0.92	0.80	0.58	0.57	0.59	0.69	1.05	0.78	0.61
	Sway	0.16	0.20	0.19	0.22	0.40	1.03	0.36	0.32	0.32	0.38	0.80	1.07	0.46	0.42	0.45	0.57	1.36	1.04	0.52	0.50	0.58	0.79	2.03	1.00	0.56
	Heave	0.30	0.19	0.17	0.22	0.37	0.69	0.53	0.47	0.43	0.43	0.60	0.79	0.64	0.60	0.58	0.61	0.83	0.85	0.65	0.60	0.57	0.62	0.84	0.82	0.67
	Roll	0.17	0.19	0.17	0.21	0.39	0.81	0.30	0.21	0.21	0.28	0.58	0.80	0.34	0.26	0.26	0.36	0.82	0.69	0.36	0.28	0.30	0.44	1.06	0.63	0.36
	Pitch	0.32	0.42	0.47	0.52	0.66	0.82	0.54	0.50	0.53	0.55	0.74	0.83	0.58	0.57	0.57	0.59	0.87	0.78	0.57	0.56	0.57	0.66	1.02	0.75	0.61
	Yaw	0.58	0.46	0.45	0.55	0.93	1.20	0.67	0.54	0.52	0.60	0.87	0.94	0.69	0.60	0.61	0.77	1.18	0.95	0.66	0.60	0.68	0.90	1.12	0.81	0.68
GP (Periodic RQ)	Surge	0.25	0.46	0.47	0.49	0.68	0.88	0.55	0.49	0.52	0.55	0.81	0.91	0.61	0.57	0.57	0.59	0.87	0.77	0.56	0.55	0.56	0.65	1.00	0.74	0.59
	Sway	0.13	0.16	0.15	0.18	0.33	0.85	0.28	0.21	0.20	0.26	0.55	0.75	0.32	0.25	0.25	0.35	0.86	0.67	0.34	0.28	0.30	0.44	1.22	0.62	0.36
	Heave	0.31	0.18	0.17	0.22	0.37	0.71	0.51	0.45	0.41	0.42	0.63	0.82	0.62	0.58	0.57	0.61	0.89	0.91	0.66	0.60	0.58	0.66	0.95	0.89	0.68
	Roll	0.16	0.18	0.17	0.21	0.39	0.82	0.30	0.22	0.21	0.29	0.61	0.83	0.35	0.27	0.27	0.39	0.91	0.74	0.38	0.30	0.32	0.49	1.26	0.70	0.40
	Pitch	0.32	0.43	0.48	0.53	0.69	0.85	0.55	0.51	0.54	0.56	0.74	0.83	0.59	0.58	0.57	0.60	0.88	0.79	0.59	0.57	0.57	0.67	1.03	0.76	0.62
	Yaw	0.57	0.46	0.43	0.51	0.85	1.05	0.62	0.52	0.52	0.63	0.97	0.96	0.65	0.57	0.59	0.75	1.17	0.92	0.64	0.60	0.66	0.91	1.17	0.80	0.63

Key:

> 1.0	Bad
0.99	Poor
0.94	
0.89	
0.84	
0.79	
0.74	
0.69	
0.64	
0.59	
0.54	
0.49	
0.44	
0.39	
0.34	
0.29	
0.24	
0.19	
0.14	
0.09	
0.04	Good
0.00	Perfect

TABLE 3.2: Standard Error for the forecasts of the Antarctic AUV data.

		Forecast Lead (s)																								
		0.02	*0.2*	*0.6*	*0.8*	*1.0*	*1.2*	*1.4*	*1.6*	*1.8*	*2.0*	*2.2*	*2.4*	*2.6*	*2.8*	*3.0*	*3.2*	*3.4*	*3.6*	*3.8*	*4.0*	*4.2*	*4.4*	*4.6*	*4.8*	*5.0*
ARMA(40,0)	Surge	0.37	3.74	3.62	3.89	3.87	3.70	3.93	4.52	4.53	4.70	4.78	4.60	5.31	5.53	5.71	5.83	5.99	5.93	6.53	6.69	6.93	7.10	7.36	7.75	8.55
	Sway	0.39	3.92	4.20	3.99	3.94	3.63	3.88	4.89	4.90	4.65	5.03	4.59	5.00	5.85	5.62	5.57	6.04	5.58	6.08	6.62	6.25	6.58	6.97	6.58	7.23
	Heav	0.31	2.43	2.73	2.76	2.82	2.73	2.84	3.74	4.07	4.32	4.46	4.19	4.21	4.82	5.02	5.27	5.47	5.13	5.26	5.63	5.75	6.02	6.17	5.91	6.36
	Roll	0.37	4.21	4.13	4.23	4.53	4.13	3.79	4.55	4.35	4.41	4.90	4.44	4.75	5.46	5.06	5.28	5.74	5.22	5.59	5.86	5.49	6.01	6.26	6.01	6.74
	Pitch	0.37	3.81	3.84	4.34	4.45	4.27	4.22	4.43	4.62	4.86	5.01	4.93	5.38	5.50	5.79	5.94	6.08	6.03	6.38	6.52	6.82	7.04	7.25	7.56	8.03
	Yaw	0.27	1.73	1.74	1.66	1.66	1.74	2.15	2.30	2.28	2.28	2.35	2.49	2.78	2.85	2.84	2.92	3.05	3.31	3.63	3.84	4.10	4.44	4.85	5.62	6.66
ARMA(40,1)	Surge	0.89	4.63	4.45	4.58	4.62	4.67	5.60	5.83	6.03	6.17	6.32	6.59	7.56	7.73	8.06	8.35	8.74	9.34	10.1	10.7	11.4	12.2	13.3	15.4	17.9
	Sway	0.73	4.76	4.79	4.44	4.28	4.16	5.05	5.92	5.74	5.38	5.73	5.47	6.42	7.20	6.70	6.71	7.23	7.01	7.89	8.41	7.74	8.46	8.87	8.67	10.0
	Heav	0.40	2.49	2.70	2.72	2.79	2.71	2.99	3.84	4.10	4.34	4.52	4.30	4.48	5.06	5.26	5.54	5.77	5.56	5.83	6.18	6.35	6.73	6.94	6.84	7.43
	Roll	0.77	4.93	4.73	4.88	5.19	4.64	4.73	5.27	5.10	5.33	5.74	5.33	6.15	6.68	6.29	6.96	7.32	6.74	7.32	7.52	7.26	8.34	8.43	8.41	9.99
	Pitch	0.70	4.36	4.63	5.09	5.17	5.07	5.29	5.43	5.83	6.05	6.21	6.30	6.90	7.12	7.54	7.76	8.07	8.27	8.84	9.32	9.91	10.4	11.1	12.1	13.5
	Yaw	0.40	1.79	1.72	1.61	1.62	1.76	2.19	2.31	2.26	2.26	2.35	2.52	2.82	2.88	2.88	2.97	3.12	3.45	3.81	4.02	4.32	4.72	5.25	6.27	7.75
Fourier Series (m = 5)	Surge	0.99	3.67	3.50	3.10	2.76	2.63	2.79	2.79	2.66	2.44	2.36	2.37	2.46	2.43	2.25	1.82	1.73	1.80	1.62	1.58	1.55	1.41	1.34	1.39	3.11
	Sway	1.02	3.20	2.90	2.75	2.61	2.36	2.65	2.76	2.69	2.67	2.41	2.41	2.42	2.33	2.43	2.35	2.14	2.14	2.28	2.14	2.14	1.88	1.86	2.06	5.24
	Heav	0.85	3.26	3.06	2.80	2.47	2.33	2.39	2.44	2.33	2.21	2.09	2.07	2.04	1.96	1.90	1.70	1.55	1.56	1.55	1.49	1.40	1.33	1.22	1.25	3.11
	Roll	1.10	3.66	3.31	3.09	2.90	2.66	2.79	2.54	2.45	2.41	2.14	2.25	2.43	2.19	2.13	2.22	2.03	2.13	2.12	2.08	2.00	1.84	1.72	1.81	4.43
	Pitch	0.99	3.52	3.40	3.07	2.80	2.59	2.51	2.43	2.29	2.24	2.12	2.10	2.19	2.12	2.03	1.70	1.56	1.47	1.60	1.47	1.45	1.41	1.39	1.39	3.35
	Yaw	0.31	1.04	0.93	0.90	0.81	0.78	0.80	0.77	0.71	0.68	0.66	0.65	0.65	0.63	0.62	0.61	0.60	0.61	0.67	0.62	0.61	0.58	0.57	0.57	1.06
Fourier Series (m = 10)	Surge	0.53	1.60	1.53	1.41	1.35	1.28	1.31	1.25	1.22	1.12	1.10	1.09	1.10	1.08	1.03	0.94	0.96	1.01	0.96	0.97	0.94	0.90	0.87	0.87	2.01
	Sway	0.81	2.38	2.32	2.27	2.19	2.02	2.10	1.90	1.88	2.12	1.79	1.64	1.86	1.58	1.71	1.66	1.63	1.67	1.62	1.73	1.77	1.55	1.60	1.53	2.96
	Heav	0.41	1.33	1.31	1.22	1.14	1.13	1.17	1.22	1.17	1.04	1.00	0.96	0.97	0.98	0.96	0.95	0.91	0.90	0.91	0.89	0.87	0.86	0.87	0.80	2.64
	Roll	0.68	2.07	1.92	1.91	1.79	1.65	1.64	1.58	1.50	1.55	1.42	1.33	1.46	1.32	1.31	1.30	1.21	1.20	1.28	1.17	1.17	1.16	1.13	1.08	2.43
	Pitch	0.63	1.90	1.79	1.63	1.59	1.50	1.45	1.42	1.33	1.32	1.29	1.25	1.28	1.22	1.16	1.12	1.08	1.07	1.13	1.07	1.05	0.98	1.01	0.94	2.26
	Yaw	0.25	0.74	0.71	0.70	0.64	0.62	0.63	0.61	0.60	0.57	0.54	0.53	0.54	0.53	0.51	0.50	0.47	0.49	0.49	0.47	0.47	0.45	0.44	0.45	0.99
GP (Matern)	Surge	0.76	5.25	4.40	3.85	3.38	2.88	2.83	2.82	2.80	2.70	2.54	2.33	2.39	2.37	2.36	2.28	2.18	2.01	1.98	1.97	1.99	1.95	1.90	1.84	1.81
	Sway	0.78	4.76	4.11	3.56	3.15	2.95	3.36	3.79	3.63	3.46	3.31	3.16	3.43	3.79	3.72	3.62	3.49	3.36	3.54	3.81	3.78	3.67	3.57	3.45	3.58
	Heav	0.88	2.34	1.98	2.10	2.25	2.10	2.34	2.65	2.54	2.44	2.53	2.56	2.52	2.55	2.52	2.46	2.41	2.37	2.30	2.25	2.18	2.12	2.06	2.01	1.98
	Roll	0.73	4.12	3.40	3.10	2.86	2.57	2.51	2.45	2.38	2.47	2.45	2.33	2.37	2.35	2.27	2.31	2.27	2.21	2.25	2.20	2.17	2.19	2.16	2.13	2.17
	Pitch	0.83	4.00	3.54	3.28	2.89	2.61	2.44	2.31	2.27	2.19	2.06	1.95	1.94	1.93	1.90	1.84	1.76	1.67	1.66	1.63	1.63	1.60	1.55	1.52	1.53
	Yaw	0.80	2.53	2.19	1.97	1.82	1.72	1.60	1.55	1.43	1.29	1.18	1.23	1.33	1.32	1.26	1.20	1.17	1.16	1.15	1.15	1.14	1.07	1.03	1.05	1.10
GP (Periodic RQ)	Surge	0.74	5.18	4.32	3.77	3.34	2.84	2.80	2.76	2.74	2.63	2.48	2.27	2.32	2.32	2.29	2.17	2.07	1.93	1.92	1.89	1.91	1.85	1.80	1.75	1.76
	Sway	0.74	4.54	3.88	3.36	2.94	2.74	3.01	3.19	3.05	2.90	2.75	2.65	2.83	2.93	2.87	2.80	2.70	2.66	2.80	2.83	2.78	2.73	2.66	2.65	2.74
	Heav	0.84	2.13	1.85	1.97	2.07	1.94	2.20	2.46	2.36	2.28	2.40	2.41	2.38	2.45	2.42	2.36	2.35	2.33	2.26	2.23	2.18	2.12	2.08	2.03	1.98
	Roll	0.76	4.30	3.55	3.21	2.96	2.69	2.67	2.66	2.58	2.69	2.63	2.51	2.56	2.55	2.48	2.55	2.48	2.45	2.49	2.45	2.44	2.47	2.41	2.41	2.44
	Pitch	0.83	4.04	3.53	3.30	2.93	2.62	2.45	2.31	2.21	2.17	1.99	1.89	1.89	1.87	1.85	1.81	1.72	1.65	1.65	1.61	1.59	1.57	1.51	1.49	1.52
	Yaw	0.74	2.42	2.01	1.74	1.58	1.45	1.43	1.45	1.36	1.29	1.24	1.20	1.19	1.20	1.16	1.13	1.11	1.08	1.07	1.09	1.06	1.04	1.02	0.99	0.98

Key:

3.00	Poor
2.99	
2.84	
2.69	
2.54	
2.39	
2.24	
2.09	
1.94	Good
1.79	
1.64	
1.49	
1.34	
1.19	
1.04	
0.89	
0.74	
0.59	
0.44	
0.29	
0.14	Poor
0.00	Bad

3.5.3 Submerged Pile Inspection Robot (SPIR)

The SPIR weighs approximately 45 kg. As with the Antarctic AUV, the different prediction methods were run for 60 seconds of data. A 30 second sample of this can be seen in Fig. 3.5.

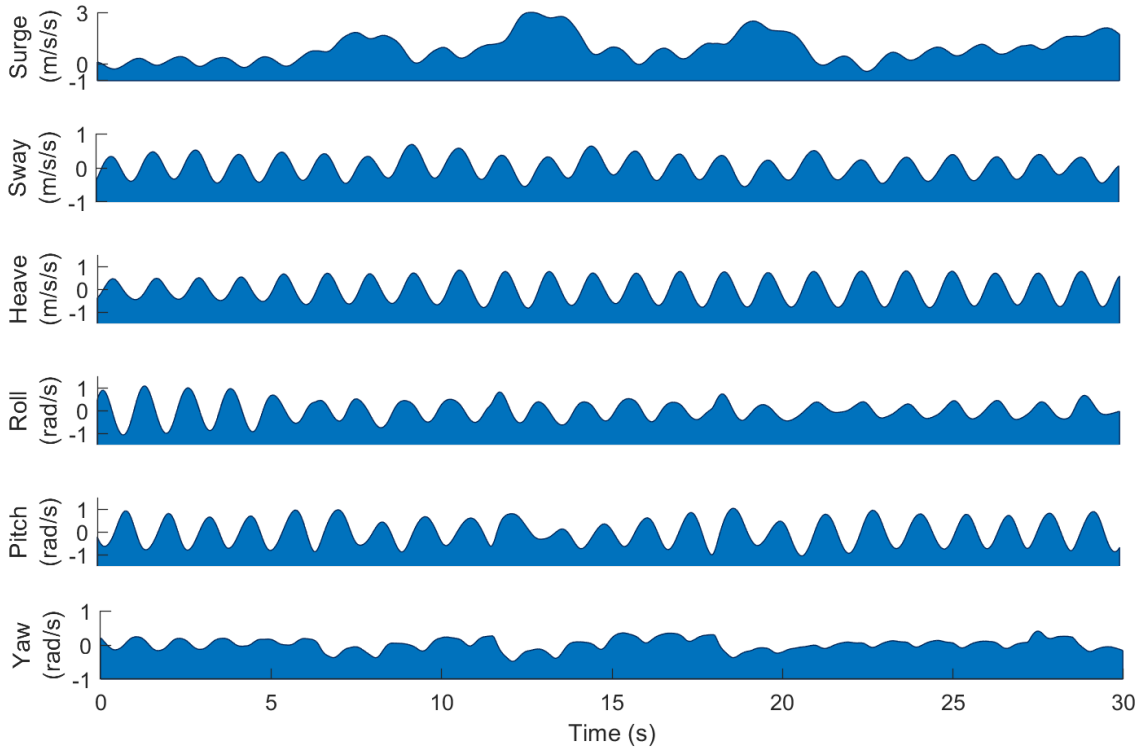

FIGURE 3.5: A sample of the IMU data captured for the SPIR.

3.5.3.1 Mean Forecast Accuracy

The motion data of the SPIR proved difficult to predict for all the forecasting methods (Table 3.3). Again, time series has better long-term predictions over Fourier series, whereas the latter has slightly better short-term predictions. The GP method with Matérn covariance function performed poorly for long-term predictions, compared to the Antarctic AUV data. The Periodic and Rational Quadratic kernel once more prove best for short and long term with 1-step-ahead predictions of $U < 0.01$.

All the prediction models tested performed poorly on the surge (forward) motion of the SPIR. Since $U > 1$ (Table 3.3), it would be better to use a last-value predictor in practice. On further analysis of the SPIR motion data, it was found to be nonstationary. The partial autocorrelation values for a sample of data (Fig. 3.6) are over-inflated, and the

autocovariance matrix $\mathbf{\Sigma}_\gamma$ is not positive-definite. This may explain the poorer results of the forecasting methods compared to the Antarctic AUV. Nonstationary models may be an area of future research to improve long-term forecast performance. Ironically, the Fourier series with m = 5 is better at forecasting surge motion than all other models for this data set.

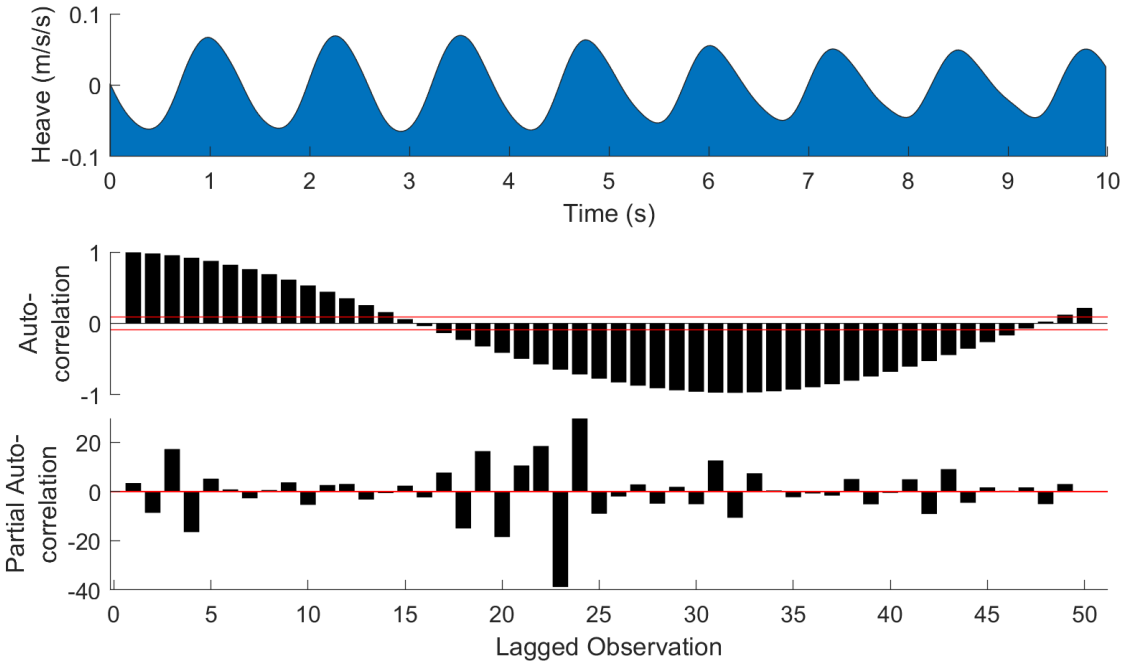

FIGURE 3.6: Correlograms for the heave motion of the SPIR v 3.0. The over-inflated partial-autocorrelation values are due to the nonstationary nature of the data.

3.5.3.2 Forecast Uncertainty

The results of the forecast uncertainty (Table 3.4) are much the same for the SPIR as the Antarctic AUV. The time series is overconfident with forecast uncertainty with $\sigma_{\text{SE}} \gg 3$ for t > 0.6s, exceeding the 99.7% confidence bounds. The Fourier series with m = 5 appears to produce the best results in terms of forecast uncertainty. The GPR with the Periodic-Rational Quadratic kernel has significantly large standard errors, greater than time series. Other kernel functions may produce better forecasts and uncertainty bounds for the nonstationary data, such as that used by Brahim-Belhouari & Bermak (2004).

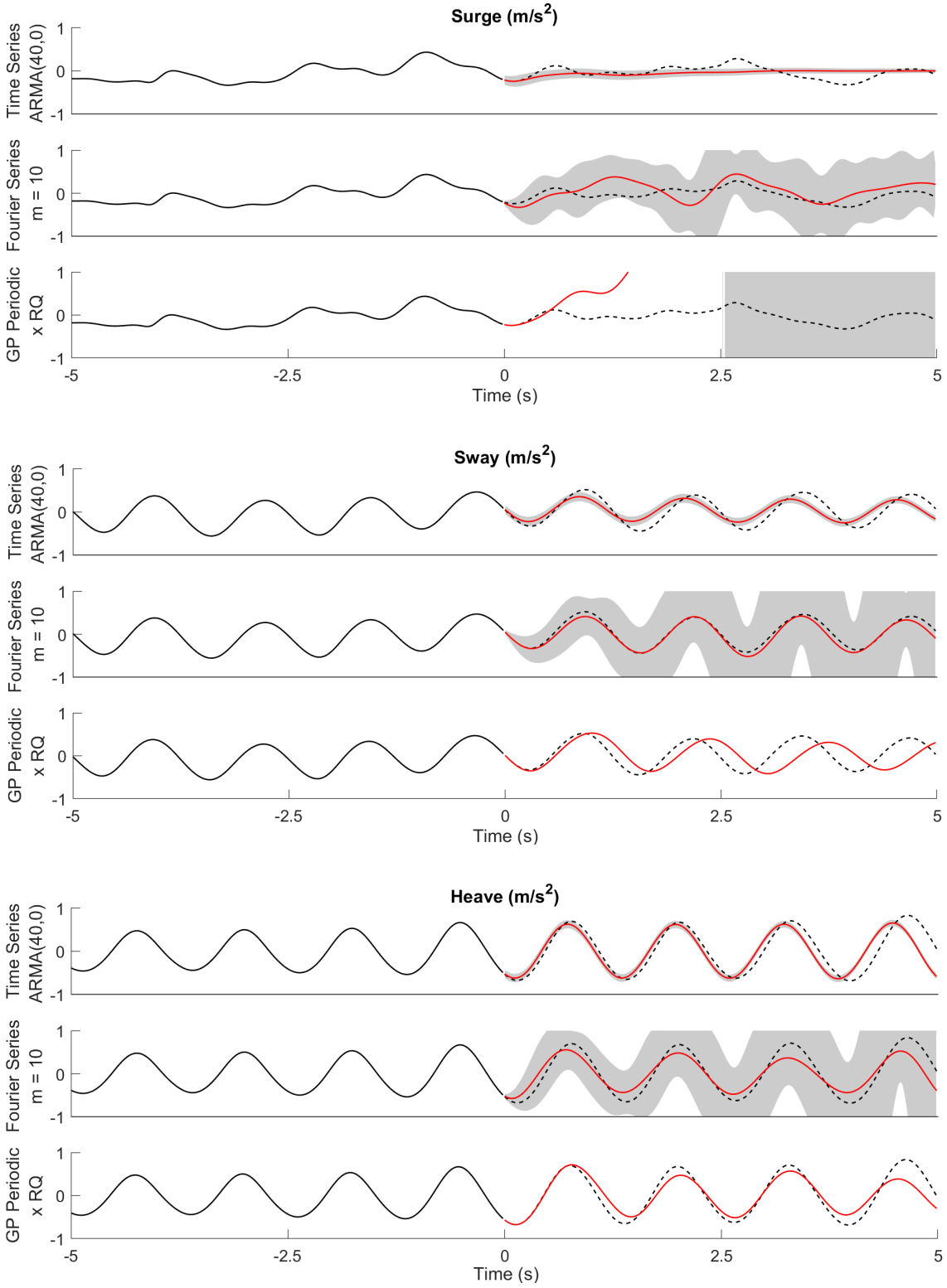

FIGURE 3.7: Forecasts of linear motion for the SPIR (red), with 95% confidence interval (grey).

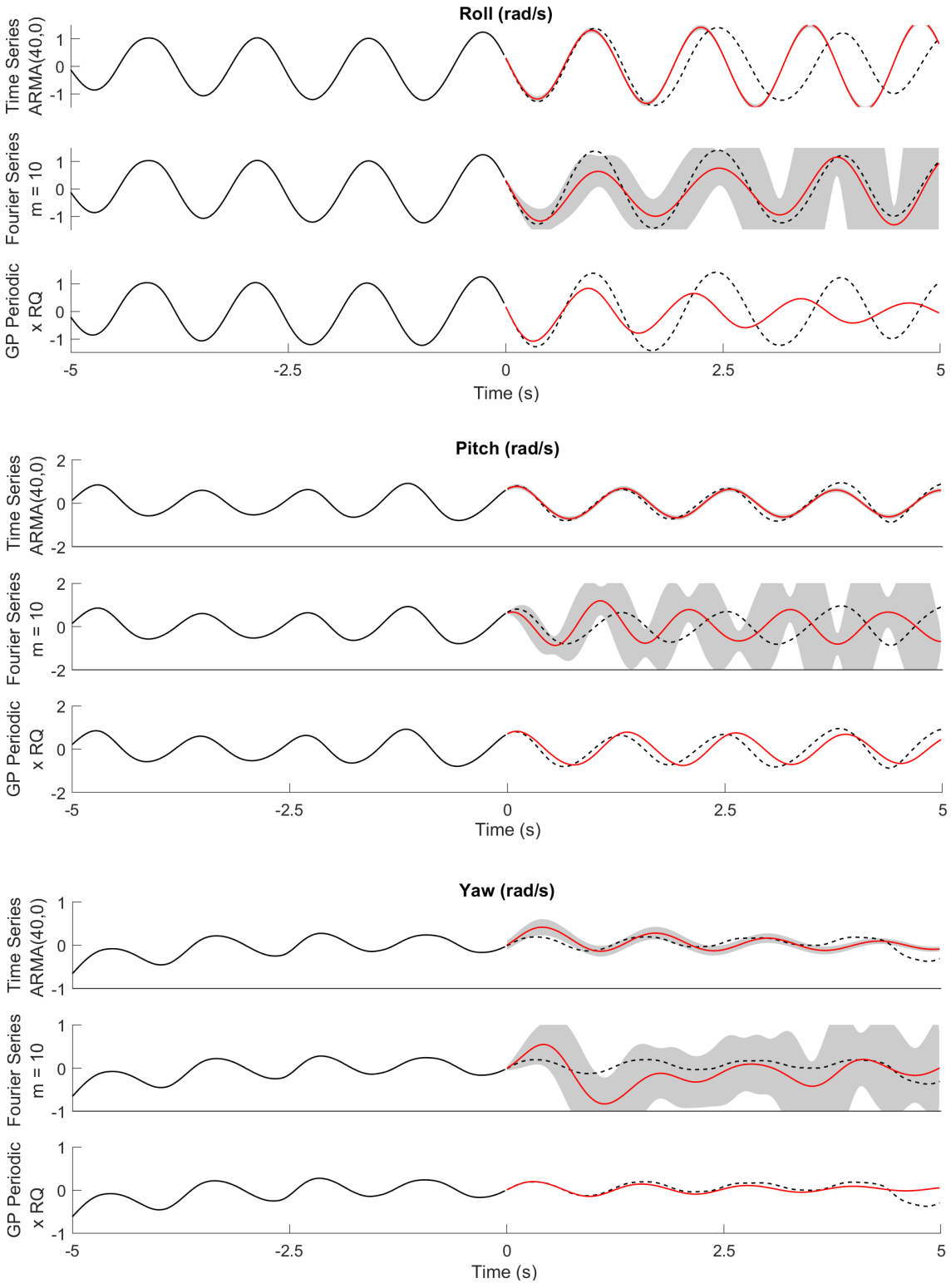

FIGURE 3.8: Forecasts of angular motion for the SPIR (red) with 95% confidence interval (grey).

TABLE 3.3: Theil's Coefficient for forecasts of the SPIR motion data.

		Forecast Lead (s)																									
		0.02	*0.2*	*0.6*	*0.8*	*1.0*	*1.2*	*1.4*	*1.6*	*1.8*	*2.0*	*2.2*	*2.4*	*2.6*	*2.8*	*3.0*	*3.2*	*3.4*	*3.6*	*3.8*	*4.0*	*4.2*	*4.4*	*4.6*	*4.8*	*5.0*
ARMA(40,0)	Surge	127	179	249	307	340	341	322	306	307	320	338	353	359	359	360	366	381	401	421	435	442	449	463	487	517
	Sway	0.51	0.37	0.40	0.43	0.53	0.81	0.90	0.61	0.50	0.48	0.54	0.74	1.02	0.92	0.70	0.62	0.63	0.72	0.92	1.04	0.90	0.75	0.69	0.71	0.82
	Heav	0.25	0.15	0.13	0.16	0.29	0.64	0.77	0.42	0.32	0.31	0.40	0.62	1.01	0.73	0.51	0.44	0.48	0.63	0.92	0.97	0.71	0.57	0.56	0.66	0.86
	Roll	0.31	0.24	0.22	0.24	0.41	0.91	0.85	0.50	0.42	0.41	0.52	0.88	1.29	0.82	0.63	0.56	0.60	0.84	1.27	1.08	0.76	0.65	0.63	0.76	1.09
	Pitch	0.29	0.27	0.27	0.29	0.42	0.84	0.91	0.56	0.46	0.45	0.54	0.79	1.07	0.88	0.69	0.62	0.66	0.81	1.02	1.03	0.87	0.77	0.76	0.84	0.97
	Yaw	1.01	0.77	0.80	0.84	0.94	1.05	0.96	0.83	0.78	0.77	0.81	0.90	0.92	0.83	0.76	0.73	0.73	0.80	0.88	0.86	0.76	0.71	0.70	0.73	0.81
ARMA(40,1)	Surge	14.4	20.2	27.9	33.7	36.4	36.0	33.8	31.5	30.2	29.9	30.0	29.9	29.5	28.7	28.1	28.0	28.6	29.8	31.0	31.7	32.0	32.2	32.8	34.2	36.0
	Sway	0.52	0.29	0.31	0.33	0.45	0.83	0.85	0.54	0.47	0.46	0.54	0.79	1.10	0.82	0.63	0.58	0.61	0.76	1.05	1.04	0.78	0.66	0.64	0.72	0.91
	Heav	0.32	0.15	0.13	0.17	0.29	0.64	0.77	0.42	0.32	0.31	0.39	0.62	1.00	0.72	0.50	0.43	0.47	0.62	0.90	0.95	0.69	0.56	0.54	0.64	0.84
	Roll	0.46	0.23	0.21	0.23	0.37	0.82	0.77	0.44	0.36	0.35	0.45	0.75	1.09	0.71	0.53	0.47	0.52	0.71	1.06	0.92	0.64	0.54	0.54	0.65	0.92
	Pitch	0.44	0.26	0.24	0.26	0.40	0.78	0.84	0.52	0.42	0.40	0.49	0.73	0.98	0.81	0.63	0.56	0.60	0.74	0.92	0.93	0.79	0.69	0.68	0.76	0.88
	Yaw	1.69	0.71	0.70	0.72	0.80	0.90	0.85	0.74	0.67	0.65	0.69	0.77	0.80	0.74	0.67	0.63	0.63	0.70	0.77	0.77	0.71	0.65	0.64	0.68	0.76
Fourier Series (m = 5)	Surge	0.62	1.14	1.28	1.31	1.25	1.12	1.01	0.94	0.91	0.89	0.88	0.86	0.84	0.83	0.83	0.83	0.84	0.84	0.85	0.86	0.88	0.91	0.95	0.99	1.02
	Sway	0.17	0.31	0.35	0.40	0.53	0.94	0.98	0.56	0.45	0.45	0.53	0.81	1.17	0.85	0.62	0.56	0.58	0.77	1.14	1.08	0.77	0.66	0.65	0.75	1.03
	Heav	0.10	0.19	0.18	0.21	0.33	0.74	0.90	0.46	0.37	0.36	0.45	0.70	1.14	0.80	0.56	0.49	0.52	0.66	0.99	1.03	0.76	0.64	0.62	0.70	0.95
	Roll	0.20	0.31	0.30	0.31	0.46	0.97	0.92	0.56	0.47	0.48	0.60	0.97	1.31	0.85	0.64	0.58	0.66	0.96	1.45	1.02	0.72	0.64	0.64	0.84	1.32
	Pitch	0.19	0.33	0.32	0.33	0.47	0.87	0.94	0.58	0.47	0.46	0.55	0.81	1.09	0.90	0.71	0.65	0.70	0.85	1.06	1.08	0.90	0.81	0.85	0.93	1.04
	Yaw	0.62	0.99	1.11	1.21	1.34	1.50	1.43	1.22	1.11	1.09	1.14	1.19	1.20	1.15	1.07	0.98	0.95	1.00	1.04	1.08	1.06	0.95	0.86	0.93	1.07
Fourier Series (m = 10)	Surge	0.57	1.18	1.40	1.53	1.57	1.52	1.42	1.37	1.39	1.46	1.54	1.60	1.63	1.64	1.66	1.72	1.82	1.92	2.00	2.06	2.09	2.14	2.23	2.38	2.55
	Sway	0.18	0.41	0.39	0.40	0.54	0.97	1.04	0.62	0.50	0.48	0.57	0.85	1.18	0.87	0.65	0.59	0.63	0.83	1.18	1.14	0.84	0.71	0.69	0.80	1.07
	Heav	0.09	0.18	0.17	0.19	0.31	0.70	0.83	0.43	0.34	0.33	0.40	0.64	1.05	0.74	0.53	0.46	0.49	0.63	0.95	0.98	0.71	0.60	0.59	0.68	0.92
	Roll	0.18	0.36	0.33	0.35	0.51	1.03	0.98	0.57	0.48	0.49	0.63	1.00	1.35	0.86	0.63	0.56	0.67	1.00	1.48	1.11	0.82	0.69	0.71	0.98	1.44
	Pitch	0.19	0.39	0.39	0.41	0.60	1.18	1.28	0.76	0.60	0.60	0.71	0.95	1.31	1.09	0.82	0.75	0.81	0.97	1.21	1.18	1.01	0.89	0.86	0.98	1.15
	Yaw	0.51	1.01	0.90	0.86	0.95	1.10	1.03	0.87	0.78	0.75	0.79	0.88	0.93	0.87	0.78	0.76	0.78	0.84	0.91	0.91	0.84	0.79	0.79	0.85	0.96
GP (Matern)	Surge	0.02	1.31	1.96	2.80	5.15	20.6	169	522	612	735	764	779	790	779	756	749	762	794	834	880	910	944	1006	1134	1300
	Sway	0.01	0.47	1.00	1.61	5.72	80.9	501	482	646	949	1541	2656	4236	3229	2366	2168	2254	2896	4123	3964	2934	2429	2273	2572	3426
	Heav	0.00	0.12	0.17	0.20	0.29	0.72	1.00	0.52	0.46	0.48	0.91	2.30	7.66	16.8	47.1	114	235	438	793	915	712	628	657	795	1073
	Roll	0.01	0.23	0.24	0.25	0.39	0.87	0.81	0.46	0.39	0.37	0.70	5.12	66.7	86.0	61.9	55.0	59.7	79.0	117	103	70.6	58.6	59.1	71.7	101
	Pitch	0.01	0.27	0.38	0.46	1.13	9.22	78.2	226	251	246	314	594	1154	1172	997	988	1097	1407	1865	1984	1704	1513	1512	1685	1971
	Yaw	0.10	0.91	0.84	0.82	0.93	1.12	1.10	1.00	0.88	0.82	0.84	0.93	1.04	1.01	0.92	0.81	0.76	0.86	1.02	1.03	0.91	0.82	0.78	0.85	1.03
GP (Periodic RQ)	Surge	0.01	1.06	2.69	15.9	82.8	140	207	216	286	328	406	484	562	619	647	693	706	713	714	719	723	730	741	784	792
	Sway	0.00	0.18	0.29	0.38	0.52	0.98	1.03	0.56	0.46	0.48	0.63	1.02	1.47	1.21	0.96	0.90	1.04	1.25	1.75	1.97	1.54	1.29	1.23	1.29	1.69
	Heav	0.00	0.11	0.18	0.22	0.31	0.72	0.90	0.43	0.36	0.37	0.42	0.63	1.06	0.73	0.49	0.45	0.48	0.59	0.91	0.97	0.68	0.57	0.57	0.63	0.83
	Roll	0.01	0.20	0.23	0.25	0.38	0.86	0.83	0.47	0.40	0.39	0.47	0.77	1.13	0.71	0.53	0.48	0.50	0.68	1.01	0.85	0.61	0.52	0.50	0.67	1.14
	Pitch	0.01	0.23	0.28	0.28	0.38	0.84	0.93	0.52	0.45	0.44	0.51	0.78	1.05	0.85	0.67	0.59	0.60	0.74	0.93	0.93	0.77	0.69	0.67	0.74	0.86
	Yaw	0.07	0.64	0.72	0.76	0.82	0.92	0.86	0.75	0.71	0.71	0.72	0.79	0.83	0.77	0.70	0.65	0.65	0.70	0.76	0.76	0.70	0.65	0.63	0.66	0.71

Key:

> 1.0	Bad
0.99	Poor
0.94	
0.89	
0.84	
0.79	
0.74	
0.69	
0.64	
0.59	
0.54	
0.49	
0.44	
0.39	
0.34	
0.29	
0.24	
0.19	
0.14	
0.09	
0.04	Good
0.00	Perfect

TABLE 3.4: Standard Error for the forecasts of the SPIR motion data.

		Forecast Lead (s)																								
		0.02	*0.2*	*0.6*	*0.8*	*1.0*	*1.2*	*1.4*	*1.6*	*1.8*	*2.0*	*2.2*	*2.4*	*2.6*	*2.8*	*3.0*	*3.2*	*3.4*	*3.6*	*3.8*	*4.0*	*4.2*	*4.4*	*4.6*	*4.8*	*5.0*
ARMA(40,0)	Surge	24.3	42.7	45.0	46.5	47.5	47.9	47.7	47.9	48.0	48.2	48.3	48.4	48.4	48.4	48.4	48.4	48.5	48.5	48.5	48.6	48.6	48.6	48.6	48.7	48.8
	Sway	0.19	2.06	2.91	3.16	3.12	3.27	3.26	3.18	3.45	3.73	3.86	4.10	4.30	4.30	4.43	4.71	4.91	5.11	5.27	5.38	5.55	5.78	5.96	6.15	6.46
	Heav	0.21	2.09	2.26	2.60	3.41	3.77	3.87	4.67	5.18	5.27	5.83	6.38	6.45	6.96	7.58	7.62	8.03	8.72	8.79	9.11	9.9	10.1	10.4	11.2	11.6
	Roll	0.25	3.02	3.64	3.53	4.17	5.06	4.82	5.11	6.13	6.34	6.26	7.17	7.52	7.19	7.88	8.44	8.13	8.48	9.05	8.72	8.93	9.6	9.30	9.4	10.2
	Pitch	0.28	3.64	4.71	4.84	5.57	6.34	6.21	6.77	7.7	7.90	8.26	9.1	9.2	9.4	10.1	10.3	10.4	11.0	11.3	11.2	11.8	12.0	12.0	12.5	12.7
	Yaw	0.28	2.69	3.51	3.94	3.89	3.89	3.77	3.78	3.99	4.25	4.36	4.40	4.45	4.42	4.52	4.69	4.86	5.04	5.25	5.41	5.55	5.85	6.27	6.94	7.98
ARMA(40,1)	Surge	4.92	23.1	27.1	30.0	31.0	31.0	30.9	31.1	31.3	31.6	31.6	31.2	30.8	30.7	30.5	30.4	30.0	29.6	29.4	29.4	29.5	29.1	28.5	29.1	29.5
	Sway	0.25	2.19	2.92	3.08	3.18	3.37	3.29	3.58	4.23	4.51	4.58	4.89	4.99	4.95	5.38	5.83	5.98	6.21	6.42	6.41	6.74	7.36	7.71	8.00	8.41
	Heav	0.26	2.14	2.28	2.67	3.52	3.89	4.00	4.83	5.40	5.49	6.05	6.65	6.78	7.27	7.91	8.08	8.49	9.20	9.41	9.79	10.7	11.0	11.3	12.3	12.8
	Roll	0.38	3.17	3.59	3.55	4.27	4.99	4.75	5.19	6.06	6.06	6.24	7.17	7.29	7.16	8.01	8.43	8.10	8.69	9.27	8.90	9.30	10.1	9.84	10.1	11.0
	Pitch	1.23	5.54	6.17	6.19	7.30	8.07	7.83	8.77	10.0	9.88	9.99	11.0	11.2	11.1	12.0	12.6	12.2	12.6	13.2	13.0	13.2	13.8	14.1	13.8	14.3
	Yaw	0.45	2.97	3.75	4.04	4.01	4.06	4.07	4.28	4.65	4.93	5.01	5.16	5.32	5.37	5.58	5.85	6.05	6.32	6.71	6.95	7.15	7.61	8.28	9.21	10.7
Fourier Series (m = 5)	Surge	0.57	2.72	3.14	3.37	3.26	3.01	2.95	2.97	3.12	3.23	3.06	2.84	2.75	2.79	2.73	2.76	2.76	2.53	2.34	2.28	2.36	2.19	2.31	2.36	4.19
	Sway	0.19	0.91	1.00	1.02	0.94	0.90	0.87	0.82	0.83	0.84	0.83	0.83	0.86	0.82	0.83	0.80	0.76	0.75	0.81	0.75	0.76	0.76	0.74	0.73	1.40
	Heav	0.23	0.95	0.96	0.98	1.05	1.10	1.10	1.15	1.24	1.25	1.25	1.30	1.32	1.30	1.31	1.32	1.31	1.30	1.24	1.23	1.20	1.14	1.17	1.12	1.91
	Roll	0.35	1.39	1.38	1.28	1.26	1.24	1.19	1.19	1.27	1.23	1.21	1.21	1.19	1.23	1.20	1.21	1.23	1.28	1.16	1.21	1.19	1.15	1.23	1.19	3.92
	Pitch	0.53	2.27	2.56	2.31	2.43	2.28	2.23	2.41	2.39	2.43	2.49	2.52	2.44	2.08	2.11	2.22	2.12	2.03	2.10	1.99	1.93	1.93	1.98	1.83	3.01
	Yaw	0.35	1.51	1.61	1.67	1.58	1.49	1.44	1.40	1.40	1.34	1.25	1.18	1.15	1.17	1.18	1.08	1.06	0.99	0.96	1.01	1.04	0.91	0.83	0.80	2.02
Fourier Series (m = 10)	Surge	0.46	1.79	2.04	2.11	2.10	1.96	1.87	1.83	1.93	1.98	1.86	1.77	1.69	1.73	1.77	1.73	1.69	1.85	1.81	1.65	1.73	1.82	1.80	1.63	2.87
	Sway	0.16	0.73	0.76	0.70	0.68	0.66	0.65	0.65	0.67	0.67	0.68	0.68	0.67	0.65	0.66	0.67	0.66	0.66	0.66	0.66	0.66	0.67	0.67	0.65	1.12
	Heav	0.17	0.63	0.64	0.64	0.67	0.68	0.67	0.69	0.71	0.73	0.72	0.72	0.76	0.77	0.76	0.75	0.77	0.75	0.71	0.79	0.75	0.71	0.73	0.74	1.15
	Roll	0.27	1.07	1.07	1.02	1.01	0.99	0.94	0.95	0.99	0.98	0.97	0.98	0.96	0.98	0.96	0.94	0.94	0.95	0.90	0.90	1.01	0.91	0.90	0.97	1.68
	Pitch	0.51	1.96	2.23	2.02	1.96	1.96	2.01	1.90	1.81	1.78	1.76	1.73	1.58	1.56	1.49	1.36	1.44	1.33	1.26	1.27	1.27	1.27	1.15	1.16	1.93
	Yaw	0.23	0.94	0.95	0.88	0.85	0.84	0.82	0.81	0.80	0.78	0.76	0.74	0.76	0.75	0.73	0.74	0.72	0.73	0.69	0.67	0.66	0.65	0.64	0.64	1.07
GP (Matern)	Surge	0.55	153	243	286	291	287	281	284	279	246	215	180	149	118	87.3	66.3	54.8	48.3	44.7	40.3	36.1	33.1	30.1	27.4	24.8
	Sway	0.54	170	277	304	259	165	82.4	43.2	28.8	19.4	12.4	10.9	12.0	12.8	9.58	5.80	4.92	4.61	5.15	4.11	2.98	1.52	0.64	1.09	0.62
	Heav	0.60	78.4	110	105	99.2	108	116	109	114	122	119	115	120	118	117	125	124	121	125	125	121	126	129	124	126
	Roll	0.54	64.2	68.2	57.6	58.6	59.6	55.1	54.6	57.6	54.4	54.4	56.6	54.2	52.6	55.2	53.5	50.5	52.1	50.7	47.2	48.2	48.6	45.5	45.3	44.9
	Pitch	0.57	86.7	120	111	94.2	107	102	91.1	98.2	100	91.6	88.2	86.0	81.8	81.9	82.5	79.0	74.8	72.6	70.6	68.6	68.0	67.0	64.6	62.3
	Yaw	0.89	47.6	49.5	43.4	38.3	36.5	34.2	34.6	35.8	33.2	32.1	29.6	26.7	26.6	27.2	25.6	24.5	23.9	22.8	21.9	22.2	21.9	20.4	19.5	19.4
GP (Periodic RQ)	Surge	0.64	482	1105	1584	1676	1469	1152	879	674	510	391	313	247	201	183	187	191	184	172	157	149	150	148	137	129
	Sway	0.66	191	303	337	313	280	255	234	241	254	251	250	260	262	258	259	253	245	247	251	248	252	260	259	256
	Heav	0.56	214	331	333	305	316	328	317	342	369	348	333	343	337	329	348	345	331	343	350	341	352	358	343	343
	Roll	0.48	66.0	72.5	64.1	64.5	66.6	62.7	63.8	67.5	64.1	62.3	64.0	61.5	59.5	61.5	59.6	55.9	56.1	54.7	51.4	51.9	51.3	48.3	47.4	46.9
	Pitch	0.64	75.3	89.2	77.1	70.8	77.4	75.7	72.5	79.1	79.3	77.2	81.4	81.5	78.3	79.0	78.6	75.5	75.3	75.9	73.7	72.1	72.3	70.8	69.4	69.1
	Yaw	0.94	48.3	54.9	51.0	43.6	38.9	36.7	36.6	37.9	36.7	33.7	31.9	30.9	29.9	29.3	28.0	26.5	25.7	25.1	24.0	23.0	22.2	21.4	20.6	19.7

Key:

3.00	Poor
2.99	
2.84	
2.69	
2.54	
2.39	
2.24	
2.09	
1.94	Good
1.79	
1.64	
1.49	
1.34	
1.19	
1.04	
0.89	
0.74	
0.59	
0.44	
0.29	
0.14	Poor
0.00	

3.6 Discussion

3.6.1 Limitations

In this chapter, the scope of the motion prediction problem was restricted to AUVs under wave excitation in shallow bathymetry. Therefore, extrapolation of these results to other predictive control problems should be done with prudence. The performance of the time series and Fourier series for the Antarctic AUV are in close agreement with the results for the ship motion data predictions by From et al. (2011). Other scenarios with periodic motion data, such heart motion (Yuen et al., 2008; Bowthorpe & Tavakoli; 2016), and hand-tremor for teleoperated surgery (Becker et al., 2008) are also tractable to the prediction models presented here.

However, this type of periodicity in the motion data might not always apply to other situations, such as UAVs or ground vehicles for example. This would rule out the application of the Fourier series of the GPR with the periodic kernel. However, both the time series and GPR are malleable in this regard and could still be used with the right model parameters.

One contribution of this chapter was the need for a statistical analysis of the data before applying a prediction model. A superposition of sinusoids is often assumed for modelling and predicting wave motion based on theory (Dean & Dalrymple, 1991). However, the time series analysis indicated a high order AR model would be sufficient. The results of this chapter, and even the research by From et al. (2011) both favour time series over Fourier series. Caution also needs to be applied in discerning stationarity of the data. All three models presented in this chapter assume stationarity, and the results showed this assumption leads to poor long-term forecasts for nonstationary data.

3.6.2 Time series vs Fourier Series

Based on the literature review in Chapter 2, there was no clear consensus as to whether time series or Fourier series would be most suitable for periodic motion prediction. To reiterate, From et al. (2011) stated that AR was better than Fourier series (without an EKF) for ship motion prediction. But Yang et al. (2008) had claimed AR to be a poor choice for ship motion prediction. Then Yuen et al. (2008) had found the Fourier series with EKF to be better than AR for predicting heart motion.

This chapter compared AR to Fourier series with the EKF on motion data for two different shallow water AUVs. The results revealed that an ARMA(40,0) model can indeed outperform the EKF for motion prediction of marine vessels. Actually, these results are not unexpected based on the origin of the method by Parker & Anderson (1990). The original intent of this method was to use the EKF to track changes in hidden (unobservable) frequencies in periodic, noisy data. The poor long-term forecasts when using this method are therefore not unreasonable.

3.6.3 Model Parameters

In attempting to predict hand-tremor for tele-operated microsurgery, Becker et al. (2008) had concluded that an ARMA model had lower RMSE than a pure AR model. The question was posed at the beginning of this chapter as to whether adding the MA term would improve predictions for marine vessel motion. Early analysis of AUV motion data (Fig. 3.1) had hinted that the data was indeed a high order AR process. The results of the analysis support these inferences. The inclusion of even a single MA term to correct forecasts based on the last prediction error did not improve the forecasts for AUV motion prediction.

Also, the Fourier series with EKF using 10 harmonics appeared to produce the best results across all 6-DOF of vehicle motion. This is commensurate with the 8 harmonics used by Yuen et al. (2008) with heart motion prediction. As previously mentioned, too many harmonics over-fits the model to noise, whereas too few fails to model the more complex wave forms.

3.6.4 Forecast Uncertainty

Earlier in Chapter 2, it was highlighted that forecast uncertainty can play a crucial role in predictive control strategies (From et al., 2011; Hyunh et al., 2015; Jones & Hollinger, 2017). However, very few had considered assessing the validity of the uncertainty for a given prediction model. From et al. (2011) noted that time series had lower prediction error variance to that of Fourier series for ship motion prediction. This was the same case for this chapter when predicting AUV motion in waves. However, this low variance lead to large standard errors in the predictions (Table 3.2, Table 3.4). The reason for this result is clear. Equation (3.11) describes the propagation of uncertainty for the time series model, which is a function of the prediction error variance. Thus, a small variance leads to

low uncertainty and hence overconfidence in the forecast. Likewise, the GPR method also underestimates prediction error when applied to the SPIR motion data. If these methods are to be applied to predictive control, then the forecast uncertainty would need to be manually inflated to account for this overconfidence.

3.6.5 Vehicle Morphology & Stationarity

The application of an AR model (Yuen et al., 2008; Yang et al., 2008; From et al., 2011; Woolfrey et al., 2016) has an implicit assumption that the data has stationarity. However, it was found here that the SPIR motion data was nonstationary (Fig. 3.6). This led to poorer prediction accuracy for all the prediction methods presented in this chapter.

Both the Antarctic AUV and SPIR motion data were collected in the same test tank. According to Dean & Dalrymple (1991), an unpropelled object floating on the surface of the water is dominated by particle accelerations and the pressure field around it. As such, the geometry between the two AUVs may explain the discrepancy in performance.

The wavelengths during data collection were 4m in length (due to harmonics) and approximately 320mm in height. Both the vehicles sit fully submerged in the water column. Figure 3.9 shows the pressure gradients surrounding the two different vehicles. As the length of the body for the SPIR is longer than that of the Antarctic AUV, this would result in a minute net force acting on the body as a wave passes by. This would cause it to drift over time with the passing waves, resulting in an underlying signal in the data not captured by the length of the historical state window.

Moreover, the force in the x-direction of such a pressure field is given by:

$$\mathrm{F_x} = \frac{-2\mathrm{gH}}{\mathrm{ksin}(\theta)} \cdot \frac{\mathrm{sinh(kh)sinh(k(h-d))}}{\mathrm{kcosh(kh)}} \cdot \delta, \tag{3.38}$$

where:

$$\delta = \sin(\tfrac{1}{2}\mathrm{kl_x}\cos(\theta))\sin(\tfrac{1}{2}\mathrm{kl_y}\sin(\theta))\sin(\omega \mathrm{t}) \tag{3.39}$$

and:

- d is the draught (depth of submersion),
- g is the gravitational acceleration,
- h is the wavelength,
- H is the wave height,

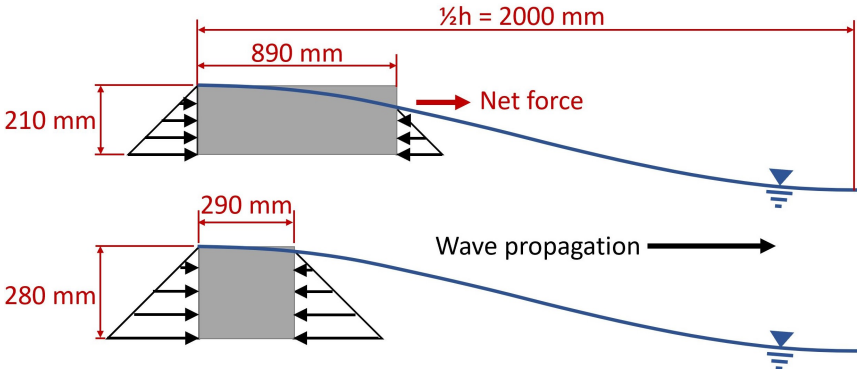

FIGURE 3.9: A small net force is generated on the SPIR due to its size relative to the passing wave.

- k is a constant,
- l_x, l_y are the length and width of the vessel respectively,
- ρ is the fluid density,
- θ is the angle of wave propagation w.r.t. the vehicle, and
- ω is the wave frequency.

The force imposed on the vehicle is a function of the heading relative to the wave propagation. Because the SPIR is rectangular, there would be uneven forces in the x and y directions, leading to a net moment acting on the vehicle. This moment will then lead to a change in θ and hence further drift in the linear accelerations on the body. This may further lead to nonstationarity in the data. Conversely, the Antarctic AUV is cylindrical in shape and therefore uneven pressure fields cannot be generated around its circumference from a passing wave. This would mean there is little yaw motion in the data, as can be seen in Fig. 3.8.

These results show that vehicle morphology with respect to the geometry of the surrounding environmental disturbances may play a crucial role in deciding which forecasting method to apply.

3.7 Conclusion

In this chapter, three different forecasting methods were studied in predicting AUV motion in waves, with a view to disturbance prediction of manipulators operating on mobile platforms. These were:

1. Time series,
2. Fourier series, and
3. Gaussian Process Regression (GPR).

Both time series and Fourier series have been applied successfully to predictive control methods across different fields. However, a review of literature (Chapter 2) showed that different authors choose different parameters for different methods and assess the prediction quality using different criteria. Different authors reached different conclusions about which prediction model is the most accurate. However, it is not evident whether the differences in accuracy were a consequence of the type of data used, the number of parameters, or the metrics used to select them.

To resolve this conundrum, two AUVs designed for intervention tasks in shallow bathymetry were used as a case study. IMU data was collected from each under wave excitation in a test tank. Mean forecast accuracy was assessed using Theil's Inequality Coefficient (Theil, 1966). Results showed that GPR with a periodic kernel has better short-term forecasts than time series or Fourier series. And, for the long term, both time series and GPR had similar performance.

Another important factor not often assessed in the relevant literature was the forecast uncertainty of each model. Analysis of the standard error for the forecasts showed that time series is overconfident with its uncertainty bounds, whereas Fourier series is the most conservative. The GPR was overconfident for short-term forecasts but had the most desirable uncertainty bounds for the long-term.

Time series forecasting is used throughout the rest of this thesis for the following reasons:

1. There is no assumption made about periodicity of disturbances for the remaining chapters, and hence this excludes Fourier series and the GPR with the periodic kernel.
2. Time series parameters can be fit with convex optimization and does not require training hyperparameters like GPR, and can therefore be applied to any data set with minimal effort.
3. The state space format (Eqn. (3.10)) produces forecasts for the entire prediction horizon simultaneously, whereas GPR requires iterative, 1-step-ahead forecasts.

An important note, however, is that all work presented in the proceeding chapters are independent of the prediction method. As such, any method can be readily substituted. All that is required hereon is a forecast for the base pose of the manipulator.

Chapter 4

Predictive Control of Manipulators on Moving Platforms

4.1 Problem Scenario

Mobile manipulators operating in the field may be required to perform manipulation tasks with the physical environment in some manner. A natural frame of reference for specifying such a task would be with respect to some fixed frame in the world, typically denoted as the inertial frame {I}. However, as was discussed in Chapter 1, the base may be moving from the vehicle control or unwanted disturbance. As such, there is some desired pose or target for the end-effector {D}, relative to the fixed frame {I}. Then the manipulator must regulate the end-effector {E} whilst the base {B} moves relative to {I} (Fig. 4.1).

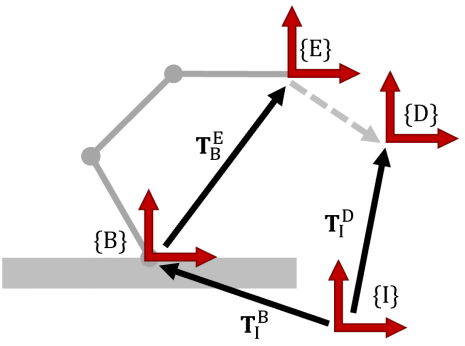

FIGURE 4.1: Relative frames in a mobile manipulation scenario.

But consider an alternate perspective of the problem. All motion is relative. Therefore, a fixed target in {I} will appear as a moving target if all motion is expressed relative to the manipulator's base {B} (Fig 4.2). The problem of a manipulator attempting to maintain a fixed end-effector pose in the inertial frame then becomes a problem of tracking a trajectory from the persepctive of {B}. By extension, tracking a trajectory specified in {I} requires following a transformed trajectory in {B}. By tracking this transformed trajectory, the manipulator is effectively moving to negate the base motion disturbances.

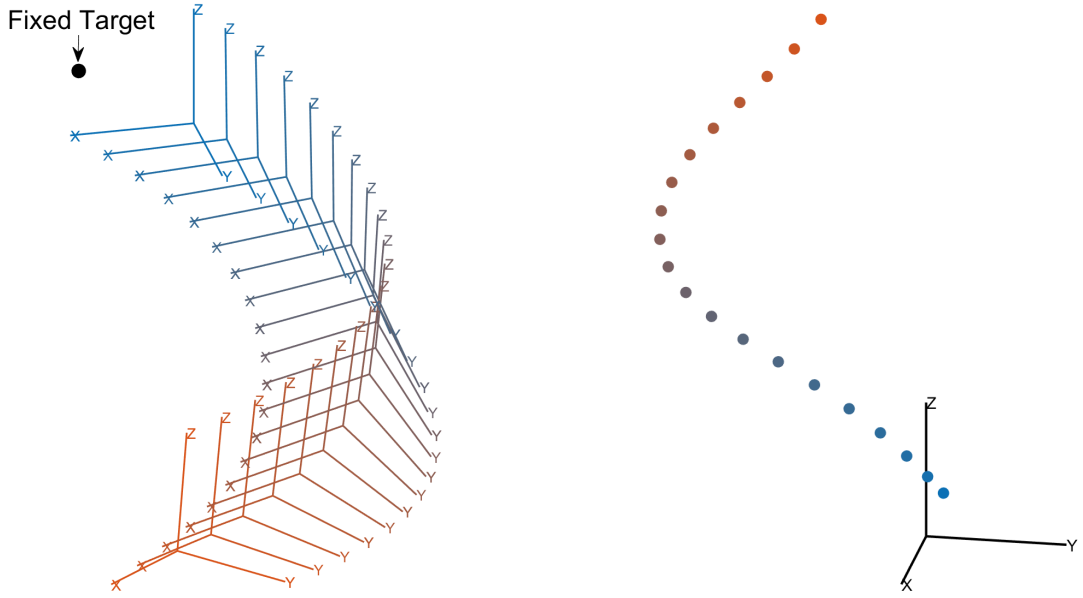

(A) Moving reference frame relative to a fixed targe.

(B) Fixed target from the perspective of the moving frame.

FIGURE 4.2: A fixed target with respect to a moving frame can be conceptualized as a sequence of moving targets from the perspective of the moving frame.

In Chapter 1, it was suggested that the future transform of the base {B} with respect to the inertial frame {I} could be constructed if predictions of the base motion were available. Then in Chapter 3, three different forecasting methods were shown to predict motion of two different AUVs under wave excitation. Given these forecasts, a pose for the end-effector in {I} can be readily transformed to the future, predicted base frame {B}:

$$\hat{\mathbf{T}}_{\mathrm{B}}^{\mathrm{D}}(\mathrm{t}+\mathrm{i}) = \hat{\mathbf{T}}_{\mathrm{B}}^{\mathrm{I}}(\mathrm{t}+\mathrm{i})\mathbf{T}_{\mathrm{I}}^{\mathrm{D}}(\mathrm{t}+\mathrm{i}) \tag{4.1}$$

$$= \left(\hat{\mathbf{T}}_{\mathrm{I}}^{\mathrm{B}}(\mathrm{t}+\mathrm{i})\right)^{-1}\mathbf{T}_{\mathrm{I}}^{\mathrm{D}}(\mathrm{t}+\mathrm{i}), \tag{4.2}$$

for $\mathrm{i} \in \{1, ..., \mathrm{L}\}$. The purpose of this chapter is to thus formulate an efficient online control strategy track this pose whilst obeying kinematic constraints.

As was seen in Chapter 2, there was little research dealing with this type of problem. From et al. (2011) and Nguyen & Dancowicz (2015) had studied the effects of inertial forces on mobile manipulators with moving platforms. However, the task was specified with respect to the platform itself, not an external fixed frame. As such, there was no need to account for the relative motion among the manipulator, its base, and the target.

The research conducted by Bowthorpe & Tavakoli (2016) is more relevant in this regard. They applied the Fourier series with EKF to predict heart motion, as proposed by Yuen et al. (2008). A predictive control method was then developed which to enable a tele-operated surgical device to track the surface of a beating heart. Other applications that combine forecasts with MPC include regulation of feed-flow rates in chemical processing (Ohshima et al., 1995) and weather forecasting to reduce energy consumption in building climate control (Olderwurtel et al., 2012).

In previous literature (Woolfrey et al., 2016), it was shown that by predicting base motion of a mobile manipulator, the arm could move to counter the disturbance to reduce pose error of the end-effector. This MPC strategy was solved in the joint space of the manipulator, in order to satisfy constraints on the joint position and speed limits. However, this required nonlinear constraints to satisfy the end-effector pose. As such, the optimisation problem grows in complexity with increasing forecast horizon and degrees of freedom in the arm.

In this chapter, the predictive control problem is solved in the task space (i.e., Cartesian space) of the manipulator. This enables the problem to be solved via QP, which is known for its fast solutions in real-time control. To satisfy joint constraints, only the first control action in the control horizon is constrained. This is feasible as only this action is executed each control loop, after which the problem is resolved in the next control loop. Although this may seem an expedient solution, it allows for linear inequality constraints on the QP problem, affording fast, real-time solutions. To validate its efficacy, this method is compared to a PID feedback controller. Admittedly, feedback control does not constitute the state of the art in control theory. However, it is universally understood and stands as a benchmark with which to evaluate the proposed predictive control method. Both simulations and experiments are conducted, which show that the proposed method can reduce tracking error and satisfy kinematic constraints compared to an unconstrained solution or feedback control.

4.2 Problem Formulation

4.2.1 Manipulator Kinematics

For a redundant manipulator, a general solution for controlling the end-effector is given by the following equation (see Appendix C):

$$\dot{\mathbf{q}} = \mathbf{J}_{\mathrm{W}}^{\dagger}\dot{\mathbf{x}} + \mathbf{N}_{\mathrm{W}}\dot{\mathbf{q}}_{\mathrm{r}}, \tag{4.3}$$

where:

- $\dot{\mathbf{q}} \in \mathbb{R}^{\mathrm{n}}$ is the joint velocities for controlling the manipulator,
- $\dot{\mathbf{x}} \in \mathbb{R}^{\mathrm{m}}$ is the end-effector velocity vector,
- $\mathbf{J}_{\mathrm{W}}^{\dagger} \in \mathbb{R}^{\mathrm{n}\times\mathrm{m}}$ is the weighted, pseudoinverse Jacobian,
- $\mathbf{N}_{\mathrm{W}} \in \mathbb{R}^{\mathrm{n}\times\mathrm{n}}$ is the weighted null-space projection matrix, and
- $\dot{\mathbf{q}}_{\mathrm{r}} \in \mathbb{R}^{\mathrm{n}}$ is a secondary, redundant task projected on to the null space.

The use of a redundant manipulator has several advantages for real-time control of a mobile manipulator. Firstly, by setting $\dot{\mathbf{q}}_{\mathrm{r}} = \mathbf{0}$, and the weighting matrix as the identity matrix, Eqn. (4.3) becomes an instantaneous minimization of the joint velocities given a desired end-effector motion. This can help avoid hitting joint velocity limits. Furthermore, it is possible to construct the weighting matrix for joint limit avoidance (Chan & Dubey, 1995). Also, the redundant task $\dot{\mathbf{q}}_{\mathrm{r}}$ can be used for singularity avoidance (Yoshikawa, 1984; Marani & Yuh, 2014).

That said, the proceeding predictive control method in this chapter does not rely on redundancy. It is able to account for limits on joint speed and joint positions. Furthermore, singularity avoidance can be achieved with well-known methods (Wampler, 1986; Chiaverini et al., 1991), albeit at the expense of task accuracy. For a non-redundant manipulator (m = n), Eqn. (4.3) reduces to:

$$\dot{\mathbf{q}} = \mathbf{J}^{-1}\dot{\mathbf{x}}. \tag{4.4}$$

For this chapter, the end-effector velocity is assumed to be $\dot{\mathbf{x}} \in \mathbb{R}^6$:

$$\dot{\mathbf{x}} = \begin{bmatrix} \mathbf{v}^{\mathrm{T}} & \boldsymbol{\omega}^{\mathrm{T}} \end{bmatrix}^{\mathrm{T}}, \tag{4.5}$$

in which $\mathbf{v} \in \mathbb{R}^3$ is the linear velocity and $\boldsymbol{\omega} \in \mathbb{R}^3$ is the angular velocity. Suppose also that a series of predicted poses are given for the end-effector to track, based on the base motion predictions presented in Chapter 3:

$$\hat{\mathbf{T}}_{\mathrm{B}}^{\mathrm{D}}(\mathrm{t}+\mathrm{i}) = \hat{\mathbf{T}}_{\mathrm{B}}^{\mathrm{I}}(\mathrm{t}+\mathrm{i})\mathbf{T}_{\mathrm{I}}^{\mathrm{D}}(\mathrm{t}+\mathrm{i}), \tag{4.6}$$

for $\mathrm{i} \in \{1, ..., \mathrm{L}\}$. The question then becomes, how should the end-effector velocity $\dot{\mathbf{x}}$ move to enable the current end-effector pose $\mathbf{T}_{\mathrm{B}}^{\mathrm{E}}(\mathrm{t})$ to converge on the predicted, desired poses $\hat{\mathbf{T}}_{\mathrm{B}}^{\mathrm{D}}(\mathrm{t}+\mathrm{i}),\ \forall \mathrm{i}$ (Fig. 4.1)?

4.2.2 Predictive End-Effector Control (PEEC)

Consider the propagation of the end-effector position $\mathbf{p} \in \mathbb{R}^3$ in discrete time, as a function of discrete control inputs $\mathbf{v}$ at each time step:

$$\mathbf{p}(\mathrm{t}+1) = \mathbf{p}(\mathrm{t}) + \Delta\mathrm{t}\mathbf{v}(\mathrm{t}) \tag{4.7}$$

$$\mathbf{p}(\mathrm{t}+2) = \mathbf{p}(\mathrm{t}+1) + \Delta\mathrm{t}\mathbf{v}(\mathrm{t}+1) \tag{4.8}$$

$$= \mathbf{p}(\mathrm{t}) + \Delta\mathrm{t}\mathbf{v}(\mathrm{t}) + \Delta\mathrm{t}\mathbf{v}(\mathrm{t}+1) \tag{4.9}$$

$$\vdots$$

$$\mathbf{p}(\mathrm{t}+\mathrm{L}) = \mathbf{p}(\mathrm{t}) + \Delta\mathrm{t}\sum_{\mathrm{i}=0}^{\mathrm{L}-1}\mathbf{v}(\mathrm{t}+\mathrm{i}), \tag{4.10}$$

where $\Delta\mathrm{t}^{-1}$ is the control frequency. The error between the current end-effector position $\mathbf{p}_{\mathrm{B}}^{\mathrm{E}}(\mathrm{t})$ and a predicted, desired future position $\hat{\mathbf{p}}_{\mathrm{B}}^{\mathrm{D}}(\mathrm{t}+\mathrm{i})$ at i time-steps ahead in the base frame $\{\mathrm{B}\}$ can then be denoted as:

$$\hat{\mathbf{e}}_{\mathrm{p}}(\mathrm{t}+\mathrm{i}) = \hat{\mathbf{p}}_{\mathrm{B}}^{\mathrm{D}}(\mathrm{t}+\mathrm{i}) - \mathbf{p}_{\mathrm{B}}^{\mathrm{E}}(\mathrm{t}), \tag{4.11}$$

for $\mathrm{i} \in \{1, ..., \mathrm{L}\}$. Substituting this in to Eqn. (4.7) to Eqn. (4.10), and rearranging leads to:

$$\hat{\mathbf{e}}_{\mathrm{p}}(\mathrm{t}+\mathrm{i}) - \Delta\mathrm{t}\sum_{\mathrm{j}=0}^{\mathrm{i}-1}\mathbf{v}(\mathrm{t}+\mathrm{j}) = \mathbf{0}. \tag{4.12}$$

That is, we want to find some sequence of control actions $\mathbf{v}(\mathrm{t}+\mathrm{j})$ for $\mathrm{j} \in \{0, ..., \mathrm{i}-1\}$ that will minimize the position error of the end-effector across the prediction horizon $\mathrm{i} \in \{1, ..., \mathrm{L}\}$ (Fig. 4.3).

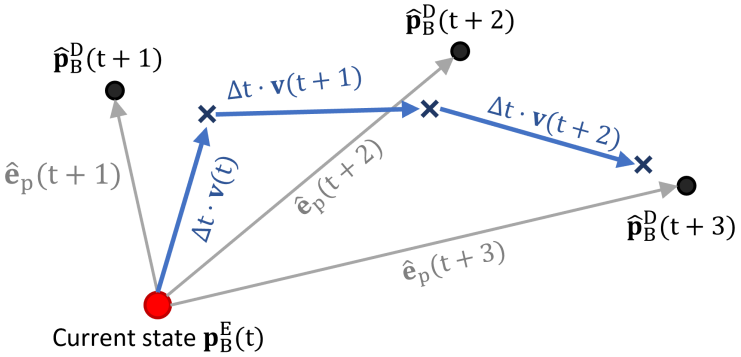

FIGURE 4.3: The objective of the predictive control is to find a sequence of control actions to minimize the error across the prediction horizon.

Yuan (1988) showed that it is sufficient to express orientation error via the vector component of a quaternion $\boldsymbol{\varepsilon}$. As such, the error between the current orientation $\mathcal{Q}(\mathrm{t})$ and the predicted, desired orientation $\hat{\mathcal{Q}}_{\mathrm{d}}(\mathrm{t}+\mathrm{i})$ for $\mathrm{i} \in \{1, ..., \mathrm{L}\}$ steps can be represented as:

$$\hat{\mathcal{Q}}_{\mathrm{e}}(\mathrm{t}+\mathrm{i}) = \hat{\mathcal{Q}}_{\mathrm{d}}(\mathrm{t}+\mathrm{i}) * \bar{\mathcal{Q}}(\mathrm{t}) \tag{4.13}$$

$$= \{\hat{\eta}_{\mathrm{e}}(\mathrm{t}+\mathrm{i}), \hat{\boldsymbol{\varepsilon}}_{\mathrm{e}}(\mathrm{t}+\mathrm{i})\}, \tag{4.14}$$

where $\bar{\mathcal{Q}}$ is the conjugate of $\mathcal{Q}$. Details of quaternion multiplication and orientation error calculations are given in Appendix B. Proof of orientation feedback via quaternions is given in Appendix C.

Following the same logic as the position control, the orientation control problem can be expressed as:

$$\hat{\boldsymbol{\varepsilon}}_{\mathrm{e}}(\mathrm{t}+\mathrm{i}) - \Delta \mathrm{t} \sum_{\mathrm{j}=0}^{\mathrm{i}-1} \boldsymbol{\omega}(\mathrm{t}+\mathrm{j}) = \mathbf{0}, \tag{4.15}$$

for $\mathrm{i} \in \{1, ..., \mathrm{L}\}$. The predicted position and orientation error can be concatenated as:

$$\hat{\mathbf{e}}(\mathrm{t}+\mathrm{i}) = \begin{bmatrix} \hat{\mathbf{e}}_{\mathrm{p}}(\mathrm{t}+\mathrm{i}) \\ \hat{\boldsymbol{\varepsilon}}_{\mathrm{e}}(\mathrm{t}+\mathrm{i}) \end{bmatrix}. \tag{4.16}$$

Then, incorporating Eqn. (4.12) and Eqn. (4.15), the dual problem of position and orientation control across the prediction horizon is:

$$\hat{\mathbf{e}}(\mathrm{t}+\mathrm{i}) - \Delta \mathrm{t} \sum_{\mathrm{j}=0}^{\mathrm{i}-1} \dot{\mathbf{x}}(\mathrm{t}+\mathrm{j}) = \mathbf{0}. \tag{4.17}$$

This problem can be written across the entire forecast horizon $\mathrm{i} \in \{1, ..., \mathrm{L}\}$ as:

$$\begin{bmatrix} \hat{\mathbf{e}}(\mathrm{t}+1) \\ \vdots \\ \hat{\mathbf{e}}(\mathrm{t}+\mathrm{L}) \end{bmatrix} - \Delta\mathrm{t} \begin{bmatrix} \mathbf{I}_6 & & \\ \vdots & \ddots & \\ \mathbf{I}_6 & \cdots & \mathbf{I}_6 \end{bmatrix} \begin{bmatrix} \dot{\mathbf{x}}(\mathrm{t}) \\ \vdots \\ \dot{\mathbf{x}}(\mathrm{t}+\mathrm{L}-1) \end{bmatrix} = \mathbf{0} \tag{4.18}$$

$$\hat{\mathbf{e}} - \mathbf{A}\mathbf{u} = \mathbf{0}, \tag{4.19}$$

where:

- $\hat{\mathbf{e}} = \begin{bmatrix} \hat{\mathbf{e}}^{\mathrm{T}}(\mathrm{t}+1) & \cdots & \hat{\mathbf{e}}^{\mathrm{T}}(\mathrm{t}+\mathrm{L}) \end{bmatrix}^{\mathrm{T}} \in \mathbb{R}^{6\mathrm{L}\times 1}$ is a vector of errors between the current end-effector pose and the future, predicted targets,
- $\mathbf{u} = \begin{bmatrix} \dot{\mathbf{x}}^{\mathrm{T}}(\mathrm{t}) & \cdots & \dot{\mathbf{x}}^{\mathrm{T}}(\mathrm{t}+\mathrm{L}-\mathrm{i}) \end{bmatrix}^{\mathrm{T}} \in \mathbb{R}^{6\mathrm{L}\times 1}$ is a vector of the end-effector velocities across the prediction horizon,
- $\mathbf{A} = \Delta\mathrm{t} \begin{bmatrix} \mathbf{I}_6 & & \\ \vdots & \ddots & \\ \mathbf{I}_6 & \cdots & \mathbf{I}_6 \end{bmatrix} \in \mathbb{R}^{6\mathrm{L}\times 6\mathrm{L}}$ propagates the control action from velocity to displacement, and
- $\mathbf{I}_6 \in \mathbb{R}^{6\times 6}$ is the identity matrix.

This problem can be solved via QP with the following cost function:

$$\min_{\mathbf{u}} \|\hat{\mathbf{e}} - \mathbf{A}\mathbf{u}\|_{\mathrm{G}}^2 = \big(\hat{\mathbf{e}} - \mathbf{A}\mathbf{u}\big)^{\mathrm{T}} \mathbf{G} \big(\hat{\mathbf{e}} - \mathbf{A}\mathbf{u}\big), \tag{4.20}$$

for some positive-definite weighting matrix $\mathbf{G} \in \mathbb{R}^{6\mathrm{L}\times 6\mathrm{L}}$. This optimization problem solves the velocities to minimize the sum-of-squared errors, which can result in discontinuity of the end-effector control and hence sharp accelerations. This may be exacerbated by shocks to the manipulator base, or forecast outliers in the prediction horizon.

To smooth the velocities across the control horizon, a secondary problem can be formulated that minimizes the difference between sequential control actions:

$$\begin{bmatrix} \dot{\mathbf{x}}(\mathrm{t}+1) - \mathbf{J}\big(\mathbf{q}(\mathrm{t}-1)\big)\dot{\mathbf{q}}(\mathrm{t}-1) \\ \vdots \\ \dot{\mathbf{x}}(\mathrm{t}+\mathrm{L}) - \dot{\mathbf{x}}(\mathrm{t}+\mathrm{L}-1) \end{bmatrix} = \mathbf{0} \tag{4.21}$$

$$\begin{bmatrix} \mathbf{J}\big(\mathbf{q}(\mathrm{t}-1)\big)\dot{\mathbf{q}}(\mathrm{t}-1)\big) \\ \mathbf{0} \\ \vdots \\ \mathbf{0} \end{bmatrix} - \begin{bmatrix} \mathbf{I}_6 & & & \\ -\mathbf{I}_6 & \mathbf{I}_6 & & \\ & \ddots & \ddots & \\ & & -\mathbf{I}_6 & \mathbf{I}_6 \end{bmatrix} \begin{bmatrix} \dot{\mathbf{x}}(\mathrm{t}+1) \\ \dot{\mathbf{x}}(\mathrm{t}+2) \\ \vdots \\ \dot{\mathbf{x}}(\mathrm{t}+\mathrm{L}) \end{bmatrix} = \mathbf{0} \tag{4.22}$$

$$\mathbf{u}_0 - \mathbf{B}\mathbf{u} = \mathbf{0}, \tag{4.23}$$

where:

- $\mathbf{u}_0 = \begin{bmatrix} \mathbf{J}\big(\mathbf{q}(\mathrm{t}-1)\big)\dot{\mathbf{q}}(\mathrm{t}-1) \\ \mathbf{0} \end{bmatrix} \in \mathbb{R}^{6\mathrm{L}\times 1}$ contains the previous control action taken by the manipulator, and
- $\mathbf{B} = \begin{bmatrix} \mathbf{I}_6 & & & \\ -\mathbf{I}_6 & \mathbf{I}_6 & & \\ & \ddots & \ddots & \\ & & -\mathbf{I}_6 & \mathbf{I}_6 \end{bmatrix} \in \mathbb{R}^{6\mathrm{L}\times 6\mathrm{L}}$ gives the difference between sequential control actions.

This could also be written as its own QP problem:

$$\min_{\mathrm{u}} \|\mathbf{u}_0 - \mathbf{B}\mathbf{u}\|_{\mathrm{Q}}^2 = \big(\mathbf{u}_0 - \mathbf{B}\mathbf{u}\big)^{\mathrm{T}}\mathbf{Q}\big(\mathbf{u}_0 - \mathbf{B}\mathbf{u}\big), \tag{4.24}$$

where $\mathbf{Q} \in \mathbb{R}^{6\mathrm{L}\times 6\mathrm{L}}$ is a positive-definite weighting matrix. The optimal solution to Eqn. (4.24) is:

$$\dot{\mathbf{x}}(\mathrm{t}+\mathrm{i}) = \mathbf{J}\big(\mathbf{q}(\mathrm{t}-1)\big)\dot{\mathbf{q}}(\mathrm{t}-1) \ \forall \mathrm{i}. \tag{4.25}$$

That is, the end-effector maintains a constant velocity for all time; or zero acceleration. Obviously this is impractical, but Eqn. (4.24) can be added as a penalty term to Eqn. (4.20) which leads to:

$$\min_{\mathbf{u}} \ \|\hat{\mathbf{e}} - \mathbf{A}\mathbf{u}\|_{\mathrm{G}}^2 + \|\mathbf{u}_0 - \mathbf{B}\mathbf{u}\|_{\mathrm{Q}}^2 \tag{4.26}$$

$$= \big(\hat{\mathbf{e}} - \mathbf{A}\mathbf{u}\big)^{\mathrm{T}}\mathbf{G}\big(\hat{\mathbf{e}} - \mathbf{A}\mathbf{u}\big) + \big(\mathbf{u}_0 - \mathbf{B}\mathbf{u}\big)^{\mathrm{T}}\mathbf{Q}\big(\mathbf{u}_0 - \mathbf{B}\mathbf{u}\big). \tag{4.27}$$

Using the MPC framework, the optimal solution for the end-effector control at the current time, $\dot{\mathbf{x}}(t)$ is extracted from $\mathbf{u}$. This is then substituted in to Eqn. (4.3) or Eqn. (4.4) to obtain the required joint velocity control.

Generally, $\|\mathbf{Q}\| \ll \|\mathbf{G}\|$ to ensure minimum error for the end-effector task. Figure 4.4 illustrates how increasing the weighting $\mathbf{Q}$ can smooth the trajectory but can increase tracking error for target points that deviate far from the current trajectory. Again, this may not be undesirable per se, as deviations and outliers in the forecast may be ignored under certain circumstances.

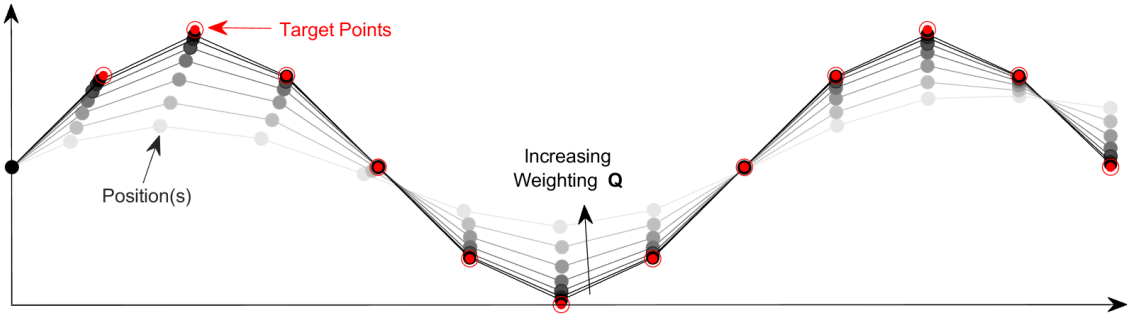

FIGURE 4.4: Increasing the penalty term on the sequential control actions can be used to smooth the velocities, but increases tracking error.

Constrained solution: Equation (4.26) expresses a problem of how to move the end-effector of the manipulator across the control horizon, defined in Cartesian space. However, it is independent of the manipulator and thus model-free. On one hand, this is desirable as the state propagation is linear and solving this problem is trivial with convex optimisation techniques. On the other, the solution may not be feasible for the manipulator to execute. Solving the control in the joint space makes satisfying joint constraints simple. But satisfying a desired end-effector pose would involve propagating nonlinear constraints across the control horizon. However, exploiting properties of MPC enables an expedient solution for applying joint constraints to Eqns. (4.26) and (4.27). Only the first set of end-effector controls, $\dot{\mathbf{x}}(t)$, is executed within the sequence $\mathbf{u}$. During the next control loop, the optimal control problem is re-solved with new state information. It is thus possible to only restrict $\dot{\mathbf{x}}(t)$ with the following linear inequality constraint:

$$\min_{\mathbf{u}} \|\hat{\mathbf{e}} - \mathbf{A}\mathbf{u}\|_{\mathrm{G}}^2 + \|\mathbf{u}_0 - \mathbf{B}\mathbf{u}\|_{\mathrm{Q}}^2 \tag{4.28}$$

$$\text{subject to: } \begin{bmatrix} \mathbf{J}_{\mathrm{W}}^{\dagger} & \mathbf{0} \\ -\mathbf{J}_{\mathrm{W}}^{\dagger} & \mathbf{0} \end{bmatrix} \mathbf{u} \leq \begin{bmatrix} \dot{\mathbf{q}}_{\max} \\ \dot{\mathbf{q}}_{\min} \end{bmatrix}, \tag{4.29}$$

where $\mathbf{J}_{\mathrm{W}}^{\dagger} \in \mathbb{R}^{\mathrm{n}\times 6}$ is the general weighted pseudoinverse Jacobian (see Appendix C). Using this approach, the constraints on $\dot{\mathbf{x}}(\mathrm{t}+\mathrm{j}),\ \mathrm{j} \in \{1, ..., \mathrm{L}-1\}$ can be relaxed. This circumvents the need for finding a feasible solution for the entire control horizon, enabling fast solutions for real-time control.

Also consider the propagation of the joint state in discrete time,

$$\mathbf{q}(\mathrm{t}+\mathrm{i}|\mathrm{t}) = \mathbf{q}(\mathrm{t}|\mathrm{t}) + \Delta\mathrm{t}\sum_{\mathrm{j}=0}^{\mathrm{i}-1}\mathbf{J}_{\mathrm{W}}^{\dagger}\big(\mathbf{q}(\mathrm{t}+\mathrm{j}|\mathrm{t})\big)\dot{\mathbf{x}}(\mathrm{t}+\mathrm{j}|\mathrm{t}), \tag{4.30}$$

for $\mathrm{i} = 1, ..., \mathrm{N}$. the solution for $\dot{\mathbf{x}}(\mathrm{t}|\mathrm{t})$ is feasible from the output of the constrained QP problem, then it also holds that $\mathbf{q}(\mathrm{t}+1|\mathrm{t})$ is also feasible. During the update of the joint state during the next control loop, the new current state becomes:

$$\mathbf{q}(\mathrm{t}+1|\mathrm{t}+1) = \mathbf{q}(\mathrm{t}+1|\mathrm{t}). \tag{4.31}$$

As such, $\mathbf{q}(\mathrm{t}+\mathrm{i}|\mathrm{t}+\mathrm{i})$ is feasible $\forall$i. The actual joint trajectory executed by the manipulator will obey joint constraints, even if future (unexecuted) control actions in the predictive control horizon may not be. Simulation results show the validity of this approach.

Another point worth mentioning is that the penalty term $\|\mathbf{u}_0 - \mathbf{B}\mathbf{u}\|_{\mathrm{Q}}^2$ will propagate part of the joint constraint through the control horizon. That is, $\dot{\mathbf{x}}(\mathrm{t}+1)$ will not deviate too far from $\dot{\mathbf{x}}(\mathrm{t})$ which is guaranteed to be kinematically feasible. Likewise, $\dot{\mathbf{x}}(\mathrm{t}+2)$ will not deviate far from $\dot{\mathbf{x}}(\mathrm{t}+1)$ and so on.

As aforementioned, the weighting matrix in the pseudoinverse Jacobian $\mathbf{J}_{\mathrm{W}}^{\dagger}$ (Eqn. (4.3)) can be used for real-time joint limit avoidance (Chan & Dubey, 1995). However, the proposed QP problem proposed in this chapter can satisfy joint constraints for a non-redundant manipulator by constraining the permissable joint velocities. If the manipulator is redundant, any secondary task projected on to the null space must be scaled to fit within the remaining joint velocity capacity:

$$\dot{\mathbf{q}}_{\min} - \mathbf{J}_{\mathrm{W}}^{\dagger}\dot{\mathbf{x}}^{\star}(\mathrm{t}) \leq \mathbf{N}_{\mathrm{W}}\dot{\mathbf{q}}_{\mathrm{r}} \leq \dot{\mathbf{q}}_{\max} - \mathbf{J}_{\mathrm{W}}^{\dagger}\dot{\mathbf{x}}^{\star}(\mathrm{t}). \tag{4.32}$$

Unconstrained solution: Since Eqn. (4.26) is convex in $\mathbf{u}$, a global solution is readily available when no kinematic constraints are required:

$$\mathbf{u}^{\star} = \big(\mathbf{A}^{\mathrm{T}}\mathbf{G}\mathbf{A} + \mathbf{B}^{\mathrm{T}}\mathbf{Q}\mathbf{B}\big)^{-1}\big(\mathbf{A}^{\mathrm{T}}\mathbf{G}\hat{\mathbf{e}} + \mathbf{B}^{\mathrm{T}}\mathbf{Q}\mathbf{u}_0\big). \tag{4.33}$$

This solution is also used as a comparison to the constrained case in the simulations.

4.3 Verification of the Predictive End-Effector Control Method

The PEEC method presented in this paper is verified through both simulation and experiment. For the simulation, the base motion of the manipulator is generated from IMU data collected from an AUV under wave disturbances in shallow bathymetry. It is assumed in the simulation that the dynamics of the manipulator will have negligible effect on the base motion. This assumption is validated from the physical experiments. On the other hand, using the exact same base motion allows for an objective comparison between the control method derived in this chapter versus a conventional PID feedback controller.

For the experiments, a small manipulator is maneuvered on a platform by hand whilst it attemps to maintain a steady end-effector. It is difficult to replicate the same base motion in this case, so experiments are also done with a fixed base and moving target. This reflects the thought experiment of the perspective problem introduced at the start of this chapter.

4.3.1 Simulation

Outline: A 7DOF manipulator based on the kinematics of the Sawyer by Rethink Robotics was required to track a straight line in the inertial frame. Base motion was generated from motion data captured from the Antarctic AUV using a similar sample as that in Chapter 3. A plot of the base pose is given in Fig. 4.5.

The simulation was first run without any constraints on the maximum joint speed. Any joint velocities exceeding their limits were scaled to maintain the desired end-effector direction for the trajectory tracking. Then the simulation was repeated with joint velocities capped at 10 RPM. An ARMA(5,0) time-series model was used to predict the base pose, with a moving window of $l = 100$ state observations used to fit the coefficients for Eqn. (3.4) every time step. These were then recomputed in to state space form, Eqn. (3.10), coupled with a KF. Parameters for the feedback control gains and weighting matrices for the predictive control are given in Table **??**.

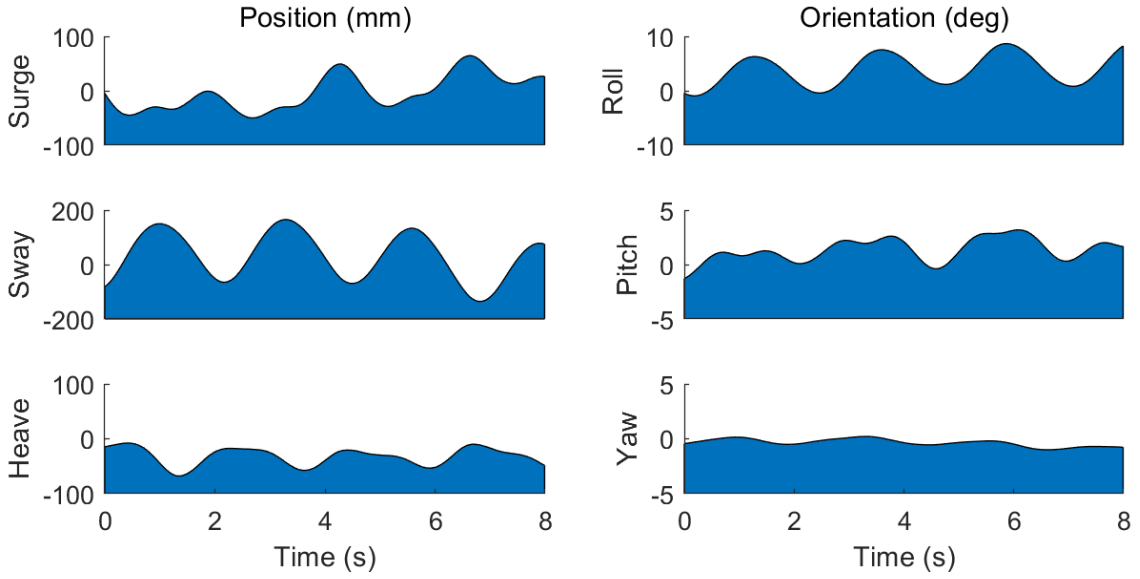

FIGURE 4.5: Base motion for the predictive control simulation was generated from motion data of an AUV in waves.

TABLE 4.1: Feedback control gains and weighting matrices in the predictive control for the simulation.

	Control Parameters				
Scenario	$\mathbf{K}_\mathrm{p}$	$\mathbf{K}_\mathrm{i}$	$\mathbf{K}_\mathrm{o}$	**G**	**Q**
Unconstrained	10.0	3.0	10.0	**I**	1E-3
Constrained	10.0	3.0	10.0	**I**	1E-1

Results for the Unconstrained Case: A plot of the trajectory tracking error over the duration of the simulation is given in Fig. 4.6, and a summary of the performance results in Table 4.2. From this simulation, both the position and orientation error of the end-effector is minimized by predicting the base motion disturbance, as opposed to a conventional PID controller. The PEEC method in this chapter shows an improvement of approximately 60% by anticipating and negating disturbances. In addition, two different forecast horizons were tested: L = 5 (0.05s) and L = 10 (0.10s), though the differences in performance were negligible. Even a short forecast horizon shows a marked improvement compared to the classic feedback method.

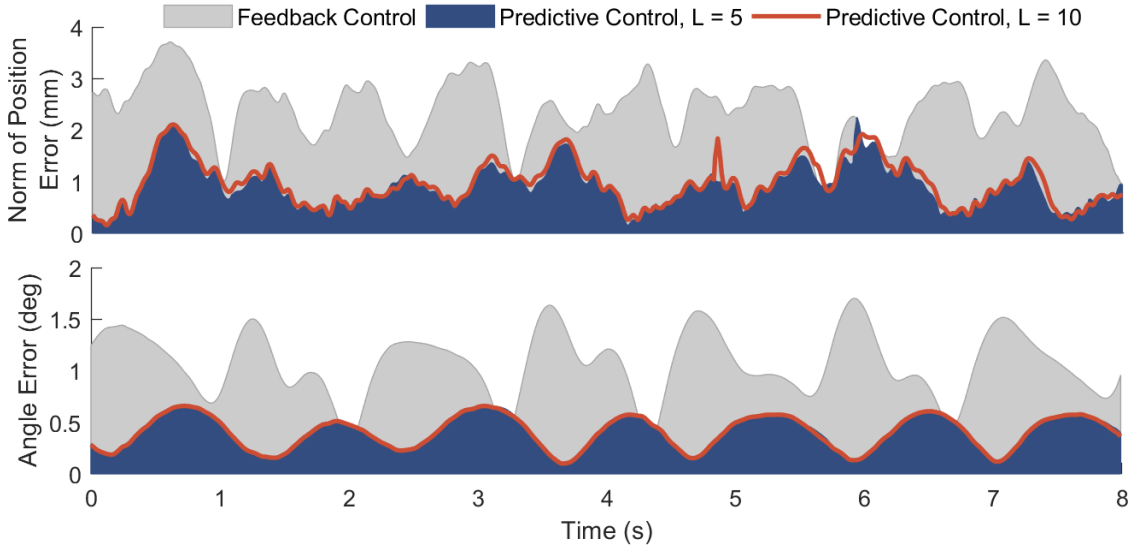

FIGURE 4.6: The predictive control method reduced tracking error when the base is under disturbance.

TABLE 4.2: Summary of performance results for the simulation.

Norm of Position Error (mm)

	Mean	Min	Max	Mean Improvement
Feedback Control	2.50	0.12	8.73	
Predictive Control (L = 5)	0.92	0.12	2.25	63%
Predictive Control (L = 10)	0.99	0.15	4.16	60%

Angle Error (deg)

	Mean	Min	Max	Mean Improvement
Feedback Control	1.05	0.02	1.76	
Predictive Control (L = 5)	0.41	0.02	0.67	61%
Predictive Control (L = 10)	0.40	0.10	0.66	62%

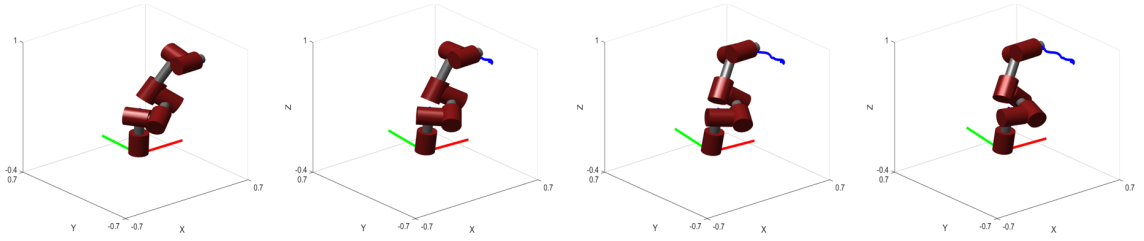

(A) Feedback Control.

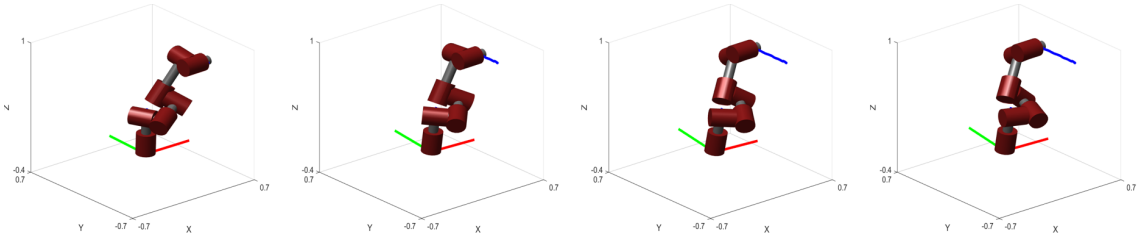

(B) The PEEC method.

FIGURE 4.7: Screenshots for the trajectory tracking simulation.

Results for the Constrained Case: The same simulation scenario was conducted, but with joint velocities capped at 10 RPM to test the constrained QP formulation proposed in this chapter. The weighting matrix $\mathbf{Q}$ was also increased to help smooth the joint velocities over the unconstrained case (Table 4.1). For the feedback control, joint velocities were scaled to maintain the end-effector direction whilst remaining bounded. Trajectory tracking error is shown in Fig 4.8. Three different scenarios were run under the reduced joint speeds:

1. PID feedback control,
2. Predictive control without the inequality constraint, and
3. Predictive control with the inequality constaint.

The results show that by accounting for joint speed constraints, the trajectory tracking error can be reduced even further. The constrained QP formulation was able to reduce tracking error compared to a PID feedback controller by up to 80%, with a further 10% improvement over the unconstrained QP (Table 4.3). In addition to improved tracking performance, these results also show that it is not necessary to find feasible end-effector controls for the entire control horizon. It is sufficient to only constrain the first control action in the sequence.

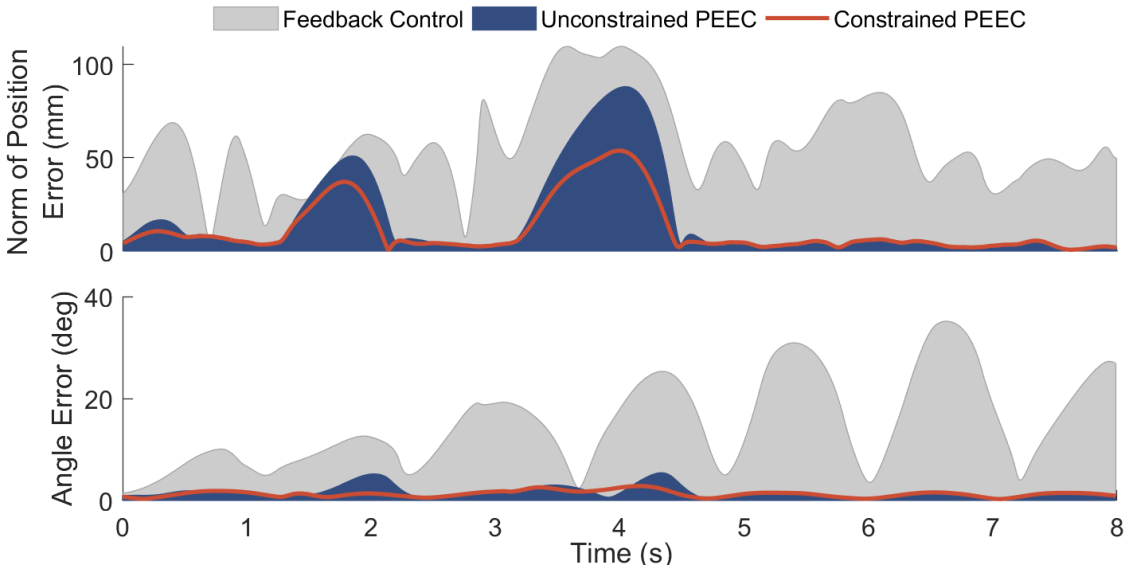

FIGURE 4.8: Using constraints on the kinematic feasibility, the predictive control method can satisfy joint constraints and reduce tracking error from disturbance.

A plot of the joint velocities for the simulation with limited joint speeds is also shown in Fig. 4.9. It can be seen that all three scenarios hit various speed limits at different times during the simulation. However, the constrained QP problem proposed in this chapter is able to solve for a combination of joint velocities that results in minimized task error. In addition, the joint velocities are smoother than than the feedback control and unconstrained QP, as intended.

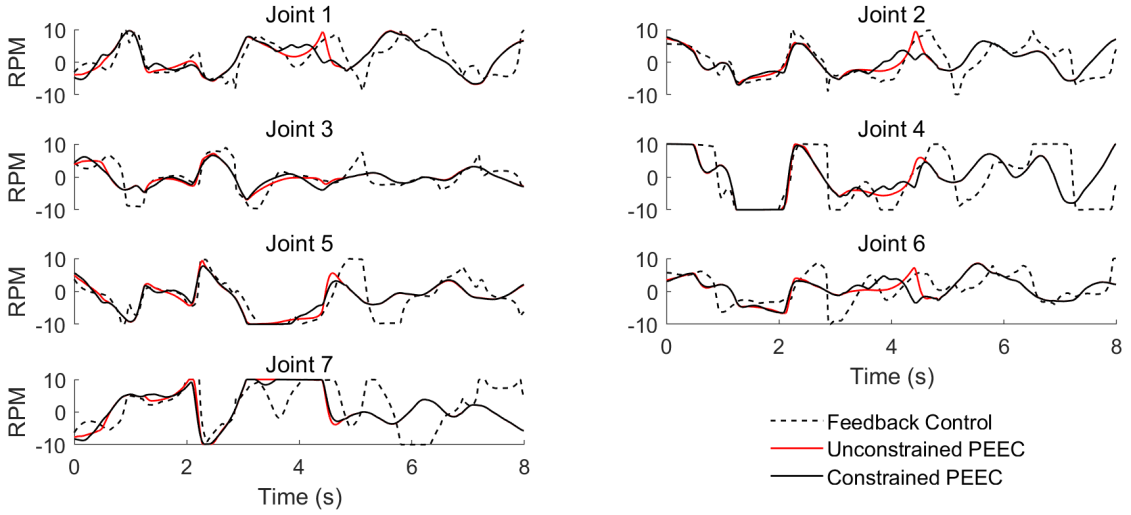

FIGURE 4.9: Maximum joint speeds can be satisfied whilst reducing tracking error with the proposed method.

TABLE 4.3: Summary of results with joint velocities capped at 10 RPM.

Norm of Position Error (mm)

	Mean	Min	Max	Mean Improvement
Feedback Control	57.39	2.79	109.78	
Unconstrained PEEC	16.93	0.74	88.18	70%
Constrained PEEC	11.54	0.64	53.87	80%

Angle Error (deg)

	Mean	Min	Max	Mean Improvement
Feedback Control	15.06	1.36	35.14	
Unconstrained PEEC	1.67	0.28	5.43	89%
Constrained PEEC	1.28	0.28	2.84	91%

4.3.2 Experimental Results

The experimental results were conducted in a lab set up by moving a manipulator on a free-moving base by hand. The proposed PEEC was originally tested on the SPIR platform, but the control frequency of the arm ran at approximately 2Hz and as such did not generate good results. In the simulations, a model of the Sawyer manipulator was used. This weighs approximately 19kg, and therefore makes it dangerous to lift and maneuver. It also has a reach of 1.26m, which could swing and collide with a person or object if it were to lose control. The 6DOF UR3 manipulator from Universal Robots was used instead. This arm weighs approximately 11kg and is much safer to carry. Furthermore, it has a reach of 0.5m which means it can operate in a fairly confined space.

The UR3 operates at a frequency of 125Hz. This is 60 times faster than the SPIR manipulator, and is fast enough to demonstrate the PEEC control. The PID feedback control gains for the physical experiments were manually tuned by increasing them to their maximum values without the manipulator overshooting its target end-effector pose, or introducing chattering in to the system. It was found that when running the predictive control, the safety controller on the UR3 would frequently override joint velocity commands and stop the robot. As such, the velocity controls sent to the system had to be reduced by 60% from the optimal calculated solutions. Control parameters for these experiments are given in Table 4.4. For the motion prediction, an ARMA(2,0) time series model was used. The length of the moving window for optimising the time-series coefficients was $l = 50$.

TABLE 4.4: Feedback control gains and predictive control weightings for the experiments on the UR3.

	Control Parameters				
	$\mathbf{K}_\mathrm{p}$	$\mathbf{K}_\mathrm{i}$	$\mathbf{K}_\mathrm{o}$	**G**	**Q**
Relative Motion	6.0	1E-3	6.0	**I**	1E-4
Moving Base	6.0	1E-3	6.0	**I**	1E-4

Outline for the Relative Motion Test: As proposed at the beginning of this chapter, a fixed target with respect to a manipulator on a moving platform appears as a moving target from the perspective of the manipulator. In order to compare the PEEC to feedback control method, two UR3 manipulators were fixed to a bench. A board with markers was attached to the end-effector of one manipulator, which was programmed to follow a fixed trajectory. A Blackfly S camera (BFS-U3-16S2C-CS) from FLIR was set up on a tripod to view the markers, running at approximately 122 frames per second. The ar_track_alvar

package in Robot Operating System (ROS) was then used to detect the markers and publish a transform for the second manipulator to track relative to its base (Fig. 4.10).

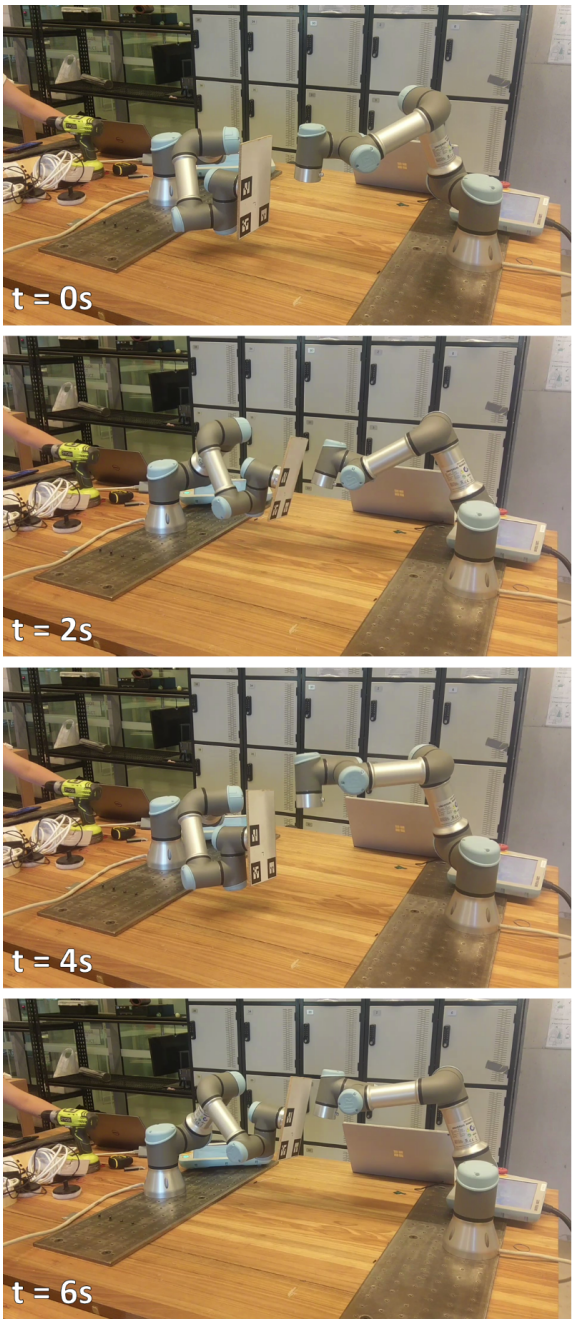

FIGURE 4.10: Photos taken during the relative motion test for the predictive control with the UR3.

Results for Relative Motion Test: Trajectory tracking error for the relative motion test is given in Fig 4.11. It can be seen that the PEEC method reduces the tracking error against a moving target. This resulted in roughly 65% reduction in position error compared to a PID feedback controller (Table 4.5). These results are of similar magnitude to the simulation. The reason for the poor performance of the feedback control is evident. The end-effector speed is proportional to the error, and only instigates motion after the target position begins to deviate. Conversely, the predictive control begins to anticipate the motion of the target and move where it expects it to be, thus reducing tracking error. As with the simulations, two different forecast horizons of L = 5 and L = 10 were tested. And, as before, the length of the forecast horizon appears to have negligble effect on the tracking performance.

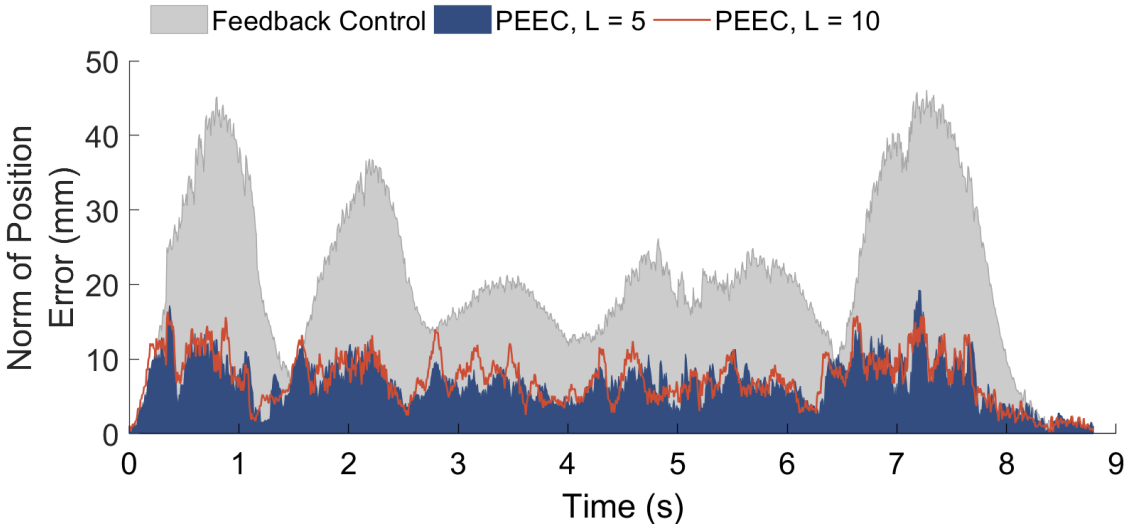

FIGURE 4.11: The predictive control method can better track a moving target relative to the manipulator base frame.

TABLE 4.5: Summary of performance for the relative motion test.

Norm of Position Error (mm)

	Mean	Min	Max	Mean Improvement
Feedback Control	21.1	0.3	46.1	
PEEC (L = 5)	6.9	0.3	19.3	67%
PEEC (L = 10)	7.2	0.2	16.4	66%

Outline for the Moving Base Test: For the moving base test, a UR3 was mounted on a sheet of plybood. A board was fixed to the base with markers to give the transform of the base {B} relative to the fixed camera frame {C} (Fig. 4.12). A desired pose {D} was specified relative to the camera frame for the manipulator to try and maintain. The base was then moved around by hand following the same sequence for both the feedback control and predictive control:

1. Roll about x-axis back-and-forth four times,
2. Pitch about y-axis back-and-forth four times,
3. Move in a circular trajectory about the x-y plane four times.

Images from a video of the PEEC method can be seen in Fig 4.13. An ARMA(2,0) time series model was used to forecast the base motion. As with the relative-motion experiment, the predictive control had to be attenuated to 60% due to the intervention of the safety controller on the UR3.

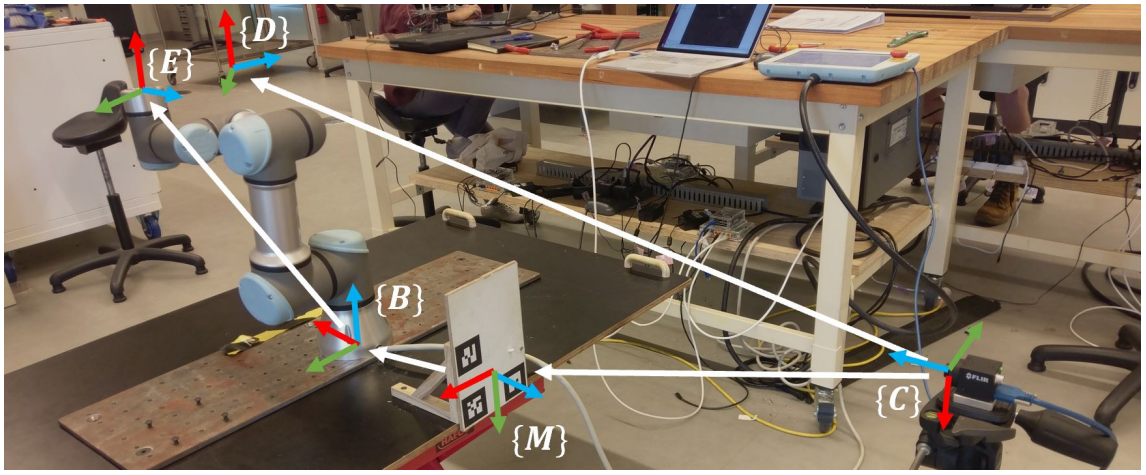

FIGURE 4.12: Set up for the moving base test.

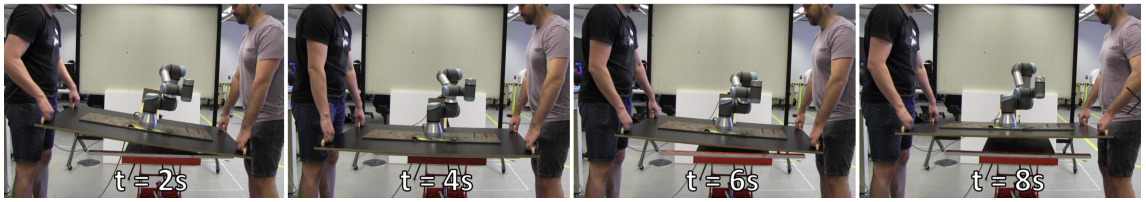

FIGURE 4.13: Images from the video recording of the moving base test.

Results for the Moving Base Test: The results for the moving base experiments on a real manipulator show an even better improvement in pose error than the simulation or relative motion test. The PEEC method showed a roughly 75% reduction in position error over feedback control (Table 4.6). Remarkably, this was achieved with the predictive control running at 60% of its capacity. A plot of the position and orientation error over the duration of the experiments are shown in Fig 4.14. It can be seen that the orientation error only showed a modest improvement of 7-10%. This may be because the orientation of the base was forecast in quaternion space, whereas the simulation used Euler angles. These results confirm that, using the proposed method, it is possible to anticipate basse motion and negate disturbances to the end-effector to improve task accuracy on a mobile platform.

The difference between the feedback control and the predictive control is most apparent when the position error is plotted in Cartesian space (Fig 4.15). The feedback control has difficulty minimizing the error between the end-effector and the desired pose as it is reactive by design. The circular motion of the base made during the experiments can be seen propagating through to the trajectory of the end-effector when using feedback control. It is never able to full overcome the disturbance. Conversely, the PEEC method can anticipate this motion and cancel these oscillations. The distribution of the position error using this method is much smaller, as the end-effector remains closer to the desired end-effector pose.

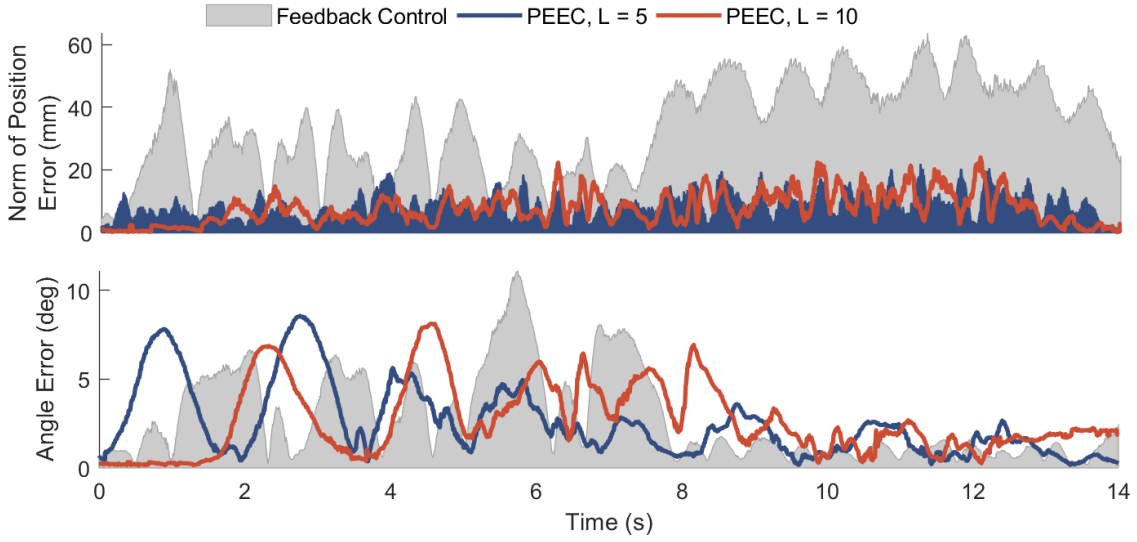

FIGURE 4.14: The predictive control method reduce position and orientation error for the free-moving base experiment.

TABLE 4.6: Performance results for the moving base test.

Norm of Position Error (mm)

	Mean	Min	Max	Mean Improvement
Feedback Control	33.6	1.4	63.7	
PEEC (L = 5)	7.7	0.1	24.0	77%
PEEC (L = 10)	8.6	0.6	21.9	74%

Angle Error (deg)

	Mean	Min	Max	Mean Improvement
Feedback Control	2.8	0.2	11.1	
PEEC (L = 5)	2.6	0.1	8.1	7%
PEEC (L = 10)	2.5	0.2	8.6	10%

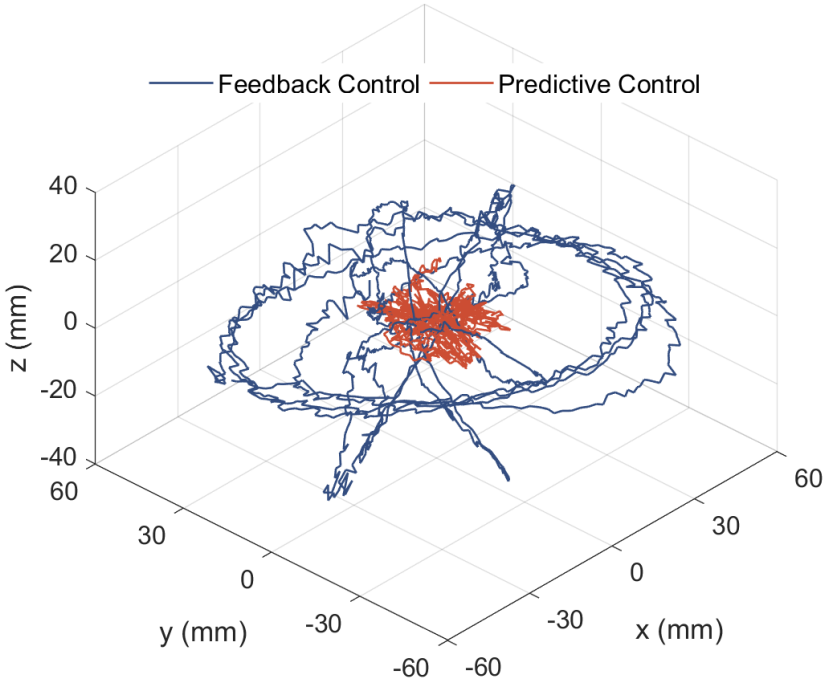

FIGURE 4.15: Plot of the position error of the end-effector in Cartesian space for the moving base test.

4.4 Discussion

4.4.1 Orientation Error

The simulation and experiments presented in this chapter showed over 60% reducting in error using the PEEC compared to a PID feedback controller. However, the experiments only showed a marginal improvement for the orientation error compared to the simulations. There may be several reasons for this discrepency:

1. The base orientation for the experiments used quaternions, as this is the default representation for orientation in ROS. Euler angles were used for the simulation, the same as From et al. (2011) and Woolfrey et al. (2016). Euler angles may be more appropriate for forecasting, whereas orientation error and control can be done with quaternions.
2. The optimal control signal calculated during experiments had to be reduced by 60% before being sent to the UR3 due to safety control issues. It is possible that a greater improvement in orientation tracking would be observed if this attenuation was not required.
3. The change in orientation of the base during experiments was small. Larger angular motion may reveal larger differences in performance between the feedback control and predictive control methods.

4.4.2 Dynamic Forces

The PEEC method proposed in this chapter was formulated at the velocity level. It was assumed that any inertial effects between the base and manipulator would have negligble impact oon the base motion, and the subsequent prediction and control. Furthermore, compensation for gravitational forces were deferred to the dynamic controller of the UR3 manipulator to be solved. Results of the moving base experiments confirmed that these assumptions are valid, and that the proposed control method can reduce task error over feedback control.

However, this may not translate to manipulators with large inertia, or where there may be hard accelerations of the base. Future work may involve developing the control problem at the acceleration level to better synthesise with dynamic control of the manipulator. Furthermore, a point of interest may be to use redundancy in the system to use the

inertial forces to reduce joint torque, rather than work against them. A similar idea was studied by From et al. (2011). In Chapter 5, this idea will be explored in more detail. Research in to workspace recovery methods for space manipulation may provide some insights on how to address this (Giordano et al., 2018).

4.4.3 Base Motion Disturbance

One of the limitations to this PEEC method is the magnitude of the disturbance, i.e., the displacement of the manipulator base. It was assumed for both the simulations and experiments that the motion of the base remains bounded such that the end-effector task is always within the workspace of the manipulator. This might not be gauranteed in some scenarios, particularly if the base cannot be adequately controlled. Over-extension of the arm leads to singular configurations, and a subsequent loss of control in the manipulator. Not only is it difficult to recover from this problem, but there is also the danger of collision with itself or the environment. The Damped Least Squares (DLS) technique can be used to maintain control (Wampler, 1986; Chiaverini et al., 1991). However, high-level planning and control could be used to intervene when base displacement becomes too great.

4.4.4 Feedback Control & Future Development

The PEEC method was compared to a PID feedback controller in this chapter. It was acknowledged that the latter is not the state of the art, but its universality in control theory makes it a decent benchmark for comparing results. It is worth noting that the frequency of the UR3 manipulator, and that of the camera, were bottlenecks in the system that limited the magnitude of the control gains. With faster frequencies, the control gains could be increased and the feedback control method would likely show better results. However, this also demonstrates that the PEEC is robust to delays in the system from low control frequencies by planning ahead.

Some other forms of control, such as adaptive control and output regulation theory, and their limitations were discussed in Chapter 2. Future work could look at comparing or even synthesizing the PEEC method with these other ones to improve results.

4.5 Conclusion

This chapter presented a predictive end-effector control (PEEC) method to regulate the end-effector of a manipulator operating on a moving platform under disturbance. Based on the analysis of forecasting methods in Chapter 3, time series was used to predict the base motion of a mobile manipulator. A desired pose for the end-effector, specified in a fixed frame, was then transformed to a predicted trajectory for the manipulator track. Given this trajectory, a QP problem was formulated to optimize the end-effector control to track said trajectory across the prediction horizon, thus minimizing tracking error.

The proposed method was formulated in the task space for the manipulator. The advantage to this method is that it avoids the need for nonlinear constraints based on the kinematic feasibility of the joints. To satisfy joint constraints, a key property of MPC was exploited. Since only the first control action in the control horizon is executed per control cycle, only the first set of actions was constrained. This permitted linear inequality constraints on the QP formulation for fast solutions. A penalty term was also added that minimized the difference between sequential control actions which smoothed the velocities of the manipulator. This had the additional benefity of propagating some of the kinematic constraint throughout the control horizon.

The PEEC method was verified through simulation and experiments. The results showed that it is possible to simultaneously minimize tracking error whilst adhering to joint constraints of the manipulator whilst under disturbance. Both simulation and experimental results showed that this predictive control method can reduce tracking error, under the specific test conditions, by over 60% compared to a PID feedback controller.

Chapter 5

Joint Torque Minimization of Manipulators on Moving Platforms

5.1 Problem Scenario

Manipulators operating on moving platforms are subject to inertial forces from the acceleration of the base, and centripetal forces from its angular velocity. Additionally, the change in gravitational forces relative to the manipulator must be accounted (Fig. 5.1). A redundant manipulator has more degrees of freedom than required by the task. This allows for theoretically infinite solutions for the joint motion to achieve a required end-effector control. Therefore, instead of fighting these disturbances, it may be possible to utilize these the base motion to assist the manipulator. This will reduce the effort needed to perform the trajectory tracking task.

Given predictions of the future base pose, the gravity vector in the inertial frame could be transformed to the manipulator's frame of reference. Alternatively, the gravity with respect to the manipulator could be forecast directly from IMU data. It was shown in Chapter 3 that forecasts could be made for marine vessel motion in waves that were more accurate than a last-value predictor up to 5 seconds ahead. And, in Chapter 4 it was shown that base motion prediction could improve trajectory tracking for a mobile manipulator. Based on these revelations, the purpose of this chapter is to use this base

motion disturbance to reduce joint torque on a redundant manipulator whilst performing end-effector control.

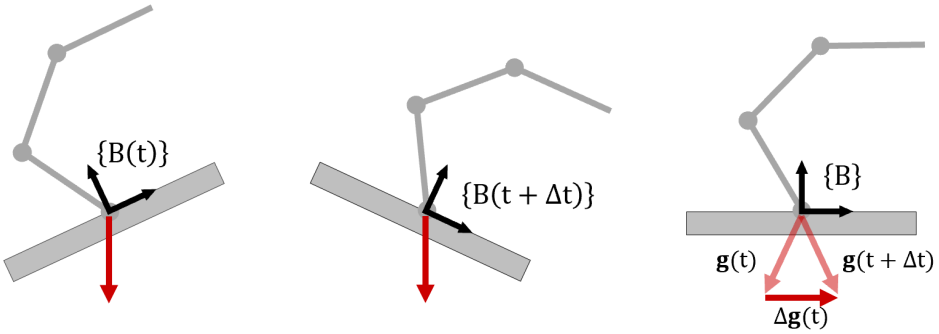

FIGURE 5.1: Relative change in gravity from the perspective of the manipulator.

As was shown in Chapter 2, the problem of torque minimization for redundant manipulators on *fixed* bases have been thoroughly studied. To reiterate the main points, Hollerbach & Suh (1987) used redundancy in a manipulator to keep joint torques at the midpoint of their performance range. Nedungadi & Kazerouinian (1989) proved a local joint acceleration control equation that guarantees global kinetic energy minimization for a redundant manipulator to execute a trajectory tracking task of the end-effector. Both these aforementioned methods, however, can manifest in long-term instability in the joint state. This prompted Kang & Freeman (1992) to develop the null-space damping control method. They authors claimed this helped improve torque minimization over previous research.

More relevant research has been conducted by From et al. (2009) and From et al. (2011) with manipulators operating on ship platforms. Dynamic modelling between the base and manipulator was developed, from which motion planning of the manipulator could be achieved that accounted for base motion disturbances. By forecasting the base motion, it was shown that the inertial forces could be utilized to reduce joint torque in the manipulator. Despite these similarities, the key limitations of their research that distinguish it from this chapter ought to be made clear:

1. The manipulator task was in reference to the ship platform. As such, there was no change in the transform between manipulator and task which had to be accounted for due to the base motion.

2. The motion planning and control of the manipulator was specified in the joint space. The end-effector was not required to follow a specified trajectory and was only constrained at the beginning and end of the motion plan. Real-time feedback control

for end-effector tracking was not required. This property was afforded by the first condition.

3. The manipulator was not redundant. This condition is borne from the first two. Since the end-effector was not constrained, joints could move without constraint to take advantage of the base motion between the endpoints of the joint trajectory.

In this chapter, the problem of torque minimization for a manipulator operating on a non-inertial platform is considered whereby the end-effector is constrained by a task specified in the inertial frame. This necessarily requires a redundancy in the system to achieve.

5.2 Modelling of the Manipulator and Platform

A dynamic model between the manipulator and platform is first derived to illuminate the effects that disturbances have on the system. Love et al. (2004) developed symbolic calculations for a manipulator operating on a ship via Lagrangian mechanics. From et al. (2009) took a similar approach. However, numerical methods exist that are more pragmatic for real-time implementation, and easily scalable to systems with many degrees of freedom (Angeles, 2002).

The velocity for the base of the manipulator and the centre of mass for each link can be expressed as a coupled system:

$$\begin{bmatrix} \dot{\mathbf{c}} \\ \dot{\mathbf{b}} \end{bmatrix} = \begin{bmatrix} \mathbf{J}_\mathrm{q} & \mathbf{J}_\mathrm{b} \\ \mathbf{0} & \mathbf{I}_6 \end{bmatrix} \begin{bmatrix} \dot{\mathbf{q}} \\ \dot{\mathbf{b}} \end{bmatrix} \tag{5.1}$$

where:

- $\dot{\mathbf{x}}_\mathrm{c} \in \mathbb{R}^{6\mathrm{n}}$ is a vector for linear and angular velocity of the centre of mass of each link on the manipulator,
- $\dot{\mathbf{b}} \in \mathbb{R}^6$ is the linear and angular velocity of the base,
- $\dot{\mathbf{q}} \in \mathbb{R}^\mathrm{n}$ is the joint velocity vector,
- $\mathbf{J}_\mathrm{q} \in \mathbb{R}^{6\mathrm{n}\times\mathrm{n}}$ maps the joint velocities to the centre-of-mass velocities,
- $\mathbf{J}_\mathrm{b} \in \mathbb{R}^{6\mathrm{n}\times 6}$ maps the base velocity to the centre-of-mass velocities.

Taking the time-derivative of Eqn. (5.1) yields:

$$\begin{bmatrix} \ddot{\mathbf{c}} \\ \ddot{\mathbf{b}} \end{bmatrix} = \begin{bmatrix} \mathbf{J}_\mathrm{q} & \mathbf{J}_\mathrm{b} \\ \mathbf{0} & \mathbf{I}_6 \end{bmatrix} \begin{bmatrix} \ddot{\mathbf{q}} \\ \ddot{\mathbf{b}} \end{bmatrix} + \begin{bmatrix} \dot{\mathbf{J}}_\mathrm{q} & \dot{\mathbf{J}}_\mathrm{b} \\ \mathbf{0} & \mathbf{0} \end{bmatrix} \begin{bmatrix} \dot{\mathbf{q}} \\ \dot{\mathbf{b}} \end{bmatrix}. \tag{5.2}$$

The linear and angular momentum for the manipulator $\boldsymbol{\upsilon}_\mathrm{c}$ and base $\boldsymbol{\upsilon}_\mathrm{b}$ is then computed by multiplying the inertia matrices by Eqn. (5.1):

$$\begin{bmatrix} \boldsymbol{\upsilon}_\mathrm{c} \\ \boldsymbol{\upsilon}_\mathrm{b} \end{bmatrix} = \begin{bmatrix} \mathbf{H} & \mathbf{0} \\ \mathbf{0} & \mathbf{G} \end{bmatrix} \begin{bmatrix} \dot{\mathbf{c}} \\ \dot{\mathbf{b}} \end{bmatrix}, \tag{5.3}$$

where $\mathbf{H} \in \mathbb{R}^{6\mathrm{n}\times 6\mathrm{n}}$ is the mass-inertia matrix of the manipulator in Cartesian space, and $\mathbf{G} \in \mathbb{R}^{6\times 6}$ is the mass-inertia matrix of the platform.

The forces and torques acting at the centre of mass for each link $\mathbf{w}_\mathrm{c} \in \mathbb{R}^{6\mathrm{n}}$, and on the base $\mathbf{w}_\mathrm{b} \in \mathbb{R}^6$, are then arrived at by taking the time-derivative of Eqn. (5.3):

$$\begin{bmatrix} \mathbf{w}_\mathrm{c} \\ \mathbf{w}_\mathrm{b} \end{bmatrix} = \begin{bmatrix} \mathbf{H} & \mathbf{0} \\ \mathbf{0} & \mathbf{G} \end{bmatrix} \begin{bmatrix} \ddot{\mathbf{c}} \\ \ddot{\mathbf{b}} \end{bmatrix} + \begin{bmatrix} \dot{\mathbf{H}} & \mathbf{0} \\ \mathbf{0} & \mathbf{0} \end{bmatrix} \begin{bmatrix} \dot{\mathbf{c}} \\ \dot{\mathbf{b}} \end{bmatrix}. \tag{5.4}$$

Equations (5.1) and (5.2) can be substituted in to (5.4) which results in:

$$\begin{bmatrix} \mathbf{w}_\mathrm{c} \\ \mathbf{w}_\mathrm{b} \end{bmatrix} = \begin{bmatrix} \mathbf{H}\mathbf{J}_\mathrm{q} & \mathbf{H}\mathbf{J}_\mathrm{b} \\ \mathbf{0} & \mathbf{G} \end{bmatrix} \begin{bmatrix} \ddot{\mathbf{q}} \\ \ddot{\mathbf{b}} \end{bmatrix} + \begin{bmatrix} \dot{\mathbf{H}}\mathbf{J}_\mathrm{q} + \mathbf{H}\dot{\mathbf{J}}_\mathrm{q} & \dot{\mathbf{H}}\mathbf{J}_\mathrm{b} + \mathbf{H}\dot{\mathbf{J}}_\mathrm{b} \\ \mathbf{0} & \mathbf{0} \end{bmatrix} \begin{bmatrix} \dot{\mathbf{q}} \\ \dot{\mathbf{b}} \end{bmatrix}, \tag{5.5}$$

Finally, Eqn. (1.2) from Chapter 1 is arrived at through:

$$\begin{bmatrix} \boldsymbol{\tau} \\ \mathbf{f}_\mathrm{b} \end{bmatrix} = \begin{bmatrix} \mathbf{J}_\mathrm{q} & \mathbf{J}_\mathrm{b} \\ \mathbf{0} & \mathbf{I}_6 \end{bmatrix}^\mathrm{T} \begin{bmatrix} \mathbf{w}_\mathrm{c} \\ \mathbf{w}_\mathrm{b} \end{bmatrix} \tag{5.6}$$

$$= \begin{bmatrix} \mathbf{M}_\mathrm{qq} & \mathbf{M}_\mathrm{qb} \\ \mathbf{M}_\mathrm{bq} & \mathbf{M}_\mathrm{bb} + \mathbf{G} \end{bmatrix} \begin{bmatrix} \ddot{\mathbf{q}} \\ \ddot{\mathbf{b}} \end{bmatrix} + \begin{bmatrix} \mathbf{C}_\mathrm{qq} & \mathbf{C}_\mathrm{qb} \\ \mathbf{C}_\mathrm{bq} & \mathbf{C}_\mathrm{bb} \end{bmatrix} \begin{bmatrix} \dot{\mathbf{q}} \\ \dot{\mathbf{b}} \end{bmatrix}, \tag{5.7}$$

whereby:

- $\boldsymbol{\tau} \in \mathbb{R}^\mathrm{n}$ is the vector of joint torques,
- $\mathbf{f}_\mathrm{b} \in \mathbb{R}^6$ are the forces and torques on the base,
- $\mathbf{M}_{\mathrm{j,k}} = \mathbf{J}_\mathrm{j}^\mathrm{T}\mathbf{H}\mathbf{J}_\mathrm{k}$ is an inertia matrix, for $\mathrm{j,k} \in \{\mathrm{q,b}\}$, and
- $\mathbf{C}_{\mathrm{j,k}} = \mathbf{J}_\mathrm{j}^\mathrm{T}\big(\dot{\mathbf{H}}\mathbf{J}_\mathrm{k} + \mathbf{H}\dot{\mathbf{J}}_\mathrm{k}\big)$ is a Coriolis matrix for $\mathrm{j,k} \in \{\mathrm{q,b}\}$.

It is noted once more that the dynamic forces induced in the manipulator from the base motion are independent of the base inertia, $\mathbf{G}$. The joint torques can be isolated from Eqn. (5.7) and simplified to the following form for convenience:

$$\boldsymbol{\tau} = \mathbf{M}\ddot{\mathbf{q}} + \boldsymbol{\tau}_{\mathrm{c}} + \boldsymbol{\tau}_{\mathrm{b}}, \tag{5.8}$$

in which:

- $\mathbf{M} \equiv \mathbf{M}_{\mathrm{qq}} \in \mathbb{R}^{\mathrm{n}\times\mathrm{n}}$ is the inertia matrix of the manipulator in joint space,
- $\boldsymbol{\tau}_{\mathrm{c}} = \mathbf{C}_{\mathrm{qq}}\dot{\mathbf{q}} \in \mathbb{R}^{\mathrm{n}}$ is the vector of Coriolis and centripetal torques,
- $\boldsymbol{\tau}_{\mathrm{b}} = \mathbf{M}_{\mathrm{qb}}\ddot{\mathbf{b}} + \mathbf{C}_{\mathrm{qb}}\dot{\mathbf{b}} \in \mathbb{R}^{\mathrm{n}}$ are the joint torques from the base motion.

To execute a required joint motion $\ddot{\mathbf{q}}$, the manipulator must apply additional torques $\boldsymbol{\tau}_{\mathrm{b}}$ to account for the inertial coupling with the base. By using a redundant manipulator, these joint torques can instead assist the joint motion whilst simultaneously tracking an end-effector trajectory.

5.3 Manipulator Control

A WLN method for joint torque minimization is first presented, based on previous methods in literature. This involves a local optimization in the dynamic torque equation for the manipulator control. This is also used as a baseline performance measure. The proposed method takes a slightly alternative approach. The control equations are first defined at the velocity level, then derived to obtain the acceleration control. This ensures stability of the null space. Then, the results of the WLN method are integrated into the proposed framework. This is then expanded to include predictions of the change in gravity and shown to improve the torque minimization control.

5.3.1 Weighted Least Norm (WLN) of the Joint Torques

To reiterate from Chapter 1, a redundant manipulator is one in which there are more degrees of freedom in the joint space than required by the task. Given this property, Nedungadi & Kazerouinian (1989) proposed to minimize the weighted joint-torque norm given kinematic constraints on the end-effector motion. They showed that this local minimum of the joint torques leads to a global minimum in kinetic energy of the manipulator

system. Applying the same framework, the weighted norm of Eqn. (5.8) can be minimized like so:

$$\min_{\ddot{\mathbf{q}}} \tfrac{1}{2}\boldsymbol{\tau}^{\mathrm{T}}\mathbf{M}^{-1}\boldsymbol{\tau} \tag{5.9}$$

$$\text{subject to: } \ddot{\mathbf{x}} - \mathbf{J}\ddot{\mathbf{q}} - \dot{\mathbf{J}}\dot{\mathbf{q}} = \mathbf{0}. \tag{5.10}$$

Due to the equality constraint, the solution to this problem is readily solved via Lagrange multipliers which yields the following joint acceleration control equation:

$$\ddot{\mathbf{q}} = \mathbf{J}_{\mathrm{W}}^{\dagger}\big(\ddot{\mathbf{x}} - \dot{\mathbf{J}}\dot{\mathbf{q}}\big) - \mathbf{N}_{\mathrm{W}}\mathbf{M}^{-1}\big(\boldsymbol{\tau}_{\mathrm{c}} + \boldsymbol{\tau}_{\mathrm{b}}\big), \tag{5.11}$$

in which:

- $\mathbf{J}_{\mathrm{W}}^{\dagger} = \mathbf{W}^{-1}\mathbf{J}^{\mathrm{T}}\big(\mathbf{J}\mathbf{W}^{-1}\mathbf{J}^{\mathrm{T}}\big)^{-1} \in \mathbb{R}^{\mathrm{n}\times\mathrm{m}}$ is the weighted, pseudoinverse Jacobian,
- $\mathbf{N}_{\mathrm{W}} = \mathbf{I} - \mathbf{J}_{\mathrm{W}}^{\dagger}\mathbf{J} \in \mathbb{R}^{\mathrm{n}\times\mathrm{n}}$ is the weighted null space projection matrix, and
- $\mathbf{W} \equiv \mathbf{M}$.

As with Nedungadi & Kazerouinian (1989), the gravitational torques have been excluded to only account for dynamic effects in the system. Both Hollerbach & Suh (1988) and Nedungadi &Kazerouinian (1989) noted that instantaneous kinetic energy minimization can lead to instability of the manipulator. This prompted several authors to propose various solutions (Hsu et al., 1989; Kang & Freeman, 1992; Natale et al., 1999). A simple method is to employ null space damping (Kang & Freeman, 1992), which extends Eqn. (5.11) like so:

$$\ddot{\mathbf{q}} = \mathbf{J}_{\mathrm{W}}^{\dagger}\big(\ddot{\mathbf{x}} - \dot{\mathbf{J}}\dot{\mathbf{q}}\big) - \mathbf{N}_{\mathrm{W}}\big(\mathbf{M}^{-1}(\boldsymbol{\tau}_{\mathrm{c}} + \boldsymbol{\tau}_{\mathrm{b}}) + \gamma\dot{\mathbf{q}}\big), \tag{5.12}$$

where $\gamma > 0$ is the damping term to reduce joint velocities in the null space. The authors noted that this equation has better performance in terms of joint torque minimization than that of Eqn. (5.11).

5.3.2 Predictive Joint Torque Minimization (PJTM)

Joint Control Resolution: Instead of minimizing the joint accelerations directly, it is proposed in this chapter to first define the control at the velocity level. A weighted

minimum velocity optimisation can be evaluated given kinematic constraints on the end-effector (see Appendix C). The velocity control equation becomes:

$$\dot{\mathbf{q}} = \mathbf{J}_{\mathrm{W}}^{\dagger}\dot{\mathbf{x}} + \mathbf{N}_{\mathrm{W}}\dot{\mathbf{q}}_{\mathrm{r}}, \tag{5.13}$$

where $\dot{\mathbf{q}}_{\mathrm{r}} \in \mathbb{R}^{\mathrm{n}}$ is a vector of joint velocities defining a secondary, redundant task projected on to the null space. The acceleration level is then equated by taking the time derivative:

$$\ddot{\mathbf{q}} = \mathbf{J}_{\mathrm{W}}^{\dagger}\big(\ddot{\mathbf{x}} - \dot{\mathbf{J}}\dot{\mathbf{q}}_{\mathrm{c}}\big) + \mathbf{N}_{\mathrm{W}}\ddot{\mathbf{q}}_{\mathrm{r}} + \mathbf{N}_{\mathrm{W}}\dot{\mathbf{J}}^{\mathrm{T}}\mathbf{J}_{\mathrm{W}}^{\dagger\mathrm{T}}\big(\dot{\mathbf{q}} - \dot{\mathbf{q}}_{\mathrm{r}}\big). \tag{5.14}$$

This ensures that the joint motion remains stable, as the null space velocities are clearly defined. This derivation was also suggested by Slotine (1991) due to its inherent stability.

The redundant task at the acceleration level can be defined as:

$$\ddot{\mathbf{q}}_{\mathrm{r}} = \mathbf{W}^{-1}\big(\Delta\bar{\boldsymbol{\tau}}_{\mathrm{g}} - \boldsymbol{\tau}_{\mathrm{c}} - \boldsymbol{\tau}_{\mathrm{b}}\big) - \gamma\dot{\mathbf{q}}, \tag{5.15}$$

where $\mathbf{W} \equiv \mathbf{M}$ and $\Delta\bar{\boldsymbol{\tau}}_{\mathrm{g}}$ represents the torque from the average predicted change in the gravitational acceleration relative the manipulator. The inclusion of this term enables the manipulator to take advantage of the change in gravity as the base tilts, further reducing joint torque. Also, despite Eqn. (5.14) being stable, the damping term $-\gamma\dot{\mathbf{q}}$ is still included. This is used to enervate the kinetic energy that accumulates in the manipulator due to the base motion.

The velocity-level task can be approximated in discrete time for the next control loop as:

$$\dot{\mathbf{q}}_{\mathrm{r}}(\mathrm{t} + \Delta\mathrm{t}) = \mathbf{N}_{\mathrm{W}}\dot{\mathbf{q}}(\mathrm{t}) + \Delta\mathrm{t}\ddot{\mathbf{q}}_{\mathrm{r}}(\mathrm{t}), \tag{5.16}$$

where $\mathbf{N}_{\mathrm{W}}\dot{\mathbf{q}}(\mathrm{t})$ gives the observed null space velocities in the system at the current time.

Predictions of gravitational forces: The change in the gravitational forces can be utilized as the manipulator base rotates relative to the inertial frame (Fig. 5.1). Given forecasts of the base orientation, the average change in the gravity vector with respect to the base can be estimated as:

$$\Delta\bar{\mathbf{g}} = \mathrm{L}^{-1}\sum_{\mathrm{i}=1}^{\mathrm{L}}\Big(\hat{\mathbf{R}}_{\mathrm{B}}^{\mathrm{I}}(\mathrm{t}+\mathrm{i}) - \mathbf{R}_{\mathrm{B}}^{\mathrm{I}}(\mathrm{t})\Big)\mathbf{g}, \tag{5.17}$$

where:

- $\mathbf{R}_{\mathrm{B}}^{\mathrm{I}}(t) \in \mathbb{SO}(3)$ is the rotation from the base to inertial frame at the current time,
- $\hat{\mathbf{R}}_{\mathrm{B}}^{\mathrm{I}}(t+i) \in \mathbb{SO}(3)$ is the predicted rotation at i time-steps ahead,
- L is the length of the forecast horizon, and
- $\mathbf{g} \in \mathbb{R}^3$ is the gravitational acceleration in the inertial frame.

Alternatively, the gravity vector can be forecast directly in the base frame:

$$\Delta\bar{\mathbf{g}}_{\mathrm{b}} = \mathrm{L}^{-1} \sum_{i=1}^{L} \mathbf{g}_{\mathrm{b}}(t+i) - \mathbf{g}_{\mathrm{b}}(t) \tag{5.18}$$

$$= \bar{\mathbf{g}}_{\mathrm{b}}(t+L) - \mathbf{g}_{\mathrm{b}}(t). \tag{5.19}$$

By taking the mean of the predictions, more information about the future tendencies of gravity can be utilised in contrast to a discrete difference at L time-steps ahead. This idea is illustrated in Fig. 5.2. For an exponential trend, taking the average better reflects the tendency for the change in gravity to linger at lower levels toward the end of the slope (Fig. 5.2a). Similarly, a discrete difference over a quadratic trend would result in no change, whereas the mean gives a better intuition about the convexity of the state over time (Fig. 5.2b). Then there is also the case where there may be sinusoidal behaviour (Fig. 5.2c). In this situation, taking the mean negates capricious behaviour that might result from rapid oscillations.

Calculations for the torque vector $\Delta\bar{\boldsymbol{\tau}}_{\mathrm{g}}$ can then be computed by substituting the gravity vector $\mathbf{g}$ for $\Delta\bar{\mathbf{g}}_{\mathrm{b}}$ in computing gravitational torques (Appendix C).

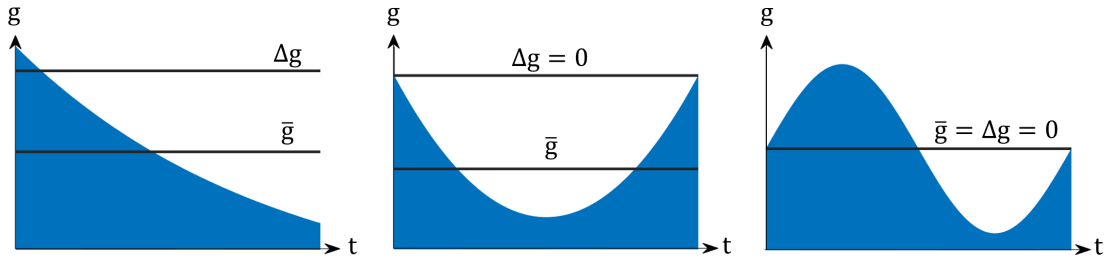

(A) Exponential trend. (B) Quadratic trend. (C) Sinusoidal trend.

FIGURE 5.2: Taking the arithmetic mean of the change in gravity across the prediction horizon reveals more information about the trend than a simple difference.

5.3.3 End-Effector Control

For this chapter, Proportional-Derivative (PD) control is used to enable end-effector tracking of the manipulator. The end-effector accelerations are specified as:

$$\begin{bmatrix} \dot{\mathbf{v}} \\ \dot{\boldsymbol{\omega}} \end{bmatrix} = \begin{bmatrix} \dot{\mathbf{v}}_\mathrm{d} + \mathbf{K}_\mathrm{p}\mathbf{e}_\mathrm{p} + \mathbf{K}_\mathrm{v}\dot{\mathbf{e}}_\mathrm{p} - \dot{\mathbf{v}}_\mathrm{b} - S(\dot{\boldsymbol{\omega}}_\mathrm{b})\mathbf{r} - 2S(\boldsymbol{\omega}_\mathrm{b})\mathbf{r} - 2S(\boldsymbol{\omega}_\mathrm{b})\dot{\mathbf{r}} \\ \dot{\boldsymbol{\omega}}_\mathrm{d} + \mathbf{K}_\mathrm{o}\mathbf{e}_\mathrm{o} + \mathbf{K}_\omega\dot{\mathbf{e}}_\mathrm{o} - \dot{\boldsymbol{\omega}}_\mathrm{b} \end{bmatrix}, \tag{5.20}$$

where:

- $\dot{\mathbf{v}}_\mathrm{d}, \dot{\boldsymbol{\omega}}_\mathrm{d} \in \mathbb{R}^3$ are the desired linear and angular velocities of the end-effector respectively,
- $\mathbf{e}_\mathrm{p}, \mathbf{e}_\mathrm{o} \in \mathbb{R}^3$ are the position and orientation errors of the end-effector,
- $\mathbf{K}_\mathrm{p}, \mathbf{K}_\mathrm{v}, \mathbf{K}_\mathrm{o}, \mathbf{K}_\omega \in \mathbb{R}^{3\times3}$ are gain matrices,
- $\dot{\mathbf{v}}_\mathrm{b}, \dot{\boldsymbol{\omega}}_\mathrm{b} \in \mathbb{R}^3$ are the linear and angular velocities of the base, respectively, and
- $\mathbf{r} \in \mathbb{R}^3$ is the distance from the base to the end-effector.

For this and the following chapter it is assumed the current base state (i.e., position, velocity, acceleration) is known.

5.4 Verification of the Predictive Joint Torque Minimization

5.4.1 Implementation

To validate the PJTM method, a 7DOF manipulator was simulated on a moving base under disturbance. The manipulator was required to track a straight line with its end-effector, which was specified in the inertial frame. To generate the base motion, IMU data was collected from the SPIR under wave excitation in a test tank. This data was extrapolated from the acceleration and velocity levels through to the position level. Again, it is assumed that the motion of the manipulator has no effect on the base. Though this is not 100% realistic, it does have the advantage that different control methods can be objectively evaluated under the exact same external conditions. A plot of the base pose over the course of the simulation is given in Fig. 5.3.

The WLN torque minimization method presented earlier is used as a baseline to compare with the proposed control method in this chapter. Different forecast horizons, from L = 0

through to L = 50 (0.5s) were used for predicting the base motion. A damping coefficient of $\gamma = 0.5$ was used for most cases, although this had to be increased to reduce instability for long-term forecasts of L > 40 steps.

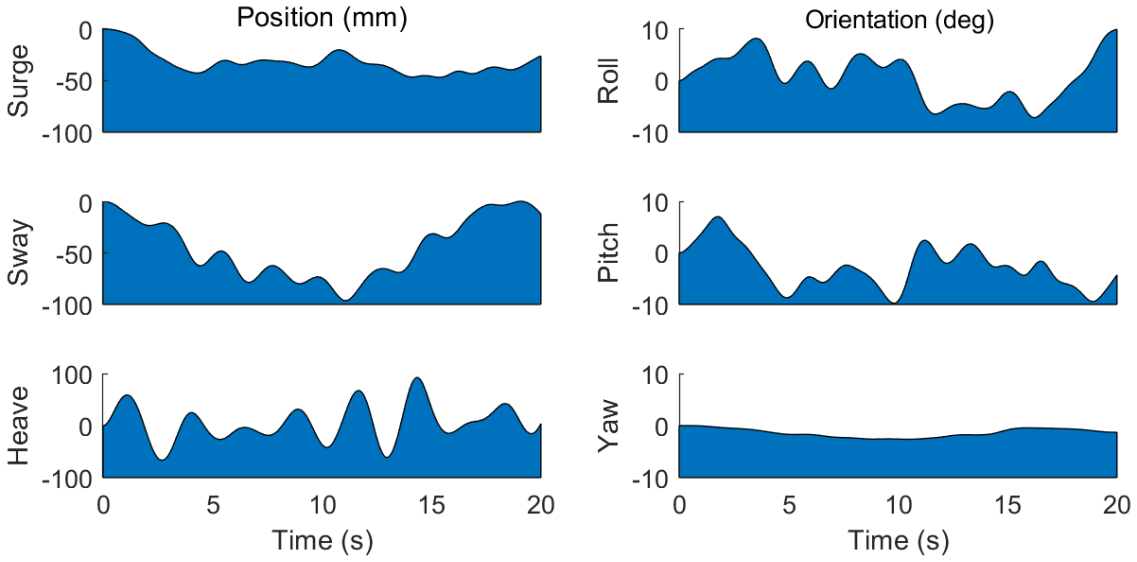

FIGURE 5.3: Base motion of the manipulator used in the simulation was generated from motion data captured from an AUV under wave excitation.

TABLE 5.1: Control parameters for torque minimization with base disturbance.

	Control Parameters			
	$\mathbf{K}_\mathrm{p}$	$\mathbf{K}_\mathrm{v}$	$\mathbf{K}_\omega$	β
WLN Method	30	12	12	0.2
PJTM Method	30	12	12	0.2

5.4.2 Results

Results of the simulation show that the proposed method can successfully reduce the joint torque in the manipulator compared to the conventional WLN method (Table 5.2). Furthermore, the introduction of the gravity predictions helps further reduce the joint torque as anticipated. A plot of the sum of absolute joint torques for the different cases is given in Fig. 5.4. Using no gravity prediction (L = 0), the proposed method showed a marginal improvement of approximately 12%. Larger reductions up to 20% were observed for L = 10 (0.1s), and up to 27% for L = 30 (0.3s).

The damping coefficient γ had to be increased for L $\geq$ 40 as the kinetic energy in the manipulator accumulated to such a point that it began to lose control. About this point the improvements from the gravity prediction begin to diminish. This could be for two reason.

First, the damping term had to be increased to keep the joint velocities at manageable speeds. And second, the average change in gravity for long-term forecasts began to diverge from the local effects influencing the manipulator at the current time.

Plots of the joint torques, and joint angles are given in Fig. 5.5 and Fig. 5.6, respectively. These figures are for the case where L = 30. It can be seen from Fig. 5.5 that the proposed control method reduces joint torque on joints 2 through to 6. There was little-to-no difference in the performance of joints 1 and 7.

TABLE 5.2: Mean Sum of Absolute Joint Torques

Method	Damping γ	Mean Absolute Torque (Nm)	Improvement
WLN	0.5	46.8	
PJTM (L = 0)	0.5	41.3	12%
PJTM (L = 10)	0.5	37.6	20%
PJTM (L = 20)	0.5	35.7	24%
PJTM (L = 30)	0.5	33.1	27%
PJTM (L = 40)	0.6	33.4	28%
PJTM (L = 50)	0.8	33.8	28%

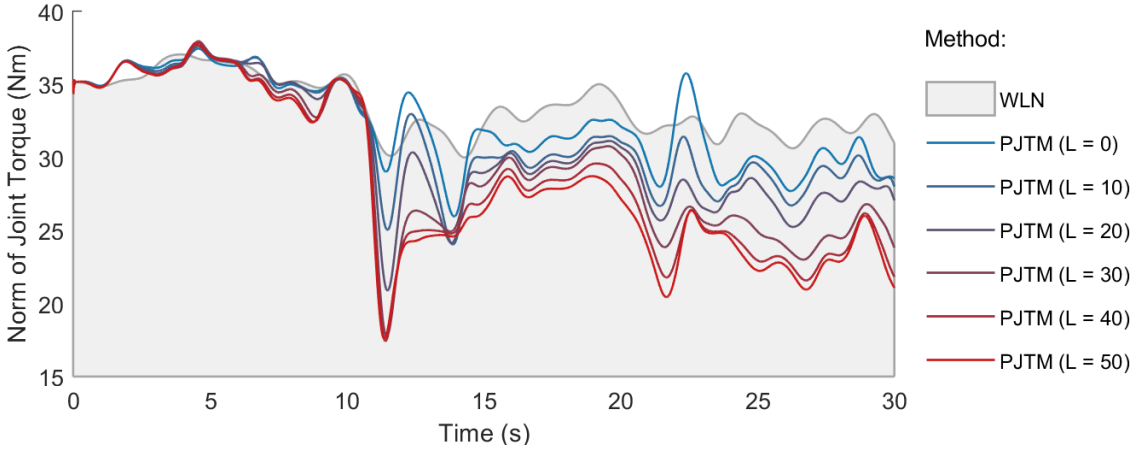

FIGURE 5.4: Norm of joint torques for torque minimization under base disturbance. By forecasting the change in base orientation, the shift in gravity can be utilized to reduce joint torque over the long term.

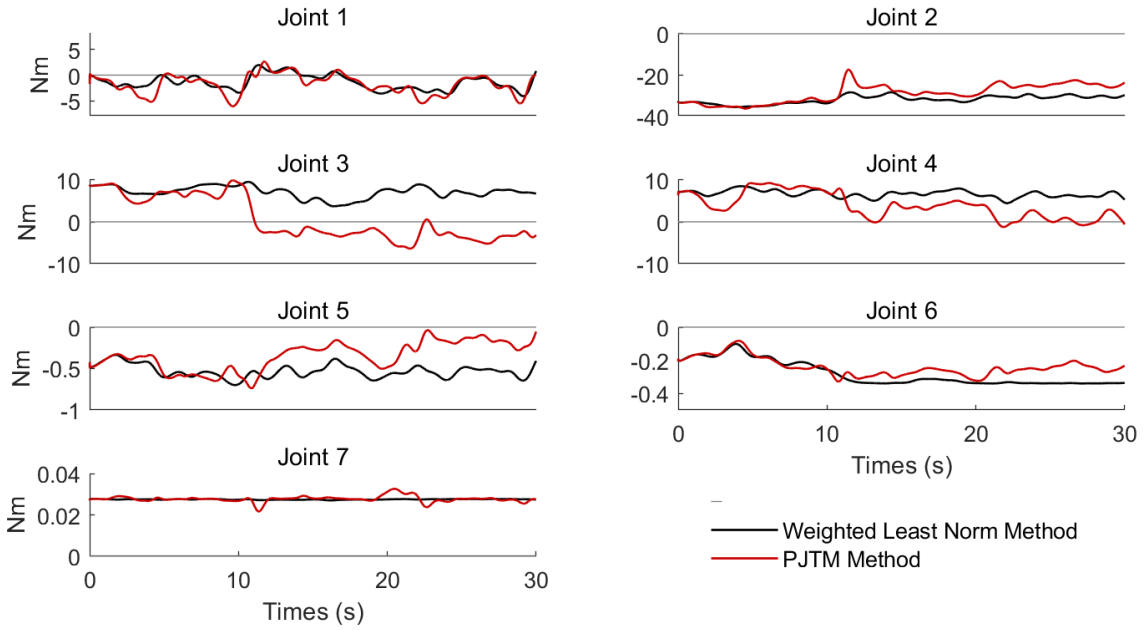

FIGURE 5.5: Individual joint torques for trajectory tracking with a moving base. The proposed control method shows reduced torque for joints 3, 4, 5 and 6.

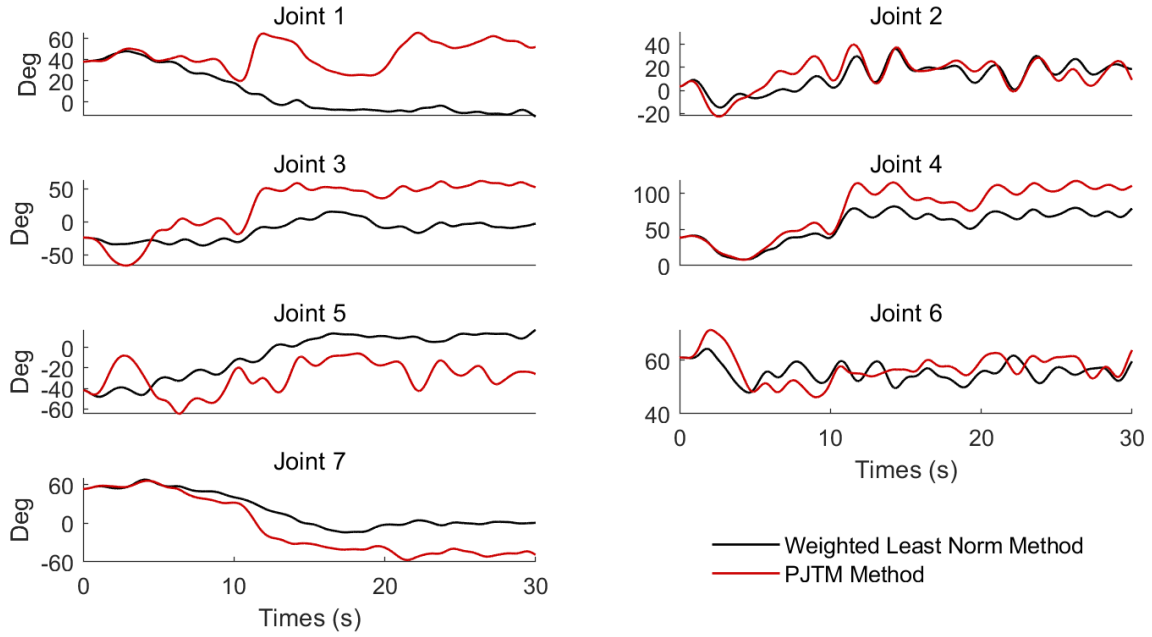

FIGURE 5.6: Joint positions over time for trajectory tracking under disturbance using torque minimization.

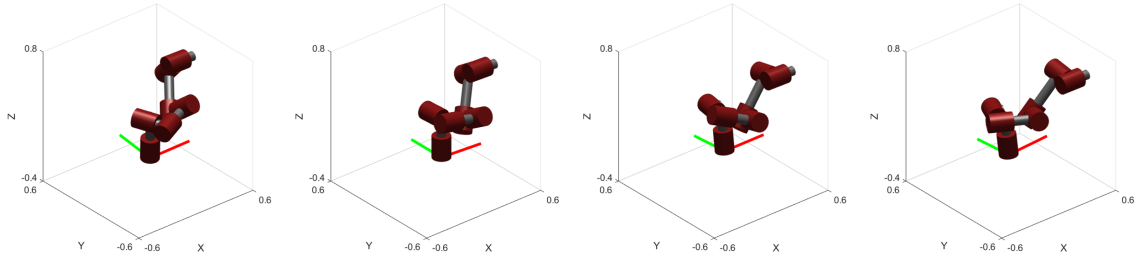

(A) WLN Method.

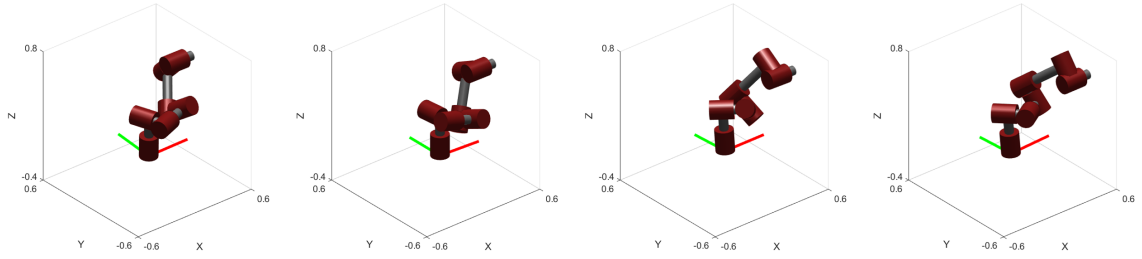

(B) PJTM Method.

FIGURE 5.7: Screenshots from the simulation of joint torque minimization with base motion disturbance.

5.5 Discussion

5.5.1 Choice of Forecast Horizon

An important consideration for the predictive torque minimization proposed in this chapter is the length of the forecast horizon, L. There are numerous interacting factors, and compromises to be made with each choice. A longer forecast horizon showed a greater reduction in joint torque due to the ability to anticipate the change in base orientation. However, there was diminishing returns in torque reduction as the forecast horizon increased in length (see Fig.5.4). This is due to two factors:

1. As the forecast horizon increases, the mean prediction accuracy decreases. Poor long-term forecasts mean the manipulator will not reconfigure itself in a manner that is commensurate with the actual change in the gravitational forces.
2. The mean change in gravity increases in magnitude, and the phase appears to advance as the forecast horizon increases (Fig. 5.8). This has two consequences:
   (a) The magnitude of $\Delta\bar{\tau}_g$ also increases, thereby increasing the kinetic energy in the manipulator. This can accumulate to such a point that the system loses control. As such, the damping term γ had to be increased to compensate. This can nullify any torque minimization that might be gained from the change in gravitational forces.
   (b) The phase shift means the manipulator is not acting in accordance with the actual change in gravitational forces at the current time, resulting in reduced performance.

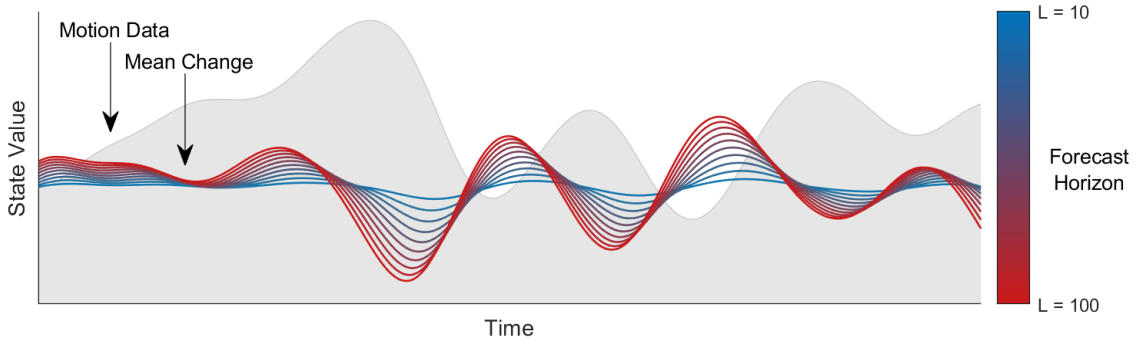

FIGURE 5.8: Average change in base orientation for different prediction lengths.

One other consideration is that an expected value of the change in gravity could be used rather than the arithmetic mean. This may help by factoring in forecast uncertainty,

particularly when shocks to the system disrupt the forecast. But, as was shown in Chapter 3, the choice of forecasting method, its mean prediction accuracy, and forecast uncertainty, are dependent on both the environment and system.

5.5.2 Null Space Damping & Energy Enervation

As noted by authors implementing kinetic energy minimization (Hollerbach & Suh, 1988, Nedungadi & Kazerouinian 1989), instability seemed an inevitable outcome. This prompted Kang & Freeman (1992) to develop the null space damping method. They claimed that it improved kinetic energy minimization. When operating on a moving base, the base motion transmits kinetic energy in the manipulator system. As such, this null space damping method also had to be applied to the PJTM method, lest the joint velocities increase to such a degree that joint collisions or instability ensue. This necessarily detracts from the joint torque minimization method, which is undesirable.

How best to proceed with determining the optimal damping is unclear at this stage. In this chapter it was manually adjusted to achieve satisfactory results. It also had to be increased with the lengthening of the forecast horizon, L, to prevent any joint limit violations. One potential avenue could be to modulate the damping coefficient with respect to the total kinetic energy in the manipulator. In this manner, the manipulator is free to leverage the torque minimization capabilies at low energy levels, but decelerate itself when the energy levels become too large. An ideal solution would be to find a control formulation that circumvents the need for the null space damping entirely. This could be an avenue for future research.

5.5.3 Limitations

As with the predictive control method in Chapter 4, there are some performance limitations and assumptions made behind the control method developed in this chapter:

1. It was assumed that the inertia of the platform is large enough that the motion of the manipulator has little effect. This is a reasonable when using small, lightweight manipulators, manipulators on ship platforms, or terrestrial vehicles which have ground support.
2. The end-effector task must remain within the manipulator's workspace. If the desired pose is too far from the manipulator, it could extend to a singular configuration.

Conversely, as the base moves forward, the manipulator may move back and collide with itself. This may not be too difficult to avoid, particularly if the manipulator were mounted on a controllable vehicle. It may also be possible to implement control policies to avoid either of these problems when the base location is not ideal.

5.6 Conclusion

In this chapter, a predictive joint torque minimization (PJTM) was proposed for redundant manipulators operating on non-inertial platforms under disturbance. The method developed in this paper is distinguished from previous literature in that a) the end-effector of the manipulator is constrained to track a trajectory, and b) the method relies on real time null space control, rather than motion planning. Furthermore, the control equations were derived at the velocity level, and derived for the acceleration. In doing so, this circumvented the null space instability that can occur in acceleration control of redundant manipulators.

A torque optimization problem was first presented based on previous literature that equates to WLN in the control of a redundant manipulator. This method was built upon to incorporate predictions of the change in gravitational forces due to the base motion disturbance. Simulations were conducted in which base motion was generated from real IMU data of a vessel undergoing wave excitation. The results showed that by including the gravity prediction term, the PJTM method can reduce joint torque by up to 28% compared to a local minimization of the weighted torque norm for this scenario.

Furthermore, it was found that the proposed derivation from the velocity level resulted in reduced trajectory tracking error of the end-effector when the manipulator base was subject to unwanted motion. This phenomenon requires further study.

Chapter 6

Joint Torque Minimization with Large External Forces

6.1 Problem Scenario

The widespread adaptation of robotic manipulators in manufacturing is arguably down to two main factors:

1. Robotic systems can perform repetitious tasks swiftly and accurately compared to humans, and
2. Manipulators can handle larger forces when lifting, blasting, etc.

As the development of field robotics advances, autonomous mobile systems will be required to handle large payloads through some form of manipulation. Some of the examples presented in Chapter 1 and Chapter 2 included:

- Underwater object recover (Marani et al., 2009; Simetti et al., 2014),
- Underwater valve turning (Cieslak et al., 2015; Maurelli et al., 2016),
- Object retrieval with UAVMS (Garimella & Kobilarov, 2016; Lunni et al., 2017),
- Surface inspection with UAVs (Jiminez-Cano et al., 2015),
- Harvesting agriculture (Lehnert et al., 2016), and
- Digging with a planetary rover (Bussmann et al., 2018).

Forces may also be imposed by means other than physical objects. For instance, the intention SPIR is to conduct high-pressure water cleaning of submerged infrastructure (Liu et al., 2014; Woolfrey et al., 2016). Previously related work in robotic high-pressure blasting presented issues for the control due to the "heavily laden manipulator" (Paul et al., 2010). The large nozzle reaction forces have implications on the physical design of the robot as well. Initially, a large manipulator was chosen for this research project (Liu et al., 2008) but its size caused issues with logistics (Manamperi et al., 2011). Nozzle reaction forces reached up to 108N during field trials (Paul et al., 2010). However, the manipulator that was used had maximum payload capacity of 13kg (127.53N) with specific pose requirements above 11kg (107.91N) (DensoWave Inc, 2018).

Kirchner et al. (2006) had attempted to address the issue of large nozzle reaction forces for grit-blasting through purely mechanical solutions. Reaction forces from the nozzle can be re-directed to the shoulder of the operator through the shape of the hose being used. However, the drawback to this method is that it does not generalize to a robotic manipulator that does not have such physiology.

In Chapter 5, a method was developed to reduce joint torques for a redundant manipulator under base motion. This was achieved whilst simultaneously tracking a desired end-effector trajectory. In the same manner, redundancy can be used to rearrange the joints in real time and minimize joint torques for lifiting, blasting, or any other task requiring large force applications. The purpose of this chapter is to developed such a control method to achieve this goal. The problem is first considered with a fixed base. Then, the control method is applied to a scenario with a moving base. The PJTM method from Chapter 5 is also integrated, which shows a further reduction in joint torque.

6.2 Problem Formulation

The joint torque equation for a serial-link manipulator with external forces acting on the end-effector is given by the following equation:

$$\boldsymbol{\tau} = \mathbf{M}\ddot{\mathbf{q}} + \boldsymbol{\tau}_{\mathrm{c}} + \boldsymbol{\tau}_{\mathrm{g}} + \mathbf{J}^{\mathrm{T}}\mathbf{R}\mathbf{w}, \tag{6.1}$$

in which $\mathbf{w} \in \mathbb{R}^{\mathrm{m}}$ is a wrench of forces and torques in Cartesian space with respect to some arbitrary frame {i} on the manipulator, and $\mathbf{R} \in \mathbb{SO}(\mathrm{m})$ is a rotation matrix from the origin frame {0} to frame {i}. Note that the torques from the base motion $\boldsymbol{\tau}_{\mathrm{b}}$ has been

left out for now. If m = 6, the rotation matrix $\mathbf{R}$ can be decomposed as:

$$\mathbf{R} = \begin{bmatrix} \mathbf{R}_0^{\mathrm{i}} & \mathbf{0}_{3\times3} \\ \mathbf{0}_{3\times3} & \mathbf{R}_0^{\mathrm{i}} \end{bmatrix}, \tag{6.2}$$

where $\mathbf{R}_0^{\mathrm{i}} \in \mathbb{SO}(3)$ is the rotation between {0} and {i}. The joint control $\ddot{\mathbf{q}}_{\mathrm{c}}$ is defined the same as in Chapter 5 by first solving the velocity level equation, then taking the time-derivative:

$$\dot{\mathbf{q}} = \mathbf{J}_{\mathrm{W}}^{\dagger}\dot{\mathbf{x}} + \mathbf{N}_{\mathrm{W}}\dot{\mathbf{q}}_{\mathrm{r}} \tag{6.3}$$

$$\ddot{\mathbf{q}} = \mathbf{J}_{\mathrm{W}}^{\dagger}\big(\ddot{\mathbf{x}} - \dot{\mathbf{J}}\dot{\mathbf{q}}\big) + \mathbf{N}_{\mathrm{W}}\ddot{\mathbf{q}}_{\mathrm{r}} + \mathbf{N}_{\mathrm{W}}\dot{\mathbf{J}}^{\mathrm{T}}\mathbf{J}_{\mathrm{W}}^{\dagger\mathrm{T}}\big(\dot{\mathbf{q}} - \dot{\mathbf{q}}_{\mathrm{r}}\big), \tag{6.4}$$

where $\dot{\mathbf{x}},\ \ddot{\mathbf{x}} \in \mathbb{R}^6$ defines the required end-effector motion control, and $\dot{\mathbf{q}}_{\mathrm{r}},\ \ddot{\mathbf{q}}_{\mathrm{r}}$ pertains to the joint motions for a redundant task projected on to the null space. The same end-effector control from Eqn. (5.20) in Chapter 5 is applied here.

Equation (5.20) is substituted in to Eqn. (6.4) to determine the necessary joint accelerations. Then, Eqn. (6.4) is substituted in to Eqn. (6.1) to obtain the joint torques to control the manipulator.

Note that the joint control equations give a general, weighted solution for a redundant manipulator. The term $\mathbf{J}_{\mathrm{W}}^{\dagger} \in \mathbb{R}^{\mathrm{n}\times\mathrm{m}}$ is the weighted, pseudoinverse Jacobian and $\mathbf{N}_{\mathrm{W}} \in \mathbb{R}^{\mathrm{n}\times\mathrm{n}}$ is the weighted null space projection matrix (see Appendix C). Setting the weighting matrix in these equations equivalent to the inertia matrix, $\mathbf{W} = \mathbf{M}$, will afford kinetic energy minimization. The manipulator will use the least effort as possible for self-motion.

The problem thus becomes finding an equation for $\dot{\mathbf{q}}_{\mathrm{r}},\ \ddot{\mathbf{q}}_{\mathrm{r}}$ that can be used to reduce $\|\mathbf{J}^{\mathrm{T}}\mathbf{R}\mathbf{w}\|$ and/or $\|\boldsymbol{\tau}\|$. All the literature on torque minimization presented in Chapter 2 are concerned with minimizing the local dynamic torque of a redundant manipulator for self motion. However, if $\|\mathbf{J}^{\mathrm{T}}\mathbf{R}\mathbf{w}\| \gg \|\mathbf{M}\ddot{\mathbf{q}} + \boldsymbol{\tau}_{\mathrm{c}}\|$, a more prudent approach would to be arrange the joint configuration to resist the wrench $\mathbf{w}$.

6.3 Joint Torque Minimization With External Forces

6.3.1 Weighted Least Norm Solution

As a baseline performance measure, the WLN solution that was used in Chapter 5 is also considered here. The exact same optimization problem as Eqn. (5.9) and Eqn. (5.10) can

be solved given the torque equation (6.1). The resultant joint acceleration for this problem then yields:

$$\ddot{\mathbf{q}} = \mathbf{J}_{\mathrm{M}}^{\dagger}\big(\ddot{\mathbf{x}} - \dot{\mathbf{J}}\dot{\mathbf{q}}\big) + \mathbf{N}_{\mathrm{M}}\mathbf{M}^{-1}(\boldsymbol{\tau}_{\mathrm{c}} + \mathbf{J}^{\mathrm{T}}\mathbf{R}\mathbf{w}). \tag{6.5}$$

The inertia-weighted pseudoinverse Jacobian and null space projection matrix have been used here. Also, as with Nedungadi & Kazerouinian (1989), the gravity torque has been ignored to only account for dynamic effects. Also note that the observed joint velocity $\mathbf{q}$ is used in Eqn. (6.5), as opposed to the control velocity $\dot{\mathbf{q}}_{\mathrm{c}}$ in Eqn. (6.4). To ensure stability, the null space damping method proposed by Kang & Freeman (1992) is then added:

$$\ddot{\mathbf{q}} = \mathbf{J}_{\mathrm{M}}^{\dagger}\big(\ddot{\mathbf{x}} - \dot{\mathbf{J}}\dot{\mathbf{q}}\big) + \mathbf{N}_{\mathrm{M}}\big(\mathbf{M}^{-1}(\boldsymbol{\tau}_{\mathrm{c}} + \mathbf{J}^{\mathrm{T}}\mathbf{R}\mathbf{w}) - \gamma\dot{\mathbf{q}}\big), \tag{6.6}$$

with damping coefficient $\gamma = (0, 1)$.

6.3.2 External Joint Torque Minimization (EJTM) Method

Yoshikawa (1984) proposed the idea of projecting the gradient vector of a scalar performance function on to the null space of a redundant manipulator. In doing so, the manipulator would autonomously rearrange itself to either decrease or increase this criterion. Some demonstrated examples were singularity avoidance and obstacle avoidance.

Consider the following cost function, aimed at reducing the sum-of-squared torques from forces acting on the manipulator:

$$\mathrm{c}(\mathbf{q}) = \tfrac{1}{2}\hat{\boldsymbol{\tau}}^{\mathrm{T}}\mathbf{G}\hat{\boldsymbol{\tau}} \tag{6.7}$$

where:

- $\hat{\boldsymbol{\tau}} = \mathbf{J}^{\mathrm{T}}\mathbf{R}\hat{\mathbf{w}} \in \mathbb{R}^{\mathrm{n}}$ are the joint torques from a unit wrench on the end-effector,
- $\hat{\mathbf{w}} = \mathbf{w}/\|\mathbf{w}\| \in \mathbb{R}^{\mathrm{m}}$ gives the direction in which the forces $\mathbf{w}$ are acting on the manipulator, and
- $\mathbf{G} \in \mathbb{R}^{\mathrm{n}\times\mathrm{n}}$ is a positive-definite weighting matrix.

A prudent choice for $\mathbf{G}$ might be to set the diagonal elements inversely proportional to the square of the maximum joint torques:

$$\mathbf{G} = \begin{bmatrix} \tau_{\mathrm{max,1}}^{-2} & & \\ & \ddots & \\ & & \tau_{\mathrm{max,n}}^{-2} \end{bmatrix}, \tag{6.8}$$

in which $\boldsymbol{\tau}_{\mathrm{i}}$ for $\mathrm{i} = 1, ..., \mathrm{n}$ is the maximum joint torque for the i^{th} joint. This approach was taken by Ajoudani et al. (2015) for stiffness optimisation of redundant manipulators. The gradient vector of Eqn. (6.7) is then:

$$\nabla \mathrm{c}(\mathbf{q}) = (\partial \hat{\boldsymbol{\tau}}/\partial \mathbf{q})^{\mathrm{T}} \mathbf{G} \mathbf{J}^{\mathrm{T}} \mathbf{R} \hat{\mathbf{w}}. \tag{6.9}$$

The partial-derivative for each element in Eqn. (6.9) is calculated as:

$$\partial \mathrm{c}/\partial \mathrm{q_j} = \hat{\mathbf{w}} \left(\frac{\partial \mathbf{R}^{\mathrm{T}}}{\partial \mathrm{q_j}} \mathbf{J} + \mathbf{R}^{\mathrm{T}} \frac{\partial \mathbf{J}}{\partial \mathrm{q_j}} \right) \mathbf{G} \mathbf{J}^{\mathrm{T}} \mathbf{R} \hat{\mathbf{w}}, \quad \mathrm{j} \in \{1, ..., \mathrm{n}\}. \tag{6.10}$$

Numerical methods for obtaining the partial-derivative of the Jacobian matrix, $\partial \mathbf{J}/\partial \mathbf{q} \in \mathbb{R}^{\mathrm{m} \times \mathrm{n} \times \mathrm{n}}$ have been shown by Bruyninckx and De Schutter (1996) and Pohl & Lipkin (1991). where $\mathbf{R}_0^{\mathrm{i}} \in \mathbb{SO}(3)$ is a rotation from frame $\{0\}$ to frame $\{\mathrm{i}\}$ on the manipulator. The partial derivative of this matrix, $\partial \mathbf{R}_0^{\mathrm{i}}/\partial \mathbf{q} \in \mathbb{R}^{3 \times 3 \times \mathrm{n}}$, and hence $\partial \mathbf{R}/\partial \mathbf{q} \in \mathbb{R}^{6 \times 6 \times \mathrm{n}}$ can also be computed numerically (Bruyninckx & De Schutter, 1996).

Setting the secondary redundant task proportional to Eqn. (6.9) will optimise Eqn. (6.7) in the null space of the manipulator:

$$\dot{\mathbf{q}}_{\mathrm{r}} = \alpha \mathbf{W}^{-1} \nabla \mathrm{c}(\mathbf{q}), \tag{6.11}$$

where $\mathbf{W} \in \mathbb{R}^{\mathrm{n} \times \mathrm{n}}$ is a positive-definite weighting matrix. Assigning the scalar $\alpha < 0$ will minimize Eqn. (6.7). In doing so, the manipulator will reconfigure itself to minimize joint torques induced by the wrench $\mathbf{w}$ whilst the end-effector is constrained to a particular pose. Equation (6.9) can be substituted directly in to Eqn. (6.3) to evaluate the velocity level control equations.

The time-derivative of Eqn. (6.11) is:

$$\ddot{\mathbf{q}}_{\mathrm{r}} = \alpha \mathbf{W}^{-1} \cdot \frac{\mathrm{d}}{\mathrm{dt}}\big(\nabla \mathrm{c}(\mathbf{q})\big) \tag{6.12}$$

$$= \alpha \mathbf{W}^{-1} \cdot \frac{\mathrm{d}}{\mathrm{d}\mathbf{q}}\big(\nabla \mathrm{c}(\mathbf{q})\big)\dot{\mathbf{q}} \tag{6.13}$$

$$= \alpha \mathbf{W}^{-1} \cdot \mathbf{H}(\mathbf{q})\dot{\mathbf{q}}, \tag{6.14}$$

in which $\mathbf{H}(\mathbf{q}) \in \mathbb{R}^{\mathrm{n}\times\mathrm{n}}$ is the Hessian of $\mathrm{c}(\mathbf{q})$. The Hessian for Eqn. (6.7) is difficult to calculate. But in practice, it is sufficient to use backwards-differencing to approximate the acceleration:

$$\ddot{\mathbf{q}}_{\mathrm{r}}(\mathrm{t}) \approx \Delta \mathrm{t}^{-1}\big(\dot{\mathbf{q}}_{\mathrm{r}}(\mathrm{t}) - \dot{\mathbf{q}}_{\mathrm{r}}(\mathrm{t}-\Delta \mathrm{t})),\big) \tag{6.15}$$

where $\Delta \mathrm{t}^{-1}$ is the control frequency. Using Eqn. (6.3) and Eqn. (6.4) the null space velocities are inherently stable and there is no need to add damping (Kang & Freeman, 1992) or null space velocity control (Hsu et al., 1989; Natale et al., 1999).

Another thing to consider is that the manipulator may move quickly to reduce the cost function Eqn. (6.7) when far from an optimal solution. This will increase the kinetic energy in the manipulator and increase the joint torque. To circumvent this problem, Eqn. (6.15) can be modified by subtracting the local effects of the joint torques:

$$\ddot{\mathbf{q}}_{\mathrm{r}}(\mathrm{t}) = \Delta \mathrm{t}^{-1}\big(\dot{\mathbf{q}}_{\mathrm{r}}(\mathrm{t}) - \dot{\mathbf{q}}_{\mathrm{r}}(\mathrm{t}-\Delta \mathrm{t})) - \beta \mathbf{M}^{-1}\big(\boldsymbol{\tau}_{\mathrm{c}} + \mathbf{J}^{\mathrm{T}}\mathbf{R}\mathbf{w}\big). \tag{6.16}$$

The coefficient α in Eqn. (6.11) determines the magnitude of the velocity for the null space task. Here in Eqn. (6.16), the coefficient β can be used to attenuate the local dynamic accelerations to produce the desired results.

6.3.3 Incorporation of Physical Constraints

The joint velocity equation, Eqn. (6.3), is defined by a WLN problem (Appendix C). Because of this, it is possible to account for physical constraints on the solution via the construction of the weighting matrix $\mathbf{W}$. Some examples of this include joint-limit avoidance (Chan & Dubey, 1995), self-collision avoidance (Dariush et al., 2010), and obstacle avoidance (Chen at al., 2015). Here, the joint-limit avoidance case is applied. Using the weighting matrix for collision avoidance is particularly useful for real-time control where pre-planned joint motions are not feasible. This is of particular interest for manipulators on mobile platforms operating under disturbance. In fact, this joint limit avoidance method was also applied by Sarkar et al. (1999) for an underwater manipulator.

The weighting matrix as proposed by Chan & Dubey (1995) is extended here to include the manipulator's inertia:

$$\mathbf{W}_{ij} = \mathbf{M}_{ij} \qquad \forall\, i \neq j \tag{6.17}$$

$$\mathbf{W}_{ii} = \begin{cases} \mathbf{M}_{ii} + |d(q_i)| & \text{for} \Delta d(q_i) > 0 \\ \mathbf{M}_{ii} & \text{otherwise} \end{cases}, \tag{6.18}$$

where $d(q_i),\ i \in \{1, ..., n\}$ is the cost function which grows to infinity near joint limits. This slows down joints approaching their limits, and permits free movement when moving away from limits. Furthermore, the addition of the inertia matrix will help reduce kinetic energy in the system.

6.4 Case Studies on Fixed Bases

The EJTM method is first applied to manipulators on fixed bases. This is then extended to non-inertial platforms under disturbance, with the combined PJTM method proposed in Chapter 5.

The first scenario in this section involves a manipulator lifting and moving a heavy object. The manipulator must work against gravitational forces when raising the object, but also maintain a steady descent when lowering it (Fig 6.1). Additionally, the object is inertially couped with the manipulator and hence the momentum of the object must also be managed by the manipulator as it moves.

The second scenario involves a simulation of robotic high-pressure blasting. As per Paul et al. (2010), a nozzle is attached to the end-effector for directing either grit for sand-blasting, or high-pressure water in the case of the SPIR. The manipulator must exert forces at the nozzle equal-and-opposite to the reaction forces produced by the high-velocity fluids exiting the nozzle. In addition, the wrench denoting these forces is constant with respect to the end-effector frame. Thus, the wrench with respect to the origin frame of the manipulator is continually changing as the manipulator redirects the fluid stream for cleaning a surface.

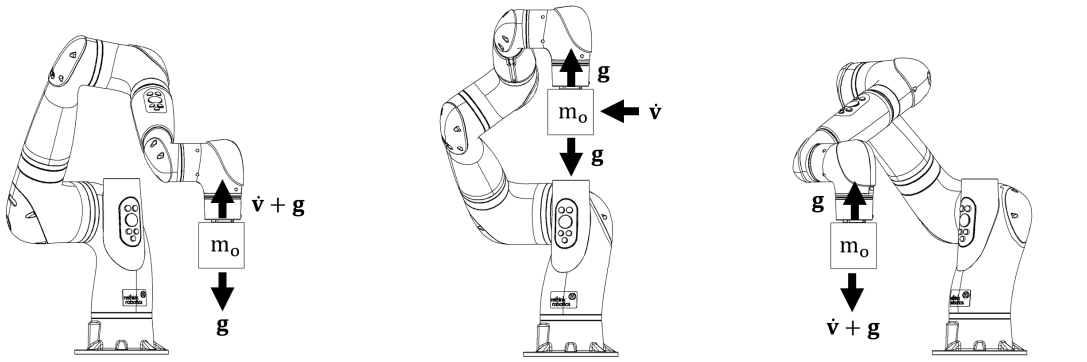

(A) Lifting a heavy object. (B) Lateral motion. (C) Lowering a heavy object.

FIGURE 6.1: The manipulator must overcome gravitational forces when lifting and lowering the object, but must also account for the object's momentum.

6.4.1 Torque Minimization for Heavy Lifting

In this first case study, a kinematic and dynamic model of the 7DOF Sawyer robot from Rethink Robotics is simulated. Physical properties of the manipulator are given in Table 6.1.

The task requirement here is to lift a heavy object 600mm, move it 800mm laterally, then lower it back down. The wrench on the end-effector is computed as:

$$\mathbf{w} = \begin{bmatrix} m_o(\dot{\mathbf{v}}_o + \mathbf{g}) \\ \mathbf{H}_o\dot{\boldsymbol{\omega}}_o + \dot{\mathbf{H}}\boldsymbol{\omega}_o \end{bmatrix}, \tag{6.19}$$

where:

- $m_o = 5$kg is the mass of the object,
- $\mathbf{g} \in \mathbb{R}^3$ is the gravitational acceleration in the origin frame,
- $\dot{\mathbf{v}}_o \in \mathbb{R}^3$ is the linear acceleration of the object,
- $\boldsymbol{\omega}_o,\ \dot{\boldsymbol{\omega}}_o \in \mathbb{R}^3$ is the angular velocity and acceleration of the object, and
- $\mathbf{H}_o,\ \dot{\mathbf{H}}_o \in \mathbb{R}^3$ is the inertia matrix for the object.

If the object is moving slow enough Eqn. (6.19) reduces to:

$$\mathbf{w} = \begin{bmatrix} m_o\mathbf{g}^T & \mathbf{0}_{1\times 3} \end{bmatrix}^T. \tag{6.20}$$

TABLE 6.1: Physical properties of the Sawyer manipulator

	Joint No.						
	1	2	3	4	5	6	7
Link Mass (kg)	5.3	4.5	1.7	2.5	1.1	1.6	0.3
Max. Joint Torque (N)	80	80	40	40	9	9	9

Having said that, the full dynamic calculations in Eqn. (6.19) can be computed without too much extra effort. Since this wrench is specified in the origin frame $\{0\}$, the rotation matrix in Eqn. (6.9) and Eqn. (6.10) is the identity matrix $\mathbf{R} = \mathbf{I}_6$. The partial-derivative is then $\partial\mathbf{R}/\partial\mathbf{q} = \mathbf{0}_{6\times6\times7}$.

The proposed control method was compared against WLN derivation with null space damping in Eqn. (68). Details of the feedback control gains and weighting parameters are given in the Table 6.2.

TABLE 6.2: Control parameters in the heavy-lifting scenario.

	Parameter						
	$\mathbf{K}_\mathrm{p}$	$\mathbf{K}_\mathrm{i}$	$\mathbf{K}_\mathrm{v}$	$\mathbf{K}_\omega$	α	β	γ
WLN Method	30	0	12	12			0.2
EJTM Method	30				0.8	0.1	0.0

Results: The heavy lifting simulation was conducted using the WLN method as a baseline comparison to the EJTM method developed in this chapter. The norm of the joint torques are plotted in Fig. 6.2. The results of this simulation show that the proposed method can successfully minimize the joint torques against an external wrench acting on the manipulator.

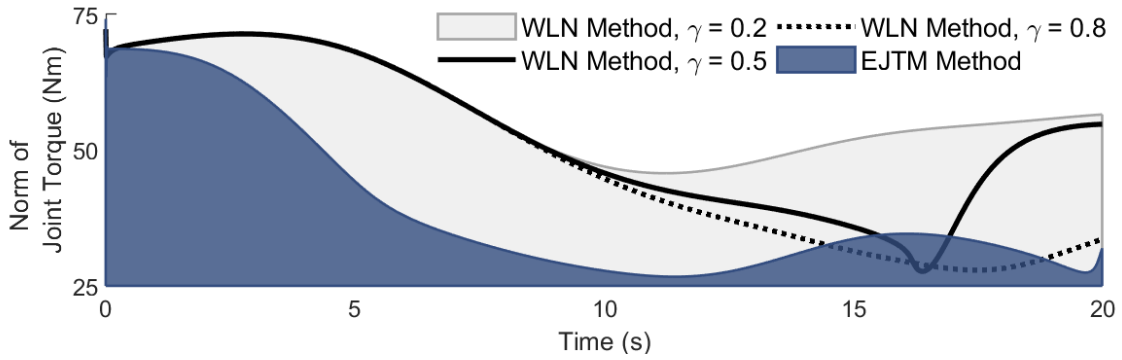

FIGURE 6.2: The proposed torque minimization method can reduce the torque required for heavy lifting by reconfiguring the redundant portion of the manipulator.

The WLN method was first run with a null space damping coefficient of $\gamma = 0.2$, then $\gamma = 0.5$, and finally $\gamma = 0.8$. It can be seen in Fig. 6.2 that progressively increasing the null space damping further reduces the joint torque required for the heavy lifting task. However, the EJTM method still has better performance overall.

Although the WLN method sometimes reduces the total joint torque over the proposed control method, it does not always obey joint constraints. A plot of the joint angles are shown in Fig. 6.4 for the case where $\gamma = 0.5$. It can be seen that the WLN method violates limits for joint 3 at approximately 18s. This effectly negates any reduction in joint torque performance as such a maneouvre is physically impossible on the real system. In contrast, the proposed method incorporated joint limit avoidance in the control equations. Joints 4 and 5 both come close to their limits, but remain in bounds as intended. These results show that it is possible to both minimize joint torque and obey joint limits simultaneously.

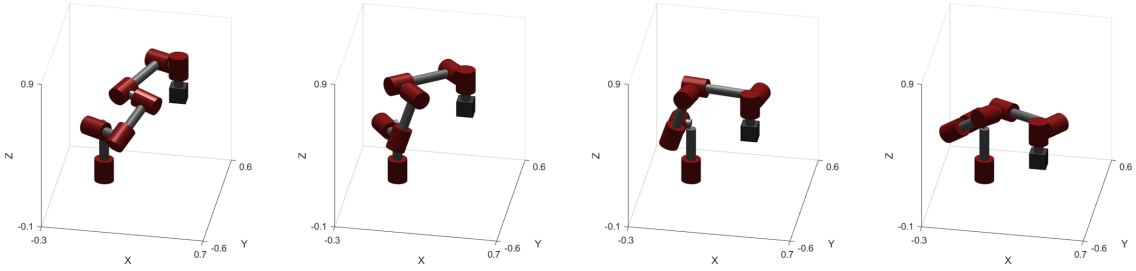

(A) WLN Method.

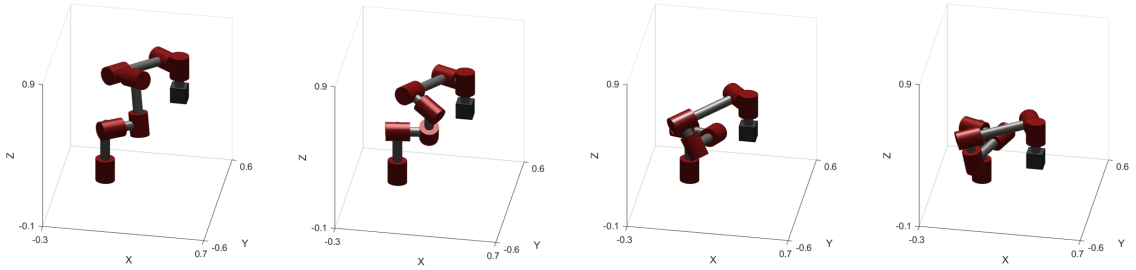

(B) EJTM Method.

FIGURE 6.3: Screenshots of the heavy lifting simulation. Notice that the EJTM method brings joint 3 under the arm to provide support.

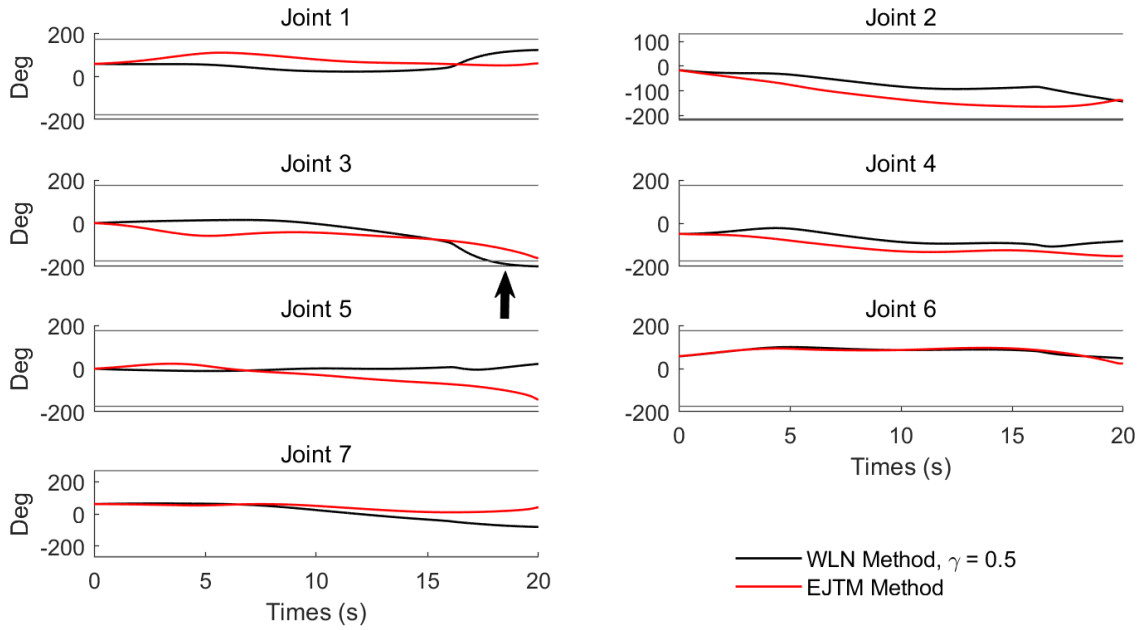

FIGURE 6.4: Joint angles for the heavy lifting scenario. The WLN method violates joint constraints. The EJTM method satisfies constraints and minimizes total joint torque.

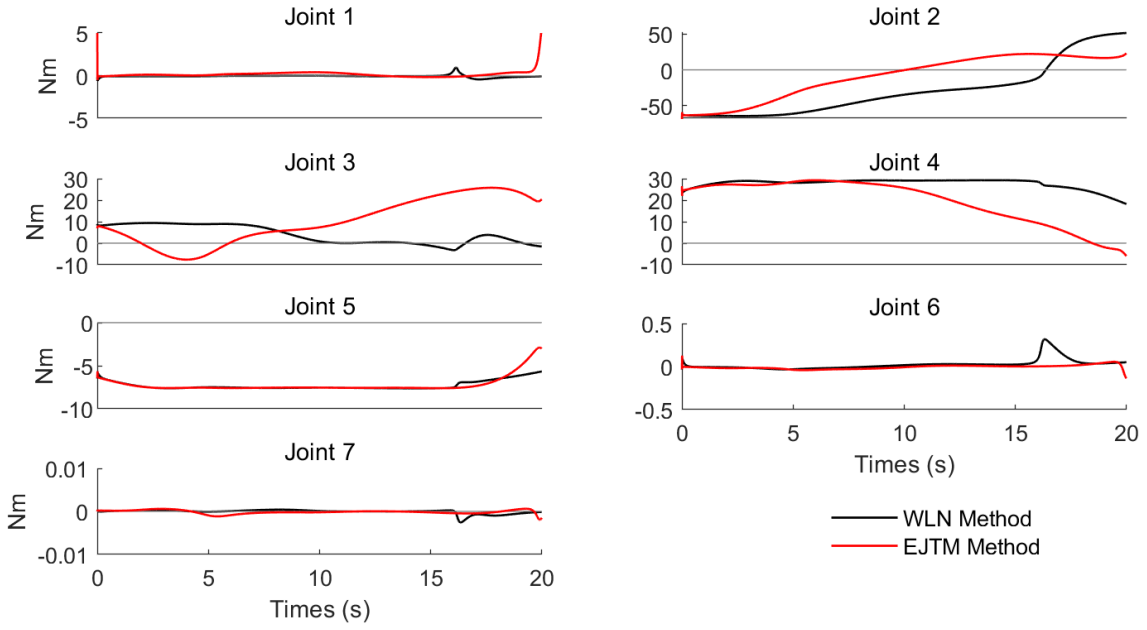

FIGURE 6.5: Joint torques for the heavy lifting scenario.

The joint torque minimization method was also applied to a real Sawyer manipulator with a fixed end-effector pose. The manipulator was first configured in a compliant joint configuration and a PID feedback controller was applied to maintain a fixed end-effector pose. A 3kg block was then placed on the end-effector to see if the manipulator could carry the load. Figure 6.6 shows how the end-effector deflects from the desired pose as the joint torques are overloaded from the external force.

The joint torque minimization method was then applied, with $\hat{\mathbf{w}} = \begin{bmatrix} 0 & 0 & 1 & 0 & 0 & 0 \end{bmatrix}^{\mathrm{T}}$, meaning the manipulator should reconfigure itself to minimize joint torques from forces in the z-axis of the base frame. Figure 6.7 shows how the proposed control method enables the manipulator to autonomously reconfigure itself whilst maintaining the end-effector constraint. The 3kg block was then placed on the end-effector again. This time, the joint torques did not saturate and the end-effector did not deflect. The proposed control method successfully found a joint configuration to minimizes joint torques from forces on the end-effector.

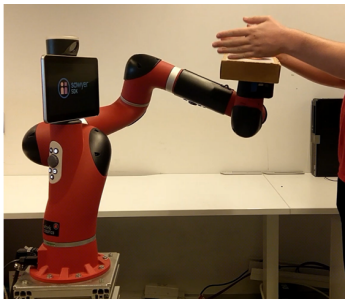

FIGURE 6.6: A 3kg load on the end-effector overloads the joint torques in a sub-optimal joint configuration

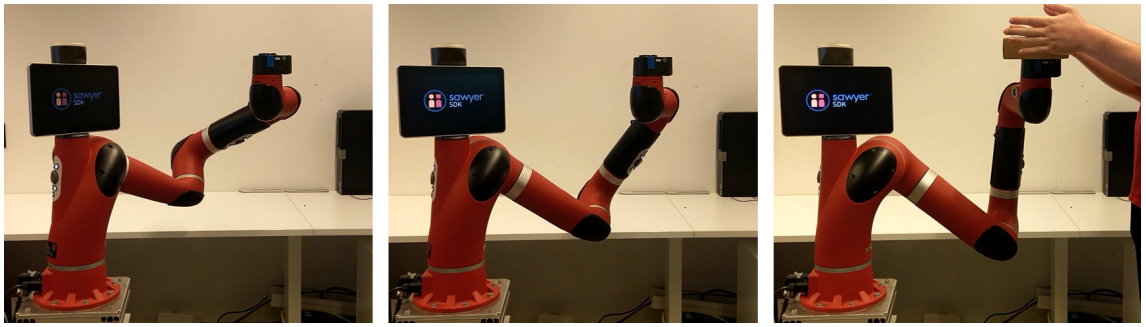

FIGURE 6.7: The manipulator autonomously reconfigures itself to a stiff posture, and is now able to support the 3kg weight.

6.4.2 Torque Minimization for High-Pressure Blasting

Outline In this case study, the problem of high-pressure blasting is studied. The grit-blasting robot project used a 6DOF manipulator for cleaning the surface of steel bridge structures (Paul et al., 2010, Liu et al., 2014). The previous version of the SPIR featured a cable-driven, 6DOF manipulator, whereas the latest version has a 3DOF manipulator. For this chapter, a 6DOF manipulator is considered due to its ability to achieve a task in $\mathbb{SE}(3)$.

To obtain redundancy in the system, the task requirements for high-pressure blasting are exploited. A nozzle is mounted on the 6th link of the manipulator (i.e., the end-effector), in which the nozzle outlet can be considered coincident with frame $\{6\}$ in the kinematic model (Fig. 6.9a). The manipulator is then required to direct the fluid stream at a point on a surface with a precise offset distance for optimal cleaning. Therefore, it is convenient to denote a virtual end-effector that is offset from frame $\{6\}$ at the optimal cleaning distance (Fig. 6.8a). The angle of attack with respect to the cleaning surface also permits some leniency. As such, a virtual ball joint, which has 3DOF, can be appended to the model (Fig. 6.8b). This brings the total system to 9DOF. Another advantage here is that the approach angle of the working fluid can also be controlled using this construction.

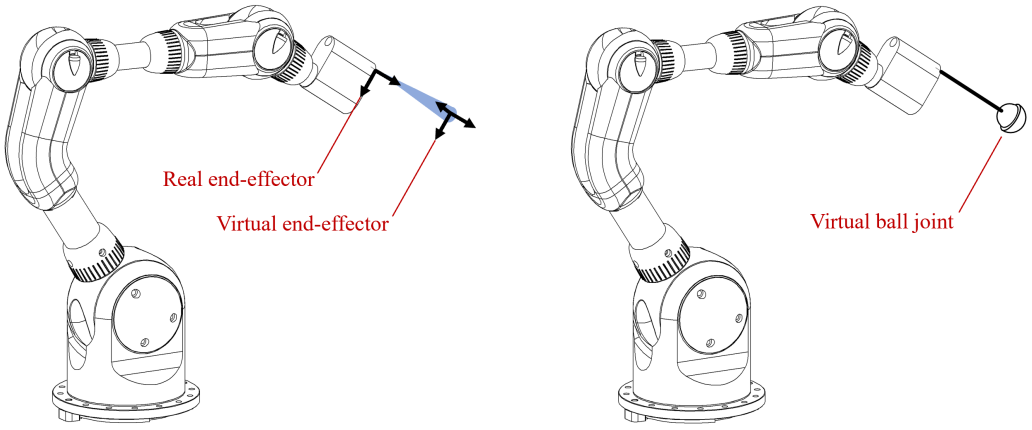

(A) A virtual end-effector can be placed at the desired blasting distance.

(B) A virtual ball joint coincident with the virtual end-effector.

FIGURE 6.8: A virtual end-effector with a virtual ball joint can be appended to the model to permit control over the blasting angle, and add redundancy to the system.

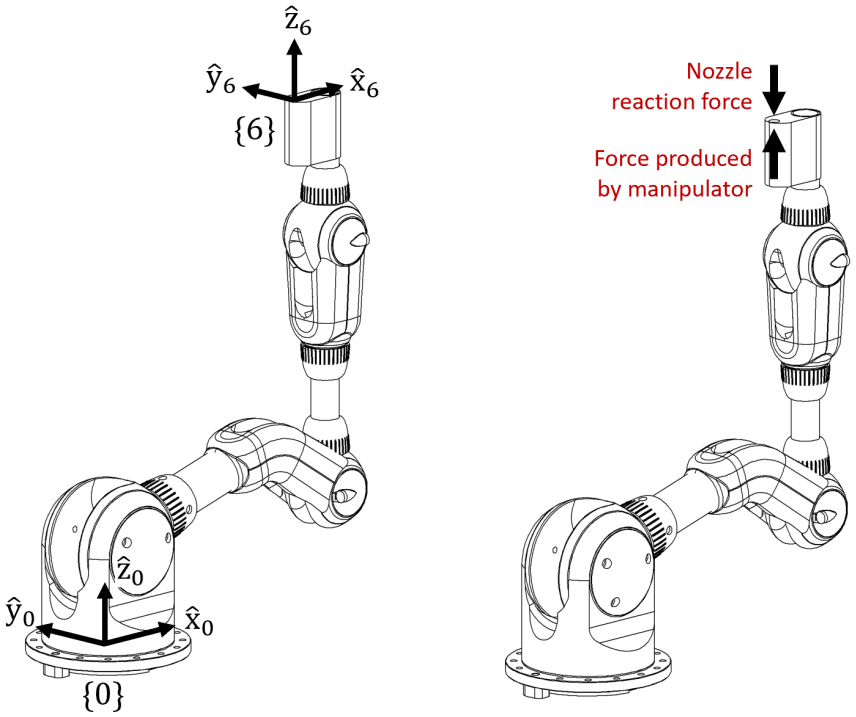

(A) Base frame {0} and real end-effector frame {6}.

(B) Forces on the end-effector.

FIGURE 6.9: Nozzle reaction forces are referenced in frame {6} for blasting.

It should also be noted that since the nozzle outlet is specified as frame {6}, the wrench on the end-effector $\mathbf{w}$ also acts in {6}. The manipulator must apply 25N along the z-axis in the direction of the fluid stream (Fig. 6.9b). This is 5 times greater than the advertised payload capacity for the igus Robolink of 5kg (4.9N) (igus.com, 2018).

$$\mathbf{w} = \begin{bmatrix} 0 & 0 & 25 & 0 & 0 & 0 \end{bmatrix}^{\mathrm{T}}. \tag{6.21}$$

Also, the virtual ball joint has no effect on the direction of these reaction forces as they are all coincident about the same axis. The rotation matrix for the dynamic model (Eqn. (6.1)) is then:

$$\mathbf{R} \triangleq \begin{bmatrix} \mathbf{R}_0^6 & \mathbf{0}_{3\times3} \\ \mathbf{0}_{3\times3} & \mathbf{R}_0^6 \end{bmatrix}, \tag{6.22}$$

with $\mathbf{R}_0^6 \in \mathbb{SO}(3)$ available from the forward kinematic chain of the manipulator.

For this case study, the igus Robolink manipulator that was used on SPIR v2.0 is simulated. The physical properties of this manipulator are listed in the Table 6.3.

TABLE 6.3: Physical properties of the igus Robolink manipulator

	Joint No.					
	1	2	3	4	5	6
Link Mass (kg)	0.57	0.87	0.12	0.27	0.12	0.35
Max. Joint Torque (N)	10	20	12	5	12	5

Joints 7, 8, and 9 are virtual and hence have no mass. As such, $\text{rank}(\mathbf{M}) = 6$ and cannot be inverted for the weighted joint solutions. For the WLN method, the inverse of the matrix can be defined as:

$$\tilde{\mathbf{M}}^{-1} = \begin{bmatrix} \mathbf{M}_{\text{R}}^{-1} & \mathbf{0}_{6\times3} \\ \mathbf{0}_{3\times6} & \mathbf{0}_{3\times3} \end{bmatrix}, \tag{6.23}$$

where $\mathbf{M}_{\text{R}} \in \mathbb{R}^{6\times6}$ is the inertia matrix for the real manipulator. This can then be readily substituted in to the weighted joint control equations (Appendix C), and the redundant task Eqn. (6.7).

For the EJTM method, the inverse of the weighting matrix needed for control Eqn. (6.3) and Eqn. (6.4) can be computed as:

$$\tilde{\mathbf{W}}^{-1} = \left(\mathbf{W}^{-1} + \tilde{\mathbf{M}}^{-1}\right)^{-1} \tag{6.24}$$

The task requirement in the blasting process is for the manipulator to trace a rectangle within its workspace 300mm wide and 150mm tall. In doing so, the initial and final poses of the end-effector are identical. It is expected that using the proposed control method, the manipulator will autonomously reconfigure its joint to reduce the total joint torque once it returns to the start point of the trajectory. The control parameters for the blasting scenario are given in Table 6.4.

TABLE 6.4: Control parameters for the high-pressure blasting scenario

	Parameter					
	$\mathbf{K}_{\text{p}}$	$\mathbf{K}_{\text{v}}$	$\mathbf{K}_{\omega}$	α	β	γ
WLN Method	30	12	12			0.2
EJTM Method	30	12	12	10	1	0.0

Results: As with the heavy lifting, the EJTM control method is also able to reduce joint torques for high-pressure blasting. A plot of the norm of joint torques is given in Fig. 6.10 which shows how once more, optimizing the joint configuration against external forces can outperform the WLN method. In this scenario, increased the damping coefficient γ had little effect on the results. Likewise, increasing α or γ for the proposed control method did not drastically alter the performance. This is likey due to the fact that the inertia of the manipulator is quite small in comparison to the torques imposed by the wrench on the end-effector; $\|\mathbf{M}\ddot{\mathbf{q}} + \boldsymbol{\tau}_c\| \ll \|\mathbf{J}^T\mathbf{R}\mathbf{w}\|$.

Also, by examining the individual joint torques, it can be seen that the WLN method violates the capacity for joint 4 (Fig. 6.12). In contrast, the proposed control method is able to reduce the torques and keep all of them within limits. The reason for this behaviour is due to the fact that the WLN method equates to a local minimization of the joint torques. Because of this, it sometimes leads to joint configurations that exacerbate the effects of the wrench. In contrast, by optimising for the proposed cost function Eqn. (6.5), the manipulator is continuously working towards a locally optimal joint configuration.

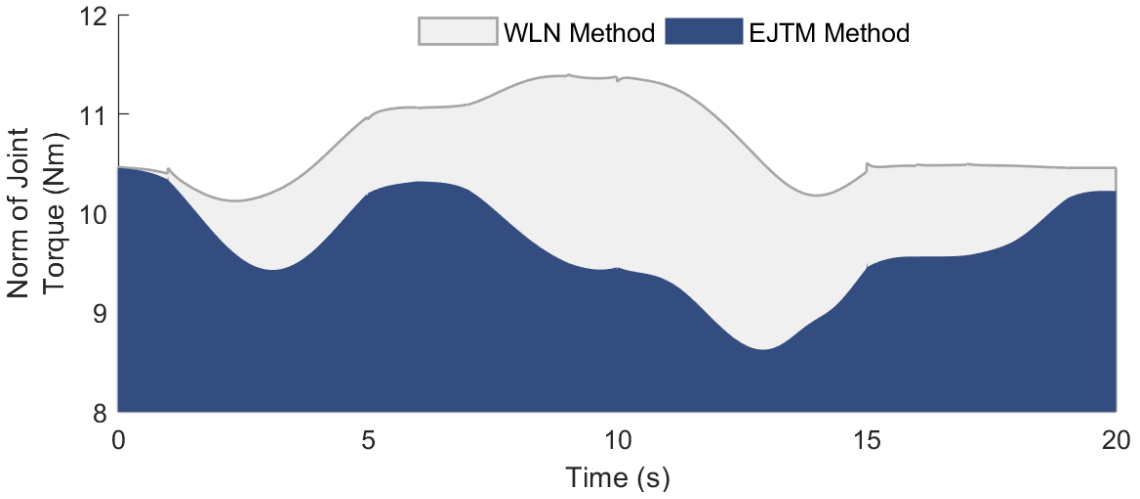

FIGURE 6.10: Using the proposed control method, the total joint torques required are reduce for high-pressure blasting.

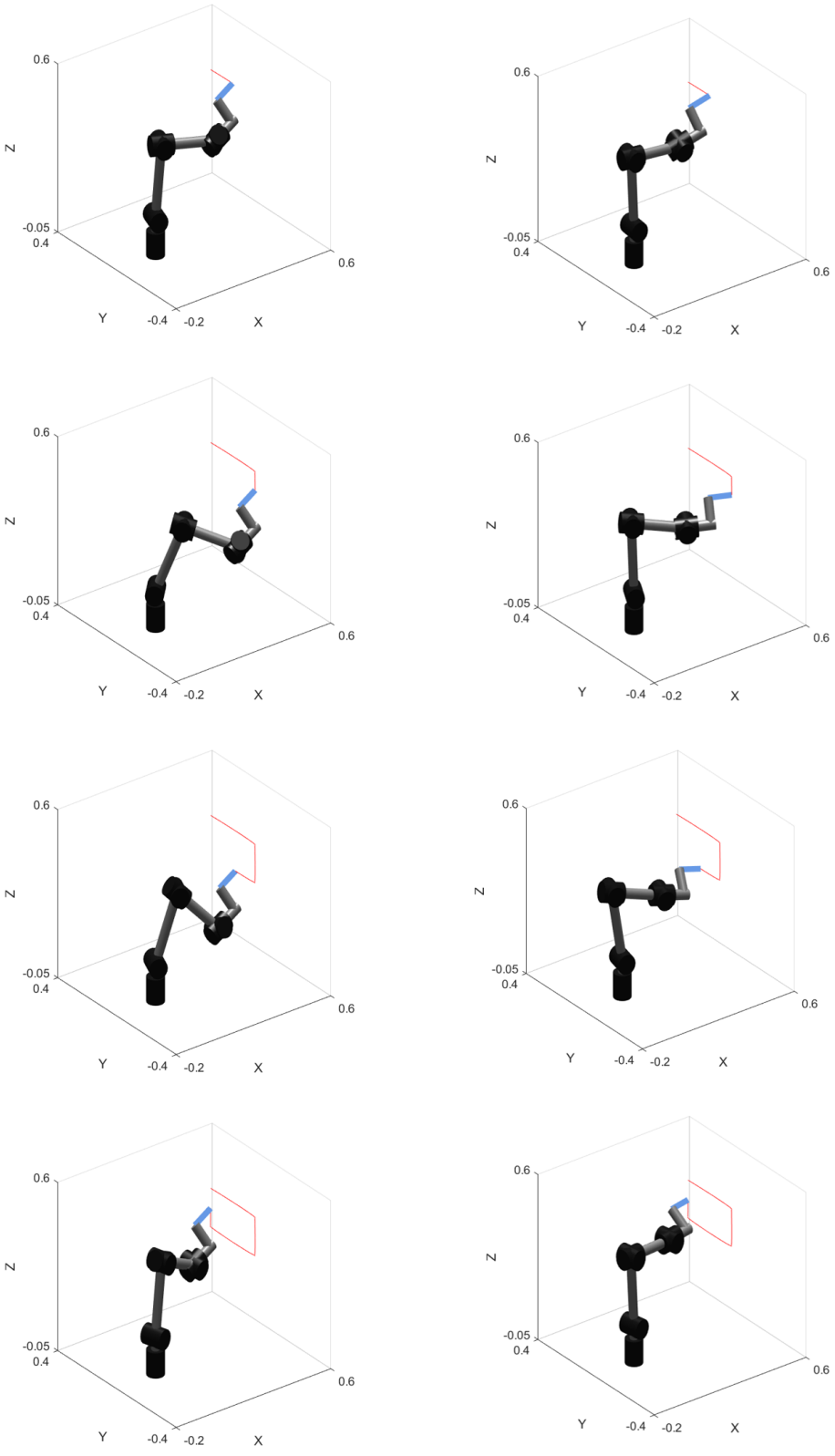

(A) WLN Method.

(B) EJTM Method.

FIGURE 6.11: Screenshots of the high-pressure blasting simulation.

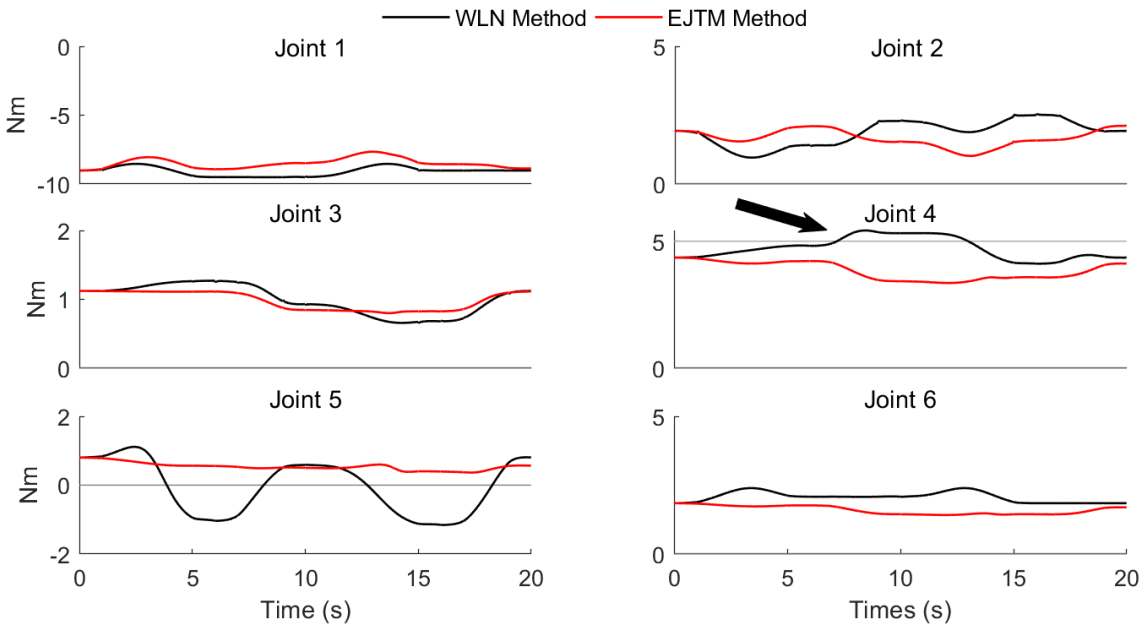

FIGURE 6.12: The proposed control method is able to keep all joint torques within limits, even with large payload forces. The WLN method violated the torque limit for joint 4.

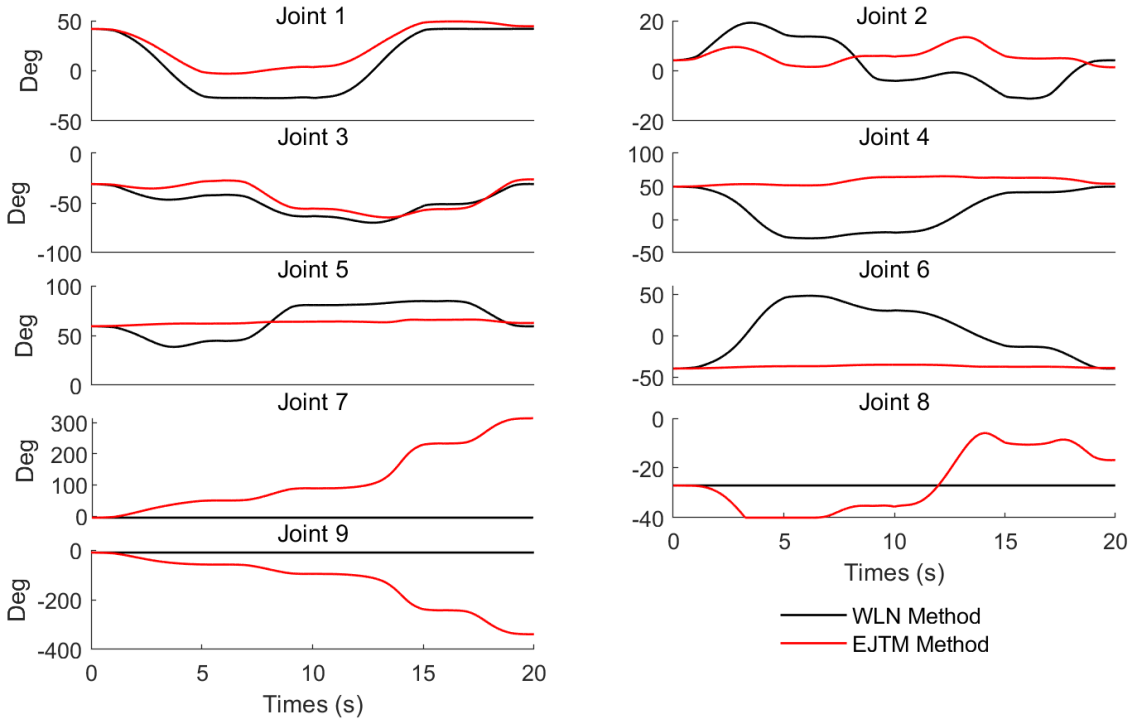

FIGURE 6.13: The proposed method is able to satisfy joint constraints, even for the virtual joints in the model.

6.5 Case Study With A Moving Base

Outline: Having shown that it is possible to minimize joint torque with large external forces for a manipulator on a fixed base, the problem is now extended to a moving base example. In this scenario, the 7DOF Sawyer manipulator is simulated tracking a trajectory whilst holding an object of 3kg in mass. The end-effector control equations are the same as Eqn. (**??**) where the effects of the base motion must be accounted for. The acceleration level equation for the redundant task is now extended to include the joint torques induced by the base motion:

$$\ddot{\mathbf{q}}_{\mathrm{r}}(\mathrm{t}) = \Delta \mathrm{t}^{-1}\big(\dot{\mathbf{q}}_{\mathrm{r}}(\mathrm{t}) - \dot{\mathbf{q}}_{\mathrm{r}}(\mathrm{t}-\Delta\mathrm{t})\big) + \beta \mathbf{M}^{-1}\big(\Delta\bar{\boldsymbol{\tau}}_{\mathrm{g}} - \boldsymbol{\tau}_c - \boldsymbol{\tau}_{\mathrm{b}} - \mathbf{J}^{\mathrm{T}}\mathbf{R}\mathbf{w}\big) - \gamma\dot{\mathbf{q}}, \tag{6.25}$$

where $\Delta\bar{\boldsymbol{\tau}}_{\mathrm{g}}$ is the torque due to the average predicted change in gravitational forces, and $\boldsymbol{\tau}_{\mathrm{b}}$ is the joint torques caused by the base motion (Chapter 5).

For this case study, three different scenarios are considered:

1. The WLN method for torque minimization,
2. The EJTM method developed in this chapter,
3. The EJTM method combined with the PJTM method proposed in Chapter 5.

The parameters used in the simulation are given in the Table 6.5. As with the moving base simulations in Chapter 5 the base motions here is generated using IMU data collected from an AUV, albeit with a different sample. A plot of the base position and orientation over time can be seen in Fig. 6.14.

Table 6.5: Control parameters for torque minimization with external forces and moving base.

	Parameter					
	$\mathbf{K}_{\mathrm{p}}$	$\mathbf{K}_{\mathrm{v}}$	$\mathbf{K}_{\omega}$	α	β	γ
WLN Method	30	12	12			0.2
EJTM Method	30	12	12	0.8	1	0.2
EJTM + PJTM	30	12	12	0.8	1	0.2

Results: The norm of the joint torques for the three different scenarios are plotted in Fig. 6.15. As with the heavy-lifting scenario on a fixed base, the proposed method of torque minimization is still able to successfully reduce the total torque even with base disturbances. Furthermore, marginal gains are made by including the gravity prediction term from Chapter 5. Although, this time, increasing the forecast horizon did not appear to improve the results as it did in the previous chapter. The reason for this is not entirely clear. It is likely that the term in Eqn. (6.16) which relates to optimizing the cost function Eqn. (6.7) outweighs the other components. It also it appears that small reductions in joint torque from the gravity prediction term accrue over time. Performance results only begin to diverge after 15 seconds, with the largest differences occuring toward the end of the simulation. This was also the case for the results in Chapter 5.

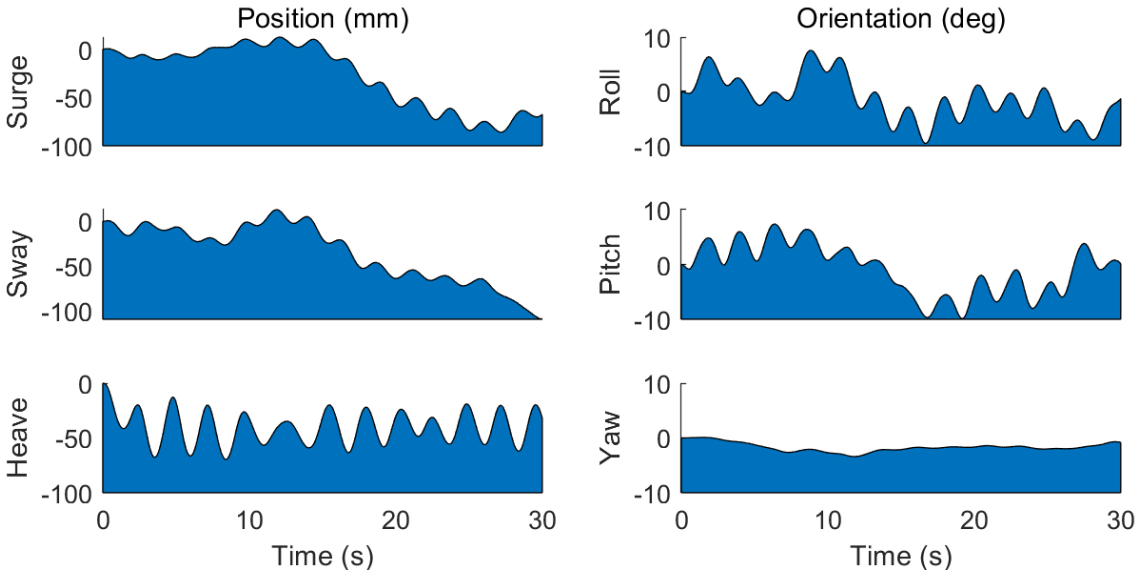

FIGURE 6.14: Base motion for the torque minimization with added end-effector forces, generated from IMU data of an AUV in waves.

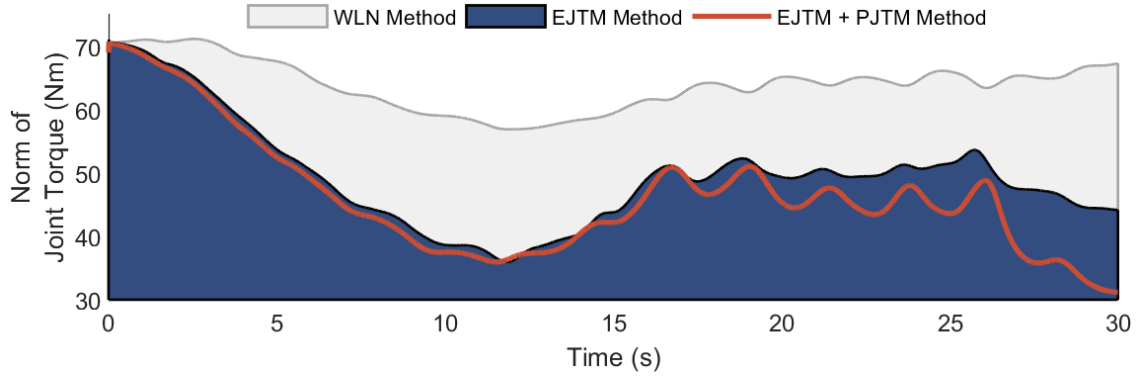

FIGURE 6.15: Torque minimization with large payload forces can still be gauranteed even with base motion disturbance.

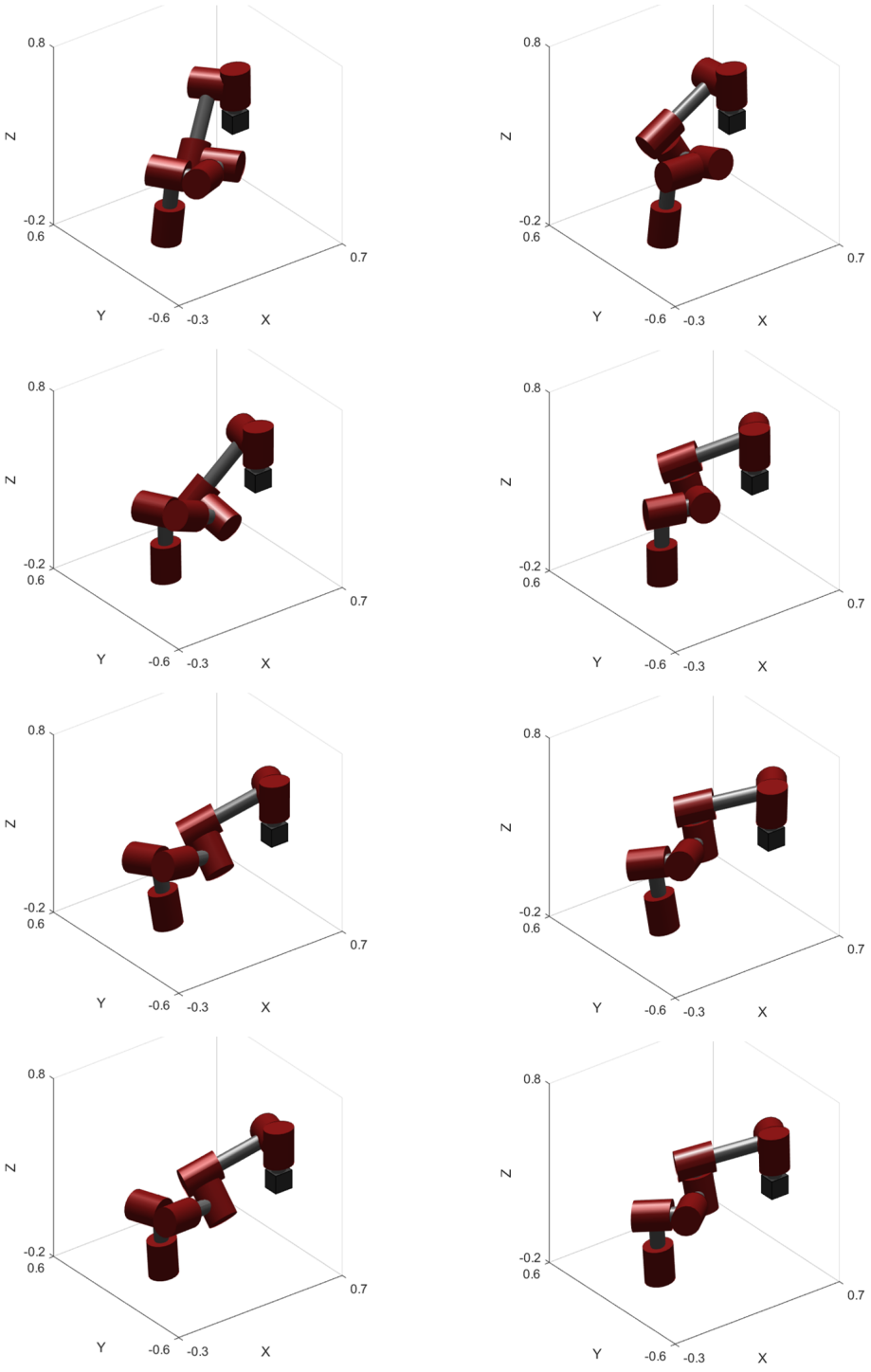

(A) WLN Method.

(B) EJTM + PJTM Methods.

FIGURE 6.16: Screenshots for the weight lifting with moving base simulation.

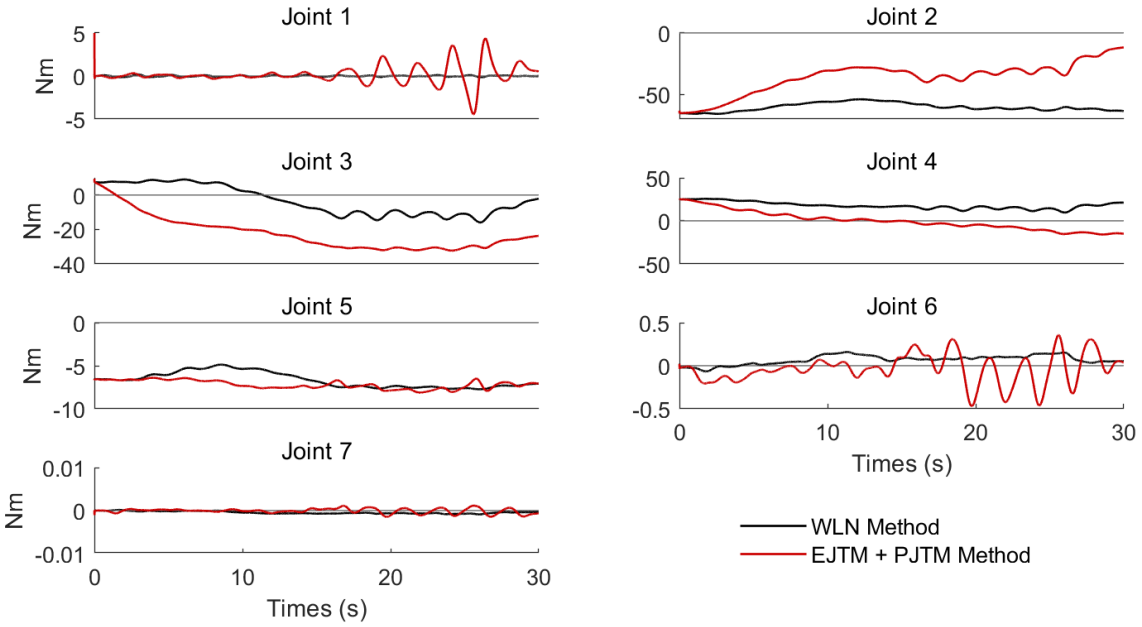

FIGURE 6.17: Individual joint torques for the heavy lifting scenario with moving base.

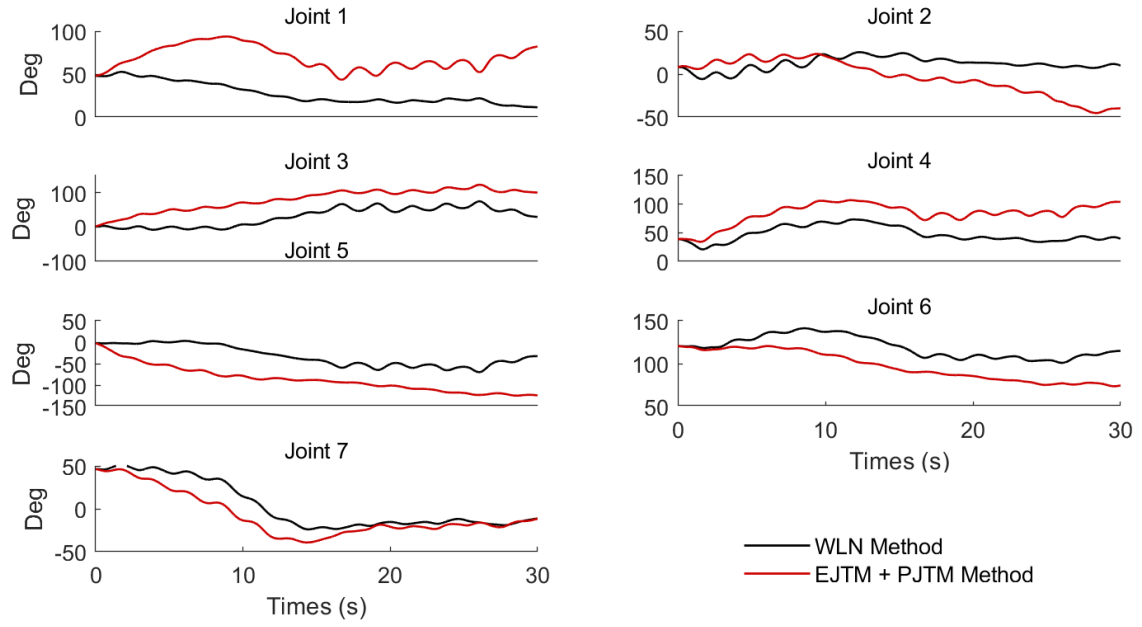

FIGURE 6.18: Individual joint angles with large payload forces and moving base disturbances.

6.6 Discussion

6.6.1 Choice of Control Parameters

The control equations used in this chapter for torque minimization featured 3 different scalars to weight the different components of the control equations:

- α was used to weight the magnitude of the gradient vector in Eqn. (6.11),
- β was used to weight the dynamic torque minimization component in Eqn. (6.16) and Eqn. (6.25), and
- γ was used to weight the null space damping in Eqn. (6.25).

These parameters and their respective control components have complex interactions. For instance, increasing α increases the speed at which the manipulator will reconfigure itself and reduce the torques caused by the wrench $\mathbf{w}$. However, this will increase the dynamic torque component which may be undesirable. The β coefficient can be used to reduce dynamic torques, but if this is too high this may interfere with the ability of the manipulator to reduce the torque component $\mathbf{J}^{\mathrm{T}}\mathbf{R}\mathbf{w}$. In these simulations, $\|\mathbf{J}^{\mathrm{T}}\mathbf{R}\mathbf{w}\| \gg \|\boldsymbol{\tau}_{\mathrm{c}}\|$, and hence β was kept relatively small. How they ineract and how best to balance them may be a point of future research. Lastly, the damping coefficient γ was only introduced for the moving-base scenario. The base motion introduces torques to the manipulator, and hence kinetic energy (Eqn. (**??**)). It was found this parameter was a necessity for stability, even when applying Eqn. (6.4) which is otherwise stable on a stationary base. Ideally, this term should be minimal so as not to interfere with the torque optimization, but large enough to negate high-kinetic energy build up.

6.6.2 Considerations and Limitations

In the case studies presented, the joint torques produced by the wrench were assumed to be the dominant term in Eqn. (6.1). That is, $\|\mathbf{J}^{\mathrm{T}}\mathbf{R}\mathbf{w}\| \gg \|\mathbf{M}\ddot{\mathbf{q}} + \boldsymbol{\tau}_{\mathrm{c}}\|$. However, this may not always be the case for smaller payload forces, or manipulators with large inertia. In this case, the WLN with null space damping may be sufficient. It may also be possible to apply dynamic coefficients for α and β that account for the relative magnitude of the torque components to achieve optimal results. This could warrant further research.

In the heavy lifting case study with a steady base, the payload wrench was 1.25 times greater than the manipulator's advertised payload capacity. And for the blasting scenario, the forces were 5 times greater than the advertised payload capacity. In both scenarios, the EJTM method was able to reduce the joint torque below their maximum capacity, even when the manipulator was performing beyond its operational limits. One one had, this demonstrates the efficacy of the proposed method.

However, this kind of performance result cannot be gauranteed for every situation. For one, the end-effector task must be specified well within the manipulator's workspace to afford a multitude of feasible joint configurations. This is also constrained by the amount of redundancy in the manipulator, and the span of the upper and lower joint limits to allow for multiple joint combinations. The simulation of the igus robolink manipulator performed well in this respect, as the joint limits are quite constrained. But this was aided by the additional 3DOF from the task requirements. Additionally, the redundant task, Eqn. (6.9) locally optimises the joint configuration. Hence there is no gaurantee that the best possible joint configuration will be found at any given time. Nevertheless, with reasonable demands on the manipulator, good results can be achieved as was demonstrated in the simulations.

6.6.3 Relationship to Cartesian Stiffness Control

Cartesian stiffness control is a method for regulating the deflection of the end-effector of a manipulator when subject to external forces (Choi & Chung, 1994; Ang & Andeen, 1995; Li & Kao, 2004; Ajoudani et al., 2015; Gasparri et al., 2016). Typically, a desired Cartesian stiffness is designed which denotes how much the end-effector will deflect given forces imposed on it. A subsequent joint configuration can then be optimized in order to try and satisfy it. This can be done for a fixed joint configuration (Gasparri et al., 2016), or using a null space optimization method if the manipulator is redundant [**?**] (Ajoudani et al., 2015).

In this chapter, the objective was to minimize joint torques given external forces acting on the manipulator. However, by examining the mathematical equations between the two methods, it can be seen that this proposed method is also indirectly optimising the Cartesian stiffness. The Cartesian stiffness matrix, $\mathbf{K}_\mathrm{c} \in \mathbb{R}^{\mathrm{m}\times\mathrm{m}}$ maps deflections of the end-effector to a wrench:

$$\Delta\mathbf{w} = \mathbf{K}_\mathrm{c}\Delta\mathbf{x}. \tag{6.26}$$

Likewise, deflections in the joint positions are related to the (static) joint torques via the joint stiffness matrix:

$$\Delta\boldsymbol{\tau} = \mathbf{K}_{\mathrm{q}}\Delta\mathbf{q}. \tag{6.27}$$

Using the wrench-torque relationship $\boldsymbol{\tau} = \mathbf{J}^{\mathrm{T}}\mathbf{w}$, Eqn. (6.26) and Eqn. (6.27) can be combined to form:

$$\mathbf{K}_{\mathrm{q}}\Delta\mathbf{q} = \mathbf{J}^{\mathrm{T}}\mathbf{K}_{\mathrm{c}}\Delta\mathbf{x}. \tag{6.28}$$

Then using the kinematic relationship $\dot{\mathbf{x}} = \mathbf{J}\dot{\mathbf{q}}$, it can be seen that:

$$\mathbf{K}_{\mathrm{q}}\Delta\mathbf{q} = \mathbf{J}^{\mathrm{T}}\mathbf{K}_{\mathrm{c}}\mathbf{J}\Delta\mathbf{x} \tag{6.29}$$

$$\mathbf{K}_{\mathrm{q}} = \mathbf{J}^{\mathrm{T}}\mathbf{K}_{\mathrm{c}}\mathbf{J}. \tag{6.30}$$

This equation can be used to solve the necessary joint stiffness given a desired Cartesian stiffness. It can be seen from Eqn. (6.27) that:

$$\partial\boldsymbol{\tau}/\partial\mathbf{q} = \mathbf{K}_{\mathrm{q}}. \tag{6.31}$$

This relationship can be substituted in to Eqn. (6.9) which yields:

$$\nabla \mathrm{c}(\mathbf{q}) = \mathbf{K}_{\mathrm{q}}\mathbf{G}\mathbf{J}^{\mathrm{T}}\mathbf{R}\hat{\mathbf{w}}. \tag{6.32}$$

Equation (6.32) can be interpreted as follows:

- $\mathbf{R}\hat{\mathbf{w}}$ gives the direction in which to stiffen the end-effector with respect to the origin frame of the manipulator,
- $\mathbf{J}^{\mathrm{T}}$ maps the forces from the task space to the joint space,
- $\mathbf{G}$ weights the torques, and
- $\mathbf{K}_{\mathrm{q}}$ modulates the result by the current joint stiffness.

That is, the redundant task of the proposed control method will increase the joint stiffness against the wrench acting on the manipulator. Both Cartesian stiffness control and the control method derived in this chapter involve optimization via joint stiffness. This warrants further research to gain more insights in to these relationships.

6.7 Conclusion

Robotic manipulators may be required to handle forces beyond their payload capacity when interacting with various objects. And, as mobile robots are further required to conduct intervention tasks in unstructured environments, the ability to minimize joint torque when forces are large or uncertain is desirable. This objective becomes even more relevant for manipulators operating on non-inertial platforms, as they must adapt to disturbances in real time to maintain a suitable joint configuration for the required task. A review of joint torque minimization in literature revealed that the majority is concerned with minimizing the internal dynamic torque of redundant manipulators during self-motion. However, when external forces are incoporporated in to these control equations, these locally optimal solutions may lead to joint configurations that can violate joint torque limits.

To address this problem, this chapter presentd the External Joint Torque Minimization (EJTM) method. Using null space control, a redundant manipulator was reconfigured to reduce the joint torques produced by a wrench acting on the end-effector. Additionally, a term was included to help reduce the local dynamic torque effects. The EJTM method was validated with two case studies: lifting and moving a heavy object, and high-pressure blasting. Results showed that the proposed method can successfully reduce the total joint torque compared to an WLN of the local joint torques.

The EJTM method was also applied to a moving-base scenario. The base motion was generated from IMU data collected from an AUV under wave excitation. The simulation results showed that this method is robust enough to be applied to a mobile manipulator with unwanted base motion disturbance. Furthermore, the PJTM method proposed in Chapter 5 can be easily integrated with the EJTM method and reduce joint torques even further.

Chapter 7

Conclusions

This thesis has presented several control methods for manipulators operating on moving bases subject to unwanted disturbances. Current state of the art in mobile manipulation is limited to situations in which base motion has minimal impact on the manipulator dynamics and kinematics. This is often because a vehicle is used to drive the manipulator, which can help provide support. Or, in the case of rovers and land vehicles, the ground provides a rigid platform from which to conduct intervention tasks.

However, there are many scenarios in which the natural environment may impose disturbances on the manipulator base that cannot be negated. This can cause displacement of the end-effector, and introduces inertial forces in the manipulator itself. Both factors may make it difficult to perform accurate intervention tasks. Conventional control methods may either be inadequate or inefficient in at compensating for these kinematic and dynamic disturbances.

It was posited that, by anticipating these base motion disturbances, a mobile manipulator could act in advance to help negate these effects. A novel predictive control method was thus developed that allowed the manipulator to perform predictive end-effector control (PEEC). This method improved trajectory tracking performance over an PID feedback controller.

Moreover, by using a redundant manipulator, a control method was developed for predictive joint torque minimization (PJTM). This method allowed the manipulator to use the inertial forces produced by the base motion to reduce joint torque required for trajectory tracking and disturbance compensation. Forecasts of said motion were also used to predict the change in the gravitational forces, which further reduced the total joint

torques. A novel control method was also proposed to reduce joint torques required to conduct manipulation tasks with large payload forces applied to the end-effector. This external joint torque minimization (EJTM) method was shown to reduce the effort required for weightlifting and high-pressure blasting. This was then synthesized with the PJTM method to reduce joint torque requirements for manipulation of a heavy load with unwanted base motion.

The control methods developed in this thesis can enabled mobile manipulators operating in difficult environments to perform intervention tasks more accurately and efficiently.

7.1 Summary of Contributions

7.1.1 Comparison of Forecasting Models

Many different forecasting methods have been applied successfully to predictive control strategies across different fields. However, there is little consensus across the literature about which prediction method is apt for motion prediction. A systematic comparison was made between time series, Fourier series, and GPR using IMU data from 2 AUVs as a case study.

The results of the statistical analysis on the prediction accuracy and forecast uncertainties revealed that:

- GPR had better short-term forecast accuracy than either time series or Fourier series. This presents a potential new method for marine vessel motion prediction in waves and may improve the performance of predictive control strategies in the field.
- Time series was overconfident in the forecast uncertainty. Often, motion planning and predictive control strategies weight the variables by the state uncertainty. This discovery could affect the robustness of said methods. Manual inflation of the uncertainty should be considered if this method were to be applied in practice.
- Fourier series had large uncertainty bounds and was also poor at forecasting periodicity in the data. This superposition of sinusoids is standard for wave theory, and thus employed in many planning and control strategies for ships and AUVs. However, both time series and GPR may be better alternatives.
- The size and shape of the vessel changed the statistical properties of the IMU data, despite being recorded under similar external conditions. The three methods tested

in this chapter provided sound results for one of the AUVs, and not the other. This reinforces the need to perform adequate statistical modelling and analysis before deciding on a prediction model.

7.1.2 Predictive Control of Manipulators on Moving Platforms

A novel predictive control method was developed that allowed for a mobile manipulator to proactively manoeuvre itself to negate unwanted base motion. By forecasting the base motion, a desired end-effector trajectory in the inertial or fixed frame was transformed to an equivalent trajectory in the predicted base frame of the manipulator. Then, a QP problem was devised for the end-effector control to track this trajectory across a finite prediction-control horizon. Kinematic constraints on the manipulator control were only placed on the first control action in the predicted control sequence. This allowed for linear inequality constraints to be implemented, and fast solutions for the optimisation for real time control.

This predictive end-effector control (PEEC) method was verified through both simulation and experiment. The results showed that tracking error of the end-effector could be reduced by 60% compared to a PID feedback controller. Remarkably, this improvement was still achieved when the control signal using the proposed method had to be reduced by 40%. Simulation results also showed that this method could simultaneously satisfy joint limitations and reduce tracking error by using the aforementioned linear equality constraint.

7.1.3 Joint Torque Minimization on Moving Platforms

A predictive joint torque minimization (PJTM) method was proposed for redundant manipulators on non-inertial platforms. This enabled a manipulator to use the base motion disturbance to assist with self-motion whilst simultaneously tracking an end-effector trajectory. In addition, predictions of the relative change in gravity with respect to the manipulator's frame of reference were incorporated into the control. In doing so, the manipulator was able to utilize the gravitational forces to further reduce joint torque. The PJTM method was compared to a WLN of the joint torques and shown to reduce the total torque by approximately 25%.

It is also common to derive the dynamic control of a redundant manipulator directly from the acceleration level. This can lead to instability, and several methods to rectify the

problem have been proposed in literature over the decades. However, for this specific problem, the control equations were first defined at the velocity level the differentiated. This was done to ensure stability of the null space control. However, simulations showed this reduced trajectory tracking error of the end-effector under base motion disturbance compared to a PD feedback controller. This warrants further investigation.

7.1.4 Joint Torque Minimization with External Forces

A novel control method was developed that enables a redundant manipulator to reduce joint torque when dealing with large external forces on the end-effector, or EJTM. Many joint torque minimization methods only address the internal dynamics required for self-motion, which could lead to joint configurations that exacerbate the joint torques from external loads. The proposed EJTM method instead uses null space control to optimize the joint configuration to reduce these joint torques, also accounting for the dynamic torque effects. Three different case studies were considered:

- Heavy lifting with a fixed base,
- High-pressure blasting with a fixed base, and
- Heavy lifting with a moving base under disturbance.

The EJTM method was shown to reduce the joint torque requirements compared to a WLN method for all three scenarios. Furthermore, it was robust at minimizing joint torques on a free-moving platform under disturbances. Additional joint torque reduction was also achieved by integrating the aforementioned PJTM method.

7.2 Limitations

7.2.1 Base Motion

As a case study in motion prediction in Chapter 3, IMU data was recorded from 2 different AUVs designed for shallow water intervention tasks. Simulations for the predictive control methods developed in Chapter 4 and Chapter 5 then used different samples of this data to generate base motion disturbance for a mobile manipulator.

This type of motion data is not indicative of all the types of disturbance that might be experienced by a mobile manipulator out in the field. As such, the same performance of

the control methods may not be guaranteed for situations that do not exhibit this type of periodic, stationary data. However, these control methods are agnostic to the type of prediction method used. If a suitable forecasting method can be found for the problem at hand, then the methods developed in this thesis should garner similar performance results.

For example, it was shown in Chapter 3 that the SPIR motion data was nonstationary. All three forecasting methods performed poorly at predicting this data. This rules out Fourier series for any data that does not exhibit periodicity. However, both time series and GPR can be modified to account for this problem. Actually, to this point, no assumptions were made about the nature of the base motion for the experiments in Chapter 4, but the predictive control method still performed better than feedback control. Further refinement of the forecasts based on the specific application may further improve the results.

Another fundamental assumption was that the displacement of the base was bounded, such that the manipulator task was always within its workspace. This might be feasible for manipulators attached to some form of vehicle. However, if the base moves too far from the specified task, the manipulator can stretch out to a singular configuration and lose control. Simple control policies could be implemented to avoid this kind of over-extension. Conversely, if the base moves forward too far, this may cause the manipulator to collide with itself. How this might affect performance, and how it ought to be accounted for will be for future consideration.

7.2.2 Base Inertia and Dynamics

Just as the base motion affects the manipulator due to their inertial coupling, so too does the manipulator movement affect the base. However, for this thesis, the effect the manipulator has on the base was assumed to be negligible. This is not entirely unreasonable, particularly if the inertia of the base is significantly larger than that of the manipulator, or if a vehicle could be controlled to counteract these influences. The simulations used to validate the proposed control methods applied the exact same base motion. In this regard, ignoring the inertial effects on the base allowed for objective results when evaluating the control methods. The experimental results from Chapter 4 also support this assumption.

However, this condition is not always guaranteed, particularly on non-inertial platforms. Other prediction and control methods will need to be developed that account for this inertial coupling between base and manipulator.

7.3 Future Work

7.3.1 Prediction Methods for Nonstationary Data

In Chapter 3, three different prediction methods were applied to the motion data of two different AUVs. The results of the analysis showed that all the methods were much poorer at producing long-term forecasts for the SPIR data. Time series analysis of the data showed that it was nonstationary, which explains these results. Future research could involve extending the prediction methods to nonstationary formats. For instance, the stationary ARMA model could be expanded to Autogression Integrated Moving Average (ARIMA). Likewise, for the GPR, nonstationary kernels could be considered.

7.3.2 Disturbance Predictions

For this thesis, the disturbance to a manipulator was regarded as the unwanted motion of its base. This in turn caused displacement of the end-effector, and dynamic forces in the manipulator structure itself. However, disturbance compensation in the control of AUVs or UAVs is often expressed at the dynamic level. The hydrodynamic effects that the fluid has on the vehicle or manipulator is often difficult to model, and hence statistical observation and adaptive control methods have been developed. However, these adaptive control methods only act on the most recent disturbance estimations. Therefore, dynamic level disturbance prediction and control based on the research in this thesis could be developed for UVMS or UAVMS.

7.3.3 Extension to the Predictive Control Method

For this thesis, the predictive control method for the end-effector of a mobile manipulator was derived at the velocity level. Both simulations and experiments showed a successful improvement in pose error compared to a PID feedback controller. The control signal and subsequent joint motion for the simulations were quite smooth. However, there were some issues with the implementation of the experiment results. The safety controller on the UR3 manipulator would frequently override the control command for the PEEC method. The reason for this is not entirely clear.

It may be that the vision sensing used to determine the base pose was noisy, which then translated to a noisy control signal. The PEEC method did include a penalty term to

smooth control inputs but increasing this comes at the expense of task error. Deriving the control equations at the acceleration level may result in smoother velocities, and hence smoother manipulator motion. Furthermore, the predictive control for the end-effector could then easily synthesize with the torque minimization methods presented in Chapter 5 and Chapter 6. Or, better performance results might be achievable with different hardware.

7.3.4 Simultaneous Vehicle-Manipulator Control

One of the core stipulations made at the beginning of this thesis was that the base of a vehicle-manipulator system may not be able to fully compensate disturbance. Moreover, it is common in practice to separate the vehicle and manipulator control due to differences in control frequency, inertia etc. In this regard, the conceptual framework for this thesis was to develop the manipulator control independent of any assumptions about the base motion. In this sense, it could be easily applied to a decoupled control framework for a vehicle-manipulator system, or on a free-floating platform.

However, future work may involve utilizing a combined vehicle and manipulator for intervention tasks under disturbance. This could provide several improvements and advantages over the solitary manipulator case:

- The additional redundancy of a vehicle-manipulator system could be used to execute more complex tasks,
- The pose of the vehicle could be optimized to reduce disturbance to itself or provide support for the manipulator, and more importantly
- Accounting for the inertial coupling between the base and manipulator can be used to improve performance outcomes of non-inertial systems.

7.3.5 Applications and Validation with Physical Experiments

Due to time and hardware constraints, some of the methods proposed in this thesis could only be validated via simulation. Some testing was done for the PEEC method in Chapter 4 in a laboratory environment, which demonstrated the efficacy of using base motion predictions to improve task accuracy. And, in Chapter 6, a simple test was done showing that the EJTM method could enable the manipulator to autonomously reconfigure itself to withstand external forces.

In future development of the proposed control methods, there are several scenarios where these could be applied. UTS has several research projects pertaining to infrastructure inspection and maintenance. The joint torque minimization method could therefore be applied to assist with the high-pressure grit blasting which is known to cause issues with overloaded joint torques. Following on from the SPIR project, a couple of underwater manipulation research projects are being considered. The PEEC and PJTM methods could be tested here.

Appendix A

Kalman Filter Equations

The propagation of a state variable $\mathbf{x} \in \mathbb{R}^{\mathrm{n}}$ is given by the following equation:

$$\hat{\mathbf{x}}(\mathrm{k}+1|\mathrm{k}) = \mathbf{A}\hat{\mathbf{x}}(\mathrm{k}|\mathrm{k}), \tag{1}$$

in which $\hat{\mathbf{x}}(\mathrm{k}+1|\mathrm{k})$ gives the expected state outcome for step $\mathrm{k}+1$ from the step k, $\hat{\mathbf{x}}(\mathrm{k}|\mathrm{k})$ is the state estimate at k, and $\mathbf{A} \in \mathbb{R}^{\mathrm{n}\times\mathrm{n}}$ is the state propagation matrix. The propagation of uncertainty about from this system is:

$$\mathbf{\Sigma}_{\mathrm{x}}(\mathrm{k}+1|\mathrm{k}) = \mathbf{A}\mathbf{\Sigma}(\mathrm{k}|\mathrm{k})\mathbf{A}^{\mathrm{T}}, \tag{2}$$

where $\mathbf{\Sigma}_{\mathrm{x}} \in \mathbb{R}^{\mathrm{n}\times\mathrm{n}}$ is the variance-covariance matrix for random variable $\mathbf{x}$. The observation at step $\mathrm{k}+1$ is denoted as:

$$\mathbf{z}(\mathrm{k}+1) = \mathbf{C}\mathbf{x}(\mathrm{k}+1), \tag{3}$$

with observation matrix $\mathbf{C} \in \mathbb{R}^{\mathrm{m}\times\mathrm{n}}$. The Kalman Gain $\mathbf{K} \in \mathbb{R}^{\mathrm{n}\times\mathrm{m}}$ to correct the state estimate based on sensor observations is computed as:

$$\mathbf{K}(\mathrm{k}+1) = \mathbf{\Sigma}_{\mathrm{x}}(\mathrm{k}+1|\mathrm{k})\mathbf{C}^{\mathrm{T}}\Big(\mathbf{C}\mathbf{\Sigma}_{\mathrm{x}}(\mathrm{k}+1|\mathrm{k})\mathbf{C}^{\mathrm{T}} + \mathbf{\Sigma}_{\mathrm{s}}\Big)^{-1}, \tag{4}$$

in which $\mathbf{\Sigma}_{\mathrm{s}} \in \mathbb{R}^{\mathrm{n}\times\mathrm{n}}$ is the sensor noise. The state estimate and its uncertainty are then updated based on the following equations:

$$\hat{\mathbf{x}}(\mathrm{k}+1|\mathrm{k}+1) = \hat{\mathbf{x}}(\mathrm{k}+1|\mathrm{k}) + \mathbf{K}(\mathrm{k}+1)\Big(\mathbf{z}(\mathrm{k}+1) - \mathbf{C}\hat{\mathbf{x}}(\mathrm{k}+1|\mathrm{k})\Big) \tag{5}$$

$$\mathbf{\Sigma}_{\mathrm{x}}(\mathrm{k}+1|\mathrm{k}+1) = \Big(\mathbf{I} - \mathbf{K}(\mathrm{k}+1)\mathbf{C}\Big)\mathbf{\Sigma}_{\mathrm{x}}(\mathrm{k}+1|\mathrm{k}). \tag{6}$$

Appendix B

Quaternions

Define a unit quaternion $\mathcal{Q} \in \mathbb{H}$ as:

$$\mathcal{Q} = \{\eta, \boldsymbol{\varepsilon}\}, \tag{7}$$

in which:

- $\eta = \cos(\theta/2) \in \mathbb{R}$,
- $\boldsymbol{\varepsilon} = \sin(\theta/2)\hat{\mathbf{a}} \in \mathbb{R}^3$,
- $\hat{\mathbf{a}} \in \mathbb{R}^3$ is the axis of rotation between two reference frames, and
- θ is the angle of rotation.

Propagation of rotation is computed through multiplying two quaternions:

$$\mathcal{Q}_1 * \mathcal{Q}_2 = \begin{bmatrix} \eta_1\eta_2 - \boldsymbol{\varepsilon}_1^{\mathrm{T}}\boldsymbol{\varepsilon}_2 \\ \eta_1\boldsymbol{\varepsilon}_1 + \eta_2\boldsymbol{\varepsilon}_1 + S(\boldsymbol{\varepsilon}_1)\boldsymbol{\varepsilon}_2 \end{bmatrix}. \tag{8}$$

For the conjugate of a quaternion, the vector component is negated:

$$\bar{\mathcal{Q}} = \{\eta, -\boldsymbol{\varepsilon}\}. \tag{9}$$

Then the error between a desired orientation represented as a quaternion, $\mathcal{Q}_\mathrm{d}$, and the actual orientation $\mathcal{Q}$ is given by:

$$\mathcal{Q}_\mathrm{e} = \mathcal{Q}_\mathrm{d} * \bar{\mathcal{Q}} \tag{10}$$

$$= \begin{bmatrix} \eta_\mathrm{d}\eta + \boldsymbol{\varepsilon}_\mathrm{d}^\mathrm{T}\boldsymbol{\varepsilon} \\ -\eta_\mathrm{d}\boldsymbol{\varepsilon} + \eta\boldsymbol{\varepsilon}_\mathrm{d} - S(\boldsymbol{\varepsilon}_\mathrm{d})\boldsymbol{\varepsilon} \end{bmatrix} \tag{11}$$

$$= \begin{bmatrix} \eta_\mathrm{e} \\ \boldsymbol{\varepsilon}_\mathrm{e} \end{bmatrix}. \tag{12}$$

Proof of the time-derivative of a quaternion is given by Wittenburg (2007), but is also shown here. Consider the change in orientation over time from its original state, $\mathcal{Q}_0$ through quaternion propagation:

$$\mathcal{Q}(\mathrm{t} + \mathrm{dt}) = \mathcal{Q}_0 * \mathcal{Q}(\mathrm{t}), \tag{13}$$

in which:

$$\mathcal{Q}(\mathrm{t}) = \begin{bmatrix} \cos(\frac{1}{2}\dot{\theta}\mathrm{dt}) \\ \sin(\frac{1}{2}\dot{\theta}\mathrm{dt})\hat{\mathbf{a}}. \end{bmatrix} \tag{14}$$

As the elapsed time, dt, becomes infinitesimally small:

$$\lim_{\mathrm{dt}\to 0} \cos\left(\tfrac{1}{2}\dot{\theta}\mathrm{dt}\right) = 1 \tag{15}$$

$$\lim_{\mathrm{dt}\to 0} \sin\left(\tfrac{1}{2}\dot{\theta}\mathrm{dt}\right)\hat{\mathbf{a}} = \tfrac{1}{2}\boldsymbol{\omega}\mathrm{dt}. \tag{16}$$

Substituting Eqn. (15) and Eqn. (16) in to Eqn. (14) yields:

$$\mathcal{Q}(\mathrm{t} + \mathrm{dt}) = \begin{bmatrix} \eta \\ \boldsymbol{\varepsilon} \end{bmatrix} * \begin{bmatrix} 1 \\ \frac{1}{2}\boldsymbol{\omega}\mathrm{dt} \end{bmatrix}. \tag{17}$$

Taking the time-derivative of Eqn. (17) yields:

$$\begin{bmatrix} \dot{\eta} \\ \dot{\boldsymbol{\varepsilon}} \end{bmatrix} = \begin{bmatrix} \eta \\ \boldsymbol{\varepsilon} \end{bmatrix} * \begin{bmatrix} 0 \\ \frac{1}{2}\boldsymbol{\omega} \end{bmatrix} \tag{18}$$

$$= \tfrac{1}{2}\begin{bmatrix} 0 & -\boldsymbol{\omega}^\mathrm{T} \\ \boldsymbol{\omega} & -S(\boldsymbol{\omega}) \end{bmatrix}\begin{bmatrix} \eta \\ \boldsymbol{\varepsilon} \end{bmatrix}, \tag{19}$$

noting that $\frac{\mathrm{d}}{\mathrm{dt}}\mathcal{Q}_0 = 0$ as it is assumed to be fixed in time.

Appendix C

This appendix presents the fundamental kinematics, dynamics, and control equations for serial-link manipulators referred to throughout this thesis.

Statics

Joint Torques from End-Effector Forces

The work done by the joints of a manipulator must be equal to the work done by the end-effector. This can be expressed as:

$$\Delta \mathbf{q}^{\mathrm{T}} \boldsymbol{\tau} = \Delta \mathbf{x}^{\mathrm{T}} \mathbf{w}, \tag{20}$$

where:

- $\Delta \mathbf{q} \in \mathbb{R}^{\mathrm{n}}$ is a small change in the joint position $\mathbf{q}$,
- $\boldsymbol{\tau} \in \mathbb{R}^{\mathrm{n}}$ is the vector of joint torques,
- $\Delta \mathbf{x} \in \mathbb{R}^{\mathrm{m}}$ is a small change in the end-effector pose $\mathbf{x}$,
- $\mathbf{w} \in \mathbb{R}^{\mathrm{m}}$ is a wrench of forces and torques on the end-effector.

Dividing both sides by the joint displacement, $\Delta \mathbf{q}$, and solving for the joint torques $\boldsymbol{\tau}$ results in:

$$\begin{aligned} \boldsymbol{\tau} &= (\Delta \mathbf{x} / \Delta \mathbf{q})^{\mathrm{T}} \mathbf{w} && (21) \\ &= (\partial \mathbf{x} / \partial \mathbf{q})^{\mathrm{T}} \mathbf{w} && (22) \\ &= \mathbf{J}(\mathbf{q})^{\mathrm{T}} \mathbf{w}, && (23) \end{aligned}$$

where $\mathbf{J}(\mathbf{q}) \in \mathbb{R}^{\mathrm{m} \times \mathrm{n}}$ is the manipulator Jacobian.

Joint Torques from Gravitational Forces

Following the principle of Eqn. (23), the joint torques required to oppose gravitational forces acting on the manipulator are:

$$\boldsymbol{\tau}_{\mathrm{g}} = \begin{bmatrix} \mathbf{J}_{\mathrm{q,1}}^{\mathrm{T}} & \cdots & \mathbf{J}_{\mathrm{q,n}}^{\mathrm{T}} \end{bmatrix} \begin{bmatrix} \mathbf{w}_{\mathrm{g,1}} \\ \vdots \\ \mathbf{w}_{\mathrm{g,n}} \end{bmatrix}, \tag{24}$$

where:

- $\mathbf{J}_{\mathrm{q,i}} = \partial \mathbf{x}_{\mathrm{c,i}} / \partial \mathbf{q} \in \mathbb{R}^{6 \times \mathrm{n}}$ is the Jacobian from the joint space to the centre of mass of the i^{th} link of the manipulator,
- $\mathbf{x}_{\mathrm{c,i}} \in \mathbb{R}^6$ is the pose for the centre of mass of the i^{th} link,
- $\mathbf{w}_{\mathrm{g,i}} = \begin{bmatrix} \mathrm{m_i}\mathbf{g}^{\mathrm{T}} & \mathbf{0}_{3\times 1} \end{bmatrix}^{\mathrm{T}} \in \mathbb{R}^6$ is a wrench from gravitational forces at the centre of mass of the i^{th} link,
- $\mathrm{m_i} \in \mathbb{R}$ is the mass of the i^{th} link, and
- $\mathbf{g} \in \mathbb{R}^3$ is the gravitational acceleration vector.

Kinematics

The end-effector pose $\mathbf{x} \in \mathbb{R}^{\mathrm{m}}$ can be expressed as a vector function of the current joint configuration $\mathbf{q} \in \mathbb{R}^{\mathrm{n}}$ like so:

$$\mathbf{x} = \mathbf{f}(\mathbf{q}), \tag{25}$$

in which $\mathbf{f}(\mathbf{q}) : \mathbb{R}^{\mathrm{n}} \mapsto \mathbb{R}^{\mathrm{m}}$. Taking the time-derivative of Eqn. (25) yields:

$$\dot{\mathbf{x}} = \big(\partial \mathbf{f} / \partial \mathbf{q}\big)\dot{\mathbf{q}} \tag{26}$$

$$= \mathbf{J}(\mathbf{q})\dot{\mathbf{q}}, \tag{27}$$

which gives the velocity relationship. Then performing the same operation once more for acceleration results in:

$$\ddot{\mathbf{x}} = \mathbf{J}(\mathbf{q})\ddot{\mathbf{q}} + \dot{\mathbf{J}}(\mathbf{q}, \dot{\mathbf{q}})\dot{\mathbf{q}}. \tag{28}$$

Kinetics

The total dynamic torque equation for a serial-link manipulator is given by the following equation:

$$\boldsymbol{\tau} = \mathbf{M}(\mathbf{q})\ddot{\mathbf{q}} + \boldsymbol{\tau}_{\mathrm{c}}(\mathbf{q}, \dot{\mathbf{q}}) + \boldsymbol{\tau}_{\mathrm{c}}(\mathbf{g}) + \mathbf{J}(\mathbf{q})^{\mathrm{T}}\mathbf{R}\mathbf{w}, \tag{29}$$

where:

- $\mathbf{M}(\mathbf{q}) \in \mathbb{R}^{\mathrm{n}\times\mathrm{n}}$ is the inertia matrix,
- $\boldsymbol{\tau}_{\mathrm{c}}(\mathbf{q}, \dot{\mathbf{q}}) = \mathbf{C}(\mathbf{q}, \dot{\mathbf{q}})\dot{\mathbf{q}} \in \mathbb{R}^{\mathrm{n}}$ is the torque vector of Coriolis and centripetal forces,
- $\mathbf{C}(\mathbf{q}, \dot{\mathbf{q}}) \in \mathbb{R}^{\mathrm{n}\times\mathrm{n}}$ is the Coriolis matrix,
- $\mathbf{R} \in \mathbb{SO}(\mathrm{m})$ is a rotation from the base of the manipulator, $\{0\}$, to some other frame $\{\mathrm{i}\}$ on its kinematic structure, and
- $\mathbf{w} \in \mathbb{R}^{\mathrm{m}}$ is a wrench of external forces acting on the manipulator with respect to $\{\mathrm{i}\}$.

Control

Joint Control

From the Jacobian $\mathbf{J}(\mathbf{q}) \in \mathbb{R}^{\mathrm{m}\times\mathrm{n}}$, if $\mathrm{n} > \mathrm{m}$ and the matrix has full row rank, then the manipulator is considered redundant. There are multiple joint velocities $\dot{\mathbf{q}}$ that can satisfy an end-effector velocity $\dot{\mathbf{x}}$ for Eqn. (27). For a given end-effector motion, it is then possible to solve an optimisation problem of the form:

$$\min_{\dot{\mathbf{q}}} \tfrac{1}{2}(\dot{\mathbf{q}} - \dot{\mathbf{q}}_{\mathrm{r}})^{\mathrm{T}}\mathbf{W}(\dot{\mathbf{q}} - \dot{\mathbf{q}}_{\mathrm{r}}) \tag{30}$$

$$\text{subject to: } \dot{\mathbf{x}} - \mathbf{J}\dot{\mathbf{q}} = \mathbf{0} \tag{31}$$

where $\dot{\mathbf{q}}_{\mathrm{r}} \in \mathbb{R}^{\mathrm{n}}$ is a redundant task to be achieved by the manipulator only after Eqn. (31) is satisfied, and $\mathbf{W} \in \mathbb{R}^{\mathrm{n}\times\mathrm{n}}$ is a positive-definite weighting matrix. Due to the equality constraint, this problem is readily solved via Lagrange multipliers, which results in:

$$\dot{\mathbf{q}} = \mathbf{J}_{\mathrm{W}}^{\dagger}\dot{\mathbf{x}} + \mathbf{N}_{\mathrm{W}}\dot{\mathbf{q}}_{\mathrm{r}}, \tag{32}$$

in which $\mathbf{J}_{\mathrm{W}}^{\dagger} = \mathbf{W}^{-1}\mathbf{J}^{\mathrm{T}}\left(\mathbf{J}\mathbf{W}^{-1}\mathbf{J}^{\mathrm{T}}\right)^{-1} \in \mathbb{R}^{\mathrm{n}\times\mathrm{m}}$ is the weighted, pseudoinverse Jacobian and $\mathbf{N}_{\mathrm{W}} = \mathbf{I} - \mathbf{J}_{\mathrm{W}}^{\dagger}\mathbf{J} \in \mathbb{R}^{\mathrm{n}\times\mathrm{n}}$ is the weighted null space projection matrix. Note that multiplying Eqn. (32) by the Jacobian gives $\mathbf{J}\dot{\mathbf{q}} = \dot{\mathbf{x}}$, thereby satisfying the constraint Eqn. (31). The redundant task $\dot{\mathbf{q}}_{\mathrm{r}}$ will not intervene with the required end-effector motion.

To solve the kinematic control equations at the acceleration level, it is tempting to formulate an optimisation problem to minimize the weighted sum of joint accelerations:

$$\min_{\ddot{\mathbf{q}}} \ \tfrac{1}{2}\left(\ddot{\mathbf{q}} - \ddot{\mathbf{q}}_{\mathrm{r}}\right)^{\mathrm{T}}\mathbf{W}\left(\ddot{\mathbf{q}} - \ddot{\mathbf{q}}_{\mathrm{r}}\right) \tag{33}$$

$$\text{subject to: } \ddot{\mathbf{x}} - \mathbf{J}\ddot{\mathbf{q}} - \dot{\mathbf{J}}\dot{\mathbf{q}} = \mathbf{0}. \tag{34}$$

However, the resultant joint acceleration equation leads to instability as the null space velocities are undefined. This has lead several authors to propose solutions (Kang et al, 1992; Hsu et al, 1998; Natale et al, 1999; Zhang et al, 2004; Zhang et al, 2013).

An alternate approach is to directly differentiate Eqn. (32) which yields:

$$\ddot{\mathbf{q}} = \mathbf{J}_{\mathrm{W}}^{\dagger}\left(\ddot{\mathbf{x}} - \dot{\mathbf{J}}\dot{\mathbf{q}}\right) + \mathbf{N}_{\mathrm{W}}\ddot{\mathbf{q}} + \mathbf{N}_{\mathrm{W}}\dot{\mathbf{J}}^{\mathrm{T}}\mathbf{J}_{\mathrm{W}}^{\dagger\mathrm{T}}(\dot{\mathbf{q}} - \dot{\mathbf{q}}_{\mathrm{r}}). \tag{35}$$

Using this defintion for the joint acceleration, the null space velocities are propagated through from Eqn. (32). This derivation was also favoured by Slotine (1991) due to its inherent stability. In fact, the null space control equations as derived by Hsu et al (1998) and Natale et al (1999) eventually lead back to a similar form as Eqn. (35).

End-Effector Control

This section of the appendix proves the stability of feedback control for trajectory tracking with the end-effector in Cartesian space. Assuming that $\dot{\mathbf{x}} \in \mathbb{R}^6$, this can be divided in to its linear and angular components:

$$\dot{\mathbf{x}} = \begin{bmatrix}\mathbf{v}^{\mathrm{T}} & \boldsymbol{\omega}^{\mathrm{T}}\end{bmatrix}^{\mathrm{T}}, \tag{36}$$

where $\mathbf{v} \in \mathbb{R}^3$ is the linear velocity of the end-effector, and $\boldsymbol{\omega} \in \mathbb{R}^3$ is the angular velocity. Since the quaternion parameterisation of orientations is nonlinear (Appendix B), the angular velocity control must be derived separately form the linear velocity.

Linear velocity control

Denote the position error of the end-effector as:

$$\mathbf{e}_\mathrm{p} = \mathbf{p}_\mathrm{d} - \mathbf{p}, \tag{37}$$

in which $\mathbf{p}_\mathrm{d} \in \mathbb{R}^3$ is the desired end-effector position, and $\mathbf{p} \in \mathbb{R}^3$ is the actual position obtained from the forward kinematics. Taking the time-derivative of Eqn. (37):

$$\dot{\mathbf{e}}_\mathrm{p} = \dot{\mathbf{p}}_\mathrm{d} - \dot{\mathbf{p}} \tag{38}$$

$$= \mathbf{v}_\mathrm{d} - \mathbf{v}. \tag{39}$$

Then, define the linear control velocity of the end-effector as:

$$\mathbf{v} \triangleq \dot{\mathbf{v}}_\mathrm{d} + \mathbf{K}_1\mathbf{e}_\mathrm{p} + \mathbf{K}_2\mathbf{E}_\mathrm{p} + \mathbf{K}_3\dot{\mathbf{e}}_\mathrm{p}, \tag{40}$$

in which $\mathbf{E}_\mathrm{p} = \int \mathbf{e}_\mathrm{p}\mathrm{d}t$. Substituting Eqn. (40) back in to Eqn. (39) yields:

$$\dot{\mathbf{e}}_\mathrm{p} = -\mathbf{K}_1\mathbf{e}_\mathrm{p} - \mathbf{K}_2\mathbf{E}_\mathrm{p} - \mathbf{K}_3\dot{\mathbf{e}}_\mathrm{p} \tag{41}$$

$$(\mathbf{I} + \mathbf{K}_3)\dot{\mathbf{e}}_\mathrm{p} = -\mathbf{K}_1\mathbf{e}_\mathrm{p} - \mathbf{K}_2\mathbf{E}_\mathrm{p} \tag{42}$$

$$\dot{\mathbf{e}}_\mathrm{p} = -\big(\mathbf{I} + \mathbf{K}_3\big)^{-1}\big(\mathbf{K}_1\mathbf{e}_\mathrm{p} + \mathbf{K}_2\mathbf{E}_\mathrm{p}\big) \tag{43}$$

$$\dot{\mathbf{e}}_\mathrm{p} = -\mathbf{K}_\mathrm{p}\mathbf{e}_\mathrm{p} - \mathbf{K}_\mathrm{i}\mathbf{E}_\mathrm{p}. \tag{44}$$

Equations (37) and (44) can be written as a companion system:

$$\begin{bmatrix} \mathbf{e}_\mathrm{p} \\ \dot{\mathbf{e}}_\mathrm{p} \end{bmatrix} = \begin{bmatrix} \mathbf{0}_{3\times3} & \mathbf{I}_3 \\ -\mathbf{K}_\mathrm{i} & -\mathbf{K}_\mathrm{p} \end{bmatrix} \begin{bmatrix} \mathbf{E}_\mathrm{p} \\ \mathbf{e}_\mathrm{p} \end{bmatrix}. \tag{45}$$

This system of differential equations is exponentially stable if the conglomerate matrix containing $\mathbf{K}_\mathrm{i}$ and $\mathbf{K}_\mathrm{p}$ has eigenvalues with negative real parts.

Angular velocity control

Proof of stability for the angular velocity feedback is taken from Yuan (1988). A Lyapunov candidate function can be denoted as the sum-of-squared errors between the elements in a desired orientation $\mathcal{Q} = \{\eta_\mathrm{d}, \boldsymbol{\varepsilon}_\mathrm{d}\} \in \mathbb{H}$ and the actual orientation $\mathcal{Q} = \{\eta, \boldsymbol{\varepsilon}\} \in \mathbb{H}$:

$$\mathrm{V} = (\eta_\mathrm{d} - \eta)^2 + \big(\boldsymbol{\varepsilon}_\mathrm{d} - \boldsymbol{\varepsilon}\big)^\mathrm{T}\big(\boldsymbol{\varepsilon}_\mathrm{d} - \boldsymbol{\varepsilon}\big) + \tfrac{1}{2}\mathbf{E}_\mathrm{o}^\mathrm{T}\mathbf{E}_\mathrm{o} \tag{46}$$

$$= 2 - 2\big(\eta_\mathrm{d}\eta + \boldsymbol{\varepsilon}_\mathrm{d}^\mathrm{T}\boldsymbol{\varepsilon}\big) + \tfrac{1}{2}\mathbf{E}_\mathrm{o}^\mathrm{T}\mathbf{E}_\mathrm{o}, \tag{47}$$

where $\mathbf{E}_\mathrm{o} = \int_0^\mathrm{t} \mathbf{e}_\mathrm{o}\mathrm{dt}$, and $\mathbf{e}_\mathrm{o}$ is some representation of the orientation error of the end-effector. From Eqn. (12) in Appendix B, Eqn. (47) can be written as:

$$\mathrm{V} = 2 - 2\eta_\mathrm{e} + \tfrac{1}{2}\mathbf{E}_\mathrm{o}^\mathrm{T}\mathbf{E}_\mathrm{o}. \tag{48}$$

Taking the time-derivative of Eqn. (48) leads to:

$$\dot{\mathrm{V}} = 2\dot{\eta}_\mathrm{e} + \mathbf{e}_\mathrm{o}^\mathrm{T}\mathbf{E}_\mathrm{o} \tag{49}$$

$$= \boldsymbol{\omega}_\mathrm{e}^\mathrm{T}\boldsymbol{\varepsilon}_\mathrm{e} + \mathbf{e}_\mathrm{o}^\mathrm{T}\mathbf{E}_\mathrm{o}, \tag{50}$$

wherein the term $\dot{\eta}_\mathrm{e}$ was substituted using the definition of the quaternion time-derivative in Eqn. (19). If the orientation error is defined as:

$$\mathbf{e}_\mathrm{o} \triangleq \boldsymbol{\varepsilon}_\mathrm{e}, \tag{51}$$

then Eqn. (50) now becomes:

$$\dot{\mathrm{V}} = \boldsymbol{\varepsilon}_\mathrm{e}^\mathrm{T}\big(\boldsymbol{\omega}_\mathrm{e} + \mathbf{E}_\mathrm{o}\big) \tag{52}$$

$$= \boldsymbol{\varepsilon}_\mathrm{e}^\mathrm{T}\big(\boldsymbol{\omega}_\mathrm{d} - \boldsymbol{\omega} + \mathbf{E}_\mathrm{o}\big). \tag{53}$$

Then it is evident that the control equation for the angular velocity of the end-effector can be defined as

$$\boldsymbol{\omega} \triangleq \boldsymbol{\omega}_\mathrm{d} + \mathbf{K}_\mathrm{o}\boldsymbol{\varepsilon}_\mathrm{e} + \mathbf{E}_\mathrm{o}, \tag{54}$$

such that Eqn. (53) becomes:

$$\dot{\mathrm{V}} = -\boldsymbol{\varepsilon}_\mathrm{e}^\mathrm{T}\mathbf{K}_\mathrm{o}\boldsymbol{\varepsilon}_\mathrm{e}. \tag{55}$$

Equation (55) is strictly negative $\forall\boldsymbol{\varepsilon}_\mathrm{e} \neq \mathbf{0}$ given a positive-definite gain $\mathbf{K}_\mathrm{o}$. Hence, using Eqn. (54), the end-effector orientation will converge to the desired state.

The combined linear and angular velocity for controlling the end-effector can be written as:

$$\begin{bmatrix} \mathbf{v} \\ \boldsymbol{\omega} \end{bmatrix} = \begin{bmatrix} \mathbf{v}_\mathrm{d} + \mathbf{K}_\mathrm{p}\mathbf{e}_\mathrm{p} + \mathbf{K}_\mathrm{i}\mathbf{E}_\mathrm{p} \\ \boldsymbol{\omega}_\mathrm{d} + \mathbf{K}_\mathrm{o}\mathbf{e}_\mathrm{o} + \mathbf{E}_\mathrm{o} \end{bmatrix} \tag{56}$$

Linear acceleration

The time-derivative of Eqn. (39) is:

$$\ddot{\mathbf{e}}_\mathrm{p} = \dot{\mathbf{v}}_\mathrm{d} - \dot{\mathbf{v}}, \tag{57}$$

where $\dot{\mathbf{v}}_\mathrm{p}$ is the desired end-effector acceleration and $\dot{\mathbf{v}}$ is the control acceleration. This latter term can be defined as:

$$\dot{\mathbf{v}} \triangleq \dot{\mathbf{v}}_\mathrm{d} + \mathbf{K}_\mathrm{p}\mathbf{e}_\mathrm{p} + \mathbf{K}_\mathrm{i}\mathbf{E}_\mathrm{p} + \mathbf{K}_\mathrm{v}\dot{\mathbf{e}}_\mathrm{p}, \tag{58}$$

which, upon substitution in to Eqn. (57) results in:

$$\ddot{\mathbf{e}}_\mathrm{p} = -\mathbf{K}_\mathrm{p}\mathbf{e}_\mathrm{p} - \mathbf{K}_\mathrm{i}\mathbf{E}_\mathrm{p} - \mathbf{K}_\mathrm{v}\dot{\mathbf{e}}_\mathrm{p}. \tag{59}$$

Writing this as a companion system of differential equations:

$$\begin{bmatrix} \mathbf{e}_\mathrm{p} \\ \dot{\mathbf{e}}_\mathrm{p} \\ \ddot{\mathbf{e}}_\mathrm{p} \end{bmatrix} = \begin{bmatrix} \mathbf{0}_{3\times3} & \mathbf{I}_3 & \mathbf{0}_{3\times3} \\ \mathbf{0}_{3\times3} & \mathbf{0}_{3\times3} & \mathbf{I}_3 \\ -\mathbf{K}_\mathrm{i} & -\mathbf{K}_\mathrm{p} & -\mathbf{K}_\mathrm{v} \end{bmatrix} \begin{bmatrix} \mathbf{E}_\mathrm{p} \\ \mathbf{e}_\mathrm{p} \\ \dot{\mathbf{e}}_\mathrm{p} \end{bmatrix}. \tag{60}$$

This system can be made exponentially stable with appropriate choices for $\mathbf{K}_\mathrm{p}$, $\mathbf{K}_\mathrm{i}$ and $\mathbf{K}_\mathrm{v}$.

Angular acceleration

The proof of stability for the angular acceleration feedback control can also be found in Yuan et al (1988). Another Lyapunov candidate function can be defined as:

$$\mathrm{V} = (\eta_\mathrm{d} - \eta)^2 + \big(\boldsymbol{\varepsilon}_\mathrm{d} - \boldsymbol{\varepsilon}\big)^\mathrm{T}\big(\boldsymbol{\varepsilon}_\mathrm{d} - \boldsymbol{\varepsilon}\big) + \tfrac{1}{2}\big(\boldsymbol{\omega}_\mathrm{d} - \boldsymbol{\omega}\big)^\mathrm{T}\big(\boldsymbol{\omega}_\mathrm{d} - \boldsymbol{\omega}\big) \tag{61}$$

$$= 2 - 2\eta_\mathrm{e} + \tfrac{1}{2}\big(\boldsymbol{\omega}_\mathrm{d} - \boldsymbol{\omega}\big)^\mathrm{T}\big(\boldsymbol{\omega}_\mathrm{d} - \boldsymbol{\omega}\big), \tag{62}$$

in which η_e is the scalar component of the quaternion error from Eqn. (12). Taking the time-derivative of Eqn. (62) and substituting in Eqn. (19) results in:

$$\dot{V} = -2\dot{\eta}_e + \big(\boldsymbol{\omega}_d - \boldsymbol{\omega}\big)^T\big(\dot{\boldsymbol{\omega}}_d - \dot{\boldsymbol{\omega}}\big) \tag{63}$$

$$= -\big(\boldsymbol{\omega}_d - \boldsymbol{\omega}\big)^T\big(\boldsymbol{\varepsilon}_e + \dot{\boldsymbol{\omega}}_d - \dot{\boldsymbol{\omega}}\big). \tag{64}$$

From this equation, it is evident that choosing the angular acceleration control as:

$$\dot{\boldsymbol{\omega}} \triangleq \boldsymbol{\varepsilon}_e + \mathbf{K}_\omega\big(\boldsymbol{\omega}_d - \boldsymbol{\omega}\big), \tag{65}$$

will result in:

$$\dot{V} = -\big(\boldsymbol{\omega}_d - \boldsymbol{\omega}\big)^T\mathbf{K}_\omega\big(\boldsymbol{\omega}_d - \boldsymbol{\omega}\big). \tag{66}$$

This equation is also strictly negative $\forall\boldsymbol{\omega} \neq \boldsymbol{\omega}_d$ and positive-definite matrix $\mathbf{K}_\omega$. Note also that $\dot{\boldsymbol{\omega}} \neq \mathbf{0}$ if $\boldsymbol{\varepsilon}_e \neq \mathbf{0}$, hence $\boldsymbol{\omega}$ is not constant and the end-effector orientation will converge to the desired state.

The feedback control for the end-effector acceleration can then be written as

$$\begin{bmatrix}\dot{\mathbf{v}}\\ \dot{\boldsymbol{\omega}}\end{bmatrix} = \begin{bmatrix}\dot{\mathbf{v}}_d + \mathbf{K}_p\mathbf{e}_p + \mathbf{K}_i\mathbf{E}_p + \mathbf{K}_v\dot{\mathbf{e}}_p\\ \dot{\boldsymbol{\omega}}_d + \boldsymbol{\varepsilon}_e + \mathbf{K}_\omega(\boldsymbol{\omega}_d - \boldsymbol{\omega})\end{bmatrix} \tag{67}$$

Joint Limit Avoidance

Chan & Dubey (1995) proposed to use a WLN for the joint velocity control of a redundant manipulator to avoid joint limits. They defined a cost function as:

$$d(q_i) = \frac{(q_{i,max} - q_i)(q_i - q_{i,min})}{c_i(q_{i,max} - q_i)^2(q_i - q_{i,min})^2}, \tag{68}$$

for $i \in \{1, ..., n\}$ joints. The scalar c_i can be used to change the gradient of this function to suit individual joints. The diagonal elements of the weighting matrix in Eqn. (32) and Eqn. (35) can then be constructed as:

$$W_{ii} = \begin{cases} 1 + |\Delta d(q_i)| & \text{for } |\Delta d(q_i)| > 0\\ 1 & \text{otherwise.}\end{cases} \tag{69}$$

Bibliography

Ajoudani, A., Tsagarakis, N.G. and Bicchi, A., 2015, May. On the role of robot configuration in cartesian stiffness control. In 2015 IEEE International Conference on Robotics and Automation (ICRA) (pp. 1010-1016). IEEE.

Akaike, H., 1974. A new look at the statistical model identification. In Selected Papers of Hirotugu Akaike (pp. 215-222). Springer, New York, NY.

Ang, M.H. and Andeen, G.B., 1995. Specifying and achieving passive compliance based on manipulator structure. IEEE transactions on robotics and automation, 11(4), pp.504-515.

Angeles, J. and Angeles, J., 2002. Fundamentals of robotic mechanical systems (Vol. 2). New York: Springer-Verlag.

Antonelli, G. and Antonelli, G., 2014. Underwater robots (Vol. 3). Switzerland: Springer International Publishing.

Antonelli, G., Caccavale, F., Chiaverini, S. and Villani, L., 2000. Tracking control for underwater vehicle-manipulator systems with velocity estimation. IEEE Journal of Oceanic Engineering, 25(3), pp.399-413.

Autonomous Undersea Vehicle Applications Centre (AUVAC) 2020, Marine Autonomous Systems Engineering [ONLINE] Availabel at: https://auvac.org/people-organizations/view/314 (Accessed 18th February 2020).

Bowthorpe, M. and Tavakoli, M., 2016. Generalized predictive control of a surgical robot for beating-heart surgery under delayed and slowly-sampled ultrasound image data. IEEE Robotics and Automation Letters, 1(2), pp.892-899.

Brahim-Belhouari, S. and Bermak, A., 2004. Gaussian process for nonstationary time series prediction. Computational Statistics & Data Analysis, 47(4), pp.705-712.

Bruyninckx, H. and De Schutter, J., 1996. Symbolic differentiation of the velocity mapping for a serial kinematic chain. Mechanism and machine theory, 31(2), pp.135-148.

Bussmann, K., Dietrich, A. and Ott, C., 2018, May. Whole-Body Impedance Control for a Planetary Rover with Robotic Arm: Theory, Control Design, and Experimental Validation. In 2018 IEEE International Conference on Robotics and Automation (ICRA) (pp. 910-917). IEEE.

Byrnes, C.I. and Isidori, A., 2004. Nonlinear internal models for output regulation. IEEE Transactions on Automatic Control, 49(12), pp.2244-2247.

Carrera, A., Palomeras, N., Hurtos, N., Kormushev, P. and Carreras, M., 2014. Learning by demonstration applied to underwater intervention.

Chan, T.F. and Dubey, R.V., 1995. A weighted least-norm solution based scheme for avoiding joint limits for redundant joint manipulators. IEEE Transactions on Robotics and Automation, 11(2), pp.286-292.

Chen, P., Shan, C., Xiang, J. and Wei, W., 2015, May. Moving obstacle avoidance for redundant manipulator via weighted least norm method. In The 27th Chinese Control and Decision Conference (2015 CCDC) (pp. 6181-6186). IEEE.

Chen, Z. and Huang, J., 2015. Stabilization and regulation of nonlinear systems. Cham, Switzerland: Springer.

Chiaverini, S., Egeland, O. and Kanestrom, R.K., 1991, June. Achieving user-defined accuracy with damped least-squares inverse kinematics. In Fifth International Conference on Advanced Robotics' Robots in Unstructured Environments (pp. 672-677). IEEE.

Choi, H.R., Chung, W.K. and Youm, Y., 1994, May. Stiffness analysis and control of redundant manipulators. In Proceedings of the 1994 IEEE International Conference on Robotics and Automation (pp. 689-695). IEEE.

Chung, C.Y., Lee, B.H., Kim, M.S. and Lee, C.W., 2000. Torque optimizing control with singularity-robustness for kinematically redundant robots. Journal of Intelligent and Robotic Systems, 28(3), pp.231-258.

Cieslak, P., Ridao, P. and Giergiel, M., 2015, May. Autonomous underwater panel operation by GIRONA500 UVMS: A practical approach to autonomous underwater manipulation. In 2015 IEEE International Conference on Robotics and Automation (ICRA) (pp. 529-536). IEEE.

Clement, R., Dunbabin, M. and Wyeth, G., 2005. Toward robust image detection of crown-of-thorns starfish for autonomous population monitoring. In Australasian Conference on Robotics and Automation 2005. Australian Robotics and Automation Association Inc.

Dariush, B., Hammam, G.B. and Orin, D., 2010, October. Constrained resolved acceleration control for humanoids. In 2010 IEEE/RSJ International Conference on Intelligent Robots and Systems (pp. 710-717). IEEE.

Dayoub, F., Dunbabin, M. and Corke, P., 2015, September. Robotic detection and tracking of crown-of-thorns starfish. In 2015 IEEE/RSJ International Conference on Intelligent Robots and Systems (IROS) (pp. 1921-1928). IEEE.

DensoWave Incorporated, 6-Axis robots VM series specifications (Online), (http://www.denso-wave.com/en/robot/product/five-six/vm Spec.html) Accessed 12th Feb 2018

Dürichen, R., Pimentel, M.A., Clifton, L., Schweikard, A. and Clifton, D.A., 2015. Multitask Gaussian processes for multivariate physiological time-series analysis. IEEE Transactions on Biomedical Engineering, 62(1), pp.314-322.

Fang, C. and Williams, B.C., 2014, May. General probabilistic bounds for trajectories using only mean and variance. In 2014 IEEE International Conference on Robotics and Automation (ICRA) (pp. 2501-2506). IEEE.

Fernández, D.C. and Hollinger, G.A., 2017. Model predictive control for underwater robots in ocean waves. IEEE Robotics and Automation letters, 2(1), pp.88-95.

Fernández, J.J., Prats, M., Sanz, P.J., Garca, J.C., Marin, R., Robinson, M., Ribas, D. and Ridao, P., 2013. Grasping for the seabed: Developing a new underwater robot arm for shallow-water intervention. IEEE Robotics & Automation Magazine, 20(4), pp.121-130.

Flacco, F. and De Luca, A., 2015. Discrete-time redundancy resolution at the velocity level with acceleration/torque optimization properties. Robotics and Autonomous Systems, 70, pp.191-201.

From, P.J., Duindam, V., Gravdahl, J.T. and Sastry, S., 2009, May. Modeling and motion planning for mechanisms on a non-inertial base. In 2009 IEEE International Conference on Robotics and Automation (pp. 3320-3326). IEEE.

From, P.J., Gravdahl, J.T., Lillehagen, T. and Abbeel, P., 2011. Motion planning and control of robotic manipulators on seaborne platforms. Control engineering practice, 19(8), pp.809-819.

Garimella, G. and Kobilarov, M., 2015, May. Towards model-predictive control for aerial pick-and-place. In 2015 IEEE international conference on robotics and automation (ICRA) (pp. 4692-4697). IEEE.

Gasparri, G.M., Fabiani, F., Garabini, M., Pallottino, L., Catalano, M., Grioli, G., Persichin, R. and Bicchi, A., 2016, November. Robust optimization of system compliance

for physical interaction in uncertain scenarios. In 2016 IEEE-RAS 16th International Conference on Humanoid Robots (Humanoids) (pp. 911-918). IEEE.

Giordano, A.M., Calzolari, D. and Albu-Schffer, A., 2018, May. Workspace fixation for free-floating space robot operations. In 2018 IEEE International Conference on Robotics and Automation (ICRA) (pp. 889-896). IEEE.

Girona Underwater Vision and Robotics, Girona 500 AUV [ONLINE] Available at: https://cirs.udg.edu/auvs-technology/auvs/girona-500-auv/. [Accessed 15 April 2019]

Heupel, M.R. and Simpfendorfer, C.A., 2008. Movement and distribution of young bull sharks Carcharhinus leucas in a variable estuarine environment. Aquatic Biology, 1(3), pp.277-289.

Hollerbach, J. and Suh, K., 1987. Redundancy resolution of manipulators through torque optimization. IEEE Journal on Robotics and Automation, 3(4), pp.308-316.

Hsu, P., Mauser, J. and Sastry, S., 1989. Dynamic control of redundant manipulators. Journal of Robotic Systems, 6(2), pp.133-148.

Huang, J. and Chen, Z., 2004. A general framework for tackling the output regulation problem. IEEE Transactions on Automatic Control, 49(12), pp.2203-2218.

Huynh, V.T., Dunbabin, M. and Smith, R.N., 2015, May. Predictive motion planning for AUVs subject to strong time-varying currents and forecasting uncertainties. In 2015 IEEE international conference on robotics and automation (ICRA) (pp. 1144-1151). IEEE.

Igus.com, Robolink WR, (Online), (https://www.igus.com/wpck/16962/N16 10 11) , Accessed 5th Feb 2018

Industrial Relations Commission NSW, Inspector Stothard v Allied Industrial Services Pty Ltd [2011] NSWIRComm 21, 22nd March 2011

Isidori, A. and Byrnes, C.I., 1990. Output regulation of nonlinear systems. IEEE transactions on Automatic Control, 35(2), pp.131-140.

Ishitsuka, M., Sagara, S. and Ishii, K., 2004, April. Dynamics analysis and resolved acceleration control of an autonomous underwater vehicle equipped with a manipulator. In Proceedings of the 2004 International Symposium on Underwater Technology (IEEE Cat. No. 04EX869) (pp. 277-281). IEEE.

Jimenez-Cano, A.E., Braga, J., Heredia, G. and Ollero, A., 2015, September. Aerial manipulator for structure inspection by contact from the underside. In 2015 IEEE/RSJ international conference on intelligent robots and systems (IROS) (pp. 1879-1884). IEEE.

Jin, S., Bae, J., Kim, J. and Seo, T., 2017. Disturbance compensation of a dual-arm underwater robot via redundant parallel mechanism theory. Meccanica, 52(7), pp.1711-1719.

Jin, S., Kim, J., Bae, J., Seo, T. and Kim, J., 2016. Design, modeling and optimization of an underwater manipulator with four-bar mechanism and compliant linkage. Journal of mechanical science and technology, 30(9), pp.4337-4343.

Jones, D. and Hollinger, G.A., 2017. Planning energy-efficient trajectories in strong disturbances. IEEE Robotics and Automation Letters, 2(4), pp.2080-2087.

Jones, R., 2017, Aerial Manipulation for Indoor Applications, Master's Thesis, University of Illinois at Urbana-Champaign

Kajita, H. and Kosuge, K., 1997, September. Force control of robot floating on the water utilizing vehicle restoring force. In Proceedings of the 1997 IEEE/RSJ International Conference on Intelligent Robot and Systems. Innovative Robotics for Real-World Applications. IROS'97 (Vol. 1, pp. 162-167). IEEE.

Kang, H.J. and Freeman, R.A., 1992, May. Joint torque optimization of redundant manipulators via the null space damping method. In Proceedings 1992 IEEE International Conference on Robotics and Automation (pp. 520-525). IEEE.

Kashyap, R., 1980. Inconsistency of the AIC rule for estimating the order of autoregressive models. IEEE Transactions on Automatic Control, 25(5), pp.996-998.

Keshavarzi, A., Melville, B. and Ball, J., 2014. Three-dimensional analysis of coherent turbulent flow structure around a single circular bridge pier. Environmental Fluid Mechanics, 14(4), pp.821-847.

Kerckhof, F., Rumes, B., Norro, A., Jacques, T.G. and Degraer, S., 2010. Seasonal variation and vertical zonation of the marine biofouling on a concrete offshore windmill foundation on the Thornton Bank (southern North Sea). Offshore Wind Farms in the Belgian Part of the North Sea: Early Environmental Impact Assessment and Spatio-Temporal Variability.(Eds S. Degraer, R. Brabant and B. Rumes.) pp, pp.53-68.

Khatib, O., 1986. Real-time obstacle avoidance for manipulators and mobile robots. In Autonomous robot vehicles (pp. 396-404). Springer, New York, NY.

Kirchner, N., Paul, G. and Liu, D.K., 2006, January. Bridge maintenance robotic arm: mechanical technique to reduce the nozzle force of a sandblasting rig. In Proceedings of the 1st International Symposium on Digital Manufacturing.

Kormushev, P. and Caldwell, D.G., 2013, November. Improving the energy efficiency of autonomous underwater vehicles by learning to model disturbances. In 2013 IEEE/RSJ International Conference on Intelligent Robots and Systems (pp. 3885-3892). IEEE.

Kosuge, Kazuhiro, Fukuda, Toshio and Ohkubo, Hideaki, 1991, December. Control of manipulator/vehicle system floating on the water. In [1991] Proceedings of the 30th IEEE Conference on Decision and Control (pp. 2781-2786). IEEE.

Lehnert, C., Sa, I., McCool, C., Upcroft, B. and Perez, T., 2016, May. Sweet pepper pose detection and grasping for automated crop harvesting. In 2016 IEEE International Conference on Robotics and Automation (ICRA) (pp. 2428-2434). IEEE.

Li, X.R., Zhao, Z. and Jilkov, V.P., 2001, May. Practical measures and test for credibility of an estimator. In Proc. Workshop on Estimation, Tracking, and FusionA Tribute to Yaakov Bar-Shalom (pp. 481-495).

Li, Y. and Kao, I., 2004, April. Stiffness control on redundant manipulators: a unique and kinematically consistent solution. In IEEE International Conference on Robotics and Automation, 2004. Proceedings. ICRA'04. 2004 (Vol. 4, pp. 3956-3961). IEEE.

Liu, D., Dissanayake, G., Manamperi, P., Fang, G., Paul, G., Kirchner, N.G. and Chotiprayanakul, P., 2008. A robotic system for steel bridge maintenance: research challenges and system design. In Australasian Conference on Robotics and Automation. Australian Robotics and Automation Association.

Liu, D.K., Dissanayake, G., Valls Miro, J. and Waldron, K.J., 2014, January. Infrastructure robotics: Research challenges and opportunities. In 31st International Symposium on Automation and Robotics in Construction and Mining, ISARC 2014-Proceedings.

Love, L.J., Jansen, J.F. and Pin, F.G., 2004, April. On the modeling of robots operating on ships. In IEEE International Conference on Robotics and Automation, 2004. Proceedings. ICRA'04. 2004 (Vol. 3, pp. 2436-2443). IEEE.

Lunni, D., Santamaria-Navarro, A., Rossi, R., Rocco, P., Bascetta, L. and Andrade-Cetto, J., 2017, June. Nonlinear model predictive control for aerial manipulation. In 2017 International Conference on Unmanned Aircraft Systems (ICUAS) (pp. 87-93). IEEE.

Paul, G., Webb, S., Liu, D.K. and Dissanayake, G., 2010, December. A robotic system for steel bridge maintenance: Field testing. In Australasian Conference on Robotics and Automation (pp. 1-8).

Pavlov, A., Janssen, B., van de Wouw, N. and Nijmeijer, H., 2007. Experimental output regulation for a nonlinear benchmark system. IEEE Transactions on Control Systems Technology, 15(4), pp.786-793.

Manamperi, P.B., Brooks, P.A., Kaluarachchi, W., Peters, G., Ho, A., Lie, S., To, A., Paul, G., Rushton-Smith, D., Webb, S. and Liu, D.K., 2011, October. Robotic grit-blasting: engineering challenges. In Austroads Bridge Conference, 8th, 2011, Sydney, New South Wales, Australia (No. AP-G90/11).

Marani, G., Choi, S.K. and Yuh, J., 2009. Underwater autonomous manipulation for intervention missions AUVs. Ocean Engineering, 36(1), pp.15-23.

Marani, G. and Yuh, J., 2014. Introduction to autonomous manipulation. In Case Study with an Underwater Robot SAUVIM, volume 102 of Springer Tracts in Advanced Robotics. Springer.

Maurelli, F., Carreras, M., Salvi, J., Lane, D., Kyriakopoulos, K., Karras, G., Fox, M., Long, D., Kormushev, P. and Caldwell, D., 2016, April. The PANDORA project: A success story in AUV autonomy. In OCEANS 2016-Shanghai (pp. 1-8). IEEE.

Medagoda, L. and Williams, S.B., 2012, May. Model predictive control of an autonomous underwater vehicle in an in situ estimated water current profile. In 2012 Oceans-Yeosu (pp. 1-8). IEEE.

NASA, 2019. NASA's Opportunity Rover Mission on Mars Comes to End. [ONLINE] Available at: https://mars.nasa.gov/news/8413/nasas-opportunity-rover-mission-on-mars-comes-to-end/. [Accessed 13 April 2019].

Natale, C., Siciliano, B. and Villani, L., 1999. Spatial impedance control of redundant manipulators. In Proceedings 1999 IEEE International Conference on Robotics and Automation (Cat. No. 99CH36288C) (Vol. 3, pp. 1788-1793). IEEE.

Nedungadi, A. and Kazerouinian, K., 1989. A local solution with global characteristics for the joint torque optimization of a redundant manipulator. In Advanced Robotics: 1989 (pp. 559-591). Springer, Berlin, Heidelberg.

Nguyen, K.D. and Dankowicz, H., 2015. Adaptive control of underactuated robots with unmodeled dynamics. Robotics and Autonomous Systems, 64, pp.84-99.

Ohshima, M., Ohno, H., Hashimoto, I., Sasajima, M., Maejima, M., Tsuto, K. and Ogawa, T., 1995. Model predictive control with adaptive disturbance prediction and its application to fatty acid distillation column control. Journal of Process Control, 5(1), pp.41-48.

Oldewurtel, F., Parisio, A., Jones, C.N., Gyalistras, D., Gwerder, M., Stauch, V., Lehmann, B. and Morari, M., 2012. Use of model predictive control and weather forecasts for energy efficient building climate control. Energy and Buildings, 45, pp.15-27.

Parker, P.J. and Anderson, B.D., 1990. Frequency tracking of nonsinusoidal periodic signals in noise. Signal processing, 20(2), pp.127-152.

Paul, G., Webb, S., Liu, D.K. and Dissanayake, G., 2010, December. A robotic system for steel bridge maintenance: Field testing. In Australasian Conference on Robotics and Automation (pp. 1-8).

Pflimlin, J.M., Soueres, P. and Hamel, T., 2004, December. Hovering flight stabilization in wind gusts for ducted fan UAV. In 2004 43rd IEEE Conference on Decision and Control (CDC)(IEEE Cat. No. 04CH37601) (Vol. 4, pp. 3491-3496). IEEE.

Pohl, E.D. and Lipkin, H., 1991, April. A new method of robotic rate control near singularities. In Proceedings. 1991 IEEE International Conference on Robotics and Automation (pp. 1708-1713). IEEE.

Riedel, J.S., 2000. Shallow water stationkeeping of an autonomous underwater vehicle: the experimental results of a disturbance compensation controller. In OCEANS 2000 MTS/IEEE Conference and Exhibition. Conference Proceedings (Cat. No. 00CH37158) (Vol. 2, pp. 1017-1028). IEEE.

Riviere, C.N., Ang, W.T. and Khosla, P.K., 2003. Toward active tremor canceling in handheld microsurgical instruments. IEEE Transactions on Robotics and Automation, 19(5), pp.793-800.

Roberts, S., Osborne, M., Ebden, M., Reece, S., Gibson, N. and Aigrain, S., 2013. Gaussian processes for time-series modelling. Philosophical Transactions of the Royal Society A: Mathematical, Physical and Engineering Sciences, 371(1984), p.20110550.

Ryll, M., Muscio, G., Pierri, F., Cataldi, E., Antonelli, G., Caccavale, F. and Franchi, A., 2017, May. 6D physical interaction with a fully actuated aerial robot. In 2017 IEEE International Conference on Robotics and Automation (ICRA) (pp. 5190-5195). IEEE.

Sandy, T. and Buchli, J., 2017, September. Dynamically decoupling base and end-effector motion for mobile manipulation using visual-inertial sensing. In 2017 IEEE/RSJ International Conference on Intelligent Robots and Systems (IROS) (pp. 6299-6306). IEEE.

Santhakumar, M., 2013. A nonregressor nonlinear disturbance observer-based adaptive control scheme for an underwater manipulator. Advanced Robotics, 27(16), pp.1273-1283.

Sanz, P.J., Ridao, P., Oliver, G., Melchiorri, C., Casalino, G., Silvestre, C., Petillot, Y. and Turetta, A., 2010. TRIDENT: A framework for autonomous underwater intervention missions with dexterous manipulation capabilities. IFAC Proceedings Volumes, 43(16), pp.187-192.

Sarkar, N., Yuh, J. and Podder, T.K., 1999. Adaptive control of underwater vehicle-manipulator systems subject to joint limits. In Proceedings 1999 IEEE/RSJ International Conference on Intelligent Robots and Systems. Human and Environment Friendly Robots with High Intelligence and Emotional Quotients (Cat. No. 99CH36289) (Vol. 1, pp. 142-147). IEEE.

Schwarz, G., 1978. Estimating the dimension of a model. The annals of statistics, 6(2), pp.461-464.

Seo, H., Kim, S. and Kim, H.J., 2017, September. Locally optimal trajectory planning for aerial manipulation in constrained environments. In 2017 IEEE/RSJ International Conference on Intelligent Robots and Systems (IROS) (pp. 1719-1724). IEEE.

Silver, N., 2012. The signal and the noise: the art and science of prediction. Penguin UK.

Simetti, E., Casalino, G., Torelli, S., Sperinde, A. and Turetta, A., 2014. Floating underwater manipulation: Developed control methodology and experimental validation within the TRIDENT project. Journal of Field Robotics, 31(3), pp.364-385.

Slotine, S.B., 1991, June. A general framework for managing multiple tasks in highly redundant robotic systems. In proceeding of 5th International Conference on Advanced Robotics (Vol. 2, pp. 1211-1216).

Southgate, T. and Myers, A.A., 1985. Mussel fouling on the Celtic Sea Kinsale field gas platforms. Estuarine, Coastal and Shelf Science, 20(6), pp.651-659.

Takemura, F., Kobashigawa, S., Hirayama, K., Kawabata, K., Sagara, S., Yamashiro, H. and Kuraya, E., 2015. Development of an Acetic Acid Injection Device for Crown-of-Thorns Starfish Controlled by a Remotely Operated Underwater Robot. JRM, 27(5), pp.571-578.

University of Sydney, The, Australian Centre for Field Robotics - Marine Systems [ON-LINE] Available at: https://sydney.edu.au/engineering/our-research/robotics-and-intelligent-systems/australian-centre-for-field-robotics/marine-systems.html. [Accessed 20th April 2019].

Venkatesan, V., Mohan, S. and Kim, J., 2014, December. Disturbance observer based terminal sliding mode control of an underwater manipulator. In 2014 13th International Conference on Control Automation Robotics & Vision (ICARCV) (pp. 1566-1572). IEEE.

Wampler, C.W., 1986. Manipulator inverse kinematic solutions based on vector formulations and damped least-squares methods. IEEE Transactions on Systems, Man, and Cybernetics, 16(1), pp.93-101.

Whitney, D.E., 1969. Resolved motion rate control of manipulators and human prostheses. IEEE Transactions on man-machine systems, 10(2), pp.47-53.

Williams, C.K. and Rasmussen, C.E., 2006. Gaussian processes for machine learning (Vol. 2, No. 3, p. 4). Cambridge, MA: MIT Press.

Wittenburg, J., 2007. Dynamics of multibody systems. Springer Science & Business Media.

Woolfrey, J., Liu, D. and Carmichael, M., 2016, May. Kinematic control of an autonomous underwater vehicle-manipulator system (auvms) using autoregressive prediction of vehicle motion and model predictive control. In 2016 IEEE International Conference on Robotics and Automation (ICRA) (pp. 4591-4596). IEEE.

Woolfrey, J., Lu, W. and Liu, D., 2019. A Control Method for Joint Torque Minimization of Redundant Manipulators Handling Large External Forces. Journal of Intelligent & Robotic Systems, pp.1-14.

Wu, S.T. and Chuang, Y.C., 2003. Output regulation of robot manipulators with a constantly revolving arm. IEEE transactions on robotics and automation, 19(6), pp.1002-1006.

Yang, X., Pota, H., Garratt, M. and Ugrinovskii, V., 2008. Ship motion prediction for maritime flight operations. IFAC Proceedings Volumes, 41(2), pp.12407-12412.

Yoshikawa, T., 1984, May. Analysis and control of robot manipulators with redundancy. In Robotics research: the first international symposium (pp. 735-747). Cambridge, MA: MIT press.

Yuan, J.S., 1988. Closed-loop manipulator control using quaternion feedback. IEEE Journal on Robotics and Automation, 4(4), pp.434-440.

Yuh, J., Choi, S.K., Ikehara, C., Kim, G.H., McMurty, G., Ghasemi-Nejhad, M., Sarkar, N. and Sugihara, K., 1998, April. Design of a semi-autonomous underwater vehicle for intervention missions (SAUVIM). In Proceedings of 1998 International Symposium on Underwater Technology (pp. 63-68). IEEE.

Yuh, J., Zhao, S. and Lee, P.M., 2001. Application of adaptive disturbance observer control to an underwater manipulator. In Proceedings 2001 ICRA. IEEE International Conference on Robotics and Automation (Cat. No. 01CH37164) (Vol. 4, pp. 3244-3249). IEEE.

Zhang, Y., Guo, D. and Ma, S., 2013. Different-level simultaneous minimization of joint-velocity and joint-torque for redundant robot manipulators. Journal of Intelligent & Robotic Systems, 72(3-4), pp.301-323.